Okinawa Institute of Science and Technology
Graduate University

Thesis submitted for the degree

Doctor of Philosophy

Control and measurement of non-classical properties of cold atomic and optical systems

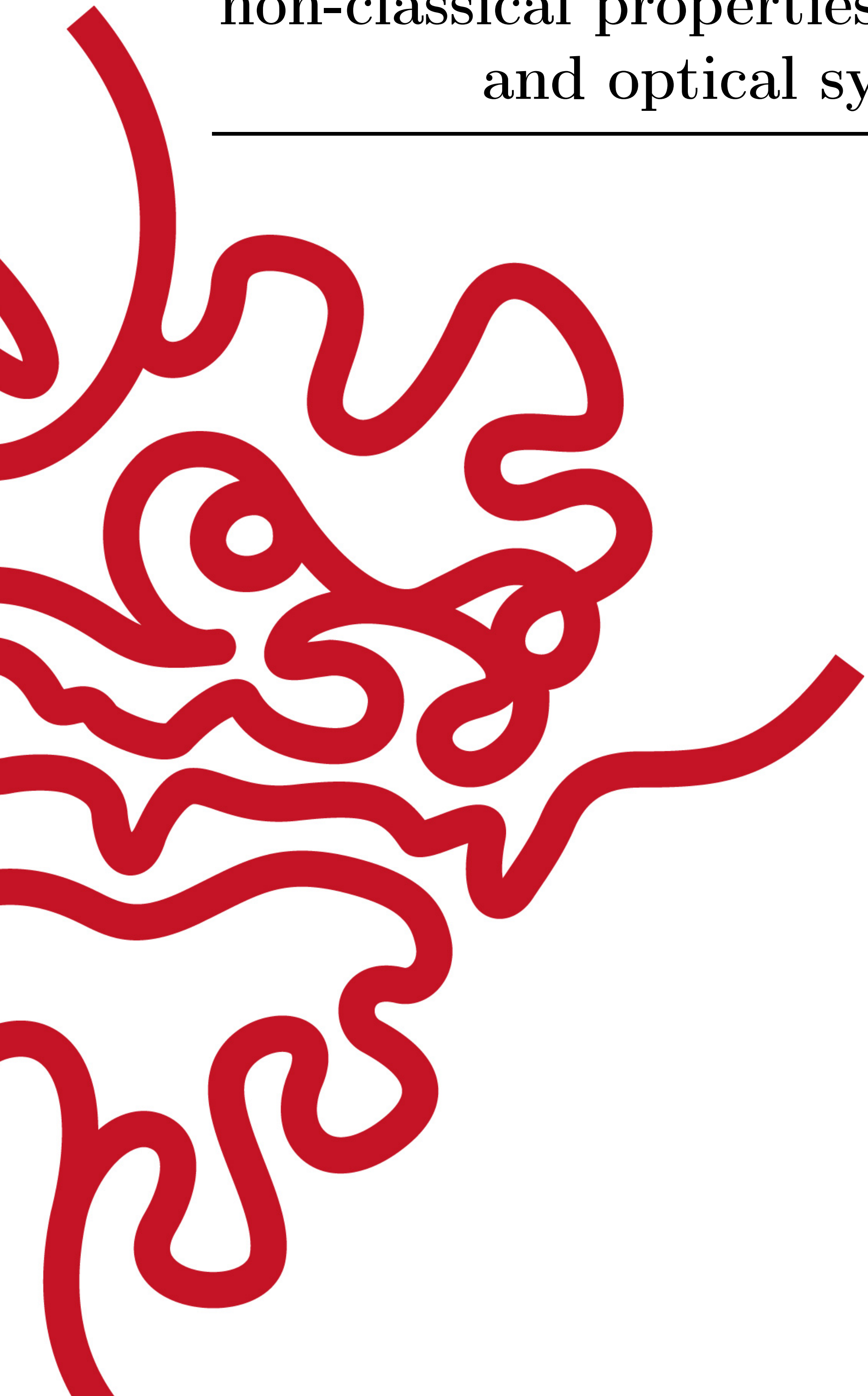

by

Ayaka Usui

Supervisor: **Thomas Busch**

18th December 2020

Declaration of Original and Sole Authorship

I, Ayaka Usui, declare that this thesis entitled *Control and measurement of non-classical properties of cold atomic and optical systems* and the data presented in it are original and my own work.

I confirm that:

- No part of this work has previously been submitted for a degree at this or any other university.
- References to the work of others have been clearly acknowledged. Quotations from the work of others have been clearly indicated, and attributed to them.
- In cases where others have contributed to part of this work, such contribution has been clearly acknowledged and distinguished from my own work.
- None of this work has been previously published elsewhere, with the exception of the following:
  - Chapter 2 and Appendix A are based on a paper published from the New Journal of Physics **33**, 013050 (2020) [1].
  - Chapter 3 is based on a paper published from the New Journal of Physics **19**, 113018 (2017) [2].
  - Chapter 4 is based on a paper published from the New Journal of Physics **20**, 103006 (2018) [3].
  - Chapter 5 is based on a manuscript submitted to Quantum Science and Technology (arXiv:2009.03709) [4].
  - Chapter 6 is based on a manuscript submitted to Quantum (arXiv:2009.03832) [5].

Date: 18th December 2020
Signature: Ayaka Usui

Abstract

Control and measurement of non-classical properties of cold atomic and optical systems

I present the work done during my PhD in the field of quantum gases, metrology, and thermodynamics, which aims at revealing and controlling non-classical correlations and features in various systems. First, I have studied two strongly interacting bosons with synthetic spin-orbit coupling. In this work, I have described the ground state beyond the mean-field regime and explored the existence of non-classical correlations. In a second project, I have investigated the dynamical phase transition in a system of cold atoms trapped in one-dimensional optical lattices. This is the first work to study the dynamical phase transition in a continuous model, and I have revealed the relation between the dynamical phase transition and temporal orthogonality. Third, I consider an impurity coupled to a gas in a two-dimensional lattice. This work has explored the dynamics of the impurity and proposed an approach to probe the local excitation spectrum of the gas at the site coupled to the impurity. Next, I present my contribution to a project on Bayesian estimation with continuous-variable systems. I have examined what is the best probe state for heterodyne or homodyne detection to estimate a single parameter. In the last project, I have explored steady states in quantum thermal machines. As dealing with multi-level and larger numbers of systems quickly becomes intractable, I have mapped them to lower-dimensional systems by utilising the idea of virtual qubits so that one can design autonomous quantum machines beyond a few qubits.

Acknowledgements

Firstly, I would like to acknowledge my PhD supervisor, Thomas Busch, who has guided me for the last four years. Without his advice on research direction and feedback on scientific writing, I could not have accomplished these works present in this thesis. He gave me not only technical advice but also big picture ideas of scientific themes, and they are still helping me decide what is interesting to do.

I would like to thank Thomás Fogarty, who has worked with me the most and given me significant amount of technical advice. Not only that, he cheered me up when I was under pressure from revising manuscripts for journals and writing grants. Without his warm support, my PhD life would be dull and more tense.

I sincerely thank Steve Campbell for his advice on my work and academic career. Even though he works in Ireland, he has given me a lot of scientific ideas and grant writing advice closely via email, Twitter, and Zoom. His attitude toward science significantly affected me during my PhD.

I would like to thank Marcus Huber and Nicolai Friis for letting me spend 100 days at IQOQI-Vienna. With their great ideas and remote help, I have finished two projects present in this thesis. I also want to thank Wolfgang Niedenzu, Simon Morelli, and Elizabeth Agudelo for working on these projects together with me. Furthermore, I want to thank Huber group, called QUITters, who are wonderful people and made me spend enjoyable time in Vienna. The QUITter cup they gave me when I left brings me happy memories.

I would especially like to thank all my collaborators including John Goold, Alessandro Silva, Jordi Mur-Petit, Berislav Buča, and Simon A. Gardiner for their help and the time they spent on our work together.

I would like to thank everyone in Busch unit including Friederike Metz, Juan Polo Gomez, Lewis Ruks, Jing Li, Muhammad Sirajul Hasan, Mohamed Boubakour, Bijita Sarma, and Tai Tran for feedback on the contents of this thesis. Thanks to Mathias Mikkelsen and Karol Gietka, I had interesting discussions during my PhD, and thanks to Christopher Campbell, I enjoyed weekend working. In addition, I am appreciative of Sawako Koki for her administrative support. I also want to give special thanks to former Busch unit members, Angela White, Albert Benseny and Yongping Zhang, who made me aware of Busch unit and encouraged me to come here when I was a master student.

I am greatly appreciative of various support from Okinawa Institute Science and Technology Graduate University and financial support from Research Fellowship of Japan

Society for the Promotion of Science for Young Scientists together with JSPS KAKENHI Grant Number 20J10006.

I cannot help noting here, thanks to Dr. Kato and Mr. Hyodo, who cared of me for a year, I was able to start my PhD, and their support was invaluable.

Importantly, I would like to thank my parents for all their support until now. Since they have never lived out of Osaka, I worried them by moving to Okinawa. I hope they are happy with me going through four years of PhD study.

Last but not least, I want to thank James Schloss for all his support including revising English in this thesis as well as my grant applications and getting me up every morning with his twitch streaming. Although the COVID19 upset our travelling plans completely, he has constantly and remotely supported me, and I appreciate it.

Contents

Chapter 1

Introduction

The state-of-the-art technology of cooling has brought us to the nano-kelvin world [6, 7]. There, we can play around with ideal bosons and fermions and move them around by using optical traps to create almost arbitrary spatial arrangements in all three dimensions [8]. Cooling technology has allowed us to experimentally demonstrate single particle and small system dynamics described by quantum mechanics. Before the invention of laser cooling, the example of a particle in a harmonic trap was purely a theoretical model. Now we can realise such systems and do experiments of isolated systems precisely [9]. Furthermore, this high controllability has been the beginning of a new area of technology, *quantum technology*, which includes quantum simulators [10–12], quantum computers [13], quantum metrology [14], quantum engines [15, 16], etc. By taking into account optical systems, the list also contains quantum communication [17] and quantum cryptography [18–20]. Optical systems can provide not only high controllability but also elegant mathematical description such as Gaussian states [21, 22]. On the other hand, cooling and controlling a system near absolute zero requires precise and flexible measurements. Here again, quantum properties help us and can offer an optimal strategy which gives a path to the Heisenberg limit [14].

For low-temperature systems, a natural but critical question is how thermodynamics is described on nano-kelvin scales [23, 24]. The framework of thermodynamics does not rely on classical mechanics but assumes the existence of many particles, so-called thermodynamics limit. How does thermodynamics work within a quantum description? Similarly to relation between thermodynamics and information in the classical regime, it can be shown that thermodynamics in the quantum regime is strongly connected to quantum information [23]. For example, quantum correlations can be used for thermodynamic tasks in some cases, and it has been reported that work can be extracted from correlations [25].

During my PhD, I worked on several topics of strongly interacting bosons, a new probe scheme for cold atomic lattice systems, a comprehensive study of Bayesian estimation with continuous-variable systems, and a new simplification approach for quantum thermal machines. Although each chapter contains enough information to follow its contents, I will present some basic ideas about them here. Section 1.1 corresponds to introduction of cold atomic systems for Chaps. 2, 3, 4. Section 1.2 reviews basic tools for describing continuous variables used in Chap. 5. Finally, Section 1.3 provides a brief commentary of quantum thermodynamics and quantum thermal machines, and will become a good starting point for Chap. 6.

1.1 Cold atoms

For systems of ideal bosons, S. Bose and A. Einstein predicted theoretically that if the temperature is finite but lower than a critical value, the particles macroscopically occupy the ground state [26]. Such a state is known as a Bose-Einstein condensate (BEC). In 1938, in a system of liquid ^{4}He at the lambda point, superfluidity was observed and was expected to have its origin in Bose-Einstein condensation [27]. However, the interactions in the helium system are too strong to regard it as an ideal Bose system, and so it was questioned that the phenomena in the helium system can be explained as Bose-Einstein condensation [28]. The realisation of BECs in cold gases with weak interaction was attempted, and succeeded in 1995 [26, 29, 30] by using the techniques of laser cooling [31], evaporative cooling [32], magneto-optical trapping [33] and optical traps [34]. Since then, Bose-Einstein condensates of cold atoms have proven to be useful theoretical and experimental tools to study quantum phenomena stemming from weak interactions.

In BECs, a significant number of particles occupy the ground state, and the system can be described by a macroscopic wave-function in the classical mean-field limit. Its dynamics can be described by the Gross-Pitaevskii equation,

$$i\hbar\frac{\partial\Psi(\vec{r},t)}{\partial t} = \left[-\frac{\hbar^2}{2m}\nabla^2 + V(\vec{r}) + \frac{g}{2}|\Psi(\vec{r},t)|^2\right]\Psi(\vec{r},t) \ , \tag{1.1}$$

where the first term on the right hand side is the kinetic term, the second one represents an external trap, and the last one describes interactions between particles and will be explained in the next section. This equation is so simple that it can be solved analytically in some regimes and generally possesses numerically tractable solutions [28]. In addition, systems of cold atoms are so controllable that one can design (i) the external trap term, (ii) the interaction term [9, 35], and (iii) additional external terms:

(i) The gases in the system can be confined in optical traps [36], and thus one can change their external geometry to, for example, harmonic potentials or double-wells. Another important example is periodic lattices [37] that can be described by Bose-Hubbard model [38] and offer a platform for studying quantum and dynamical phase transitions [39] and superfluidity [40]. Furthermore, the dimensionality of the system can be also changed by tuning trap frequencies [41].

(ii) Since the particle interaction strength g can be tuned with a Feshbach resonances [42, 43] as well as the trap frequency, one can cover a wide range of interactions from the mean-field regime to strong interaction regime.

(iii) By adding magnetic fields [28] or applying lasers such that synthetic spin-orbit coupling [44] can be realised, one can control the velocities of cold atoms. This laser-induced spin-orbit coupling is used to make spatial superposition [45] and simulate exotic states such as topological insulators found in condensed matter systems that have intrinsic spin-orbit coupling [46, 47].

Before I discuss the interaction term and its control, let me make more comments on the favourable features of cold atomic systems. Due to their controllability and flexibility, one can also design the system to simulate different types of physics such as condensed matter [35], nuclear physics [48], and high-energy physics [49, 50]. This has shed light on cold atoms as a promising quantum simulator. Furthermore, since cold atomic systems are clean and well-isolated from the environment, they are considered to be useful platforms for understanding non-equilibrium quantum dynamics and finite-time quantum thermodynamics of closed systems [51].

1.1.1 Effective description of interactions in cold atoms

Interactions in cold atomic systems are weak, and two-body interactions are the most dominant because the gases are dilute. Due to the low energy of the interactions, the theoretical description is simplified, and the process of two-body interactions is dominated by s-wave scattering [28]. One does not need to take into account the shape of the potential of the short-range interaction, but can instead use an effective interaction between two particles, which in the mean-field limit is given by

$$U(\vec{r}) = g\delta(\vec{r} - \vec{r'}). \tag{1.2}$$

This is called a contact interaction [52]. Even for stronger interactions, in one-dimensional systems one can still describe the contact interaction with a delta function, and however, in three-dimensional systems one needs to regularise this delta function if the systems are not in the mean-field regime [53, 54]. The process of s-wave scattering is characterised by the scattering length, a, which is given in the Born approximation as [28]

$$a = \frac{m}{4\pi\hbar^2}\int d\vec{r}\, U(\vec{r}) \ . \tag{1.3}$$

This means that the effective interaction coefficient g in Eq. (1.2) is given by

$$g = \frac{4\pi\hbar^2 a}{m}. \tag{1.4}$$

Feshbach resonances allow one to change the scattering length a in experiments to tune the strength of the interactions, which is a powerful tool of cold atom experiments. Feshbach resonances usually utilise Zeeman-splitting by an applied external magnetic field, but can also be created using optical fields [55–57]. In the magnetic case, the s-wave scattering length can be written as a function of the magnetic field as

$$a(B) = a_{\mathrm{bg}}\left(1 - \frac{\Delta}{B - B_0}\right), \tag{1.5}$$

where a_{bg} is the off-resonant value of the scattering length, Δ is the resonance width, and B_0 is the resonant magnetic field. Feshbach resonances in cold gases were first realised in 1998 [42], and it has been shown that the loss of particles can be significant at the resonance point, as three-body interactions are also enhanced. A more detailed explanation is given in Ref. [43].

The discussion above is in three dimensions, but the argument can be applied to one dimension as well since the effective interaction in one dimension is written as [41]

$$g_{\mathrm{1D}} = \frac{4\hbar^2 a}{m\sigma_\perp^2}\frac{1}{1 - Ca/\sigma_\perp} \tag{1.6}$$

where $C = 1.4602$ is a dimensionless value, and the trap potentials along the two confined dimensions are of the same with frequency $\omega_\perp$ with $\sigma_\perp = \sqrt{\hbar/\mu\omega_\perp}$. As seen, by strengthening the confinement $\sigma_\perp$, one can increase g_{1D} [58].

1.1.2 Exact solution of two interacting particles in a one-dimensional harmonic trap

In general, it is difficult to theoretically describe particles interacting beyond mean-field regime. However, some solvable models exist, and I will introduce two one-dimensional models below. First, I will review the exact solution of two interacting particles in a harmonic trap [54].

The Hamiltonian of two particles interacting with a point-like potential is given by

$$H = \sum_{j=1}^{2}\left[\frac{p_j^2}{2m} + \frac{1}{2}m\omega^2 x_j^2\right] + g\delta(x_1 - x_2), \tag{1.7}$$

where m is the mass of each particle, ω is the trap frequency, and g is the interaction strength. This Hamiltonian can be separated into centre-of-mass and relative motion as

$$H(X,x) = H_{\mathrm{com}}(X) + H_{\mathrm{rel}}(x), \tag{1.8a}$$

$$H_{\mathrm{com}}(X) = -\frac{\hbar^2}{2m}\frac{\partial^2}{\partial X^2} + \frac{1}{2}m\omega^2 X^2, \tag{1.8b}$$

$$H_{\mathrm{rel}}(x) = -\frac{\hbar^2}{2m}\frac{\partial^2}{\partial x^2} + \frac{1}{2}m\omega^2 x^2 + \frac{g}{\sqrt{2}}\delta(x), \tag{1.8c}$$

where the scaled centre-of-mass and relative coordinates are defined as $X = (x_1 + x_2)/\sqrt{2}$ and $x = (x_1 - x_2)/\sqrt{2}$, respectively. The full wave-function is then given by the product of the eigenstates of Hamiltonians (1.8b) and (1.8c) as

$$\Psi(X,x) = \Phi(X)\ \phi(x) \tag{1.9}$$

The eigenstates of Hamiltonian (1.8b) correspond to those of a single particle in a harmonic potential. By introducing the energy unit $\hbar\omega$ and dimensionless variables $\tilde{X} = X/a_{\mathrm{ho}}$ and $\tilde{x} = x/a_{\mathrm{ho}}$, with the harmonic oscillator length $a_{\mathrm{ho}} = \sqrt{\hbar/m\omega}$, the wave-function for the centre-of-mass motion is written as the harmonic oscillator eigenstates $\psi_n(\tilde{X}) = C_n H_n(\tilde{X})\mathrm{e}^{-\tilde{X}^2/2}$ with a normalisation constant C_n and the Hermite polynomials H_n of order n (cf. see Ref. [59]).

To find the eigenstates of Hamiltonian (1.8c), one can expand them in harmonic oscillator eigenstates $\psi_n(\tilde{x})$ as

$$\phi(\tilde{x}) = \sum_{n=0}^{\infty} a_n \psi_n(\tilde{x}) \tag{1.10}$$

with coefficients a_n. The eigenstate $\phi(\tilde{x})$ can be either an odd or an even function. When $\phi(\tilde{x})$ is an odd function, the contact interaction has no effect as the amplitude of the eigenstate is zero at the point $\tilde{x} = 0$ of the interaction potential. Therefore, the eigenstate $\phi(\tilde{x})$ is described by the standard harmonic oscillator solutions as

$$\phi^{2m+1}(\tilde{x}) = C H_{2m+1}(\tilde{x}) \mathrm{e}^{-\frac{\tilde{x}^2}{2}}, \tag{1.11}$$

where $m \geq 0$, and C is the normalisation term. Notice that the index of the eigenstate $\phi^{2m+1}(\tilde{x})$ is an odd number because the eigenstate is an odd function.

If $\phi(\tilde{x})$ is an even function, and thus labelled as $\phi^{2m}(\tilde{x})$, it is written as

$$\phi^{2m}(\tilde{x}) = \sum_{n=0}^{\infty} a_{2n}^{2m} \psi_{2n}(\tilde{x}) \tag{1.12}$$

with the harmonic oscillator eigenstates $\psi_{2n}(\tilde{x})$. By inserting Eq. (1.12) into $H_{\mathrm{rel}}\phi^{2m}(\tilde{x}) = \tilde{E}_{2m}\phi^{2m}(\tilde{x})$ with $\tilde{E}_{2m}$ being the corresponding dimensionless eingenenergy, one obtains

$$\sum_{n=0}^{\infty} a_{2n}^{2m} (\epsilon_{2n} - \tilde{E}_{2m}) \psi_{2n}(\tilde{x}) + \tilde{g}\delta(\tilde{x}) \sum_{n=0}^{\infty} a_{2n}^{2m} \psi_{2n}(\tilde{x}) = 0, \tag{1.13}$$

where $\epsilon_n = n + 1/2$ are the dimensionless eigenenergies of harmonic oscillator eigenstates, and $\tilde{g} = g/\sqrt{2}\hbar\omega a_{\mathrm{ho}}$ is the dimensionless interaction strength. By multiplying Eq. (1.13) by the complex conjugate $\psi_k^*(\tilde{x})$, one can utilise the orthogonality of the eigenstates of the Hamiltonian and integrate the whole equation to extract the coefficient, which leads to

$$a_{2k}^{2m}(\epsilon_{2k} - \tilde{E}_{2m}) + \tilde{g}\psi_{2k}(0) \left[\sum_{n=0}^{\infty} a_{2n} \psi_{2n}(\tilde{x}) \right]_{\tilde{x}\to 0} = 0. \tag{1.14}$$

This yields

$$a_{2k}^{2m} = C \frac{\psi_{2k}(0)}{\epsilon_{2k} - \tilde{E}_{2m}} \tag{1.15}$$

with the constant C independent of k. Then, by inserting the coefficient (1.15) into Eq. (1.14), one obtains

$$-\frac{1}{\tilde{g}} = \left[\sum_{n=0}^{\infty} \frac{\psi_{2n}(0)}{\epsilon_{2n} - \tilde{E}_{2m}} \psi_{2n}(\tilde{x}) \right]_{\tilde{x}\to 0} . \tag{1.16}$$

By expanding the harmonic oscillator eigenstates as $\psi_{2n}(\tilde{x}) = \mathrm{e}^{-\tilde{x}^2/2} L_n^{-1/2}(\tilde{x}^2)/\sqrt{\pi}\psi_{2n}(0)$, using Laguerre polynomials $L_n^\alpha(x)$, Eq. (1.16) becomes

$$-\frac{1}{\tilde{g}} = \frac{1}{2\sqrt{\pi}}\left[\mathrm{e}^{-\frac{\tilde{x}^2}{2}}\sum_{n=0}^{\infty}\frac{L_n^{-\frac{1}{2}}(\tilde{x}^2)}{n-\nu}\right]_{\tilde{x}\to 0}, \tag{1.17}$$

with $\nu = \tilde{E}_{2m}/2 - 1/4$. This allows one to use the three following relations [60]

$$\frac{1}{n-\nu} = \int_0^\infty dy\, \frac{1}{(1+y)^2}\left(\frac{y}{1+y}\right)^{n-\nu-1}, \tag{1.18a}$$

$$\sum_{n=0}^{\infty} z^n L_n^\alpha(\tilde{x}) = (1-z)^{-\alpha-1}\mathrm{e}^{\frac{\tilde{x}z}{z-1}}, \tag{1.18b}$$

$$\int_0^\infty dt\, \frac{1}{(1+t)^{a-1-b}}\mathrm{e}^{a-1}\mathrm{e}^{-zt} = \Gamma(a)U(a,b,z), \tag{1.18c}$$

where $\Gamma(a)$ defines the gamma function and $U(a,b,z)$ are the confluent hypergeometric functions. These reduce Eq. (1.17) to

$$-\frac{1}{\tilde{g}} = \frac{1}{2\sqrt{\pi}}\left[\mathrm{e}^{-\frac{\tilde{x}^2}{2}}\Gamma(-\nu)U\left(\nu, \frac{1}{2}, \tilde{x}^2\right)\right]_{\tilde{x}\to 0}. \tag{1.19}$$

For $\tilde{x} \to 0$, the function U satisfies $U(-\nu, 1/2, \tilde{x}^2) \to \Gamma(1/2)/\Gamma(-\nu + 1/2)$, which leads to

$$-\frac{1}{\tilde{g}} = \frac{\Gamma(-\nu)}{2\Gamma(-\nu+1/2)}. \tag{1.20}$$

Now, it is clear how the energy is affected by the interaction strength, and it is given by this relation (1.20). On the other hand, using the relations (1.18) again, the even eigenstates are given by

$$\begin{aligned}\phi^{2m}(\tilde{x}) &= \sum_{n=0}^{\infty} a_{2n}^{2m}\psi_{2n}(\tilde{x}) \\ &= \frac{C}{2\sqrt{\pi}}\mathrm{e}^{-\frac{\tilde{x}^2}{2}}\Gamma(-\nu)U\left(-\nu, \frac{1}{2}, \tilde{x}^2\right),\end{aligned} \tag{1.21}$$

where C is the normalisation term, and ν is determined through $\tilde{g}$ by using Eq. (1.20). The energy of the even eigenstates is given by $\tilde{E}_{2m} = 2\nu + 1/2$. Note that for $g = 0$, ν become integer, i.e. m, and $\tilde{E}_{2m}$ corresponds to the harmonic oscillator eigenenergy. Otherwise, ν is non-integer. As a reminder, the energy of the odd eigenstates is written as $\tilde{E}_{2m+1} = (2m+1) + 1/2$ for $m \geq 0$ such that an analogy between the even and odd states is clear. The total energy is described by the sum of centre-of-mass and relative motion parts as $\epsilon_n + \tilde{E}_{2m} = n + 2\nu + 1$ or $\epsilon_n + \tilde{E}_{2m+1} = n + 2m + 2$.

1.1.3 Tonks-Girardeau gas

In 1960, Girardeau proposed a model for the impenetrable bosons in one dimension that can be solved exactly, and showed a one-to-one correspondence with a model of non-interacting fermions [61]. The system is now called the Tonks-Girardeau (TG) gas, which I will introduce below. Consider N interacting bosons in one dimension, where the Hamiltonian describing the system is given by

$$H^{(N)} = \sum_{i=1}^{N} \left[\frac{-\hbar^2}{2m} \frac{d^2}{dx_i^2} + V(x_i) \right] + g \sum_{i<j}^{N} \delta(x_i - x_j), \tag{1.22}$$

where m is the mass of each particle, x_i is the position of the ith particle, $V(x_i)$ is a potential function, and g is the effective interaction strength between two particles. In the TG limit, $g \to \infty$, the Bose-Fermi mapping theorem enables one to write the many-body bosonic wave-function with just single-particle eigenstates. This can be understood by considering that the hard-core constraint prohibits two particles from being at the same point in space such that

$$\Psi_{\mathrm{B}}(x_1, x_2, ..., x_N) = 0 \qquad \text{if} \quad |x_i - x_j| = 0 \tag{1.23}$$

for $i < j$. This condition on the wave-function can also be satisfied by taking the fermionic formulation and utilising the Pauli principle, hence removing interaction terms. Using a Slater determinant, the fermionic many-body wave-function of the system can be written as

$$\Psi_{\mathrm{F}}(x_1, x_2, ..., x_N) = \frac{1}{\sqrt{N}} \det[\psi_n(x_i)], \tag{1.24}$$

where the $\psi_n(x_i)$ are the single-particle eigenstates of the Hamiltonian (1.22) for $g = 0$. However, since this fermionic wave-function is an antisymmetric function, it is necessary to explicitly symmetrise via

$$\Psi_{\mathrm{B}}(x_1, x_2, ..., x_N) = \prod_{i<j} \mathrm{sgn}(x_i - x_j) \Psi_{\mathrm{F}}(x_1, x_2, ..., x_N). \tag{1.25}$$

Particularly for the ground state, the bosonic wave-function is positive everywhere in space, and thus one can write

$$\Psi_{\mathrm{B}}^{\mathrm{GS}}(x_1, x_2, ..., x_N) = \left| \Psi_{\mathrm{F}}^{\mathrm{GS}}(x_1, x_2, ..., x_N) \right|. \tag{1.26}$$

Note that the mapping cannot be expanded to two or three-dimensional systems. That is because, in one dimension, particles must interact to pass each other, but in higher dimensions they have enough space to avoid collisions. Therefore, necessary conditions for the mapping are the hard-core constraint and a one-dimensional system. The mapping can be applied not only to eigenstates but also to time-evolved states.

A TG gas can be realised by making interactions strong using a Feshbach resonance or by increasing the traverse trap frequency [58, 62, 63]. Also, a lot of theoretical research on TG gases has been reported [64–68], some of which consider TG gases in harmonic potentials [69], TG gases in the presence of a delta-function barrier [70, 71], and TG gases in optical lattices [40, 72, 73]. Furthermore, the dynamics induced by rotating a barrier in a ring system has been studied [74–77], which can create a macroscopic superposition state with strongly correlated bosons, i.e. a NOON state.

Owing to the mapping, a lot of many-particle quantities can be obtained with the knowledge of the single-particle states alone, hence decreasing computation time. Here, I introduce some important examples.

Ground-state fidelity: The ground-state fidelity describes the overlap between the ground states Φ_0 and Ψ_0 in two systems, and is defined as

$$F = |\langle \Phi_0 | \Psi_0 \rangle|^2 \tag{1.27}$$

In a TG gas, the ground-state fidelity can be described with single-particle eigenstates $\phi_i(x)$ and $\psi_i(x)$ of the two systems as [39, 78]

$$F = |\det \boldsymbol{A}|^2 \tag{1.28}$$

with

$$A_{ij} = \int dx \; \phi_i^*(x)\psi_j(x). \tag{1.29}$$

In transformation from Eq. (1.27) to Eq. (1.28), the unit symmetric operator is removed when the systems are integrated.

Loschmidt echo: The Loschmidt echo shows the overlap between the initial state and time-evolved state, and is defined as

$$L(t) = |\langle \Psi(t) | \Psi(0) \rangle|^2, \tag{1.30}$$

which one can represent with single-particle states in the same way as the ground state fidelity, i.e.

$$L(t) = |\det \boldsymbol{A'}|^2 \tag{1.31}$$

with

$$A'_{ij} = \int dx \; \psi_i^*(x,t)\psi_j(x,0). \tag{1.32}$$

Momentum distribution: The momentum distribution cannot be derived with only single-particle states because the momentum operator is affected by the need to symmetrise the fermionic many-body wave-function. However, one can compute the momentum distribution using the reduced single-particle density matrix (RSPDM), which an efficient algorithm to calculate has been developed in Refs. [66, 79]. In general, the RSPDM is written as

$$\rho(x,y) = N \int dx_2 \dots dx_N \; \Psi_{\mathrm{B}}^*(x, x_2 \dots x_N)\Psi_{\mathrm{B}}(y, x_2 \dots x_N), \tag{1.33}$$

while in a TG gas this reduces to

$$\rho(x,y) = \sum_{i,j=1}^{N} \psi_i^*(x) A''_{ij}(x,y) \psi_j(y), \tag{1.34}$$

where

$$\boldsymbol{A''}(x,y) = (\boldsymbol{P}^{-1})^T \det[\boldsymbol{P}] \tag{1.35}$$

with

$$P_{ij} = \delta_{ij} - 2\int_x^y dx' \; \psi_i^*(x')\psi_j(x'). \tag{1.36}$$

Using the RSPDM, the momentum distribution is given by [69]

$$n(k) = \frac{1}{2\pi}\int_{-\infty}^{\infty} dx \int_{-\infty}^{\infty} dy \; \rho(x,y)\mathrm{e}^{-ik(x-y)}. \tag{1.37}$$

von Neumann entropy: The von Neumann entropy can be calculated using the eigenvalues of the density matrix as

$$\begin{aligned} S &= -\operatorname{Tr}[\rho\log\rho] \\ &= -\sum_j \lambda_j \log\lambda_j. \end{aligned} \tag{1.38}$$

The eigenstates of the RSPDM are obtained by solving the equation

$$\int dx \; \rho(x,y)\phi_j(x) = \lambda_j\phi_j(y). \tag{1.39}$$

This means that one can write the RSPDM with the eigenfunctions $\phi_j(x)$ and eigenvalues λ_j as

$$\rho(x,y) = \sum_j \lambda_j\phi_j^*(x)\phi_j(y). \tag{1.40}$$

Examples where it is interesting to calculate von Neumann entropy in a TG gas include cases that probe dynamical phase transitions or detect entanglement.

1.1.4 Synthetic spin-orbit coupling

Spin-orbit coupling (SOC), which describes an interaction of spins with their own motion, is a fundamental property of electrons and well studied in condensed matter physics [80, 81]. The atoms in gaseous BECs are usually charge neutral, and so systems of cold atoms do not have SOC naturally. However, by Raman-dressing BECs, one can simulate a vector potential and SOC [82], which in this case is a coupling between pseudo-spins and their momentum. A method for creating Raman-coupled BECs in one dimension for this has been proposed in Refs. [83, 84]. Through the successful implementation of synthetic magnetic [85] and electric fields [86], SOC has been realised in spin-1/2 Bose gases [44, 87], spin-1 Bose gases [88, 89] and Fermi gases [46, 47].

SOC in cold atoms can be generated experimentally as described below [44], by using, for example, ^{87}Rb in optical dipole traps [90]. By applying a homogeneous magnetic field when the atoms are in an $F = 1$ state, the energy levels split into three sublevels $m_f = 0, \pm 1$, due to the linear Zeeman effect. The system can then be considered as a pseudo-spin-1 system, and removing the third level is required to make it a pseudo-spin-1/2 system (see Fig. 1.1). This is realised by applying a large magnetic

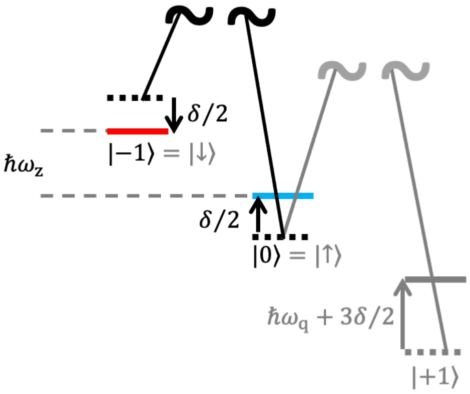

Figure 1.1: Hyperfine states for a $F = 1$ state, reproduced from Ref. [44]. A Zeeman shift creates an energy difference $\hbar\omega_z$ between the states $m_f = -1$ and $m_f = 0$. The states are coupled by lasers, indicated by the thick lines. The detuning from Raman resonance is denoted by δ. The energy gap $\hbar\omega_\mathrm{q}$ is so large that the state $m_f = 1$ can be ignored.

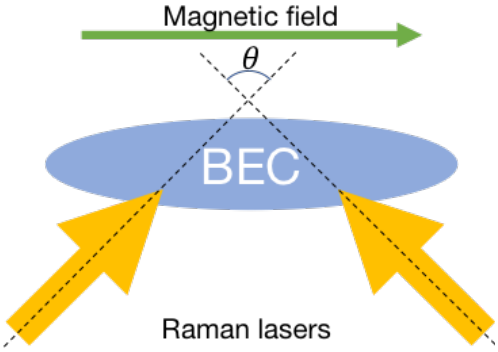

Figure 1.2: A typical experimental set-up of SOC induced by two Raman lasers that intersect at angle θ, reproduced from Ref. [90].

field, so that the energy gap between the states $m_f = -1$ and $m_f = 0$ becomes much larger than the energy gap between the states $m_f = 0$ and $m_f = 1$ due to the quadratic Zeeman effect. By tuning the frequency of the Raman lasers, one can then selectively address only the states $m_f = -1$ and $m_f = 0$. The system is then regarded as a pseudo-spin-1/2 system, or in other words a two-component BEC [28, 91, 92]. The Raman dressing between the levels is then created by a detuned two photon transition (see Fig. 1.1), and the Raman coupling is determined by the coupling strengths between the corresponding states and also the intermediate state.

To introduce the formulation of SOC, consider a two-component BEC driven by a light field in one dimension. For simple explanation, I do not take interactions and the external potential into account. The corresponding Hamiltonian for this two-component BEC is given by [93, 94]

$$\hat{H}_0 = \begin{bmatrix} \dfrac{p_x^2}{2m} + \dfrac{\hbar\delta}{2} & \dfrac{\hbar\Omega}{2}\mathrm{e}^{i2k_Rx} \\ \dfrac{\hbar\Omega}{2}\mathrm{e}^{-i2k_Rx} & \dfrac{p_x^2}{2m} - \dfrac{\hbar\delta}{2} \end{bmatrix}, \tag{1.41}$$

where $p_x = i\hbar(\partial/\partial x)$ is the momentum of the BEC, $\hbar\Omega$ is the Raman coupling strength, $\hbar\delta$ is the detuning from resonance, and k_R is the projected wave number, defined as $k_R = 2\pi/\lambda\sin(\theta/2)$. Here, λ is the wavelength of the lasers and θ is the angle of intersection between the two lasers (see Fig. 1.2). The off-diagonal elements in the

Hamiltonian can be rewritten as

$$\begin{pmatrix} 0 & \frac{\hbar\Omega}{2}\mathrm{e}^{i2k_R x} \\ \frac{\hbar\Omega}{2}\mathrm{e}^{-i2k_R x} & 0 \end{pmatrix} = \mathrm{e}^{ik_R x\hat{\sigma}_z}\frac{\hbar\Omega}{2}\hat{\sigma}_x\mathrm{e}^{-ik_R x\hat{\sigma}_z}, \tag{1.42}$$

using $\mathrm{e}^{ik_R x\hat{\sigma}_z} = I\cos k_R x + i\hat{\sigma}_z \sin k_R x$. By applying a unitary transformation, $\hat{U} = \mathrm{e}^{ik_R x\hat{\sigma}_z}$, to the Hamiltonian (1.41), it is reduced to

$$\begin{aligned} \hat{H} &= \hat{U}^\dagger \hat{H}_0 \hat{U}, \\ &= \frac{p_x^2}{2m}\hat{I} + \gamma p_x\hat{\sigma}_z + \frac{\hbar\delta}{2}\hat{\sigma}_z + \frac{\hbar\Omega}{2}\hat{\sigma}_x, \end{aligned} \tag{1.43}$$

where the SOC strength is $\gamma = \hbar k_R/m$ and some constant terms are ignored for clarity. The induced SOC term agrees with the equally-weighted combination of Rashba SOC $k_x\hat{\sigma}_z - k_z\hat{\sigma}_x$ and Dresselhaus SOC $k_x\hat{\sigma}_z + k_z\hat{\sigma}_x$. Note that, as seen in Eq. (1.41), in this scheme one cannot turn off the Raman coupling completely while keeping the SOC on, because the SOC shares its origin with the Raman coupling. Here, the pseudo-spin is coupled to the linear momentum, but it is also possible to generate coupling between pseudo-spin and angular momentum [95, 96]. Although I will focus on SOC in one dimension, a scheme for realising SOC in two-dimensional systems has been proposed [97], and SOC in two-dimensional Fermi gases has been realised recently [98].

Tunable spin-orbit coupling strength: The SOC strength depends on the projected wave number k_R of the Raman lasers. A straightforward way to change k_R is to change the angle θ between the two Raman lasers. However, practically this is hard to do once an experimental set-up is fixed, and so an alternative way has been proposed that applies a periodic modulation to the power of the Raman lasers [90, 99]

$$\Omega = \Omega_0 + \tilde{\Omega}\cos\omega t, \tag{1.44}$$

where the modulation frequency ω is much larger than any other energy scale in the system, in order to not disturb signals of other energy scales. By using a unitary transformation to remove the modulation term, the Hamiltonian is given by

$$\hat{H}_{\text{eff}} = \frac{p_x^2}{2m}\hat{I} + \left(\gamma p_x + \frac{\hbar\delta}{2}\right) J_0\left(\frac{\tilde{\Omega}}{\omega}\right)\hat{\sigma}_z + \frac{\hbar\Omega_0}{2}\hat{\sigma}_x \tag{1.45}$$

where $J_0(x)$ is the zeroth order Bessel function of the first kind, and high frequency terms such as the modulation frequency ω are ignored. Here, the tunable SOC strength can be written as $\gamma_{\text{eff}} = \gamma J_0(\tilde{\Omega}/\omega)$, which is now determined by the modulation of the Raman lasers. Similarly, the effective detuning becomes $\delta_{\text{eff}} = \delta J_0(\tilde{\Omega}/\omega)$. One can tune the SOC strength dynamically by changing the modulation amplitude $\tilde{\Omega}$, but the tuning must be slower than the modulation frequency as mentioned above. This approach has been demonstrated to work in experiments [100]. Although the discussion above does not take interactions into account, interactions give a nonlinear effect. In the case where interactions within one component are different from those within other component, the SU(2) symmetry of the pseudo-spin is broken, and this approach does not work anymore.

1.2 Continuous-variable systems

Quantum information technology has been developed over the last three decades. Small scale quantum computers have been constructed (e.g. IBM Quantum Experience[1] and Google AI Quantum[2]), and quantum communication via a satellite has been tested [101]. Already, 50-qubit systems for quantum simulators and computing have been realised [102–104]. While I have focused on atomic systems in this thesis so far, I will consider optical systems in this section. They are advantageous for implementations of quantum communication [17] and quantum cryptography [18–20]. In contrast, It is nearly impossible to send atoms over long distance while keeping them cool.

To implement devices for quantum information, one can take discrete [13] or continuous variables [21, 22] to describe quantum states and encoding information on the quantum states. For quantum optical systems, any state can be represented in the photon number basis or be rewritten in the description of continuous variables, e.g. by characterising the state with position and momentum. Which approach should be taken depends on the experimental setup and what one wants to do. I note that choice between the use of discrete and continuous variables does not lie in how many particles are treated. Even if one has a few photons, one can use either discrete or continuous variables.

I consider continuous variables in my work and thus will give a brief review of Gaussian states and Gaussian transformations, which are important tools for continuous-variable systems to encode information. Systems in Gaussian states are described by Gaussian quasi-probability functions in phase space, and Gaussian transformations map any Gaussian state to some Gaussian state. The next subsections loosely follow Ref. [22], and for simple notation, I take $\hbar = 1$.

1.2.1 Basics of Gaussian states and Gaussian transformations

A continuous-variable system is a quantum system that is equivalent to a collection of harmonic oscillators. i.e. a infinite number of bosonic modes. An N harmonic oscillator system builds a Hilbert space $\mathcal{H}^{\otimes N} = \bigotimes_{k=1}^{N} \mathcal{H}_k$ and is associated with N pairs of bosonic field operators $\{\hat{a}_k, \hat{a}_k^\dagger\}_{k=1}^{N}$. Here, $\hat{a}_k$ and $\hat{a}_k^\dagger$ are the annihilation and creation operators, respectively. I represent these operators with a vector

$$\hat{\mathbf{b}} = \left(\hat{a}_1, \hat{a}_1^\dagger, \ldots, \hat{a}_N, \hat{a}_N^\dagger\right), \tag{1.46}$$

which satisfies the bosonic commutation relations

$$\left[\hat{b}_i, \hat{b}_j\right] = \Omega_{ij}, \tag{1.47}$$

---

[1] https://www.ibm.com/quantum-computing/

[2] https://research.google/teams/applied-science/quantum/

where $i, j = 1, \ldots, 2N$, and Ω_{ij} is a component of the symplectic form,

$$\boldsymbol{\Omega} = \bigoplus_{k=1}^{N} \begin{pmatrix} 0 & 1 \\ -1 & 0 \end{pmatrix} . \tag{1.48}$$

Note that the Hilbert space of the system is separable because the Hilbert space is a tensor product of the single-mode Hilbert spaces $\mathcal{H}_k$. The Hilbert space $\mathcal{H}_k$ is an infinite-dimensional space constructed by a Fock state (photon number basis) $\{|n\rangle\}$. Since this is a set of eigenstates of the number operator $\hat{n} = \hat{a}^\dagger \hat{a}$, one can write

$$\hat{a} |0\rangle = 0, \tag{1.49a}$$
$$\hat{a} |n+1\rangle = \sqrt{n+1} |n\rangle , \tag{1.49b}$$
$$\hat{a}^\dagger |n\rangle = \sqrt{n+1} |n+1\rangle , \tag{1.49c}$$
$$\hat{n} |n\rangle = n |n\rangle \tag{1.49d}$$

for $n \geq 0$. Let me introduce other useful field operators, called the quadrature field operators $\{\hat{q}_k, \hat{p}_k\}_{k=1}^{N}$. For conveniences, these operators can be arranged in a vector similar to $\hat{\mathbf{b}}$ as

$$\hat{\mathbf{x}} = (\hat{q}_1, \hat{p}_1, , \ldots , \hat{q}_N, \hat{p}_N)^T . \tag{1.50}$$

The quadrature field operators are composed of the bosonic field operators as

$$\hat{q}_k = \frac{1}{\sqrt{2}} \left(\hat{a}_k^\dagger + \hat{a}_k \right) , \tag{1.51a}$$
$$\hat{p}_k = \frac{i}{\sqrt{2}} \left(\hat{a}_k^\dagger - \hat{a}_k \right) . \tag{1.51b}$$

They represent dimensionless canonical observables of the system. Since the considered system is equivalent to N harmonic oscillators, the quadrature field operators behave like the position and momentum operators of the quantum harmonic oscillator. Additionally, they satisfy the canonical commutation relations

$$[\hat{x}_i, \hat{x}_j] = i\Omega_{ij}. \tag{1.52}$$

Since the quadrature field operators possess continuous spectra, with $\hat{q}$ and $\hat{p}$ the position and momentum operators, one has

$$\hat{q} |q\rangle = q |q\rangle , \tag{1.53a}$$
$$\hat{p} |p\rangle = p |p\rangle , \tag{1.53b}$$

where $q, p \in \mathbb{R}$. These eigenstates $\{|q\rangle\}_{q\in\mathbb{R}}$ and $\{|p\rangle\}_{p\in\mathbb{R}}$ are associated with each other via Fourier transformations as

$$|q\rangle = \frac{1}{2\sqrt{\pi}} \int dp \; \mathrm{e}^{-iqp} \, |p\rangle \, , \tag{1.54a}$$

$$|p\rangle = \frac{1}{2\sqrt{\pi}} \int dq \; \mathrm{e}^{iqp} \, |q\rangle \, . \tag{1.54b}$$

In general, for N-mode Hilbert space, one can write

$$\hat{\mathbf{x}}^T \, |\mathbf{x}\rangle = \mathbf{x}^T \, |\mathbf{x}\rangle \, . \tag{1.55}$$

with $\mathbf{x} \in \mathbb{R}^{2N}$ and $|\mathbf{x}\rangle = (|x_1\rangle \, , \ldots , |x_{2N}\rangle)^T$. By considering the phase space as below, the quadrature eigenvalues $\mathbf{x}$ can be used for continuous variable representation.

Quantum information processing requires information to be encoded in a quantum state. A quantum state is generally represented by a density matrix ρ, and any density matrix can be expressed as a quasi-probability distribution, called a Wigner function, in a real symplectic space, called phase space. The Wigner characteristic function for a quantum state ρ is defined as

$$\chi(\xi) = \mathrm{Tr}\left[\rho \hat{D}(\xi)\right] \tag{1.56}$$

with the Weyl operator given by

$$\hat{D}(\xi) = \exp\left[i \hat{\mathbf{x}}^T \boldsymbol{\Omega} \xi\right] \tag{1.57}$$

with $\xi \in \mathbb{R}^{2N}$. The Wigner function is then obtained by performing the Fourier transform,

$$W(\mathbf{x}) = \int_{\mathbb{R}^{2N}} \frac{d^{2N}\xi}{(2\pi)^{2N}} \exp\left[-i\mathbf{x}^T \boldsymbol{\Omega} \xi\right] \chi(\xi), \tag{1.58}$$

and it is normalised to one. It is often called a quasi-probability distribution because it can be negative. As seen, any quantum state ρ of an N-mode bosonic system can be expressed in the form of a Wigner function on a $2N$-dimensional phase space.

The primary tools for describing continuous variable systems are statistical moments of quantum states. The first moment is called the displacement vector and is written as

$$\bar{\mathbf{x}} = \langle \hat{\mathbf{x}} \rangle = \mathrm{Tr}\left[\hat{\mathbf{x}} \rho\right] \tag{1.59}$$

The second moment is written as

$$\sigma_{i,j} = \frac{1}{2} \left\langle \{ \hat{x}_i - \langle \hat{x}_i \rangle \, , \hat{x}_j - \langle \hat{x}_j \rangle \} \right\rangle , \tag{1.60}$$

where $\{,\}$ is the anticommutator. This gives the covariance matrix $\boldsymbol{\Gamma} = 2\sigma$, which is a real $2N \times 2N$ matrix. Its diagonal elements are the variances of the quadrature operators $\Gamma_{ii} = \Gamma(\hat{x}_i) = \langle (\Delta \hat{x}_i)^2 \rangle$ and provide the Heisenberg relation for position and momentum,

$$\Gamma(\hat{q}_k)\Gamma(\hat{p}_k) \geq \frac{1}{4} \, . \tag{1.61}$$

Gaussian states are fully and conveniently characterised by their first and second moments and have the Wigner representation,

$$W(\mathbf{x}) = \frac{\exp\left[-\left(\mathbf{x}-\bar{\mathbf{x}}\right)^T \mathbf{\Gamma}^{-1}\left(\mathbf{x}-\bar{\mathbf{x}}\right)\right]}{\pi^N \sqrt{\det[\mathbf{\Gamma}]}} \, . \tag{1.62}$$

There are simple descriptions of transformations acting on Gaussian states. In general, a transformation is called a quantum operation if it is a linear map $\mathcal{E}$ which is completely positive with a trace, $0 \leq \mathrm{Tr}[\mathcal{E}\rho] \leq 1$ [13]. Gaussian transformations are quantum operators that keep the Gaussian properties of quantum states, and are defined as

$$\hat{U} = \exp\left\{-i\hat{H}\right\} \, , \tag{1.63}$$

with $\hat{H}$ being the Hamiltonian described by at most second-order polynomials in the field operators. By using annihilation and creation operators $\hat{\mathbf{a}} = (\hat{a}_1, \dots, \hat{a}_N)^T$ and $\hat{\mathbf{a}}^\dagger = (\hat{a}_1^\dagger, \dots, \hat{a}_N^\dagger)$, such a Hamiltonian can be written as

$$\hat{H} = i\left(\hat{a}^\dagger \boldsymbol{\alpha} + \hat{a}^\dagger \mathbf{F} \hat{a} + \hat{a}^\dagger \mathbf{G} \hat{a}^{\dagger T}\right) + \text{h.c.}, \tag{1.64}$$

where $\boldsymbol{\alpha} \in \mathbb{C}^N$, $\mathbf{F}$, and $\mathbf{G}$ are complex matrices, and "h.c." means Hermitian conjugate. For the quadrature operators $\hat{\mathbf{x}}$, a unitary operator describing a Gaussian transformation (Gaussian unitary) is simply described by an affine map,

$$\hat{\mathbf{x}} \to \mathbf{S}\hat{\mathbf{x}} + \mathbf{d} \tag{1.65}$$

with $\mathbf{d} \in \mathbb{R}^{2N}$ being a $2N$ real vector and $\mathbf{S}$ being a $2N \times 2N$ real matrix. The first and second moments are mapped in the same way,

$$\bar{\mathbf{x}} \to \mathbf{S}\bar{\mathbf{x}} + \mathbf{d}, \tag{1.66a}$$

$$\mathbf{\Gamma} \to \mathbf{S}\mathbf{\Gamma}\mathbf{S}^T. \tag{1.66b}$$

1.2.2 Examples of Gaussian states and single-mode Gaussian transformations

I will introduce some basic Gaussian states and transformations which are widely used in continuous-variable systems. At the end, I will give the representation of general single-mode Gaussian state by using them. Here, I restrict myself to pure states, but it is possible to generalise the formulations I will introduce to mixed states.

Considering multiple modes, one can implement beam splitting and two-mode squeezing to mix modes and generate mode entanglement. These operations enrich the continuous-variable systems, particularly for quantum information and metrology [21, 22]. However, I do not discuss multiple modes because it is outside the scope of the introduction needed for the work I will present.

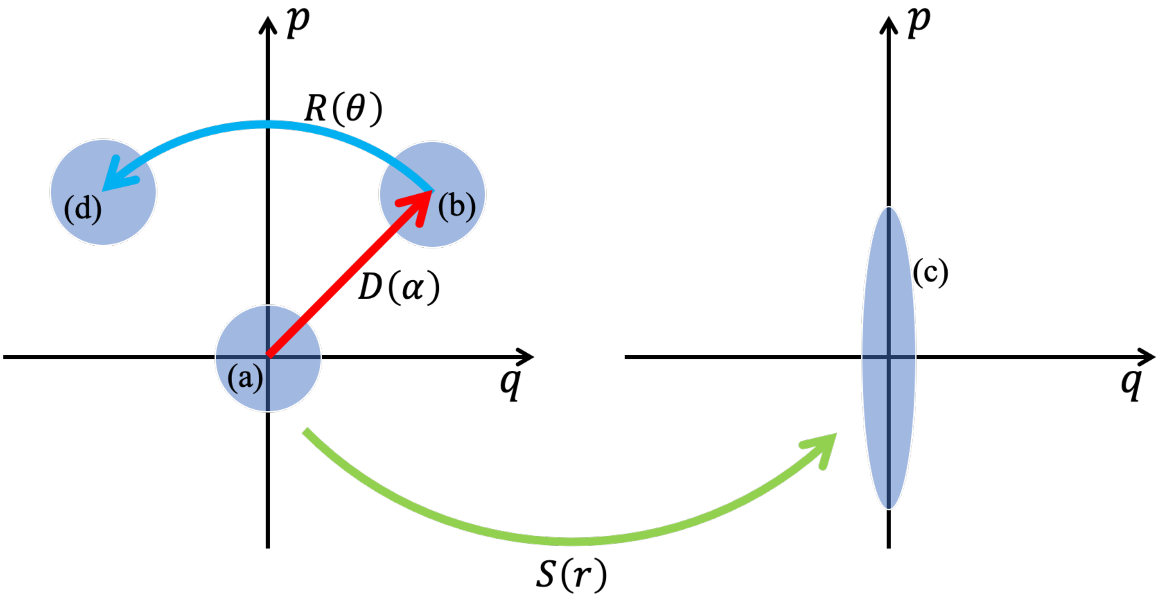

Figure 1.3: Sketch of the cross sections for the Wigner functions of some Gaussian states such as (a) the vacuum state, (b) a displaced state (coherent state), (c) a squeezed state, and (d) a phase rotated state. The widths of these Wigner functions show the variances. The arrows indicate the action of certain Gaussian unitaries on the vacuum state or a displaced state.

Vacuum state: Admittedly, the simplest Gaussian state is the vacuum state $|0\rangle$, which has no photons (see state (a) in Fig. 1.3). In this case, the first moment is zero, and the covariance matrix is the identity,

$$\mathbf{\Gamma} = \mathbf{I} \tag{1.67}$$

which means that the variances of the position and the momentum are minimised in a balanced way.

Displacement and coherent states: A basic Gaussian transformation is the displacement operator. The Hamiltonian of this operator is written by a linear term of the field operators and defined as

$$\hat{D}(\alpha) = \exp\left[\alpha \hat{a}^\dagger - \alpha^* \hat{a}\right], \tag{1.68}$$

which is a complex version of the Weyl operator (1.57) and where $\alpha = (q + ip)/\sqrt{2}$ is the complex amplitude. In the Heisenberg picture, the quadrature operators $\hat{\mathbf{x}}$ are transformed as $\hat{\mathbf{x}} \to \hat{\mathbf{x}} + \mathbf{d}$, where $\mathbf{d} = (\sqrt{2}\,\mathrm{Re}[\alpha], \sqrt{2}\,\mathrm{Im}[\alpha])^T$. Particularly, by displacing the vacuum state, a coherent state is created, $|\alpha\rangle = D(\alpha)\,|0\rangle$ (see state (b) in Fig. 1.3). Coherent states are eigenstates of the anihilation operator $\hat{a}$ such that $\hat{a}\,|\alpha\rangle = \alpha\,|\alpha\rangle$, and can be written in the Fock basis as

$$|\alpha\rangle = \exp\left(\frac{-1}{2}\,|\alpha|^2\right) \sum_{n=0}^{\infty} \frac{\alpha^n}{\sqrt{n!}}\,|n\rangle\,. \tag{1.69}$$

A useful fact is that the overlap between two coherent states $|\alpha\rangle$ and $|\beta\rangle$ is given by

$$|\langle\beta|\alpha\rangle|^2 = \exp\left[-|\beta-\alpha|^2\right]. \tag{1.70}$$

Single-mode squeezing: An interaction Hamiltonian that contains terms of quadrature squares $\hat{a}^{\dagger 2}$ and $\hat{a}^2$ is called the single-mode squeezing operator, defined by

$$\hat{S}(r) = \exp\left[\frac{r}{2}\left(\hat{a}^{\dagger 2} - \hat{a}^2\right)\right], \tag{1.71}$$

where $r \in \mathbb{R}$ is the squeezing strength. In the Heisenberg picture, the quadrature operators $\hat{\mathbf{x}} = (\hat{q}, \hat{p})^T$ are transformed as $\hat{\mathbf{x}} \to \mathbf{S}(r)\hat{\mathbf{x}}$, where

$$\mathbf{S}(r) = \begin{pmatrix} \mathrm{e}^{r} & 0 \\ 0 & \mathrm{e}^{-r} \end{pmatrix}. \tag{1.72}$$

A squeezed vacuum state is written in Fock basis as [105]

$$|0, r\rangle = \frac{1}{\sqrt{\cosh r}} \sum_{n=0}^{\infty} \frac{\sqrt{(2n)!}}{2^n n!} \left(-\tanh r\right)^n |2n\rangle. \tag{1.73}$$

The covanriance matrix is written as $\mathbf{\Gamma} = \mathbf{S}\mathbf{I}\mathbf{S}^T = \mathbf{S}(2r)$, where the variance of one quadrature is reduced below one, while the other goes above one (for $r > 0$, see state (c) in Fig. 1.3).

By replacing the real squeezing strength with a complex number, i.e. $r \to \xi = r e^{i\varphi}$, the squeezing angle is tuned by changing φ. Nevertheless, the role of this angle can be taken over by a rotation operator which will introduced below.

Phase rotation: A phase rotation is generated by a freely propagating Hamiltonian $\hat{H} = \theta \hat{a}^\dagger \hat{a}$ and defined as

$$\hat{R}(\theta) = \exp\left[-i\theta \hat{a}^\dagger \hat{a}\right] \tag{1.74}$$

In the Heisenberg picture, the quadrature operators transform as $\hat{\mathbf{x}} \to \mathbf{R}(\theta)\hat{\mathbf{x}}$, where

$$\mathbf{R}(\theta) = \begin{pmatrix} \cos\theta & \sin\theta \\ -\sin\theta & \cos\theta \end{pmatrix} \tag{1.75}$$

with θ being a rotation angle (see state (d) in Fig. 1.3).

General single-mode Gaussian state: If the squeezing strength is complex $\xi = r e^{i\varphi}$, where $r \geq 0$ and $0 \leq \varphi < 2\pi$, one can write the map as $\hat{S}(\xi) = \hat{R}(\varphi/2)\hat{S}(r)$. Any single-mode Gaussian transformation can be written by applying a map $\hat{D}(\alpha)\hat{R}(\varphi/2)\hat{S}(r)$ to the vacuum state, i.e. imposing a squeezing operator first, then a rotation operator, and finally displacement operator, and can be given by

$$|\alpha, \varphi, r\rangle = \hat{D}(\alpha)\hat{R}\left(\frac{\varphi}{2}\right)\hat{S}(r)\,|0\rangle. \tag{1.76}$$

The first moment is given by $\mathbf{d} = (\sqrt{2}\,\mathrm{Re}[\alpha], \sqrt{2}\,\mathrm{Im}[\alpha])^T$, and the covariance matrix is given by

$$\mathbf{\Gamma} = \mathbf{R}\left(\frac{\varphi}{2}\right)\mathbf{S}(2r)\mathbf{R}\left(\frac{\varphi}{2}\right)^{T}. \tag{1.77}$$

If the order of these operators is different, the resulting state also differs.

1.3 Quantum thermodynamics

In 1959, Scovil and Schulz-DuBois showed that a three-level maser can be regarded as a Carnot heat engine [106], where amplified light and population inversion between the two lower levels were interpreted using the language of thermodynamics, such as work and heat. This is said to be the first paper to show a connection between quantum mechanics and heat engines. By noting that operating an engine backwards leads to refrigeration, Geusic *et al.* proposed refrigerators by using masers [107] and lasers [108]. Interestingly, these papers were published before the famous laser cooling papers [109, 110], which have led to the realisation of atomic Bose-Einstein condensates and are not related to the thermodynamic discussion of these Refs. [107, 108]. Later, Alicki and Kosloff independently presented pioneering papers that treat a quantum open system as a heat engine [111, 112]. However, since there were few experimental setups and tools to demonstrate and examine quantum systems, these papers did not attract attention until 2000's [113].

The invention of laser cooling [6, 109, 110] has led to the experimental realisation of cold atoms and promoted the study of quantum mechanics. Cold atoms, along with trapped ions [114, 115], superconducting circuit [116–118], quantum dots [119], and nitrogen-vacancy (NV) centres [120], can be used to create qubits in clean environments that do not disturb the system. This enables us to study quantum mechanics and develop new technology that takes advantage of quantum features. In addition, the cooling techniques have provided platforms and tools to investigate thermodynamics at the small scale where the thermodynamic limit cannot be reached and non-classicality appears. Even though thermodynamics is a macroscopic theory governing processes such as the conversion between heat and work under constraints on system variables such as temperature, it is closely connected to quantum mechanics because the macroscopic behaviour must emerge from the physics at the microscale. Therefore, the field of thermodynamics in the quantum regime, *quantum thermodynamics*, has grown and attracted attention in recent years. The advent of quantum information theory has led to a slew of novel approaches and enabled great recent progress [23, 24]. We now have a much deeper understanding of the foundations of thermodynamics. However, our knowledge about the fundamental role of quantum effects in thermodynamics is still incomplete.

A fascinating attempt to study thermodynamic tasks at small scales is to design autonomous thermal machines [15]. These types of machines operate without external resources or control, and enable us to truly investigate quantum effects without classical interruptions. It is known that this class of machines plays many roles such as engines [15], refrigerators [15], heat pumps [108], clocks [121], thermometers [122], entanglement generators [123], and thermal transistors [124], and even can perform multiple tasks [125]. It is interesting to see how quantum features enhance the performance of these tasks compared to their classical counterparts and reveal the optimal limit. Simple autonomous machines such as qubit machines have been well investigated, but multi-level thermal machines have not yet because the size of larger machines leads to more complicated steady states and dynamics. However, since it has been reported that multiple levels have potential to improve thermodynamic properties [126], multi-level thermal machines should be explored and harnessed.

So far, several theoretical tools have been invented for predicting the qualitative behaviour of two-level target systems coupled to few-qubit machines and a thermal environment: virtual qubits [127], collisional models [128, 129], and reset master equations [130, 131]. For example, considering a virtual qubit for a two-qubit machine provides the virtual temperature T_{v}, which has information about which task the target system in this setup can perform: when T_{v} is positive and smaller than the temperature of the baths used for the machine, the machine can cool down the target system; when T_{v} is larger, it can warm up the target system; when T_{v} is negative, the target system can extract work from the machine [127]. However, simplification beyond simple qubit systems is still a challenge due to competing effects involved with multiple levels. To address this issue, in Chap. 6 I will propose a new tool for simplifying multi-level thermal machines. The proposed tool will contribute to the investigation of thermodynamic properties and design of multi-level thermal machines.

Chapter 2

Spin-orbit coupling in the presence of strong atomic correlations

Spin-orbit coupling (SOC) was initially found in systems of charged particles and is well studied in condensed matter physics [80, 81]. Although BECs generated by cold atomic systems have no charge, Raman-dressed BECs can be used to simulate a vector potential and mimic SOC [82]. In this case, the coupling is between a pseudo-spin and its momentum, while in condensed matter the coupling is an interaction between spins of electrons and their motion. A method to Raman-couple BECs in one dimension has been proposed in Refs. [83, 84], and SOC has been realised in spin-1/2 Bose gases [44, 87], spin-1 Bose gases [88, 89], and Fermi gases [46, 47] (cf. see Sec. 1.1.4).

A lot of research about SOC in cold atomic systems has focused on many-particle systems such as two-component BECs, for example by imposing the mean-field approximation and dealing with effective single-particle states. It has been shown that by changing parameters such as the SOC strength, the Raman coupling strength, and the contact interaction strength, BECs with SOC can undergo phase transitions between three phases: the stripe phase, the magnetised phase, and the single minimum phase [132]. In the stripe phase, the ground state is given by a superposition between a state with positive momentum and one with negative momentum. The momentum difference generates an interference pattern in the total density profile, which leads to a supersolid-like structure. In the magnetised phase, the ground state is degenerate between the positive-momentum state and the negative-momentum state. In the single minimum phase, the ground state has no momentum.

I note that the discussion in mean-field regime is limited to the weak contact interaction regime and does not fully explain many-body effects. Nevertheless, it is important to reveal effects of strong contact interaction because strong interactions are ingredients of quantum correlations such as entanglement. Moreover, while quantum systems are described with operators, with the mean-field approximation the systems are simplified to classical fields, which does not allow one to study quantum correlations. However, without the mean-field approximation, many-body systems are often difficult to solve, except fot some special cases [133–135].

Few-particle systems help one address the problems, because these systems enable one to explore the systems exactly and cover even the strong interaction regime exactly [54, 136–138]. Recently, several studies of few-boson systems with SOC have been reported [139–145]. For example, a mapping to an effective spin model has been proposed in a regime of weak Raman coupling [140], and two-particle systems were shown to acquire a maximally entangled state in the pseudo-spin space for certain parameters [142].

In this work, I investigate the ground state of a system of two interacting particles with SOC in one dimension by solving the system exactly for any strengths of the contact interaction and SOC. These results are then compared to the ground state in the mean-filed regime to see the unique effects of strong interactions. What I found is that the competition between the contact interactions and the SOC leads to a lifting of degeneracies in the energy spectrum. In some parameter regimes, this results in the appearance of a unique ground state that is not seen within the mean-field regime. I adopt a harmonic oscillator basis to describe the composition of this ground state, and show that the ground state can include a contribution from the anti-symmetric spin state, even though the system is bosonic. This state is therefore called the anti-symmetric (AS) ground state. The AS ground state does not belong to any of the three phases existing in the mean-field limit (the stripe phase, magnetised phase, and single minimum phase). Also the emergence of the AS ground state is signalled by a decay of entanglement between the real space and the pseudo-spin degrees of freedom. These results help one bridge a gap between single-particle and many-body states.

This chapter is organised as follows. In Sec. 2.1, I introduce the Hamiltonian describing the two-particle system in the presence of SOC in real space and expand the atomic position Hilbert space of the system in harmonic oscillator basis states associated with the centre of mass and relative motional degrees of freedom. In Sec. 2.2, I study the effects and competition of the interactions and SOC on the energy spectrum and the ground states. In particular, I show the emergence of the AS ground state. I also explore the entanglement in the pseudo-spin degrees of freedom and between the real space components and the pseudo-spin components. In Sec. 2.3 I conclude and give an outlook. Details about the systematic representation of the Hamiltonian in matrix form are given in Appendix A. The code to generate the data presented in this chapter is available online[1].

This project has been accomplished in collaboration with Thomás Fogarty and Steve Campbell and Simon Gardiner and Thomas Busch. I have been involved in all discussions and carried out all calculations in this project. The work presented in this chapter was published in the New Journal of Physics **33**, 013050 (2020) [1].

2.1 Formulation

I consider an effective one-dimensional model of two repulsively interacting bosons in a harmonic trap in the presence of SOC. The Hamiltonian is given by

$$H = \sum_{j=1}^{2} \left[\frac{p_j^2}{2m} + \frac{1}{2} m\omega^2 x_j^2 + \frac{\hbar k_{\mathrm{soc}}}{m} p_j \sigma_z^{(j)} + \frac{\hbar\Omega}{2} \sigma_x^{(j)} + \frac{\hbar\Delta}{2} \sigma_z^{(j)} \right] + H_{\mathrm{int}}(|x_1 - x_2|) \,, \quad (2.1)$$

---

[1] https://doi.org/10.5281/zenodo.3592115

where m is the mass of each particle, ω is the trap frequency, k_{soc} is the SOC strength, Ω is the Raman coupling strength, Δ is a detuning, and $\sigma_{x,z}$ are Pauli matrices. SOC is described by the third term, which couples the momentum and pseudo-spin degrees of freedom. At low temperatures, one can assume that the scattering between the particles has s-wave character, and particles interact only when they meet at a point, so that the interaction potentials can be described by a delta function (cf. Sec.1.1.1). The interaction strengths depend on the internal states of the particles, and so the interaction term $H_{\mathrm{int}}(|x_1 - x_2|)$ can be written as

$$\begin{aligned} &\langle x_1, \uparrow; x_2, \uparrow | H_{\mathrm{int}} | x_1, \uparrow; x_2, \uparrow \rangle = g_{\uparrow\uparrow}\delta(x_1 - x_2) \ , \\ &\langle x_1, \uparrow; x_2, \downarrow | H_{\mathrm{int}} | x_1, \uparrow; x_2, \downarrow \rangle = g_{\uparrow\downarrow}\delta(x_1 - x_2) = \langle x_1, \downarrow; x_2, \uparrow | H_{\mathrm{int}} | x_1, \downarrow; x_2, \uparrow \rangle \ , \\ &\langle x_1, \downarrow; x_2, \downarrow | H_{\mathrm{int}} | x_1, \downarrow; x_2, \downarrow \rangle = g_{\downarrow\downarrow}\delta(x_1 - x_2) \ . \end{aligned} \tag{2.2}$$

These interaction strengths are given by a function of the respective 3D scattering lengths, $a_{3\mathrm{D}}$, via $g_{i,j} = 4\hbar^2 a_{3\mathrm{D}}/\left(1 - C a_{3\mathrm{D}}/d_\perp\right) m d_\perp^2$ for $i, j =\downarrow, \uparrow$, where $d_\perp = \sqrt{\hbar/m\omega_\perp}$ quantifies the trap width in the transverse direction for a trap of frequency $\omega_\perp$, and the constant C is given by $C \approx 1.4603$ [41]. The interaction strengths can be tuned experimentally by controlling the scattering lengths, $a_{3\mathrm{D}}$, and $\omega_\perp$. For simplicity, I neglect the effects of the detuning by setting $\Delta = 0$ and restrict myself to the symmetric situation, $g_{\uparrow\uparrow} = g_{\downarrow\downarrow} = g$, although it is technically straightforward to generalise to arbitrary values of $g_{\uparrow\uparrow}$ and $g_{\downarrow\downarrow}$.

In the absence of Raman coupling, the Hamiltonian (2.1) is diagonal within the pseudo-spin basis. As discussed in Ref. [139], the solutions are then provided by the eigenstates of the bare harmonic oscillator Hamiltonian for two interacting particles with an added momentum boost of $\sqrt{2}\hbar k_{\mathrm{soc}}$ originating from the SOC. By using the two-particle solution shown in the introduction (cf. Eqs. (1.9)(1.21)(1.11)),

$$\Psi(X, x) = \Phi_m(X)\phi_n(x), \tag{2.3}$$

the eigenstates of the system are provided by

$$\psi^{\uparrow\uparrow}(X, x) = \mathrm{e}^{-i\sqrt{2}k_R X}\Psi(X, x), \tag{2.4a}$$

$$\psi^{\uparrow\downarrow}(X, x) = \mathrm{e}^{-i\sqrt{2}k_R x}\Psi(X, x), \tag{2.4b}$$

$$\psi^{\downarrow\uparrow}(X, x) = \mathrm{e}^{i\sqrt{2}k_R x}\Psi(X, x), \tag{2.4c}$$

$$\psi^{\downarrow\downarrow}(X, x) = \mathrm{e}^{i\sqrt{2}k_R X}\Psi(X, x), \tag{2.4d}$$

where the different pseudo-spin configurations gain momentum kicks in either centre-of-mass (spin up-up and down-down) or relative (spin up-down and down-up) directions. The eigenvalues of (2.4a) are all the same as $\tilde{E} = \hbar\omega + \hbar^2 k_{\mathrm{R}}^2/m$.

Due to the bosonic nature of the atoms, the system is symmetric under exchange for particles. To clarify the symmetries inherent in the system, let me introduce scaled centre-of-mass (COM) and relative coordinates as $x_\pm = (x_1 \pm x_2)/\sqrt{2}$ and an alternative pseudo-spin basis given by $|\downarrow\downarrow\rangle$, $|\uparrow\uparrow\rangle$, $|\mathrm{S}\rangle = (|\downarrow\uparrow\rangle + |\uparrow\downarrow\rangle)/\sqrt{2}$ and $|\mathrm{A}\rangle = (|\downarrow\uparrow\rangle - |\uparrow\downarrow\rangle)/\sqrt{2}$. The first three states of this basis are symmetric under exchange of pseudo-spins, and the last one is anti-symmetric. Therefore, the wave-functions of relative motion for the three symmetric basis states are symmetric, i.e. an even function of relative coordinate x_-. On the other hand, the wave-functions of the anti-symmetric basis have to be an odd function of the relative coordinate x_-. This restriction on the relative coordinate component is included when diagonalising the Hamiltonian. Expansion of the Hamiltonian in the harmonic oscillator basis makes it easier to treat this restriction. Using this pseudo-spin basis and the harmonic oscillator basis instead of the position representation, the Hamiltonian can be written as

$$\begin{aligned} H = {} & \hbar\omega\left(\hat{a}_+^\dagger \hat{a}_+ + \frac{1}{2}\right) + \hbar\omega\left(\hat{a}_-^\dagger \hat{a}_- + \frac{1}{2}\right) \\ & - i\Lambda\left(\hat{a}_+^\dagger - \hat{a}_+\right)\left(|{\downarrow\downarrow}\rangle\langle{\downarrow\downarrow}| - |{\uparrow\uparrow}\rangle\langle{\uparrow\uparrow}|\right) - i\Lambda\left(\hat{a}_-^\dagger - \hat{a}_-\right)\left(|\mathrm{S}\rangle\langle\mathrm{A}| + |\mathrm{A}\rangle\langle\mathrm{S}|\right) \\ & + \Upsilon\left(|\mathrm{S}\rangle\langle{\downarrow\downarrow}| + |{\downarrow\downarrow}\rangle\langle\mathrm{S}| + |\mathrm{S}\rangle\langle{\uparrow\uparrow}| + |{\uparrow\uparrow}\rangle\langle\mathrm{S}|\right) + H_{\mathrm{int}} \,, \end{aligned} \tag{2.5}$$

where $\hat{a}_\pm^\dagger, \hat{a}_\pm$ are the creation and annihilation operators for modes in the COM and relative coordinate space, $\Lambda = \hbar k_{\mathrm{soc}}\sqrt{\hbar\omega/m}$ and $\Upsilon = \hbar\Omega/\sqrt{2}$. The basis states of this Hamiltonian are labelled as $|n_+, n_-, \eta\rangle$ for the quantum numbers n_+, n_- of the COM and relative motion and for the pseudo-spin states given by $\eta \in \{\downarrow\downarrow, \mathrm{S}, \uparrow\uparrow, \mathrm{A}\}$. The restriction of the symmetry on the wave-functions is rewritten as a restriction on the quantum number n_- of the relative motion, given by

$$n_- = \begin{cases} 2u & \text{for} \quad \eta \in \{\downarrow\downarrow, \mathrm{S}, \uparrow\uparrow\} \\ 2u+1 & \text{for} \quad \eta \in \{\mathrm{A}\} \end{cases} \,, \tag{2.6}$$

for integer $u \geq 0$. Thus, the basis states are given by

$$|n, 2u, \downarrow\downarrow\rangle \,, |n, 2u, \mathrm{S}\rangle \,, |n, 2u, \uparrow\uparrow\rangle \,, |n, 2u+1, \mathrm{A}\rangle \,, \tag{2.7}$$

for integer $n \geq 0$. Note that there is no restriction on the COM. The eigenstates of the Hamiltonian (2.5) can be written as

$$\psi_j = \sum_{n_+, n_-, \eta} a^{(j)}_{n_+, n_-, \eta} |n_+, n_-, \eta\rangle \tag{2.8}$$

for $\{n_+, n_-, \eta\} \in \{n, 2u, \downarrow\downarrow\}, \{n, 2u, \mathrm{S}\}, \{n, 2u, \uparrow\uparrow\}, \{n, 2u+1, \mathrm{A}\}$. The interaction part of the Hamiltonian can be expanded within this basis and described using the eigenstates $\phi_n(x)$ of the harmonic oscillator by

$$\begin{aligned} \left\langle n_+, n_-, \eta \middle| H_{\mathrm{int}} \middle| n_+', n_-', \eta' \right\rangle &= g_\eta \delta_{n_+, n_+'} \delta_{\eta, \eta'} \int dx_- \; \delta(x_1 - x_2) \phi_{n_-}(x_-) \phi_{n_-'}(x_-) \\ &= \frac{g_\eta}{\sqrt{2}} \delta_{n_+, n_+'} \delta_{\eta, \eta'} \phi_{n_-}(0) \phi_{n_-'}(0) \,, \end{aligned} \tag{2.9}$$

where $g_{\mathrm{S}} = g_{\mathrm{A}} = g_{\uparrow\downarrow}$. It is worth noting that the states with $\eta = \mathrm{A}$ do not feel the contact interaction because $\phi_{n_-}(0) = 0$ for n_- being an odd number and that the interactions in general lead to energy shifts and couplings between different basis states. In Appendix A, I detail how to systematically construct a matrix representation of this

Hamiltonian.

The expansion in the harmonic oscillator basis gives a clear and intuitive interpretation of the coupling between the states. Let me start with non-interacting bosons, where the basis states can be classified by harmonic oscillator energies (rows in Fig. 2.1(a)). The SOC terms generate two possible transitions. For states that have the same pseudo-spins ($|{\downarrow\downarrow}\rangle$, $|{\uparrow\uparrow}\rangle$), the SOC terms couple states that have different COM quantum numbers n_+ and the same relative motion quantum number n_-, for example, $|m_+, m_-, {\downarrow\downarrow}\rangle$ and $|(m_+ + 1), m_-, {\downarrow\downarrow}\rangle$ for integers $m_+, m_- \geq 0$. This leads to momentum kicks for the COM motion of $\mathrm{e}^{i\sqrt{2}k_{\mathrm{soc}}x_+}$ for $|{\downarrow\downarrow}\rangle$ states and $\mathrm{e}^{-i\sqrt{2}k_{\mathrm{soc}}x_+}$ for $|{\uparrow\uparrow}\rangle$ states. On the other hand, for states that have different pseudo-spins ($|\mathrm{S}\rangle$, $|\mathrm{A}\rangle$), the SOC terms couple states that have the same COM quantum numbers n_+ and different relative motion quantum numbers n_-. This leads to momentum kicks for the relative motion of $\mathrm{e}^{i\sqrt{2}k_{\mathrm{soc}}x_-}$ for $(|\mathrm{S}\rangle + |\mathrm{A}\rangle)/\sqrt{2} = |{\downarrow\uparrow}\rangle$ and $\mathrm{e}^{-i\sqrt{2}k_{\mathrm{soc}}x_-}$ for $(|\mathrm{S}\rangle - |\mathrm{A}\rangle)/\sqrt{2} = |{\uparrow\downarrow}\rangle$. Finally, the Raman coupling couples symmetric pseudo-spin states, $|{\downarrow\downarrow}\rangle$, $|{\uparrow\uparrow}\rangle$, and $|\mathrm{S}\rangle$.

Considering finite contact interactions, the interaction terms raise the energy levels of $|{\downarrow\downarrow}\rangle$ and $|{\uparrow\uparrow}\rangle$ for finite g and those of $|\mathrm{S}\rangle$ for finite $g_{\uparrow\downarrow}$ (see Fig. 2.1(b,c)). Notice that the interaction terms do not affect the $|\mathrm{A}\rangle$ states as mentioned. These interaction energy rises can be calculated exactly and are equal to $2\nu\hbar\omega$, where ν is given by solving

$$\frac{-\sqrt{2}\hbar\omega a_{\mathrm{ho}}}{g_{ij}} = \frac{\Gamma(-\nu))}{2\Gamma(-\nu + 1/2)} \tag{2.10}$$

for $i, j = \downarrow, \uparrow$ with harmonic oscillator length $a_{\mathrm{ho}} = \sqrt{\hbar/m\omega}$ [54]. As 2ν is always smaller than 1, these interaction energy rises do not lead to level crossings or new degeneracies.

The contact interaction terms can affect other couplings. It is shown that the interaction terms cause avoided crossings in Ref. [139]. The generated energy shifts compete with the SOC, and the resulting effects depend on whether their origin is due to g or $g_{\uparrow\downarrow}$ (see Fig. 2.1(b,c)). For non-zero $g_{\uparrow\downarrow}$, the energy gaps for transitions from $|\mathrm{S}\rangle$ to $|\mathrm{A}\rangle$ shrink, while the energy gaps for transitions from $|\mathrm{A}\rangle$ to $|\mathrm{S}\rangle$ grow. (see Fig. 2.1(b)). On the other hand, for non-zero g, the energies of states with $|{\downarrow\downarrow}\rangle$ and $|{\uparrow\uparrow}\rangle$ all rise by the same amount, which means that the energy gaps between the coupled states stay fixed at $\hbar\omega$ (see Fig. 2.1(c)). Therefore, different kinds of contact interactions lead to different effects depending on the energy-level structure. The consequences of these will be explored below.

2.2 Results

In this section, I will discuss the ground state and the energy spectrum of the system for the three cases of no interactions, finite anti-aligned interactions $g_{\uparrow\downarrow}$, and finite aligned interactions g. To interpret each of the ground states, I will look at the populations of the different pseudo-spin states, their momentum and density correlations, and their entanglement properties. For clarity, I will use scaled parameters for all plots by giving all energies in units of $\hbar\omega$, all momenta in units of $\hbar/a_{\mathrm{ho}}$, and all interaction strengths in units of $\hbar\omega a_{\mathrm{ho}}$. However, throughout the text I will work with unscaled variables.

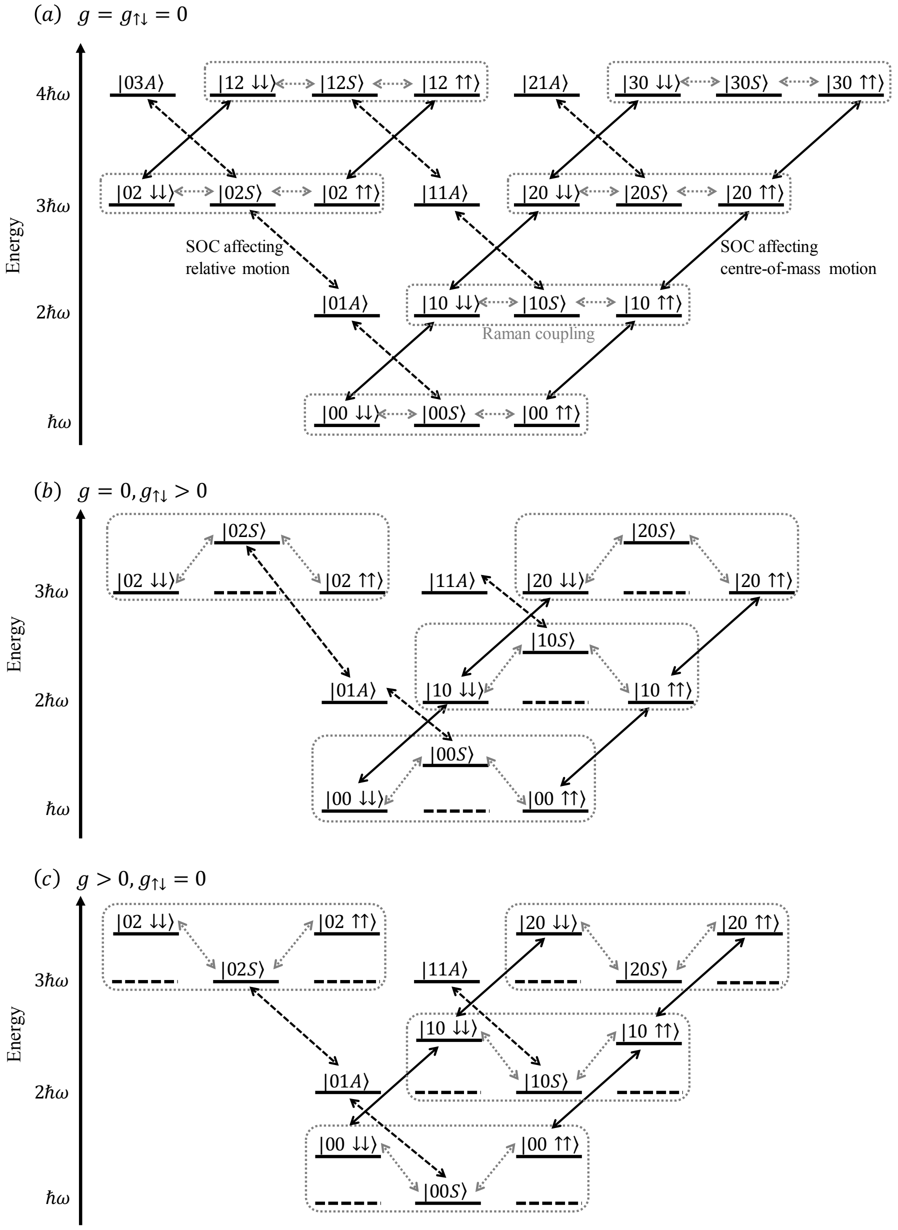

Figure 2.1: Energy level diagrams for Hamiltonian (2.5), using the harmonic oscillator basis. The basis states are labelled as $|n_+, n_-, \eta\rangle$ for the quantum numbers n_+, n_- of the COM and relative motion, and the pseudo-spin states given by $\eta \in \{\downarrow\downarrow, \mathrm{S}, \uparrow\uparrow, \mathrm{A}\}$. The black arrows represent transitions due to SOC, with full arrows exciting COM motion and dashed arrows exciting relative motion. The gray dotted arrows represent transitions due to Raman coupling. In panel (a) there are no interactions, whereas in panels (b) interactions between different pseudo-spin states exist, and in panel (c) interactions between the same pseudo-spin states exist. Level shifts due to the interactions can be seen in panels (b,c).

Before discussing two interacting bosons, I will introduce the ground state in the presence of SOC in the mean-field regime, where three different ground state phases exist [132, 146]: the stripe phase, the magnetised phase, and the single minimum phase. The stripe phase is named after the fact that an interference pattern appears due to superposition of positive and negative momenta [146]. In contrast, in the magnetised phase the gas either fully adopts positive or negative momentum. In the single minimum phase, having zero momentum gives the lowest energy, and the spectrum only possess a single minimum in the momentum. For non-interacting bosons, only the stripe phase and the single minimum phase exist. In free space, the critical point between these two phases is given by $\hbar\Omega_\mathrm{c} = 2\hbar^2 k_\mathrm{soc}^2/m$, and it is known numerically that for harmonically trapped systems the value of the critical point is lower [142].

2.2.1 Zero interactions ($g = g_{\uparrow\downarrow} = 0$)

In the non-interacting limit, the Hamiltonian of SO-coupled systems is analogous to that of certain collective spin models, namely the Dicke model [147] and the Lipkin-Meshkov-Glick (LMG) model [148]. The explicit connection between SO-coupled systems and the Dicke model was established in Refs. [149, 150], and there is a direct relation between the Dicke and LMG models shown in, for example, Ref. [151]. In the thermodynamic limit, the LMG model is a paradigmatic example of strongly interacting systems, and the ground state exhibits a second order phase transition at a critical value of an applied field [152, 153]. This corresponds to the transition between the stripe phase and the single minimum phase for SO-coupled systems when changing the Raman coupling strength. This transition in the LMG model is characterised by a divergence in the second derivative of the ground state energy and is also signalled by the lifting of existing degeneracies in the spectrum [154]. The LMG model is represented by a single large N-dimensional spin. In the thermodynamic limit, one phase is effectively given by a double-well configuration possessing a ground state energy degeneracy, while in the other phase a gapped spectrum exists. This feature is similar to the form of the dispersion relation for the stripe phase and the single minimum phase. Obviously, a two-particle system is far from the thermodynamic limit and therefore cannot be expected to exhibit all characteristics of the transition, e.g. the discontinuity in the second derivative of the energy [150]. Nevertheless, in the two SO-coupled particle system, at a value Ω, the degeneracies in the two-particle spectrum are still lifted (see Fig. 2.2 and cf. Fig. 1 of Ref. [154]). I define the value of Ω at which this happens as Ω_lift.

In the absence of Raman coupling, the ground state of the system is three-fold degenerate: $|{\downarrow\downarrow}\rangle$ with COM motion $\mathrm{e}^{ik_\mathrm{soc}x_+}$ in the positive direction, $|{\uparrow\uparrow}\rangle$ with COM motion $\mathrm{e}^{-ik_\mathrm{soc}x_+}$ in the negative direction, and the combination of $|{\downarrow\uparrow}\rangle$ and $|{\uparrow\downarrow}\rangle$ keeping the symmetry of pseudo-spin states with finite relative motion. With Raman coupling present, coherent coupling between the three states reduces the energy. In the strong Raman coupling limit, $\Omega \gg \Omega_\mathrm{lift}$, the ground state becomes an equally-weighted superposition of all pseudo-spin states, $\psi \sim \left(|{\downarrow\downarrow}\rangle - |{\downarrow\uparrow}\rangle - |{\uparrow\downarrow}\rangle + |{\uparrow\uparrow}\rangle\right)/2$.

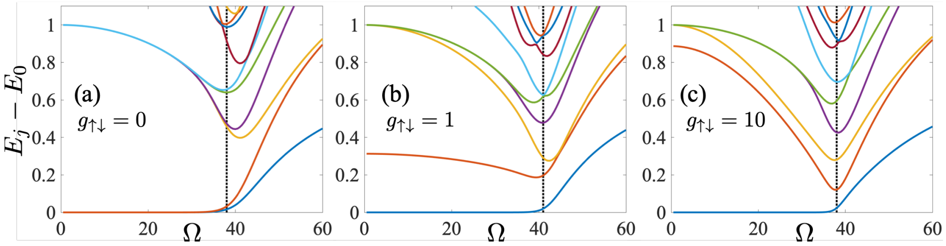

Figure 2.2: Energy differences $E_j - E_0$ between the jth excited states ($j = 1, 2, \ldots$) and the ground state, for fixed $k_\mathrm{soc} a_\mathrm{ho} = 5$ and $g/\hbar\omega a_\mathrm{ho} = 0$. (a) No interactions, $g_{\uparrow\downarrow}/\hbar\omega a_\mathrm{ho} = 0$; (b) weak interactions, $g_{\uparrow\downarrow}/\hbar\omega a_\mathrm{ho} = 1$; (c) strong interactions, $g_{\uparrow\downarrow}/\hbar\omega a_\mathrm{ho} = 10$. The dotted lines indicate the points at which the degeneracies are lifted: (a) $\Omega_\mathrm{lift}/\omega \simeq 38$ for $g_{\uparrow\downarrow}/\hbar\omega a_\mathrm{ho} = 0$, (b) $\Omega_\mathrm{lift}/\omega \simeq 41$ for $g_{\uparrow\downarrow}/\hbar\omega a_\mathrm{ho} = 1$, and (c) $\Omega_\mathrm{lift}/\omega \simeq 38$ for $g_{\uparrow\downarrow}/\hbar\omega a_\mathrm{ho} = 10$. The points are defined as the point where E_0 and E_1 start to deviate, $(E_1 - E_0)/\hbar\omega \gtrsim 10^{-2}$.

2.2.2 Anti-aligned interactions ($g_{\uparrow\downarrow} > 0,\ g = 0$)

Next, I will consider finite interactions between anti-aligned spins $g_{\uparrow\downarrow} > 0$. The energy level scheme is shown in Fig. 2.1(b), where one can see that the interaction lifts some degeneracies as the energy of the basis state $|\mathrm{S}\rangle$ increases. This degeneracy resolution is also seen in Fig. 2.2(b,c).

I will consider $\Omega \ll \Omega_\mathrm{lift}$ first. Without the interactions, the ground state is composed of three degenerate states. For $g_{\uparrow\downarrow} > 0$, the ground state is the symmetric spin state with positive momentum of the COM motion $|{\downarrow\downarrow}\rangle\, \mathrm{e}^{ik_\mathrm{soc}x_+}$ and negative one of $|{\uparrow\uparrow}\rangle\, \mathrm{e}^{-ik_\mathrm{soc}x_+}$. The first excited state is the symmetric superposition of the anti-aligned states, each of which has non-zero relative motion, $\psi \sim |{\downarrow\uparrow}\rangle\, \mathrm{e}^{ik_\mathrm{soc}x_-} + |{\uparrow\downarrow}\rangle\, \mathrm{e}^{-ik_\mathrm{soc}x_-}$. The energy shift from the ground state energy is $2\nu\hbar\omega$, where ν is given by solving Eq. (2.10) and determined by $g_{\uparrow\downarrow}$. In the strong coupling regime $\Omega \gg \Omega_\mathrm{lift}$, the effect of the interactions becomes negligible, and the ground state approaches that of no interactions, which is an equally-weighted superposition of all the pseudo-spin states. In the crossover regime between weak and strong couplings Ω, the spectrum has higher-lying avoided crossings [139], and I will focus on this regime below. Note that Ω_lift is only slightly modified by the interactions (see Fig. 2.2(b,c)), due to the fact that the resulting energy shift can be $\Delta E = \hbar\omega$ at most, which is small compared to the energy scales given by the recoil energy $\hbar^2 k_\mathrm{soc}^2/2m^2$ and the Raman coupling $\hbar\Omega$.

Let me look at the contribution to the ground state of each pseudo-spin state (see Fig. 2.3). For weak interaction ($g_{\uparrow\downarrow}/\hbar\omega a_\mathrm{ho} = 1$, see panel (a)) and for weak Raman coupling ($\Omega/\omega \lesssim 10$), the ground state is given approximately by $\psi \sim \left(|{\downarrow\downarrow}\rangle + |{\uparrow\uparrow}\rangle\right)/\sqrt{2}$. This is reminiscent of the ground state in the stripe phase in BECs with SOC, which is a single-particle state written as $\psi_\downarrow(x)\mathrm{e}^{ik_\mathrm{soc}x}\,|{\downarrow}\rangle + \psi_\uparrow(x)\mathrm{e}^{-ik_\mathrm{soc}x}\,|{\uparrow}\rangle$ [132]. For increasing Raman coupling strength Ω, a larger component of anti-aligned states emerges in the ground state, but I note that the symmetric states $\{|{\downarrow\downarrow}\rangle, |\mathrm{S}\rangle, |{\uparrow\uparrow}\rangle\}$ are dominant (see inset in panel (a)). This behaviour is also seen for systems with strong interactions ($g_{\uparrow\downarrow}/\hbar\omega a_\mathrm{ho} = 10$, see panel (b)), but one also can see that components of the aligned states ($|{\downarrow\downarrow}\rangle$, $|{\uparrow\uparrow}\rangle$) drop quickly for increasing Ω such that the population of the anti-aligned states ($|{\downarrow\uparrow}\rangle$, $|{\uparrow\downarrow}\rangle$) becomes larger. This occurs around the value of

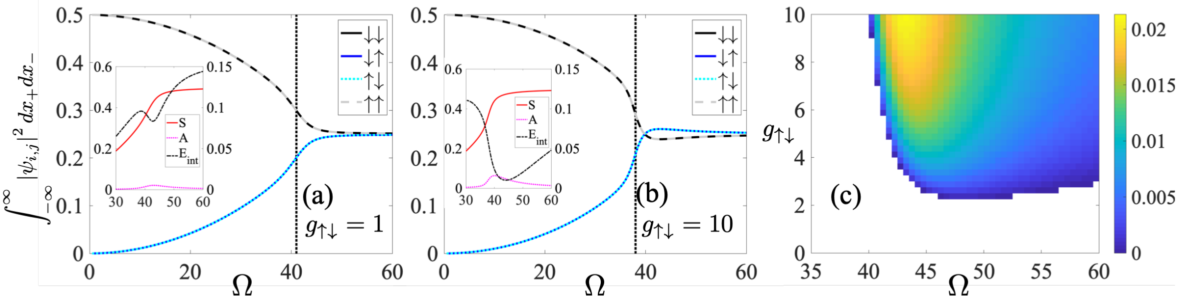

Figure 2.3: Population of each pseudo-spin state of the ground state with $k_{\rm soc}a_{\rm ho} = 5$ fixed for (a) weak interactions, $g_{\uparrow\downarrow}/\hbar\omega a_{\rm ho} = 1$ and (b) strong interactions, $g_{\uparrow\downarrow}/\hbar\omega a_{\rm ho} = 10$. The black dotted lines indicate $\Omega_{\rm lift}/\omega \simeq 41$ in (a) and $\Omega_{\rm lift}/\omega \simeq 38$ in (b). The insets show the population of the states $|{\rm S}\rangle$ (red line) and $|{\rm A}\rangle$ (pink dotted line) using the left axis and the interaction energy (black dashed line) using the right axis. (c) Population difference $\int dx_1 \int dx_2 \,(|\psi_{\downarrow\uparrow}|^2 + |\psi_{\uparrow\downarrow}|^2 - |\psi_{\downarrow\downarrow}|^2 - |\psi_{\uparrow\uparrow}|^2)$ of the ground state as a function of Ω and $g_{\uparrow\downarrow}$. Only positive values, where the anti-aligned states dominate, are shown.

$\Omega = \Omega_{\rm lift}$. This inversion is seen over a wide range of strong interactions and appears for $g_{\uparrow\downarrow}/\hbar\omega a_{\rm ho} \gtrsim 2$ (see panel (c)). This is not analogous to any phases in BECs with SOC in the weakly interacting mean-field regime. Increasing Ω even further, the inversion is getting smaller, and the ground state is becoming close to the ground state of the single minimum phase.

One may be tempted to think that the ground state contains more interaction energy when larger contribution of the anti-aligned states $|{\downarrow\uparrow}\rangle$ and $|{\uparrow\downarrow}\rangle$ are present. However, as shown in the inset in panel (b), the increase in the population from the anti-aligned states is due to an increase in the population of the anti-symmetric state $|{\rm A}\rangle$, which does not feel the interaction. As shown in insets in panels (a,b), when the anti-symmetric state $|{\rm A}\rangle$ emerges, the interaction energy decreases. This population imbalance inversion is a few-body effect, and one can also see a sign of this in Ref. [140]. Note that the inversion is not seen when treating single-particle states or BECs within the mean-field approximation. I therefore refer to the unique regime after this inversion as the AS ground state phase, as the anti-symmetric state is the dominant contribution.

The crossover from the ground state resembling the stripe phase to the AS ground state is also visible in the overall momentum and density distribution (see Fig. 2.4). For weak interaction ($g_{\uparrow\downarrow}/\hbar\omega a_{\rm ho} = 1$, see Fig. 2.4(a,b)), when the AS state is not seen, the ground state momentum distribution is dominated by a finite COM momentum for $\Omega \lesssim \Omega_{\rm lift}$ and $\Omega \gtrsim \Omega_{\rm lift}$ both. However, for strong interactions ($g_{\uparrow\downarrow}/\hbar\omega a_{\rm ho} = 10$, see Fig. 2.4(c,d)), the momentum distribution has equal contributions from the COM and relative momenta for $\Omega \gtrsim \Omega_{\rm lift}$, which means that significant amounts of the anti-aligned states $|{\downarrow\uparrow}\rangle$ and $|{\uparrow\downarrow}\rangle$ appear. On the other hand, the density distribution exhibits an interference pattern along the COM coordinate and a bisection due to the contact interaction at $x_- = 0$ for $\Omega \lesssim \Omega_{\rm lift}$ (see Fig. 2.4(e,g)). Even for increasing Ω, the interference pattern remains for weak interactions (see panel (f)). However, for strong interactions, a more pronounced pattern along the relative coordinate appears while the interference pattern disappears along the COM coordinate (see panel (h)). These

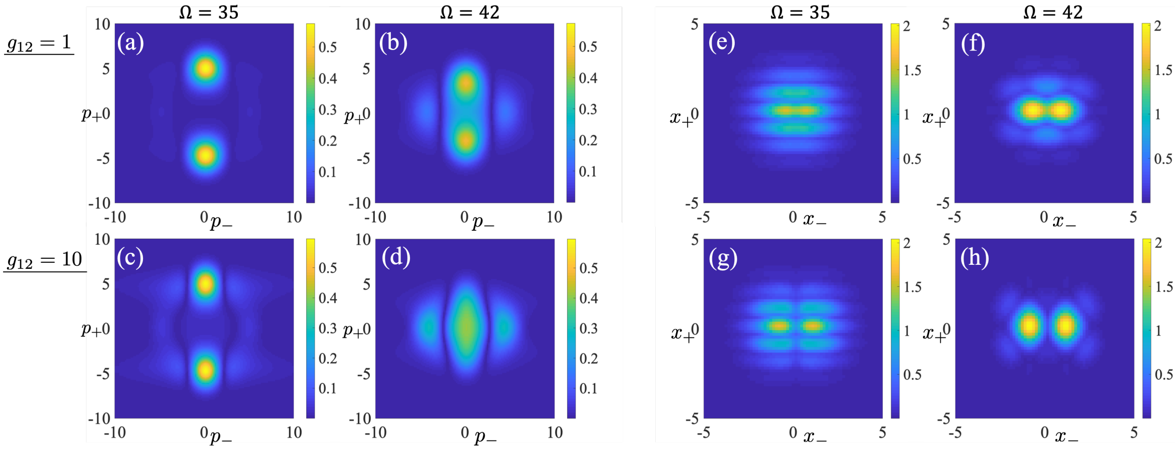

Figure 2.4: Overall momentum distributions (a-d) and overall density distributions (e-h) for weak interaction $g_{\uparrow\downarrow}/\hbar\omega a_{\text{ho}} = 1$ (upper row) and for strong interaction $g_{\uparrow\downarrow}/\hbar\omega a_{\text{ho}} = 10$ (lower row) with $k_{\text{soc}}a_{\text{ho}} = 5$ fixed. In panels (a,c,e,g), $\Omega/\omega = 35$, and in panels (b,d,f,h) $\Omega/\omega = 42$, which are below and above the value for which the inversion occurs.

changes in the density and momentum distributions imply the appearance of the AS ground state.

Next, I will discuss non-classical correlations in the system. First, I will look at the concurrence as the entanglement measure of the pseudo-spin degree of freedom, which is constructed from the density matrix after tracing over the real space components. Since the wave-function of the ground state is written as $|\psi\rangle = \sum_{\chi} \phi_{\chi}(x_1, x_2)\,|\chi\rangle$ for $\chi \in \{\downarrow\downarrow, \downarrow\uparrow, \uparrow\downarrow, \uparrow\uparrow\}$, the density matrix can be written as $\rho = |\psi\rangle\langle\psi|$, and the reduced density matrix after tracing over the position space is given by

$$\rho_{\text{spin}} = \begin{pmatrix} \theta & \beta & \beta & \gamma \\ \beta & \epsilon & \mu & \beta \\ \beta & \mu & \epsilon & \beta \\ \gamma & \beta & \beta & \theta \end{pmatrix} . \tag{2.11}$$

The inner products of the two aligned components are given by $\theta = \langle\phi_{\downarrow\downarrow}|\phi_{\downarrow\downarrow}\rangle = \langle\phi_{\uparrow\uparrow}|\phi_{\uparrow\uparrow}\rangle$ and $\gamma = \langle\phi_{\downarrow\downarrow}|\phi_{\uparrow\uparrow}\rangle = \langle\phi_{\uparrow\uparrow}|\phi_{\downarrow\downarrow}\rangle$ due to the symmetry, while the inner products of two anti-aligned components are given by $\epsilon = \langle\phi_{\downarrow\uparrow}|\phi_{\downarrow\uparrow}\rangle = \langle\phi_{\uparrow\downarrow}|\phi_{\uparrow\downarrow}\rangle$ and $\mu = \langle\phi_{\downarrow\uparrow}|\phi_{\uparrow\downarrow}\rangle = \langle\phi_{\uparrow\downarrow}|\phi_{\downarrow\uparrow}\rangle$. The diagonal elements of the density matrix are given by the population of each pseudo-spin state. Finally, the inner products of one aligned and one anti-aligned component are all equivalent due to the symmetry and given by $\beta = \langle\phi_{\downarrow\downarrow}|\phi_{\downarrow\uparrow}\rangle = \langle\phi_{\downarrow\downarrow}|\phi_{\uparrow\downarrow}\rangle = \langle\phi_{\uparrow\uparrow}|\phi_{\uparrow\downarrow}\rangle = \langle\phi_{\uparrow\uparrow}|\phi_{\downarrow\uparrow}\rangle$ and the same for their Hermitian conjugates.

The concurrence is given as

$$C_{\text{spin}} = \max\{0, \sqrt{\lambda_1} - \sqrt{\lambda_2} - \sqrt{\lambda_3} - \sqrt{\lambda_4}\} , \tag{2.12}$$

where the λ_j are the eigenvalues of $\rho_{\text{spin}}(\sigma_y \otimes \sigma_y)\rho^*_{\text{spin}}(\sigma_y \otimes \sigma_y)$ in descending order for $j = 1, 2, 3, 4$ [155, 156]. For separable states, the concurrence is zero, and for

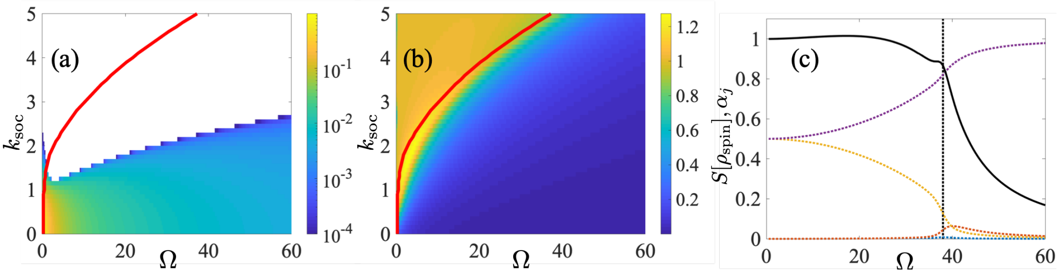

Figure 2.5: (a) Concurrence and (b) vNE of the ground state for a range of $k_{\text{soc}}a_{\text{ho}}$ with $g_{\uparrow\downarrow}/\hbar\omega a_{\text{ho}} = 10$ fixed. The red lines indicate the value of Ω_{lift} for each k_{soc}, and in (a) the white area corresponds to $C_{\text{spin}} = 0$. Even though some values of $C_{\text{spin}} = 0$ are as small as 10^{-4}, they do not come from numerical errors since the limitation of the numerically calculation is higher order than 10^{-4}. (c) vNE as a function of Ω for $k_{\text{soc}}a_{\text{ho}} = 5$ fixed (black line). The coloured, dotted lines represent the values of the eigenvalues α_j of the reduced density matrix ρ_{spin} for $j = 1, 2, 3, 4$. The black dotted line indicates $\Omega_{\text{lift}}/\omega \simeq 38$.

maximally entangled states it is equal to 1. I plot the concurrence as a function of Raman coupling Ω and SOC strength k_{soc} with contact interaction strength fixed as $g_{\uparrow\uparrow}/\hbar\omega a_{\text{ho}} = 10$ in Fig. 2.5(a). In the limit of $k_{\text{soc}}, \Omega \to 0$, the ground state is given by $\left(|\downarrow\downarrow\rangle + |\uparrow\uparrow\rangle\right)/\sqrt{2}$, which results in $C_{\text{spin}} \to 1$ since the ground state corresponds to the maximally entangled Bell state. Notice that in this limit the diagonal terms θ and the off-diagonal terms γ of the reduced density matrix (2.11) go to 1/2, and the rest of the inner products disappear. The off-diagonal terms γ show the correlation between $|\downarrow\downarrow\rangle$ and $|\uparrow\uparrow\rangle$. For finite k_{soc}, the entanglement decays because the momentum provided by the SOC suppresses the off-diagonal terms γ and kills the correlation. The SOC term acts as an effective dephasing channel on the pseudo-spin states causing the decoherences while the diagonal terms, in other words, the populations remain unaffected. As a remarkable feature, the entanglement suddenly vanishes. This phenomenon is sometimes referred to as entanglement sudden death [157]. The red line in Fig. 2.5(a) indicates the values at which the energy degeneracies are lifted. The behaviour of the entanglement is not consistent with the red line, in short the pseudo-spin entanglement is not a useful indicator of the population inversion. On the other hand, it is worth looking at entanglement between the pseudo-spin space and real space as will be shown below, because the effective dephasing caused by the SOC implies that strong correlations are established between them.

As the overall state is pure, the von Neumann entropy (vNE) of the reduced density matrix ρ_{spin} can be used as the measure of entanglement between the pseudo-spin space and real space. It is defined as

$$\begin{aligned} S[\rho_{\text{spin}}] &= -\mathrm{Tr}\left[\rho_{\text{spin}} \log_2 \rho_{\text{spin}}\right] \\ &= -\sum_{j=1}^{4} \alpha_j \log_2 \alpha_j, \end{aligned} \tag{2.13}$$

where α_j is the jth eigenvalue of the reduced density matrix, $\rho_{\text{spin}}\phi_j = \alpha_j\phi_j$. The behaviour of the vNE can be connected to the populations of the pseudo-spins through the eigenvalues of ρ_{spin} (see Fig. 2.5(c)). The two eigenvalues can be explicitely calculated as $\alpha_1 = \theta - \gamma = \langle\phi_{\downarrow\downarrow}|\phi_{\downarrow\downarrow}\rangle - \langle\phi_{\downarrow\downarrow}|\phi_{\uparrow\uparrow}\rangle$ (yellow dotted) and $\alpha_2 = \epsilon - \mu = \langle\phi_{\downarrow\uparrow}|\phi_{\downarrow\uparrow}\rangle - \langle\phi_{\downarrow\uparrow}|\phi_{\uparrow\downarrow}\rangle$ (orange dotted). Also, noticing that $\alpha_3 \approx 0$ (blue dotted) allows one to approximate the last eigenvalue as $\alpha_4 \approx \theta + \gamma + \epsilon + \mu = \langle\phi_{\downarrow\downarrow}|\phi_{\downarrow\downarrow}\rangle + \langle\phi_{\downarrow\downarrow}|\phi_{\uparrow\uparrow}\rangle + \langle\phi_{\downarrow\uparrow}|\phi_{\downarrow\uparrow}\rangle + \langle\phi_{\downarrow\uparrow}|\phi_{\uparrow\downarrow}\rangle$ (purple dotted). It is interesting to see how the vNE reacts to changes of the Raman coupling strength Ω. In the limit of $\Omega \ll \Omega_{\mathrm{lift}}$, the vNE remains close to 1, which is half its maximal value (see Fig. 2.5(c)). That is predictable since the $|\downarrow\downarrow\rangle$ and $|\uparrow\uparrow\rangle$ states which dominate the system are linked to the COM motion in the positive and negative directions, respectively, while the other states, $|\downarrow\uparrow\rangle$ and $|\uparrow\downarrow\rangle$, have lower populations and do not contribute the correlations. When Ω is close to Ω_{lift}, a kink appears in the behaviour of the vNE (see Fig. 2.5(c)), which can be linked to the increase of the population of the anti-symmetric state $|\mathrm{A}\rangle$. This is also signalled by an increase of the eigenvalue α_2. For $\Omega \gtrsim \Omega_{\mathrm{lift}}$, the vNE decreases dramatically (the dotted black line in Fig. 2.5(c) and the red line in Fig. 2.5(b) indicate $\Omega = \Omega_{\mathrm{lift}}$). Finally, I plot the vNE as a function of k_{soc} (see Fig. 2.5(b)). When the wavelength of the SOC is on the order of the width of the ground state as $\sqrt{2}k_{\mathrm{soc}} \sim 1/a_{\mathrm{ho}}$, the vNE becomes maximal due to an enhanced coupling between the spin states as a result of the finite system size.

2.2.3 Aligned interaction, $g > 0,\ g_{\uparrow\downarrow} = 0$

In this section, I investigate the case where only the aligned interactions are finite while the anti-aligned interactions are zero, as shown in Fig. 2.1(c). In this case, the basis states $|\downarrow\downarrow\rangle$ and $|\uparrow\uparrow\rangle$ are shifted in energy, while the symmetric $|\mathrm{S}\rangle$ and anti-symmetric $|\mathrm{A}\rangle$ states are unaffected. The energy spectrum is plotted in Fig. 2.6(a,b), and one can see that the ground state is non-degenerate for all values of Ω. For small Ω, the ground state is composed mostly of anti-aligned pseudo-spin states, given as $\psi \sim |\downarrow\uparrow\rangle\, \mathrm{e}^{ik_{\mathrm{soc}}x_-} + |\uparrow\downarrow\rangle\, \mathrm{e}^{-ik_{\mathrm{soc}}x_-}$. The first excited states are composed of two degenerate states with finite COM momentum, $\psi \sim |\downarrow\downarrow\rangle\, \mathrm{e}^{ik_{\mathrm{soc}}x_+}$ and $\psi \sim |\uparrow\uparrow\rangle\, \mathrm{e}^{-ik_{\mathrm{soc}}x_+}$. This degeneracy is resolved at a critical point, which is similar to the degeneracy resolution for the anti-aligned interactions. For weak aligned interactions ($g/\hbar\omega a_{\mathrm{ho}} = 0.4$, see the inset in Fig. 2.6(a)), an avoided crossing is seen between the ground state and the first excited states when $\Omega/\omega \simeq \Omega_{\mathrm{lift}}/\omega \simeq 39$. The avoided crossing is generated by the competition between the interaction and Raman coupling, each of which tries to shift the energy in the opposite directions [139]. For stronger aligned interactions ($g/\hbar\omega a_{\mathrm{soc}} = 1.5$, see Fig. 2.6(b)), the energy gap at the avoided crossing becomes larger since the contact interactions push the excited states to higher energies. The presence of the avoided crossing has an impact on the population imbalance after the population inversion. The inversion from the anti-aligned basis states to the aligned states occurs, but the behaviour is sharper than the case of finite aligned interactions (see Fig. 2.6(c)). Although the inversion is driven by the interactions, notice that it appears even for weak interactions such as $g/\hbar\omega a_{\mathrm{soc}} = 0.5$ and decays for increasing g (see Fig. 2.6(d)). This is a result of the fact that non-zero g shifts energy levels differently from non-zero $g_{\uparrow\downarrow}$. For non-zero $g_{\uparrow\downarrow}$, the $|\mathrm{A}\rangle$ state does not feel the interactions, and the inversion occurs and populates the $|\mathrm{A}\rangle$ state to reduce the interaction energy. For non-zero g, that is not the case anymore, and the $|\downarrow\downarrow\rangle$ and $|\uparrow\uparrow\rangle$ states both contribute to the

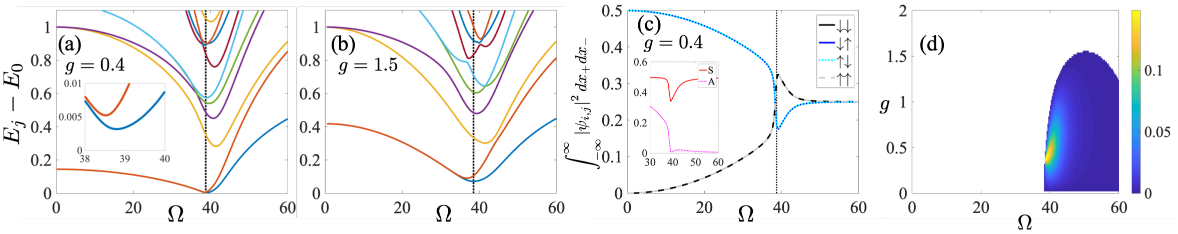

Figure 2.6: (a,b) Energy differences $E_j - E_0$ between the jth excited states ($j = 1, 2, \ldots$) and the ground state with $k_{\mathrm{soc}} a_{\mathrm{ho}} = 5$ fixed for $g/\hbar\omega a_{\mathrm{ho}} = 0.4, 1.5$, respectively. The dotted lines represent $\Omega_{\mathrm{lift}}/\omega \simeq 39$, which is the value of $\Omega_{\mathrm{lift}}/\omega$ where E_1 and E_2 starts to deviate, $(E_2 - E_1)/\hbar\omega \gtrsim 10^{-2}$. This is very close to the point where the avoided crossing between the ground state and the first excited state appears. (c) Population of each pseudo-spin state of the ground state with $g/\hbar\omega a_{\mathrm{soc}} = 0.4$ fixed. (d) Population difference $\int dx_1 \int dx_2 \, (|\psi_{\downarrow\uparrow}|^2 + |\psi_{\uparrow\downarrow}|^2 - |\psi_{\downarrow\downarrow}|^2 - |\psi_{\uparrow\uparrow}|^2)$ of the ground state as a function of Ω and g. Only positive values, where the aligned states dominate, are shown.

interaction energy. Therefore, for larger g, the inversion is no longer favourable and disappears.

One can also see the effect of the inversion in the overall momentum distribution (see Fig. 2.7(a,b)). For $\Omega \ll \Omega_{\mathrm{lift}}$, the ground state is mostly composed of the anti-aligned states $|\downarrow\uparrow\rangle$ and $|\uparrow\downarrow\rangle$, both of which acquire relative momentum due to the SOC. When $\Omega \simeq \Omega_{\mathrm{lift}}$ and the population inversion occurs, the ground state loses much of the relative momentum and obtains COM momentum since there is more population of $|\downarrow\downarrow\rangle$ and $|\uparrow\uparrow\rangle$ in the ground state. This sign can be captured in the overall density distribution exhibiting a reorientation of the interference fringes from the relative to the COM direction in the crossover region (see Figs. 2.7(c,d)).

The concurrence C_{spin} and the vNE $S[\rho_{\mathrm{spin}}]$ are also effected by the inversion ($g/\hbar\omega a_{\mathrm{ho}} = 0.4$, where the inversion is large, see Fig. 2.8(a,b)). Similar to the case of finite anti-aligned interactions, the concurrence does not react to the lifting of the energy degeneracy, but the vNE drops significantly at $\Omega \simeq \Omega_{\mathrm{lift}}$. Furthermore, a sharp spike shows up in the vNE whenever $\Omega \simeq \Omega_{\mathrm{lift}}$ ($k_{\mathrm{soc}} a_{\mathrm{ho}} = 5$, see Fig. 2.8(c)). That is caused by the avoided crossing shown in Fig. 2.6(a), where the populations of the $|\downarrow\downarrow\rangle$ and $|\uparrow\uparrow\rangle$ states suddenly increase and the other components are suppressed (see Fig. 2.6(c)). This is not seen for finite anti-aligned interactions and shows how the critical point can enhance correlations between interacting pseudo-spin components due to the competition between SOC and contact interactions.

2.3 Conclusions

In this work, I have studied two interacting particles with SOC in a harmonic potential. The finite interactions shift the energy levels and lift some energy degeneracies that are present in the energy spectrum for no interaction. I have started with finite interactions between the anti-aligned states and investigated the ground state. In the presence of the strong interactions, a unique ground state appears which contains the anti-

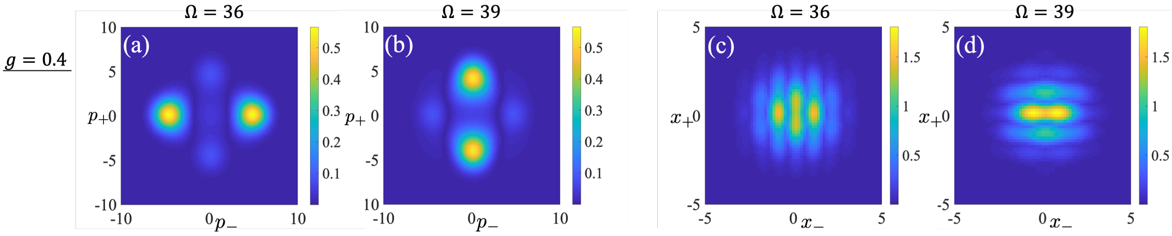

Figure 2.7: Overall momentum distributions (a,b) and density distributions (c,d) for $g/\hbar\omega a_{\text{ho}} = 0.4$ with $k_{\text{soc}} a_{\text{ho}} = 5$ fixed. In panels (a,c), $\Omega/\omega = 36$, and in panels (c,d) $\Omega/\omega = 39$, which are just below and above the value for which the inversion occurs, respectively.

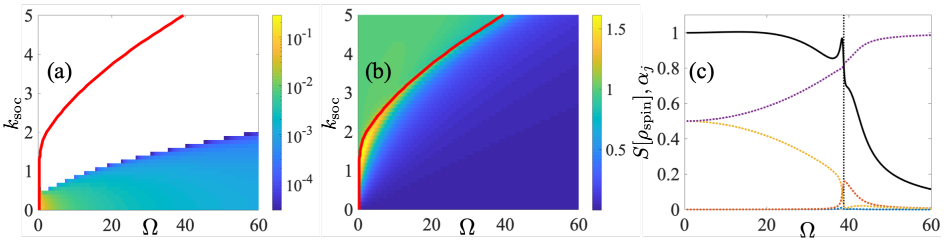

Figure 2.8: (a) Concurrence and (b) vNE of the ground state for a range of k_{soc} with $g/\hbar\omega a_{\text{ho}} = 0.4$ fixed. The white domain shows $C_{\text{spin}} = 0$. The red lines represent $\Omega_{\text{lift}}/\omega$. (c) vNE with $k_{\text{soc}} a_{\text{ho}} = 5$ fixed. The maximal value is given by $\max[S[\rho_{\text{spin}}]] = 2$. The coloured, dotted lines represent the eigenvalues α_j of the reduced density matrix ρ_{spin} for $j = 1, 2, 3, 4$. The black dotted line indicates $\Omega_{\text{lift}}/\omega \simeq 39$.

symmetric spin state. The crossover to this new type of ground state can be observed though changes in the overall density and momentum distributions but also in the entanglement between the pseudo-spin and the real space. In the opposite case where the interactions between aligned states are non-zero, a similar inversion can be seen although the inversion disappears for strong interactions. In this work, I have studied a wide range of parameters that significantly extends previous work [140]. Considering the recent progress in controlling few-particle systems experimentally with high fidelity [158, 159] and new schemes to measure their momentum distribution [160], I believe that the observation of these results such as the emergence of the population inversion is experimentally possible.

I have aimed to bridge the gap between single-particle and many-body systems. The results have revealed the role of symmetries in the energetic and entanglement characteristics of the SO-coupled systems. In addition, the analytic results can be used to investigate non-equilibrium dynamics and will, for example, allow one to simulate the dynamical generation of entanglement. This work has shown that there is a trade-off between the loss of entanglement between pseudo-spins and the generation of entanglement between pseudo-spin and real space due to the SOC. This implies that SOC can be used to create or distribute entanglement in certain degrees of freedom and can work as a control parameter of the dynamical process.

While the population inversion originates from strong interactions, it is a question if the inversion can be still seen for increasing the particle number. Since the existence of the anti-symmetric state appears for finite anti-aligned interactions, clearly the symmetry of the system in terms of particle exchange is a key point. Thus, it is not clear whether the population inversion also appears in larger systems which have different symmetries, and it is not straightforward to make general predictions.

SOC has attracted attention not only for comparison with condensed matter physics [46, 47] but also for quantum metrology [161–165] and transport. For example, non-adiabatic transport with spin flips using time-dependent SOC has been proposed [166], which revealed a possibility that SOC can lead to spatially-separated states due to coupling between their pseudo-spin and momentum. Since the approach I used here can treat strong interaction regimes, it would be interesting to study the generation of strongly spatial-entangled state such as EPR states. For example, one can create mode entanglement with contact interactions and then tune SOC to move different modes toward different directions such that the mode entanglement becomes spatial entanglement. Such spatial entanglement can be used for interferometers [167, 168].

Chapter 3

Dynamical phase transitions in one-dimensional ultra-cold quantum gases: from the continuum to the lattice

The realisation of isolated system of cold atoms has motivated many investigations into non-equilibrium phenomena and quantum thermodynamics, which are usually inaccessible in conventional condensed matter physics [9, 169]. Particularly, the non-equilibrium dynamics of a one-dimensional Bose gas has attracted strong attention [58] and inspired work on the thermalisation of observables in closed quantum systems [170–172]. Greiner *et al.* performed a pioneering experiment in isolated quantum systems [37], where the system was driven from a superfluid phase to an insulating phase, and they observed a dynamical collapse and revival of the interference peaks in momentum space. In this chapter, I focus on this non-trivial non-equilibrium dynamics and study its relation with theoretical work that indicates the emergence of dynamical phase transitions (DPTs) in quenched dynamics. The term DPTs was introduced by Heyl *et al.* in Ref. [173], where they investigated quenched dynamics in the paradigmatic transverse Ising model.

The idea of DPTs is complementary to the phenomenon of equilibrium phase transitions (EPTs). In investigating EPTs, it is convenient to use the partition function $\mathcal{Z} = \mathrm{Tr}\big[\mathrm{e}^{-\beta H}\big]$, with $\beta = 1/k_{\mathrm{B}}T$ being the inverse temperature. The locations of the zeros of the partition function $\mathcal{Z}$ are known as Fisher zeros. Since the free energy is defined as $f(z) = -\lim_{L\to\infty}(\ln \mathcal{Z})/L$ when taking the system size L to infinity, the free energy diverges at the Fisher zeros and, this is the indication of a phase transition. Heyl *et al.* proposed to expand the β in the partition function into the complex plane as $\beta \to it$ so that the partition function $\mathcal{Z}$ and the free energy $f(z)$ are analogous to the survival amplitude

$$\mathcal{G}(t) = \langle\Psi_0|\mathrm{e}^{-iHt}|\Psi_0\rangle \tag{3.1}$$

and the rate function

$$f(t) = -\frac{1}{L}\ln \mathcal{G}(t), \tag{3.2}$$

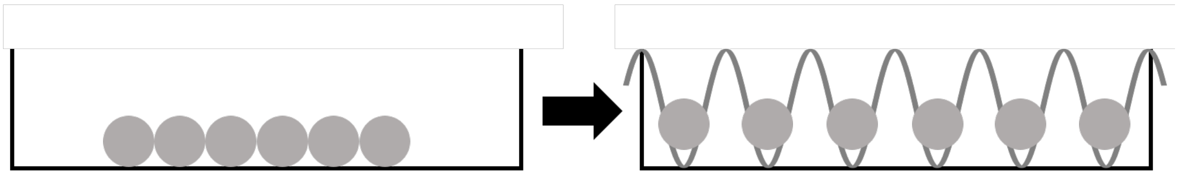

Figure 3.1: Quench to drive the system from the superfluid phase to the insulating phase.

respectively. They considered the one-dimensional transverse-field Ising model and confirmed that, in changing a characteristic parameter across different phases, critical times emerge at which the survival amplitude (3.1) becomes zero and the rate function (3.2) shows non-analytical behaviours. Since the survival amplitude (3.1) can be interpreted as the overlap between the initial state and the time-evolved state, the phase transitions triggered by dynamical parameter changes are indicated by the orthogonality between the initial state and the time-evolved state, and are named dynamical phase transitions.

The work [173] has connected this non-analyticity with the occurrence of phase transitions and claimed the connection as the indication of DPT. Since the work was published, DPTs have been studied in other spin models, however there is still a lack of generality in research of DPTs. That is, it is necessary to investigate DPTs in systems that are not spin models but for example continuous models where phase transitions such as the superfluid to Mott insulator can occur [37, 58].

In this work, I have considered a one-dimensional system of strongly interacting particles in the Tonks-Girardeau (TG) limit (cf. Sec. 1.1.3). I drive the system to see non-equilibrium dynamics by suddenly switching on a lattice potential, therefore drive the initial superfluid gas into an insulating phase via the so-called pinning transition [38] (see Fig. 3.1). TG gases allow one to map the system onto free fermions using the Bose-Fermi mapping theorem [61] and describe many-particle quantities using only the single-particle states.

In Sec. 3.1 I review the basic ideas relating to DPTs and in particular the connection with dynamical restoration of symmetry. In Sec. 3.2 I present results for the continuum model and the discrete model, and in Sec. 3.3 I follow this with an in-depth discussion of the lattice model. Finally, in Sec. 3.4, I conclude with an overall discussion about some of the issues raised.

This project has been accomplished in collaboration with Thomás Fogarty, Thomas Busch, Alessandro Silva, and John Goold. I have been involved with comprehensive discussion about this project and contributed to calculations on the system of TG gas given in Sec. 3.2.1. The work presented in this chapter has been published in the New Journal of Physics **19**, 113018 (2017) [2].

3.1 Dynamical phase transition

There is an interesting connection between orthogonality and dynamical restoration of symmetry [174, 175]. Suppose that a system has an N_s-fold symmetry. Symmetry-related ground states are described as $\{|\Psi_j\rangle\}$ for $j = 0, 1, \cdots, N_\mathrm{s} - 1$, and the initial state is given by $|\Psi_0\rangle$. The probability that the time-evolved state remains in the ground state manifold is defined as

$$P(t) = \sum_{j=0}^{N_\mathrm{s}-1} \left| \langle \Psi_j | \mathrm{e}^{-iHt} | \Psi_0 \rangle \right|^2 . \tag{3.3}$$

The probability $P(t)$ has singularities when the system traverses the boundary between different symmetry sectors. To see this case, let me consider $N_\mathrm{s} = 2$ for simplicity. The rate functions in the two symmetry sectors are defined through

$$\langle \Psi_j | \mathrm{e}^{-iHt} | \Psi_0 \rangle \equiv \mathrm{e}^{-Lf_j(t)} \tag{3.4}$$

for $j = 0, 1$. To see the amplitude of each term in $P(t)$, let me focus on the real valued rate function as $l_j(t) = \mathrm{Re}[f_j(t)]$ since the imaginary part shows just phase oscillation. When $l_0(t) > l_1(t)$, the terms associated with $l_1(t)$ are dominant in $P(t)$, while the other terms related to $l_1(t)$ are dominant when $l_0(t) < l_1(t)$. At a certain time t^* when $l_0(t) = l_1(t)$, the symmetry is dynamically restored, i.e. the probability that the time-evolved state is in one of the symmetry sectors is the same as the probability that it is in the other sector. At the time t^*, cusp singularities appear in $P(t)$, and a connection between DPTs and standard symmetry breaking in the steady state can be established [175].

The fact that the time-evolved state is orthogonal to the initial state is, however, not generally related to the dynamical restoration of symmetry. They only correspond to each other for certain initial states. Suppose that the initial state is given by a cat state

$$|0\rangle \equiv \frac{1}{\sqrt{N_s}} \sum_{j=0}^{N_s-1} |\Psi_j\rangle , \tag{3.5}$$

which is a linear superposition of the symmetry-related ground states. The survival amplitude is then provided by

$$\begin{aligned} \mathcal{G}(t) &= \langle 0 | \mathrm{e}^{-iHt} | 0 \rangle \\ &= \frac{1}{N_s} \sum_{j,k} \mathrm{e}^{-Lf_{j,k}(t)}, \end{aligned} \tag{3.6}$$

where I define the generic rate function as

$$\langle \Psi_j | \mathrm{e}^{-iHt} | \Psi_k \rangle \equiv \mathrm{e}^{-Lf_{j,k}(t)}. \tag{3.7}$$

Note that the above function $f_{j,k}(t)$ is different from the rate function (3.4) since the initial state is not necessarily $|\Psi_0\rangle$. In the thermodynamic limit ($L \to \infty$), the term with the smallest real part of $f_{j,k}(t)$ dominates $\mathcal{G}(t)$, and therefore the survival amplitude corresponds to the probability $P(t)$,

$$\lim_{L\to\infty} |\mathcal{G}(t)|^2 = P(t), \tag{3.8}$$

This means that the return probability of the state given in Eq. (3.5) is equivalent to the probability that the time-evolved state remains in the groud state manifold in the thermodynamic limit. In other words, one can confirm the dynamical restoration by looking at the orthogonality.

An interesting question of symmetries is whether properties such as the orthogonality and the dynamical restoration are reflected in local measurements or observables. For example, when the system crosses from one phase to another, the time-evolved state is orthogonal to the ground state of the initial Hamiltonian. In this case, the orthogonality is indicated by singularities in $\mathcal{G}(t)$ and $f(t)$ (or equivalently $l(t)$), and the question is whether such singularities can be detected by local observables. While previous works have explored the connection between the magnetisation and DPTs using a spin chain model with long range interactions [176, 177], in this work I will consider a different approach, using a realistic system of cold atoms where a measurable observable is their momentum distribution.

3.2 Models

I consider a continuous model and a discrete model both of which exhibit a transition between a superfluid phase and an insulator phase and are exactly solvable. The first one is the TG gas [61], a one-dimensional system of strongly interacting bosons, and the second one is the tight-binding model for a system of hard-core bosons. The continuous TG is considered in the presence of an optical lattice, whereas the tight-binding model is considered at half filling with a staggered field.

3.2.1 Continuous model: Tonks-Girardeau gas

The considered system is a one-dimensional gas of N bosons trapped in a box potential. The Hamiltonian is given by

$$H = \sum_{j=1}^{N} \left(\frac{-\hbar^2}{2m} \frac{d^2}{dx^2} + V_{\mathrm{b}}(x_j) + V(x_j) \right) + g_{1\mathrm{D}} \sum_{j>l} \delta(x_j - x_l), \tag{3.9}$$

where m is the mass of each particle, $g_{1\mathrm{D}}$ is the strength of the contact interactions, and $V_{\mathrm{b}}(x)$ is a box potential of length L. I also add a lattice potential $V(x)$, given by

$$V(x) = V_0 \cos^2 k_0 x, \tag{3.10}$$

where V_0 is the depth of the lattice and k_0 is the wavevector given by $k_0 = M\pi/L$ with M being the number of wells in the lattice. When the lattice is much deeper than the recoil energy, $V_0 \gg E_{\mathrm{R}} = \hbar^2 k_0^2/(2m)$, the system can be mapped onto the Bose-Hubbard model [9]. In the opposite limit, $V_0 \ll E_{\mathrm{R}}$, with strong interaction, the system can be mapped onto the sine-Gordon model, preserving the transition between a superfluid phase and an insulator phase when the number of the lattice wells is commensurate with the particle number [178]. This transition is called pinning transition and has been confirmed experimentally [38].

It is worth noting that, as will be introduced below, the continuous model provides some convenient ways to describe the time-evolved state numerically, but few analytical solutions have been reported. One example of the analytical approaches is introduced in Ref. [179], which shows the analytical solution of the eigenstates of the pinning system (3.9) in the TG limit by using the Mathieu functions, although the solution includes an infinite sum to compute and is not really easy to implement.

To solve the Hamiltonian (3.9) using the mapping theorem, I consider the TG limit, $g_{1\mathrm{D}} \to \infty$. In this case, the infinitely strong interaction restricts bosons from occupying the same space, such that one can demand

$$\Psi(x_1, x_2, \dots, x_N) = 0, \tag{3.11}$$

if $|x_i - x_j| = 0$ for $1 \leq i < j \leq N$. This isolates each of bosons in real space, which leads to a pinning transition for any infinitesimal lattice depth. The condition (3.11) is equivalent to the Pauli principle for the spinless fermions, allowing one to map the state of the many-body TG gas to the single-particle states of a fermionic gas (Bose-Fermi mapping theorem) [61]. The solution that satisfies the constraint (3.11) is therefore the fermionic wave-function subject to an operator that restores the bosonic symmetry under particle exchange:

$$\Psi(x_1, x_2, \dots, x_N) = \prod_{1 \leq i < j \leq N} \operatorname{sgn}(x_i - x_j) \Psi_{\mathrm{F}}(x_1, x_2, \dots, x_N), \tag{3.12}$$

where

$$\Psi_{\mathrm{F}}(x_1, x_2, \dots, x_N) = \frac{1}{\sqrt{N!}} \det_{n,j}^{N} \left[\psi_n(x_j)\right] \tag{3.13}$$

is the Slater determinant of the single-particle states. An advantage of the mapping theorem is that one can describe the many-body system using only single-particle states (cf. 1.1.3).

The mapping theorem also works when the wave-functions have time-dependence, and provides a convenient formulation of the rate function $l(t)$, which is provided by

$$\begin{aligned} l(t) &= -\frac{1}{L} \ln \left[\left| \langle \Psi_0 | \mathrm{e}^{-iH_{\mathrm{f}}t} | \Psi_0 \rangle \right|^2 \right] \\ &= -\frac{1}{L} \ln \left[\det |A_{mn}(t)|^2 \right] \end{aligned} \tag{3.14}$$

with

$$A_{mn}(t) = \int dx \; \psi_m^*(x, 0) \psi_n(x, t) \tag{3.15}$$

being the matrix elements of the overlap between single-particle states of the initial state and the quenched state. The mapping theorem therefore allows one to not deal with many-body wave-functions but with single-particle states instead, making it easy to compute $l(t)$ for large particle number. It is worth noting that similar quantities to Eq. (3.14) have been used to characterise the tunnelling decay in a TG gas [180, 181].

Another quantity I will use to characterise the quenched dynamics is the momentum distribution $n(p, t)$, which is defined as the Fourier transform of the reduced single-particle density matrix (RSPDM),

$$n(p,t) = \frac{1}{2\pi}\int dx dx' \; \mathrm{e}^{ip(x-x')}\rho(x,x',t), \tag{3.16}$$

where the RSPDM is defined as

$$\rho(x,x',t) = N\int dx_2,\ldots,dx_N \; \Psi^*(x,x_2,\ldots,x_N,t)\Psi(x',x_2,\ldots,x_N,t). \tag{3.17}$$

The mapping theorem also gives a convenient way to calculate the RSPDM $\rho(x,x',t)$ [66]. Since the many-body wave-function can be written as in Eq. (3.12), the RSPDM can be described as

$$\rho(x,x',t) = \sum_{i,j=1}^{N}\psi_i^*(x,t)A_{ij}(x,x',t)\psi_j(x',t), \tag{3.18}$$

where the matrix $\boldsymbol{A}$ is written as

$$\boldsymbol{A}(x,x',t) = \left(\boldsymbol{P}^{-1}\right)^T \det\boldsymbol{P} \tag{3.19}$$

with

$$P_{ij}(x,x',t) = \delta_{i,j} - 2\int_x^{x'} dy \; \psi_i^*(y,t)\psi_j(y,t), \tag{3.20}$$

where one assumes $x < x'$ without loss of generality. Since the momentum distribution is commonly measured in experiments, I use $n(p,t)$ as the physical observable to capture singularities which occur due to the dynamical orthogonality.

I consider three types of quenches: switching the lattice on, switching the lattice off, and changing the sign of the lattice strength. In quenching the lattice on, if the the number of the lattice wells coincides with the particle number, $M = N$, one sees temporal orthogonality between a superfluid phase and an insulating phase. In fact, switching the lattice on to a depth of $V_\mathrm{f} = E_\mathrm{R}$, non-analytical behaviours appear in the rate function $l(t)$ at $t/T_\mathrm{R} = 1/2 + \alpha$ with α being a non-negative integer and $T_\mathrm{R} = 4\pi/V_\mathrm{f}$ being the time period (see Fig. 3.2(a)). The momentum distribution shows initially a sharp peak at $p = 0$ (see Fig. 3.2(c)), which is a feature of the TG gas in an infinite well [182] and a characteristic of the superfluid-like phase. The peak then disappears at some later time (see Fig. 3.2(b,c)), and the momentum distribution broadens overall, which shows the transition to the insulating phase. The peak then oscillates as the system oscillates between the superfluid and the insulating phases. Note that the peak reaches the minimum point earlier than the first non-analytical point (see the behabiour at the solid and dashed vertical lines in Fig. 3.2(b)). This difference in time gets more significant at later times, which means that, while the non-analytical behaviour of $l(t)$ signalling the orthogonality and the collapse/revival cycle of the momentum distribution have a similar oscillation, they do not have the same periodicity. When quenching to a deeper lattice, the oscillations in the two quantities are more synchronised, as will be discussed in Sec. 3.2.2.

Next, I focus on switching the lattice off, i.e. from $V_\mathrm{i} > 0$ to $V_\mathrm{f} = 0$, and calculate

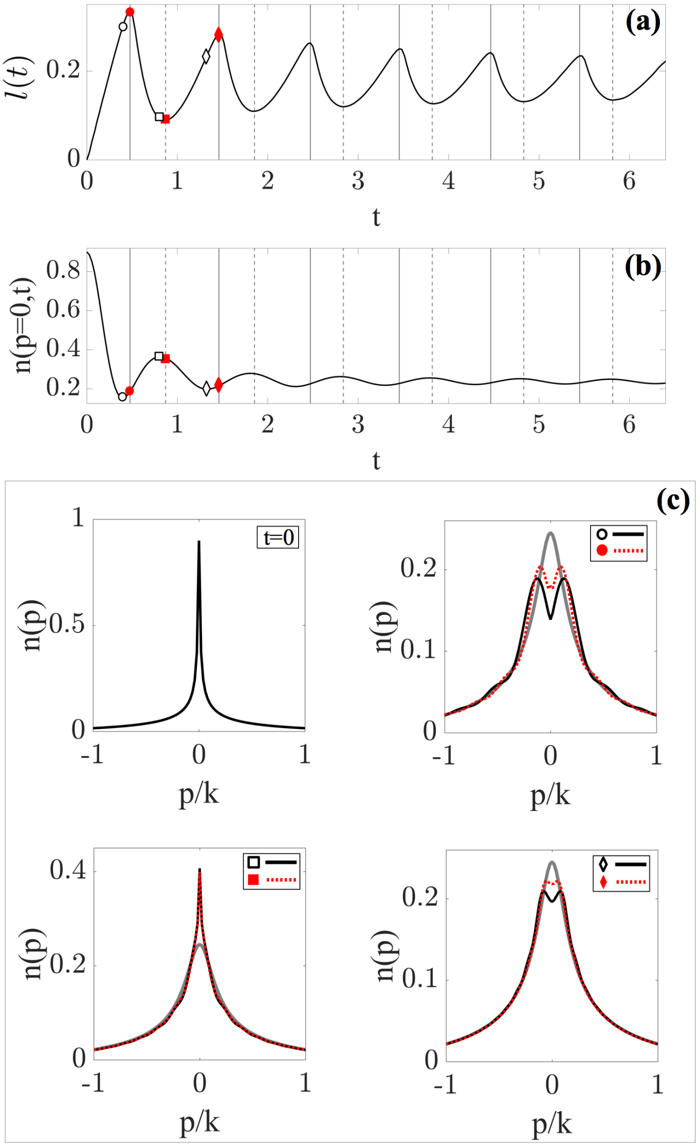

Figure 3.2: Quenched dynamics starting with a conducting phase $V_{\mathrm{i}} = 0$ to an insulating phase $V_{\mathrm{f}} = E_{\mathrm{R}}$ in a system of $N = 100$. In (a) the rate function $l(t)$ is shown and in (b) the peak of the momentum distribution $n(p,t)$ at $p = 0$ is represented with time scaled by the periodic time $T_{\mathrm{R}} = 4\pi/V_{\mathrm{f}}$. The solid vertical lines clarify when $l(t)$ shows non-analytical behaviours, and the dashed vertical lines clarify when $l(t)$ shows minima. For the times marked by symbols in (a,b), the momentum distribution $n(p,t)$ is plotted in (c). The black solid lines show $n(p,t)$ when the peak of the momentum has minima or maxima in (b), and the red dotted lines show $n(p,t)$ when $l(t)$ has minima or maxima in (a). The gray solid lines are the momentum distribution in the insulating phase in equilibrium.

the rate function $l(t)$ for different particle numbers N (see Fig. 3.3). I rescale time t with the revival time $N\pi/2E_{\mathrm{R}}$, and a revival in time can be seen at $t = 1/2 + \alpha$ with α being a non-negative integer. The behaviour of the revival seems non-analytic, however, this does not indicate the existence of DPTs. Rather, this is because the density waves propagate and interfere at the centre, which is well studied in the same model as the dynamical de-pinning effect [179]. This effect is the result of the finite system size and disappears in the thermodynamic limit ($L \to \infty$), suggesting that DPTs do not occur in the transition to the superfluid phase. I discuss this more in Sec. 3.2.2.

Lastly, I look into cases where the sign of the lattice strength changes, i.e. from $V_{\mathrm{i}} = V$ to $V_{\mathrm{f}} = -V$. This means that the system is going through the superfluid phase at $V = 0$. In this case, the dynamics is not governed by a time-scale realted to the lattice depth $|V|$. The rate function $l(t)$ and the peak of the momentum distribution are decaying more quickly than the other two cases and do not show any obvious relation between non-analytical behaviours of $l(t)$ and the momentum distribution (see Fig. 3.4(a,b)).

3.2.2 Discrete model: Tight-binding model

The model I consider next is composed of N hard-core bosons in a staggered onsite potential, for which the Hamiltonian is given by

$$H = J\sum_{j=1}^{N}\left(b_j^\dagger b_{j+1} + \mathrm{h.c.}\right) + \sum_{j=1}^{N} V(-1)^j b_j^\dagger b_j, \tag{3.21}$$

where b_j ($b_j^\dagger$) is the annihilation (creation) operator of bosons at site j, J is the tunnelling strength, N is the particle number, and V is the strength of the onsite potential. This discrete model contains essentially the same physics as the continuous model (TG gas), but an advantage over the TG gas is that this discrete model can be solved analytically.

The solution is given by a Jordan-Wigner transformation $b_j^\dagger = \mathrm{e}^{i\pi\sum_{l<j} a_l^\dagger a_j} a_j^\dagger$ and using Fourier transformed variables $a_j = \sum_k \mathrm{e}^{ikj} a_k/\sqrt{N}$ [183]. The Hamiltonian is given by

$$H = \sum_{|k|<\pi/2} \Psi_k^\dagger \hat{H}_k \Psi_k, \tag{3.22}$$

where $k = \pi(2n+1)/N$ with $n = 0, \ldots, N/4 - 1$, $\Psi_k = (a_k, a_{k+\pi})^T$, and $\hat{H}_k = 2J\cos k\boldsymbol{\sigma}^z + V\boldsymbol{\sigma}^y$, with $\boldsymbol{\sigma}^j$ being Pauli matrices. The Hamiltonian can be diagonalised in terms of the variables $\Gamma_k = \mathrm{e}^{i\theta_k\boldsymbol{\sigma}^y}\Psi_k$ with $\tan 2\theta_k = V/(2\cos k)$. The energy spectrum is characterised by the dispersion relation $\epsilon_k = \sqrt{(2J\cos k)^2 + V^2}$. It is worth noting that this model can be also solved when an external flux is present [184]. I consider half filling, where the spectrum is gapped if $V \neq 0$ and otherwise the gap closes at $k = \pm\pi/2$. In other words, for $V \neq 0$ the system belongs to an insulating charge density wave phase, and for $V = 0$ the system belongs to a superfluid phase. I consider the three cases investigated in Sec. 3.2.1: transition from the superfluid phase

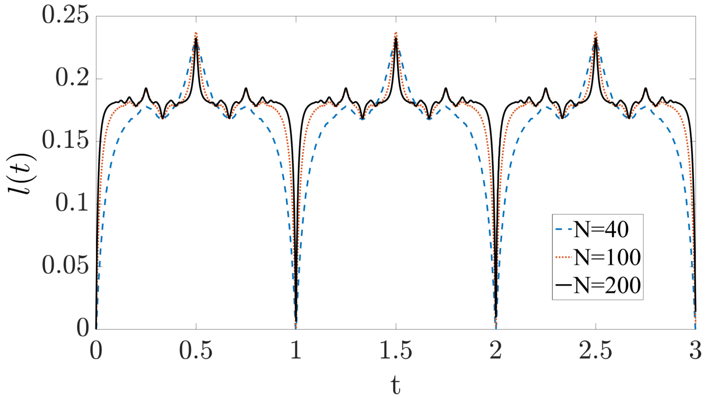

Figure 3.3: The rate function $l(t)$ during a quenched dynamics from an insulating phase ($V_{\mathrm{i}} = E_{\mathrm{R}}$) to a superfluid phase ($V_{\mathrm{i}} = 0$) for different particle number $N = 40, 100, 200$. The time is rescaled by the revival time in the box, $N\pi/2E_{\mathrm{R}}$.

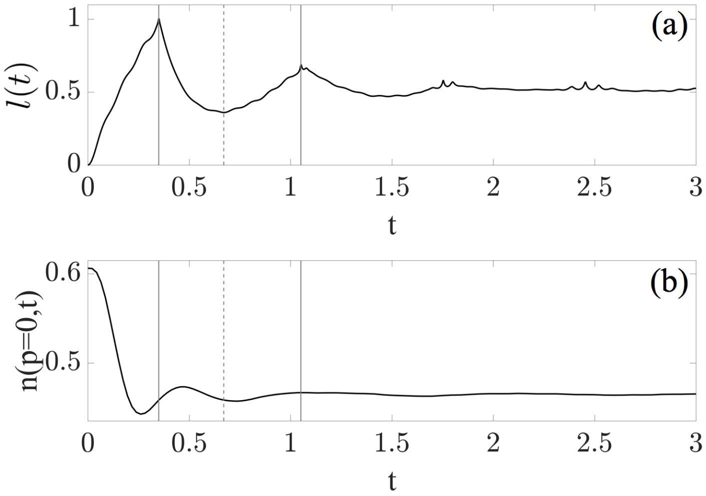

Figure 3.4: (a) The rate function $l(t)$ and (b) the peak of the momentum distribution $n(p,t)$ at $p = 0$ during a quenched dynamics from an insulating phase $V_{\mathrm{t}} = 2E_{\mathrm{R}}$ to an insulating phase $V_{\mathrm{t}} = -2E_{\mathrm{R}}$ for particle number $N = 100$. The time t is scaled by the periodic time $T_{\mathrm{R}} = 4\pi/V_{\mathrm{f}}$. The solid vertical lines clarify when non-analytical behaviours in $l(t)$ come out, and the dashed vertical lines indicate the minimum of $l(t)$.

to the insulator phase, transition to the insulator phase from the superfluid phase, and transition within the insulating phase. Below I consider $J = 1$ for simplicity.

The survival amplitude (3.1) can be computed using the Bogoliubov rotation which connects the old quasiparticles to the new ones, $\Gamma_k(V_\mathrm{f}) = \mathrm{e}^{i\Delta\theta_k\sigma_y}\Gamma_k(V_\mathrm{i})$, where $\Delta\theta_k = \theta_k(V_\mathrm{f}) - \theta_k(V_\mathrm{i})$. I write the ground state in a potential of depth V_i as

$$|0\rangle_{V_\mathrm{i}} = \frac{1}{N}\prod_{|k|<\pi/2}\Big(1 + \tan\Delta\theta_k\gamma_+^\dagger(k)\gamma_-^\dagger(k)\Big)\,|0\rangle_{V_\mathrm{f}}\,. \tag{3.23}$$

Computing the time evolution, one obtains the survival amplitude, given by

$$\mathcal{G}(z) = \prod_{|k|<\pi/2}\frac{1 + \tan^2\Delta\theta_k\mathrm{e}^{2i\epsilon_k(V_\mathrm{f}z)}}{1 + \tan^2\Delta\theta_k}\,, \tag{3.24}$$

and by solving $\mathcal{G}(z_k) = 0$, the Fisher zeros are provided by

$$z_k = \frac{(2n+1)\pi}{2\epsilon_k} + \frac{i}{\epsilon_k}\log\left(\tan\Delta\theta_k\right). \tag{3.25}$$

For quenches to an insulating phase ($V_\mathrm{f} > 0$), the Fisher zeros cross the real axis, for example when $\Delta\theta_k = \theta_k(V_\mathrm{f}) - \theta_k(V_\mathrm{i}) = \pi/4$, according to Eq. (3.25). In the case of $\Delta\theta_k = \theta_k(V_\mathrm{f}) - \theta_k(V_\mathrm{i}) = \pi/4$, one has $\tan 2\Delta\theta_k = (2\cos k(V_\mathrm{f} - V_\mathrm{i}))/(4\cos^2 k + V_\mathrm{f}V_\mathrm{i}) \to \infty$. This indicates that the Fisher zeros z_k are observed for momenta

$$k^* = \arccos\left[\sqrt{-\frac{V_\mathrm{f}V_\mathrm{i}}{4}}\right]. \tag{3.26}$$

A singurarity at $k = k^*$ corresponds to a singularity in the rate function $l(t)$ with a period,

$$T_\mathrm{R} = \frac{\pi}{\sqrt{V_\mathrm{f}(V_\mathrm{f} - V_\mathrm{i})}}. \tag{3.27}$$

On the other hand, for quenches to a superfluid phase ($V_\mathrm{f} = 0$), Eq. (3.25) always has a nonzero imaginary part, and therefore there is no singularity in the rate function $l(t)$. Nevertheless, by keeping the system size finite and rescaling the time with the system size and particle number, one can observe collapse and revival (see Fig. 3.5), in the same way as Fig. 3.3.

3.3 Orthogonality and observables

In the continuous model, I showed that the rate function has singularities when the time-evolved state is orthogonal to the initial state and that the period is connected to the period of the peak of the momentum distribution for deep quenches only. From the discrete model, it is possible to gain further understanding of this mismatch as the periodicity of the system's revivals can be computed exactly. The overlap between the

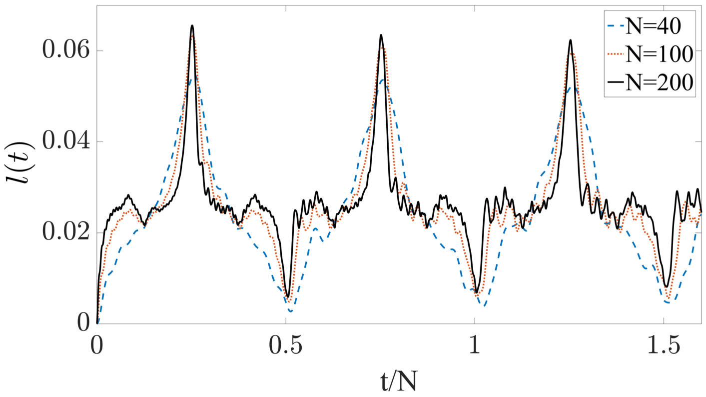

Figure 3.5: The rate function $l(t)$ for a quench from an insulator phase ($V_\mathrm{i} = 0.3$) to a superfluid phase ($V_\mathrm{f} = 0$) for different particle numbers N. The time axis is rescaled with the particle number N.

ground states of different strength V_i and V_f of the potential is given by

$$\langle \Psi_{V_\mathrm{f}} | \Psi_{V_\mathrm{i}} \rangle = \exp\left[-\frac{N}{2\pi} \int_{-\pi/2}^{\pi/2} dk \;\log\left(1 + \tan^2\theta_k\right) \right], \tag{3.28}$$

which tells one that the overlap reaches zero in the thermodynamic limit $N \to \infty$. It implies that, for quenches from the superfluid to the insulator phase, the dynamics shows collapses and revivals of the superfluid and insulator phases, and thus the orthogonality with the initial state may be established in the system when the system collapses to the insulator phase completely. This is true if the system has dissipation so that the time-evolved state can reach the ground state. However, since I consider unitary dynamics and no dissipation, the time-evolved state maintains excited states of the quenched Hamiltonian. Only in the thermodynamic limit, the system collapses to the insulator phase and attains the orthogonality. However, deep quenches make the dynamics different as shown below.

To distinguish between the superfluid phase and the insulating phase, I use the parity operator, which is experimentally accessible and is an observable characterising charge density wave order, given by

$$M = \frac{1}{N} \sum_i (-1)^i b_i^\dagger b_i. \tag{3.29}$$

In the fermionic representation, the parity operator is provided by

$$M = \frac{1}{N} \sum_{|k|<\pi/2} \hat{\Psi}^\dagger(k) \sigma_k \hat{\Psi}(k). \tag{3.30}$$

The average $\langle M(t)\rangle$ of the parity operator can be calculated to be

$$\langle M(t)\rangle = -\frac{1}{N}\sum_{|k|<\pi/2}\sin 2\theta_k(V_\mathrm{f})\cos 2\Delta\theta_k + \frac{1}{N}\sum_{|k|<\pi/2}\cos 2\theta_k(V_\mathrm{f})\sin 2\Delta\theta_k\cos 2\epsilon_k(V_\mathrm{f})t. \tag{3.31}$$

In general, this quantity oscillates as well as the rate function $l(t)$, but they do not have the same period (see Fig. 3.6). However, these oscillations synchronise in a deep quench ($V_\mathrm{f}/J \gg 1$) (see Fig. 3.7), whereby $l(t)$ shows non-analytic cusps when $\langle M(t)\rangle$ drops to the minimum value. I note that the period of $\langle M(t)\rangle$ is $T_\mathrm{M} = \pi/\sqrt{V_\mathrm{f}^2 + (2J)^2}$. Recalling that the period of $l(t)$ is given by Eq. (3.27), these periods are close when $V_\mathrm{f} \gg V_\mathrm{i}$. In this case, since $\epsilon_k = \sqrt{(2J\cos k)^2 + V^2}$, the dispersion is constant. This means that all k-modes oscillate with the same frequency characterised by V_f. Thus, the oscillation of the order parameter $\langle M(t)\rangle$ appears to coincide with the one of $l(t)$ only for deep quenches. One may argue that a different operator can be used to better observe dynamical orthogonality. For example, choosing the kinetic energy operator,

$$K = \frac{1}{N}\sum_j b_j^\dagger b_{j+1} + \mathrm{h.c.}, \tag{3.32}$$

the average of which is given by

$$\langle K(t)\rangle = -\frac{1}{N}\sum_{|k|<\pi/2} 2\cos k\left(\cos 2\theta_k\cos 2\Delta\theta_k + \sin\theta_k\sin\theta_k\cos 2\epsilon_k t\right), \tag{3.33}$$

which shows similar behaviour as $\langle M(t)\rangle$ (see Eq. (3.31)).

3.4 Conclusions

I have discussed DPTs in systems that have a superfluid to insulator transition. Considering the continuous model (TG gas), I have calculated numerically the rate function and the momentum distribution for quenches from the superfluid phase to the insulating phase, vice versa, and for quenches within the same phase. Even though the rate function displays non-analytical cusps, which signal temporal orthogonality with the initial state, these non-analyticities have slightly different behaviour from the dynamics of a local observable. Only for deep quenches, they are connected. Also, in the discrete model (tight-binding model), I have studied analytically the dynamics of the rate function and the parity operator chosen as the order parameter. These quantities show behaviours similar to the continuous model and help one understand why the orthogonality is related to the observable only for deep quenches. As known from state discrimination protocols in quantum information, it is difficult to observe global orthogonality from local measurements on pure states [185], and it is generally impossible for mixed states [186]. Considering this fact and the results obtained here, I conclude that it is in general difficult to detect orthogonality in many-body states from local observables, i.e. it is hard to observe signals from non-analyticities in the rate function in the dynamics of local observables alone. However, there is some unex-

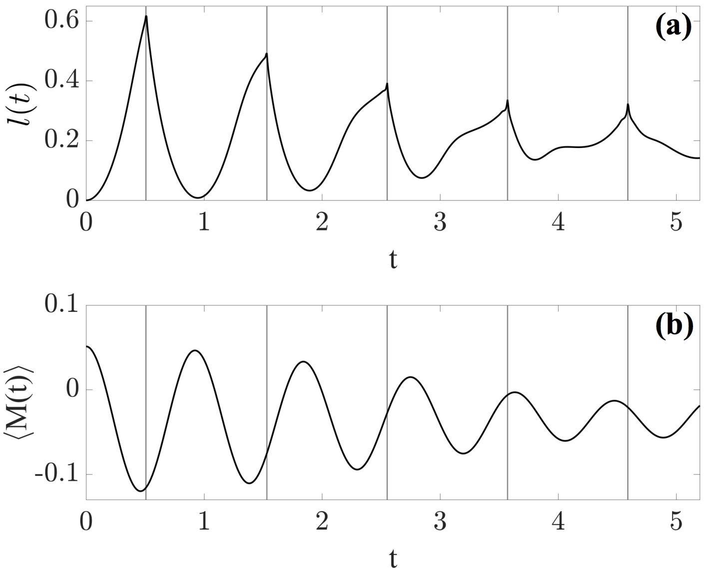

Figure 3.6: The rate function $l(t)$ and the average $\langle M(t) \rangle$ of the parity operator in a quenched dynamics from $V_{\mathrm{i}} = -1/6$ to $V_{\mathrm{f}} = 3$ for the particle number $N = 100$. The oscillation in these quantities do not coincide.

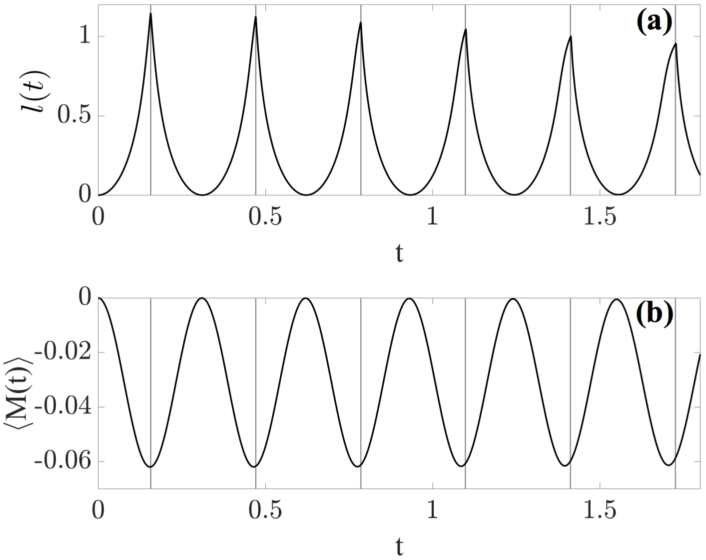

Figure 3.7: The rate function $l(t)$ and the average $\langle M(t) \rangle$ of the parity operator in a quenched dynamics from $V_{\mathrm{i}} = 0$ to $V_{\mathrm{f}} = 10$ for the particle number $N = 100$. The oscillation in these quantities synchronise at the beginning.

plored possibility to detect the non-analyticilties through non-trivial order parameters [187] or by extending ancilla based interferometry schemes which have been proposed [188–191] and experimentally implemented in local quenches in Fermi gases [192].

As future work, it would be interesting to observe the relation itself between the rate function and local observables in other critical models that can have a superfluid to insulator transition. Since this work was published, this relation have been investigated in several models. In Ref. [193], it is observed that in Bose-Hubbard model the peak of the momentum distribution and the rate function reach maxima at slightly different times. This agrees with the results shown here. In Ref. [194], it is shown that in a three-dimensional model the emergence of non-analytical behaviours is linked to the dynamical transition in the order parameter.

In general, quantum criticality in strongly correlated many-body systems is known to be sensitive to temperature [195–197]. Thus, this phenomenon has the potential to be a good thermometer [198]. As seen in this chapter, the TG system enables one to compute many-body quantities to characterise the quantum criticality. Although zero temperature is assumed in the system in this work, one can consider finite temperatures in the TG gas [199]. Therefore, one could investigate pinning transition in the TG gas at finite temperature from the perspective of thermometry.

Chapter 4

Quantum probe spectroscopy for cold atomic systems

By taking advantage of the properties and techniques of cold atoms, simulating condensed matter systems with atomic systems has become an attractive research field. For instance, by utilising the lower Fermi energies of fermions in atomic gases compared to those of electrons in a metal, investigation of low energy excitations near the Fermi surface has become possible [192]. Another example is that impurity dynamics in Bose-Einstein condensates enables one to simulate a condensed matter system and allows one to study quasiparticles called Bose polarons for longer times than in the condensed matter system [200, 201]. Furthermore, atomic gases trapped in optical lattices provide a good platform for quantum simulations of strongly correlated phases of matter [12, 202]. A powerful tool to examine lattice systems is the quantum gas microscope [203–210], which enables high-fidelity control and measurement of atoms with single-site resolution through a high resolution optical imaging systems.

To simulate other physical systems with atomic systems, it is necessary to develop a wide range of techniques to characterise and probe for instance densities, multi-particle correlations, temperature, or the excitation spectra. The progress in control and measurement methods at the single-atom level provides an approach utilising quantum impurities (e.g. single atoms in a different internal state or belonging to an entirely distinct atomic species) as nondestructive quantum probes of many-body quantum systems [211–231]. Impurities coupled to an atomic gas can extract information about the wave-function of the gas by manipulating the internal states of the impurities via a Ramsey interferometric scheme.

Below I will consider bosons in atomic gases trapped by lattice systems and show how impurities can be used to measure a wide range of the excitation energies of the gases. By embedding a two-level impurity into a lattice system and monitoring its dynamics, one can robustly detect energy gaps over a broad energy range in the spectrum of the system with the lower resolution limit being determined by the probe's dephasing rate. This protocol provides a new tool to characterise cold atomic systems in optical lattices.

In Sec. 4.1, I describe the model of a lattice system and present the proposed protocol. In Sec. 4.2, I explain the mechanism of the protocol together with an analytic description of the evolution of the probe. To show the robustness of the proposed protocol against dephasing, in Sec. 4.3 I implement exact numerical simulations of the protocol, considering two scenarios for the quantum probe: isolated or subject to dephasing. Lastly, in Sec. 4.4 I summarise the findings and give an outlook.

This project has been accomplished in collaboration with Berislav Buča and Jordi Mur-Petit. I have been involved with comprehensive discussion about this project and carried out the analytical and numerical calculations of the von Neumann equation. The work presented in this chapter was published in the New Journal of Physics **20**, 103006 (2018) [3].

4.1 Description of model and protocol

I consider bosons trapped in a lattice system as the target system to be examined and add a qubit as an impurity. In this section, I introduce the description of the lattice system as well as the description of the impurity. After that, I will explain the protocol to extract the eigenenergies of the lattice.

4.1.1 Model

I consider a tight-binding model for N atoms in a finite two-dimensional lattice with L sites. The Hamiltonian describing the system is given by

$$H_{\mathrm{latt}} = \sum_{l,m} J_{l,m}\, c_l^\dagger\, c_m + \sum_l \epsilon_l\, c_l^\dagger\, c_l, \tag{4.1}$$

where $J_{l,m}$ represents the hopping rate between nearest-neighbouring sites m and l, ϵ_l represents the single-site energy at site l, and c_l, $c_l^\dagger$ are the particle annihilation and creation operators of bosons at site l, respectively. This model is not limited to cold atoms in optical lattices [202] but can describe various experimental setups, for example, arrays of superconducting circuits [232, 233], photonic waveguides [234], microwave cavity arrays [235], and optomechanical setups [236].

The spectral properties of this Hamiltonian are known to show regular or chaotic features [237], depending on the geometry of the lattice system. For example, on a $L_x \times L_y$ square lattice, the Hamiltonian (4.1) shows a regular spectrum, which is described by a Poisson distribution of energy gaps, $P_{\mathrm{Poisson}}(s) = \mathrm{e}^{-s}$, with s the suitably normalised energy-level spacing [238]. On the other hand, in a system shaped like an athletic field (a Bunimovich stadium, e.g. see Fig. 4.3(c)), the Hamiltonian (4.1) exhibits a chaotic spectrum, which is characterised by level repulsion, i.e. no two levels are close in the energy spectrum [237]. I will discuss whether the differences between these types of energy spectra affect the protocol to extract the eigenenergies later. The flexibility of this model provides a useful testing ground to evaluate the energy resolution of a spectroscopy protocol.

When considering an impurity coupled to a Bose gas, a probe formed by two internal degrees is more susceptible to dephasing than a probe comprised by two spatial degrees [239]. Therefore, I choose a localised two-level system or qubit represented by two

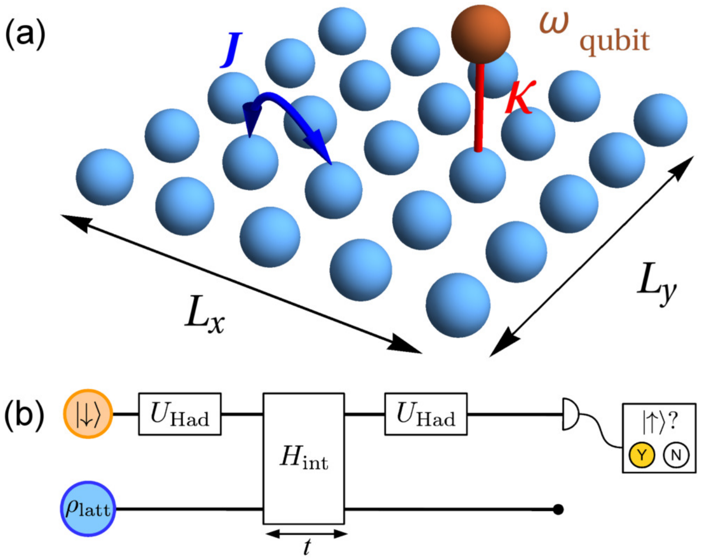

Figure 4.1: (a) Sketch of the composite system: particles can hop at a rate J (blue arrow) between nearest-neighbouring sites on a lattice of $L_x \times L_y$ sites (light blue spheres). An energy level of a quantum probe (dark orange sphere) is coupled locally to the lattice site x_{pr} with strength κ (red line). (b) Probing protocol: the probe is initialised in its ground state, $|\downarrow\rangle$, and follows a Ramsey sequence, interacting with the lattice for a time t before being measured in the $\{|\uparrow\rangle, |\downarrow\rangle\}$ basis.

internal states ($|\uparrow\rangle$, $|\downarrow\rangle$). The corresponding Hamiltonian is given by

$$H_{\mathrm{qubit}} = \frac{1}{2}\hbar\omega_{\mathrm{qubit}}\sigma_z, \tag{4.2}$$

with the energy gap $\hbar\omega_{\mathrm{qubit}}$ and Pauli matrix $\sigma_z = |\uparrow\rangle\langle\uparrow| - |\downarrow\rangle\langle\downarrow|$. The qubit is coupled locally to a single lattice site x_{pr}, as shown in Fig. 4.1(a).

The Hamiltonian of the composite system is given by

$$H = 1_{\mathrm{qubit}} \otimes H_{\mathrm{latt}} + H_{\mathrm{qubit}} \otimes 1_{\mathrm{latt}} + H_{\mathrm{int}}. \tag{4.3}$$

The interaction term H_{int} describes a state-dependent contact interaction and is given by

$$H_{\mathrm{int}} = (\kappa_\uparrow |\uparrow\rangle\langle\uparrow| + \kappa_\downarrow |\downarrow\rangle\langle\downarrow|) \otimes \hat{n}_{\mathrm{latt}}(x_{\mathrm{pr}}), \tag{4.4}$$

where each internal state couples to the density $\hat{n}_{\mathrm{latt}}(x_{\mathrm{pr}}) = c^\dagger_{x_{\mathrm{pr}}} c_{x_{\mathrm{pr}}}$ at site x_{pr} with different strengths $\kappa_\uparrow$, $\kappa_\downarrow$. For example, one can realise this type of interaction with an impurity in a cold atomic system by exploiting a Feshbach resonance. For simplicity, I set $\kappa_\uparrow(t) = \kappa$, $\kappa_\downarrow(t) = 0$, i.e. only one internal state is coupled to the lattice gas.

4.1.2 Quantum probing protocol

For weak coupling $\kappa \ll J, \omega_{\text{qubit}}$, according to perturbation theory, the interaction Hamiltonian (4.4) shifts the energy of the qubit as

$$E_{\uparrow,\downarrow} \mapsto E_{\uparrow,\downarrow} + \kappa_{\uparrow,\downarrow} n_{\text{latt}}, \tag{4.5}$$

where $n_{\text{latt}} = \text{Tr}\left[\rho_{\text{latt}} \hat{n}_{\text{latt}}(x_{\text{pr}})\right]$ is the density at the coupled site x_{pr}. To measure the density n_{latt} or extract information on the spectrum of the lattice Hamiltonian, one can initialise the qubit in a pure state and observe the time evolution of its internal states (see Fig. 4.1(b)). The full protocol is as follows:

1. Initialise the qubit probe as $|\downarrow\rangle$. The composite system is initially uncorrelated, $\rho(t=0) = \rho_{\text{qubit}} \otimes \rho_{\text{latt}}$, with $\rho_{\text{qubit}} = |\downarrow\rangle \langle\downarrow|$, and ρ_{latt} the lattice state.

2. Apply a Hadamard gate to the qubit probe

$$U_{\text{Had}} = \frac{1}{\sqrt{2}} \begin{pmatrix} 1 & 1 \\ 1 & -1 \end{pmatrix}, \tag{4.6}$$

   in the basis $\{|\downarrow\rangle, |\uparrow\rangle\}$ so that the qubit is in a superposition $(|\downarrow\rangle + |\uparrow\rangle)/\sqrt{2}$. This gate can be generated by $\pi/2$-pulse. It is not necessarily requried for the qubit to be in an equally-weighted superposition, but it is favoured in order to extract maximal information of the lattice dynamics.

3. At $t = 0$, couple the qubit to the lattice and let the composite system time-evolve. For $\kappa \neq 0$, the $|\uparrow\rangle$ state accumulates a phase dependent on n_{latt}.

4. At $t = t_{\text{fin}}$, apply a Hadamard gate to the qubit and measure the qubit in the basis $\{|\uparrow\rangle, |\downarrow\rangle\}$.

As in a standard Ramsey sequence, the last step of the protocol transforms the relative phases accumulated by the internal states into different populations of the internal states. Below for simplicity I set $J_{l,m} = J$ so that the hopping rate is uniform over the lattice.

4.2 Dynamics of the impurity

To describe the time evolution of the composite system through the protocol, I solve the von Neumann equation for the density matrix,

$$i\hbar \frac{\partial}{\partial t} \rho = [H, \rho] \,. \tag{4.7}$$

In the following, I will present details of calculations to obtain the dynamics of the qubit, and in Sec. 4.2.2, explain how the eigenenergies of the lattice are observed.

4.2.1 Solving the von Neumann equation for the probe

I start with the time evolution of step 3 in the protocol and express the von Neumann equation (4.7) in a matrix element form as,

$$i\hbar\frac{\partial}{\partial t}\rho_{s,\alpha;k,\beta} = \sum_{r,\sigma}\left[H_{s,\alpha;r,\sigma}\rho_{r,\sigma;k,\beta} - \rho_{s,\alpha;r,\sigma}H_{r,\sigma;k,\beta}\right], \tag{4.8}$$

where $\rho_{s,\alpha;k,\beta} = \langle s,\alpha|\rho|k,\beta\rangle$ are the elements of the density matrix and $H_{s,\alpha;k,\beta} = \langle s,\alpha|H|k,\beta\rangle$. I use Roman indices s,k,r to refer to probe eigenstates and Greek indices α,β,σ for lattice states. By tracing out the lattice states, the left hand side (l.h.s) of Eq. (4.8) can be recast in the form

$$\sum_{\alpha,\beta}(\text{l.h.s.})\delta_{\alpha,\beta} = \left(i\hbar\frac{\partial\tilde{\rho}_{s,k}}{\partial t} + \hbar\left(\omega_s - \omega_k\right)\tilde{\rho}_{s,k}\right)\mathrm{e}^{-i(\omega_s-\omega_k)t} \tag{4.9}$$

with the probe eigenenergies $\omega_{s(k)}$ and $\rho_{s,k}(t) = \tilde{\rho}_{s,k}(t)\mathrm{e}^{-i(\omega_s-\omega_k)t}$.

While in general the qubit and the lattice become entangled due to the interaction, here I assume that the interaction is weak enough that the density matrix is separable at all times, $\rho(t) = \rho_{\text{qubit}}(t)\otimes\rho_{\text{latt}}(t)$, which allows one to simplify some of the matrix elements in Eq. (4.8) as

$$\langle s,\alpha|\,(1_{\text{qubit}}\otimes H_{\text{latt}})\rho\,|k,\beta\rangle = \langle s|\rho_{\text{qubit}}|k\rangle\,\langle\alpha|\,H_{\text{latt}}\rho_{\text{latt}}\,|\beta\rangle\,, \tag{4.10a}$$
$$\langle s,\alpha|\,(H_{\text{qubit}}\otimes 1_{\text{latt}})\rho\,|k,\beta\rangle = \langle s|H_{\text{qubit}}\rho_{\text{qubit}}|k\rangle\,\langle\alpha|\rho_{\text{latt}}|\beta\rangle\,. \tag{4.10b}$$

I call this assumption as the separability assumption.

After tracing over the lattice system on the right hand side (r.h.s) of Eq. (4.8), one obtains

$$\sum_{\alpha,\beta}(\text{r.h.s.})\delta_{\alpha,\beta} = \hbar\left(\omega_s - \omega_k\right)\rho_{s,k} + \sum_{\alpha,r,\sigma}\left(H_{\text{int}}^{s,\alpha;r,\sigma}\rho_{r,\sigma;k,\alpha} - \rho_{s,\alpha;r,\sigma}H_{\text{int}}^{r,\sigma;k,\alpha}\right)\,. \tag{4.11}$$

For the contact interaction (4.4), the matrix elements of the interaction Hamiltonian are $H_{\text{int}}^{s,\alpha;k,\beta} = \langle s,\alpha|\,H_{\text{int}}\,|k,\beta\rangle = \kappa\,\delta_{s,k}\,\delta_{s,\uparrow}\,\langle\alpha|x_{\text{pr}}\rangle\,\langle x_{\text{pr}}|\beta\rangle$, with $\langle x_{\text{pr}}|\beta\rangle$ being the amplitude of the lattice eigenstate $|\beta\rangle$ at site x_{pr} and $\langle\alpha|x_{\text{pr}}\rangle = \langle x_{\text{pr}}|\alpha\rangle^*$. I substitute this result into Eq. (4.11), apply the separability assumption again, and finally combine it with Eq. (4.9) to rewrite Eq. (4.8) as

$$i\hbar\frac{\partial}{\partial t}\begin{pmatrix}\tilde{\rho}_{\uparrow\uparrow} & \tilde{\rho}_{\uparrow\downarrow}\\ \tilde{\rho}_{\downarrow\uparrow} & \tilde{\rho}_{\downarrow\downarrow}\end{pmatrix} = \begin{pmatrix}0 & M(t)\tilde{\rho}_{\uparrow\downarrow}\\ -M(t)\tilde{\rho}_{\downarrow\uparrow} & 0\end{pmatrix}, \tag{4.12}$$

with

$$M(t) = \sum_{\alpha}\kappa A_{\alpha\alpha} + \sum_{\alpha<\sigma}2\kappa A_{\alpha\sigma}\cos\left\{(\omega_\alpha - \omega_\sigma)t + \phi_{\alpha\sigma}\right\}, \tag{4.13}$$

where $A_{\alpha\sigma}\mathrm{e}^{i\phi_{\alpha\sigma}} = \langle\alpha|x_{\text{pr}}\rangle\langle x_{\text{pr}}|\sigma\rangle\tilde{\rho}_{\sigma\alpha}$ with real numbers $A_{\alpha\sigma} > 0$ and $\phi_{\alpha\sigma}$. The first summation in Eq. (4.13) runs over all lattice eigenstates, while the second one runs over all pairs of eigenstates. Physically, the factors $\langle\alpha|x_{\text{pr}}\rangle$ and $\langle x_{\text{pr}}|\sigma\rangle$ guarantee that only eigenstates that are populated at x_{pr} contribute to the time evolution of the probe's off-diagonal terms. It is worth noting that in this derivation the initial lattice state does not need to be a pure state but could be a general mixed density matrix, which implies that the protocol can be applied likewise to quantum gases with a nonzero thermal component [188].

From Eq. (4.12) it follows that only the off-diagonal elements evolve, which is consistent with the fact that the interaction Hamiltonian describes the dephasing of the probe state. This requires the initial state to have non-zero off-diagonal elements, and so the optimal choice is an equally-weighted superposition such as $(|{\downarrow}\rangle + |{\uparrow}\rangle)/\sqrt{2}$ (see Ref. [240]).

In step 4 of the protocol, a second Hadamard gate is applied, and the qubit state is given by

$$\rho_{\mathrm{qubit}}(t) = \begin{pmatrix} \rho_{\mathrm{qubit}}^{\uparrow\uparrow} & \rho_{\mathrm{qubit}}^{\uparrow\downarrow} \\ \rho_{\mathrm{qubit}}^{\downarrow\uparrow} & \rho_{\mathrm{qubit}}^{\downarrow\downarrow} \end{pmatrix} = \frac{1}{2} \begin{pmatrix} 1+\cos\theta(t) & i\sin\theta(t) \\ -i\sin\theta(t) & 1-\cos\theta(t) \end{pmatrix} , \tag{4.14}$$

with

$$\theta(t) = \left(\omega_{\mathrm{qubit}} + \sum_{\alpha} \frac{\kappa A_{\alpha\alpha}}{\hbar} \right) t + \sum_{\alpha<\sigma} \frac{2\kappa A_{\alpha\sigma}}{\hbar\Omega_{\alpha,\sigma}} \left[\sin\left(\Omega_{\alpha,\sigma} t + \phi_{\alpha\sigma}\right) - \sin\phi_{\alpha\sigma} \right] . \tag{4.15}$$

For compactness, I rewrite this as,

$$\theta(t) = \tilde{\omega} t + \sum_{\alpha<\sigma} \left[c_{\alpha,\sigma} \sin\Omega_{\alpha,\sigma} t + d_{\alpha,\sigma} \left(\cos\Omega_{\alpha,\sigma} t - 1\right) \right] , \tag{4.16}$$

where

$$\tilde{\omega} = \omega_{\mathrm{qubit}} + \frac{\kappa}{\hbar} \sum_{\alpha} A_{\alpha\alpha} , \tag{4.17a}$$

$$\Omega_{\alpha,\sigma} = \omega_\alpha - \omega_\sigma , \qquad \eta_{\alpha,\sigma} = \frac{2\kappa A_{\alpha\sigma}}{\hbar\Omega_{\alpha,\sigma}} , \tag{4.17b}$$

$$c_{\alpha,\sigma} = \eta_{\alpha,\sigma} \cos\phi_{\alpha\sigma} , \qquad d_{\alpha,\sigma} = \eta_{\alpha,\sigma} \sin(\phi_{\alpha\sigma}) . \tag{4.17c}$$

The summation runs over all pairs of lattice eigenstates occupying the site x_{pr}, and $\Omega_{\alpha\sigma} = \omega_\alpha - \omega_\sigma$ is the difference between the corresponding eigenenergies. The coefficients $c_{\alpha\sigma}$, $d_{\alpha\sigma}$ are functions of $\Omega_{\alpha\sigma}$, the local density n_{latt}, and the relative phase between eigenstates at the site x_{pr}.

4.2.2 Extraction of information about the lattice system from the qubit

If there is no particle at the coupled site x_{pr}, one obtains $c_{\alpha\sigma} = d_{\alpha\sigma} = 0$ and $\tilde{\omega} = \omega_{\mathrm{qubit}}$, and the qubit evolves freely. If there is only one lattice eigenstate at the site x_{pr}, one sees $c_{\alpha\sigma} = d_{\alpha\sigma} = 0$ and $\tilde{\omega} = \omega_{\mathrm{qubit}} + \kappa n_{\mathrm{latt}}/\hbar$. This case allows one to probe the density n_{latt} at the site x_{pr} through measurements of $\tilde{\omega}$.

If the coupled site x_{pr} is occupied by more eigenstates than one, the population of the qubit $P_s(t) = \langle s|\rho_{\mathrm{qubit}}(t)|s\rangle$ for $s \in \{\uparrow, \downarrow\}$ informs one about the spacings between lattice energy levels $\Omega_{\alpha\sigma}$ of the states present at x_{pr}. Let me focus first on the case where there is no degeneracy, and discuss the degenerate case at the end of this section. For simplicity, I consider the case in which two eigenstates are at the site x_{pr} and so there is only one non-zero frequency difference $\Omega_{21} = \omega_2 - \omega_1 > 0$. The time dependence in the density matrix of the qubit (4.14) is then given by

$$\begin{aligned}\cos\theta(t) &= \cos\left[\tilde{\omega}t + c_1 \sin\Omega_{21}t + d_1\left(\cos\Omega_{21}t - 1\right)\right] \\ &= \cos\left(\tilde{\omega}t - d_1\right)\big\{\cos(c_1\sin\Omega_{21}t)\cos(d_1\cos\Omega_{21}t) \\ &\qquad\qquad\qquad - \sin(c_1\sin\Omega_{21}t)\sin(d_1\cos\Omega_{21}t)\big\} \\ &\quad - \sin\left(\tilde{\omega}t - d_1\right)\big\{\sin(c_1\sin\Omega_{21}t)\cos(d_1\cos\Omega_{21}t) \\ &\qquad\qquad\qquad + \cos(c_1\sin\Omega_{21}t)\sin(d_1\cos\Omega_{21}t)\big\}. \end{aligned} \tag{4.18}$$

Trigonometric functions containing trigonometric functions such as $\cos\left(c_1\sin\Omega_{21}t\right)$ can be expanded with the Jacobi-Anger expansion [241] as

$$\cos(z\cos\phi) = J_0(z) + 2\sum_{k=1}^{\infty}(-1)^k J_{2k}(z)\cos(2k\phi), \tag{4.19a}$$

$$\cos(z\sin\phi) = J_0(z) + 2\sum_{k=1}^{\infty} J_{2k}(z)\cos(2k\phi), \tag{4.19b}$$

$$\sin(z\cos\phi) = 2\sum_{k=0}^{\infty}(-1)^k J_{2k+1}(z)\cos[(2k+1)\phi], \tag{4.19c}$$

$$\sin(z\sin\phi) = 2\sum_{k=0}^{\infty} J_{2k+1}(z)\sin[(2k+1)\phi], \tag{4.19d}$$

where the $J_k(z)$ are the Bessel functions of first kind and of order k. Thus, the function (4.18) can be decomposed into frequency-dependent terms $\tilde{\omega} \pm m\Omega_{21}$, with $m \geq 0$ integer. It is straightforward to generalise this case to an arbitrary number of lattice states, where the function (4.18) contains components of $\tilde{\omega} \pm m\Omega_{\alpha\sigma}$ with $m \geq 0$ integer and α, σ running over all pairs of lattice states. This situation is analogous to a system of trapped ions where the internal state of the ion is coupled to its motional states in the trap [242]. In this context, the qubit represents the trapped ion, and the pairs of lattice eigenstates play the role of the motional state. The qubit eigenfrequencies $\tilde{\omega} \pm m\Omega_{\alpha\sigma}$ for $m > 0$ corresponds to the motional sidebands of the trapped ion.

Finally, I consider a lattice system with energy degeneracy between eigenstate s_1 and s_2. The dynamics of the probe follows Eq. (4.12), with $M(t)$ given by

$$M(t) = \sum_{\alpha}\kappa A_{\alpha\alpha} + 2\kappa A_{s_1 s_2}\cos\phi_{s_1 s_2} + \sum_{\substack{\alpha<\sigma \\ \alpha,\sigma\neq s_1,s_2}} 2\kappa A_{\alpha\sigma}\cos\left\{(\omega_\alpha - \omega_\sigma)t + \phi_{\alpha\sigma}\right\}. \tag{4.20}$$

One can see that the second term originates from the degeneracy by comparing it with the non-degeneracy case given in Eq. (4.13). As seen, the level degeneracy shifts the frequency $\tilde{\omega}$ (see Eq. (4.17a)) but does not disturb the observation of the lattice energy levels.

4.3 Performance of the protocol

I have derived the dynamics of the probe by assuming the coupling to be weak enough for the separability assumption. In this section, to argue the reliability of the protocol, I will compare this analytical result with exact numerical calculations. First, I consider two types of lattices whose spectra show regular and chaotic features, respectively, as explained in Sec. 4.1, and see how this difference affects the protocol. Later, to consider a more realistic situation and see how robust the protocol is, I assume that the qubit is subject to an environment which leads to an extra dephasing effect.

4.3.1 Non-dephasing quantum probe

I performed numerical calculations to evaluate the probe scheme in a finite lattice showing regular or chaotic spectra, and will compare the results with the analytical ones (4.14). I set as the energy unit the hopping rate amplitute $J = 1$ and assume small interaction strengths $\kappa < 1$, which is consistent with the case of the analytical calculation.

First, I consider a 5×5 square lattice on a rectangular domain (see Fig. 4.2(c)) and add small diagonal disorder, given by on-site energies taken from a uniform random distribution $\epsilon_k \in [-0.3, 0.3]$. This noise lifts the level degeneracies due to the high symmetry of the square lattice. I also set the qubit level splitting to $\omega_{\mathrm{qubit}} = 5$. As the initial lattice state, I take an equally-weighted superposition of the four lower-energy eigenstates, which are labelled as 1, 2, 3, 4. According to the analytical results, the time evolution of the qubit contains six first-order ($m = 1$) sidebands in frequency space, given by $\tilde{\omega} \pm \Omega_{\alpha\sigma}$ for $\alpha, \sigma \in \{1, 2, 3, 4\}$.

I plot the time evolution of the population of the $|\uparrow\rangle$ state for different coupled sites x_{pr} in Fig. 4.2(a) and each Fourier transform in Fig. 4.2(b). Each of the signals shows a significant peak at $\tilde{\omega} = \omega_{\mathrm{qubit}} + \kappa n_{\mathrm{latt}} \simeq \omega_{\mathrm{qubit}}$ because κn_{latt} is small ($n_{\mathrm{latt}} \lesssim 0.1$). Also, there are another 12 peaks distributed symmetrically around the dominant peak. The frequencies of the peaks agree with the first-order sidebands at $\tilde{\omega} \pm \Omega_{\alpha\sigma}$ for $\alpha, \sigma \in \{1, \ldots, 4\}$ considering the frequency resolution $\delta\omega \simeq 0.1$ in Fig. 4.2 (b). The higher-order sidebands $\tilde{\omega} \pm m\Omega_{\alpha\sigma}$ disappear for $m \geq 2$, because the amplitude of the peaks is proportional to the Bessel function $J_m(c_{\alpha\sigma})$ or $J_m(d_{\alpha\sigma})$ with $c_{\alpha\sigma}, c_{\alpha\sigma} \propto \kappa n_{\mathrm{latt}}$. Considering $\kappa n_{\mathrm{latt}} \lesssim 10^{-2}$, the Bessel functions are $J_m(c_{\alpha\sigma}), J_m(d_{\alpha\sigma}) \lesssim 10^{-4}$ for $m \geq 2$, which is beyond the resolution in Fig. 4.2(b). To acquire enough resolution to allow the observation of the first sidebands, one has to perform measurements for a long time. I will discuss practical requirements on the measurement to achieve the required frequency resolution in Sec. 4.3.3.

Also, one can observe that coupling to different sites x_{pr} results in slightly different signals (see Fig. 4.2(b)). For example, for $x_{\mathrm{pr}} = 5$, there are two distinct peaks at $\omega \sim 4.3$. For $x_{\mathrm{pr}} = 6$, there are three similarly intense peaks around the same frequency, while for $x_{\mathrm{pr}} = 7$ only one large peak is observed. These variations come from the spatial

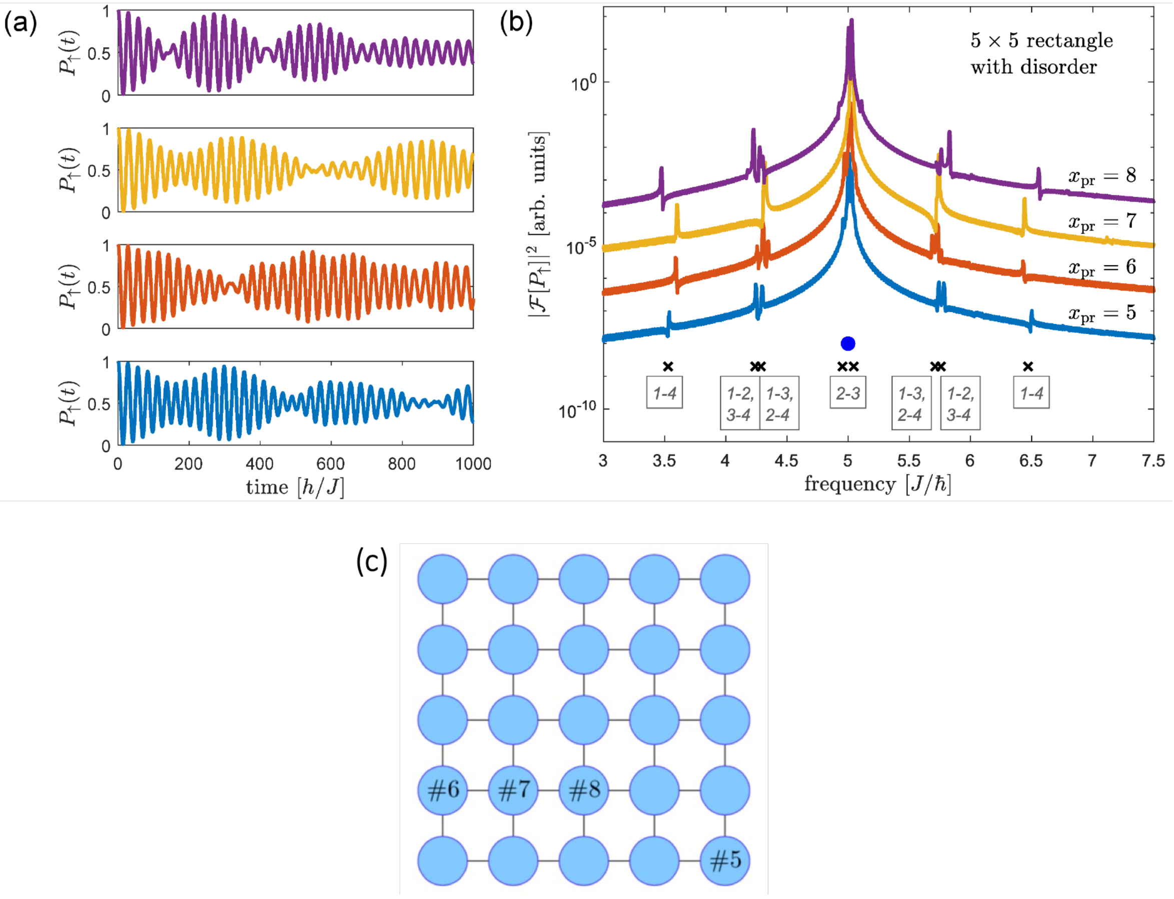

Figure 4.2: (a) Time evolution of population $P_\uparrow(t)$ of the $|\uparrow\rangle$ state of the qubit, when coupled to the lattice site $x_{\rm pr} = 8, 7, 6, 5$ (from top to bottom) of a square lattice on a 5×5 rectangular domain with diagonal disorder. (b) Fourier transform of the signals in (a), displaced vertically for clarity with the same ordering. The full circle at the bottom indicates $\omega_{\rm qubit}$, while the crosses are the expected frequencies $\tilde{\omega} \pm \Omega_{\alpha\sigma}$, with the states $\alpha, \sigma \in \{1, 2, 3, 4\}$ indicated in the boxes. In these simulations, $\omega_{\rm qubit} = 5.0$ and $\kappa = 0.3$, with the hopping rate as the energy unit, $J = 1$. (c) Schematic of the square lattice with $\#\,5$, $\#\,6$, $\#\,7$, $\#\,8$ labelling the sites to which the probe is coupled.

dependence of the various eigenstates, such as their local densities at the coupled site. This result indicates that the protocol can reveal the different energy spacings in the spectrum of a lattice system in a position-dependent way, from which the local density can be reconstructed.

To see if the lattice type affects the protocol, I switch the lattice system to a stadium-shaped system, which possesses a chaotic spectrum [238]. I have calculated the time evolution of the qubit coupled to a stadium lattice with 27 sites (see Fig. 4.3(c)). Here, I set an equally-weighted superposition of three eigenstates as the initial lattice state. The analytical results indicate six first-order sidebands around $\omega = \omega_{\text{qubit}}$ such that $\tilde{\omega} \pm \Omega_{\alpha\sigma}$ for $\alpha, \sigma \in \{1, 2, 3\}$.

I plot the time evolution of the population $P_\uparrow(t)$ of the $|\uparrow\rangle$ state when the qubit is coupled to $x_{\text{pr}} = 15$ (see the top panel in Fig. 4.3(a)), where all three eigenstates are populated. As expected, the Fourier transform of the signal shows six peaks corresponding to $\tilde{\omega} \pm \Omega_{\alpha\sigma}$ for $\alpha, \sigma \in \{1, 2, 3\}$ as well as a dominant peak at $\omega \simeq \omega_{\text{qubit}}$, like in the square lattice case (see Fig. 4.3(b)). This suggests that the protocol is powerful enough to reveal chaotic energy spectra.

As a final check, I consider the qubit coupled to the site $x_{\text{pr}} = 2$ (see the bottom panel in Fig. 4.3(a)), where none of the three eigenstates are populated. As expected, the Fourier transform of the resulting signal shows only one peak at $\omega \simeq \omega_{\text{qubit}}$ (see Fig. 4.3(b)).

4.3.2 Effect of dephasing on the quantum probe

As it is inevitable that the probe is also disturbed by the environment, I will next investigate how the accuracy of the protocol is affected by noise. If the lattice is realised by cold atoms in an optical lattice, and the qubit probe corresponds to an atom trapped in another optical lattice or optical tweezers, one can expect that the qubit is exposed to dephasing due to the trapping and ambient electromagnetic fields [243]. This can be described by the standard Markovian approach to open quantum systems [244], and the time evolution of the density matrix of the composite system is given by

$$\hbar \frac{\partial}{\partial t}\rho(t) = -i\,[H, \rho(t)] + \gamma \left(2L\rho(t)L^\dagger - \left\{L^\dagger L, \rho(t)\right\}\right), \tag{4.21}$$

where the Lindblad operator $L = \sigma_z$ represents the dephasing of the probe in the z direction (i.e. the population of ↑ and ↓), and γ is the dephasing rate.

Figure 4.4 displays the time evolution of the joint system of the lattice and the qubit with dephasing noise in a square and a stadium lattice, and presents the Fourier transform of the qubit signals. The panel (a) shows a 5×5 square lattice with disorder and dephasing $\gamma = 0.01, 0.06, 0.08$. Although for a small dephasing rate such as $\gamma \simeq 0.01$ there is no notable change, larger dephasing rates make the resolution poorer so that the peaks cannot be distinguished. For example, see the two merging peaks around $\omega \sim 5.7$ for $\gamma \gtrsim 0.06$. For $\gamma \gtrsim 0.08$, all peaks are hard to observe. In case that the dephasing rate is comparable to or larger than the energy/frequency differences between neighbouring peaks, one cannot detect the two individual peaks.

Certainly, the dephasing effect weakens the strength of the peaks in a stadium lattice as well. However, the protocol is more robust against dephasing due to the

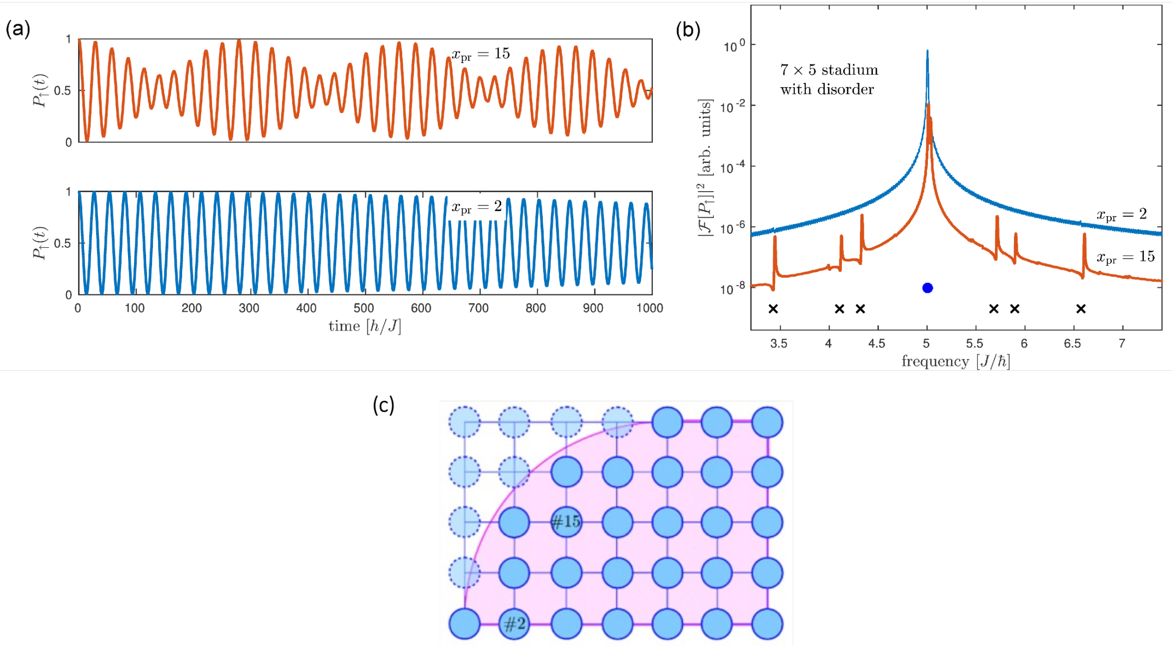

Figure 4.3: (a) Time evolution of population $P_\uparrow(t)$ of the $|\uparrow\rangle$ state of the qubit, when coupled to an occupied (top panel, $x_{\rm pr} = 15$) or empty (bottom panel, $x_{\rm pr} = 2$) site of a stadium lattice 5×7. (b) Fourier transform of the signals in (a). The crosses at the bottom represent the expected frequencies $\tilde{\omega} \pm \Omega_{\alpha\sigma}$ for $\alpha, \sigma \in \{1, 2, 3\}$, while the full circle is at $\omega = \omega_{\rm qubit}$. In these simulations, $\omega_{\rm qubit} = 5.0$ and $\kappa = 0.3$, with the hopping rate as the energy unit, $J = 1$. (c) Schematic of the stadium lattice with # 2, # 15 labelling the sites to which the probe is coupled. Due to the symmetry of the lattice shape, considering a quarter of the shape together with periodic condition is enough to simulate the dynamics.

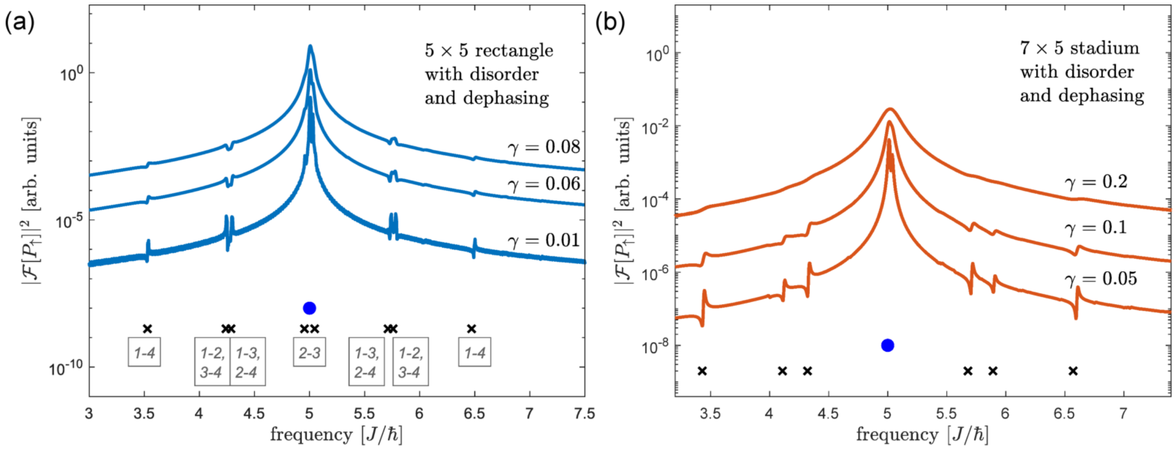

Figure 4.4: (a) Fourier transform of the signals for a probe coupled to site #5 of the 5×5 square lattice with disorder, and subject to dephasing with various dephasing rates $\gamma = 0.01, 0.06, 0.08$; other parameters and symbols are the same as in Fig. 4.2. (b) Fourier transform of the signals for a probe coupled to site #15 of the 5×7 stadium lattice with disorder, and subject to dephasing with various dephasing rates $\gamma = 0.05, 0.1, 0.2$; other parameters and symbols are the same as in Fig. 4.3. In both panels, the different traces are displaced vertically for clarity.

level repulsion. The time evolution of the qubit is illustrated in the panel (b), where a 5×7 stadium lattice is used. By increasing the dephasing rate γ, the amplitudes of the peaks become smaller. However, the peaks are not merged since all peaks are well separated, which is a feature of the chaotic spectrum.

In general, the peaks for both regular and chaotic spectra can be distinguished if one can control the dephasing rate to be below a threshold which depends on how close the neighbouring peaks are. I clarify that there is no energy exchange between the probe state and the source of the environment noise, which guarantees that the noise does not affect the energy/frequency of the Fourier peaks. In the presence of dissipative noise, this does not hold.

4.3.3 Measurement time and frequency uncertainty

I evaluate the required time duration to monitor the probe in order to extract spectral information about the lattice system, especially when the probe is subject to large dephasing rates such as $\gamma \gtrsim 0.1$. The trade-off between frequency and observation time that follows from the Fourier transform can be explained with the Wiener-Heisenberg relation between angular frequency resolution $\Delta\omega$ and measurement time t_{fin} [245, 246]

$$\Delta\omega\, t_{\mathrm{fin}} \geq \frac{1}{2}. \tag{4.22}$$

For cold atoms in optical lattices, a typical hopping rate is $J/\hbar \sim 1 - 100$ Hz. The typical system lifetime is limited by three-body losses to $\sim 10 - 70$ s [247, 248], which would enable one to resolve peaks down to $\Delta\omega \gtrsim 10^{-2}$–$10^{-1}$ Hz. This appears sufficient to observe the peaks in the most demanding situation, i.e. in the simulations shown above: nearby peaks in the disordered square lattice are separated by $\simeq 10^{-2} J/\hbar$, which corresponds to $\sim 10^{-2} - 1$ Hz, depending on J. In an experiment published in 2020 where impurities were interacting with an atomic bath, the lifetime of the impurities can be up to 1.5 s [249]. It is therefore possible to monitor the impurity dynamics enough long to see signals of the lattice.

4.4 Discussion and Conclusions

In this work, I have studied the time evolution of a qubit probe locally coupled to a lattice system. I have shown that the dynamics of the probe can encode information about the lattice system, and proposed a nondestructive protocol to measure the excitation spectrum of the lattice by using state-dependent interactions for the probe. The numerical calculations I have presented support the applicability of the protocol to investigate lattices having regular or chaotic spectra.

I will describe advantages of this protocol in the following.

(i) One selling point is that ingredients of the protocol are simple: a two level probe and a local density-density coupling to the system of interest. This protocol allows one to monitor the dynamics of the probe more easily than with a recently proposed scheme [250], where the probe is composed of a harmonic oscillator to measure the spectral density of a large structured environment. The density-density coupling to the lattice system reveals if particles exist at the coupled site. This approach is applicable to bosonic and fermionic many-body lattice systems [211–231].

(ii) Another advantage of the protocol is that it is nondestructive. It encodes the excitation spectrum into the population of the probe through a Ramsey sequence with measurements in the $|\uparrow\rangle$, $|\downarrow\rangle$ basis. This protocol has lower experimental requirements than other protocols to determine the structure or internal couplings of spin networks [251–253], which require full state tomography.

(iii) Finally, the protocol does not rely on a resonant coupling between the probe and the lattice system [222]. This advantage enables one to observe various spectral gaps simultaneously, even if the probe is subject to dephasing.

Due to these low experimental requirements, the protocol will provide a powerful tool to characterise the spectrum of systems composed of cold atoms in optical lattices. I believe that this work will help the development of new measurement techniques [213, 217, 220–226, 228, 254] utilising atomic impurities to characterise cold atomic quantum simulators [218, 227, 229–231, 255] and to study quantum chaos in finite optical lattices [238, 256].

While for this work I used the tight-binding model as a lattice system to be examined, one can also consider other models and use other interaction terms or external fields to test the versatility of the protocol. In principle, an impurity coupled to a system is obviously influenced by the system and extracts some sort of information about the system. Questions to address are how to obtain the information and how not to disturb the system. The Ramsey sequence together with weak interaction is a common method for nondestructive probing as used for this work, and for example has enabled one to observe the dynamics of a fermionic many-body system [192]. Besides weak interactions, spin-exchange collisions between a bath system and impurities can be utilised and for example used to probe the temperature of the bath system even before the system reaches equilibrium [249]. Applying pump pulses is also useful and allows one to monitor the dynamics of impurities in Bose-Einstein condensate, leading to the observation of the formation of Bose polarons [257].

Chapter 5

Bayesian parameter estimation using Gaussian states and measurements

Quantum sensing devices have the potential to outperform classical counterparts, as they can provide a fundamental increase in precision. If N is the number of probes, in ideal scenarios, the estimation precision can scale at the Heisenberg limit (HL) as $1/N$. On the other hand, classical strategies are limited by a slower scaling, the standard quantum limit, as $1/\sqrt{N}$.

In quantum optical systems, which I am interested in here, the number of probes is not well-defined due to the uncertainty of the photon number. Therefore, the precision scaling is usually represented as a function of the mean photon number or mean energy of the probe. It has been demonstrated that some quantum strategies lead to a quadratic scaling in the mean photon number, which corresponds to the HL in this context, and outperform strategies exploiting classical resource. However, implementation of such strategies is not always easy. Preparing desired probe states and carrying out the corresponding measurements can be complicated, and the resulting imperfect nature of the probe states may reduce the expected benefits. Moreover, uncorrelated noise can prevent an advantageous increase in the scaling and stop the increase [258–260], although some ways to cope with noise have been proposed [261, 262]. Thus, it is practically important to consider feasible and robust experimental setups while identifying better estimation strategies than classical ones. For parameter estimation in continuous variable (CV) systems, Gaussian states and measurements are generally implementable. It is known that CV systems can reach the HL within many local estimation scenarios [263–270].

A useful tool for indicating optimal scaling is the Cramér-Rao bound (CRB). The CRB uses unbiased estimators and provides a lower bound for the variance of the precision via the inverse Fisher information (FI). However, preparing unbiased estimators requires precise prior information on the estimated parameters. Therefore, the local estimation is well-justified only when one has many independent probes such that the CRB gives the asymptotically achievable limit on scaling. When the number of probe state is not enough, the local approach results in deviant behaviours, for example, better scaling than the HL [271, 272] or infinite FI with finite resource [273].

This motivates the study of Bayesian estimation approaches for quantum sensing. In Bayesian estimation scenarios, the prior knowledge of the parameter to be estimated is described by a probability distribution, and the probability is updated as a measurement outcome is obtained. Bayesian estimation does not demand prior information and is valid for any number of probes. In this sense, Bayesian estimation is more rigorous than local estimation. On the other hand, with growing measurement data, the prior knowledge affects the estimation less. Thus, one can use a hybrid approach: At the beginning, Bayesian estimation is applied, and later local estimation is employed as enough data is accumulated to narrow down the range of the parameter to be estimated.

In this chapter, I consider Bayesian estimation scenarios for quantum optical CV systems. In local approaches, much progress has been made for CV systems, for example, the calculations of quantum Fisher information (QFI) [263–270] and the associated optimal strategies achieving the CRB [14, 274–278] have been presented. In comparison, Bayesian estimation in CV systems has not yet been explored, even though there are some recent reports giving insights into Bayesian estimation for discrete [279] and CV states [280, 280–285]. Identifying efficient and feasible Bayesian approaches helps the development of quantum sensing technology.

In quantum optical CV systems it is advantageous to use Gaussian states and Gaussian measurements [22]. Gaussian states not only allow one to use an elegant mathematical description in phase space, but they are also relatively easy to implement and commonly used [286, 287]. Gaussian measurements such as homodyne and heterodyne detections have been shown to outperform number detection for repetitions [281] and to be more robust against noise than photon number detection and “on/off” detection, which distinguishes between the absence and presence of photons [276, 288, 289].

To broadly examine the performance of Gaussian states and measurements in Bayesian metrology, I explore three paradigmatic estimation problems: the estimation of phase-space displacement, of the phase, and of single-mode squeezing. For each task, I provide feasible strategies using single-mode Gaussian states and employing homodyne or heterodyne detection. In Sec. 5.1, I briefly review the procedures of Bayesian estimation and the relevant concepts of Gaussian quantum optics. In Sec. 5.2, I investigate the estimation of displacement and show analytical calculations for the achievable precision. In Secs. 5.3 and 5.4, I proceed with the same analysis for phase estimation and squeezing strength estimation, respectively. Finally, I discuss the results, and present conclusions and an outlook in Sec. 5.5.

This project has been accomplished in collaboration with Simon Morelli, Elizabeth Agudelo, and Nicolai Friis. I have been involved in comprehensive discussion about this project and performed all the calculations for the Bayesian phase estimation. The work presented in this chapter has been submitted to Quantum Science and Technology and is available on arXiv:2009.03709 [4].

5.1 Framework

I will give an overview over the formulation of Bayesian estimation and Gaussian states. For a comprehensive reviews of classical Bayesian estimation, see Refs [290–292]. For details of local and Bayesian estimations in quantum scenarios, see the Appendix of Ref. [293]. For basic ideas of Gaussian states, see Sec. 1.2 and Ref. [22].

5.1.1 Bayesian estimation scenario

The basic idea of Bayesian estimation is to update knowledge one has initially, based on new measurement results. Suppose that one aims to estimate a parameter θ. The initial knowledge about the parameter θ is encoded in a probability distribution $p(\theta)$, which is called the prior distribution (or "prior" for short). The prior distribution covers all the beliefs, e.g. system properties, expertise, and information such as prior experimental data. When a measurement is performed, one obtains the probability $p(m|\theta)$ of the measurement outcome m given a parameter θ, which is called likelihood, from the model describing the system and measurement. Combined with the prior $p(\theta)$, the probability to obtain an outcome m is

$$p(m) = \int d\theta \; p(m|\theta)p(\theta), \tag{5.1}$$

where the integral is to be understood as a sum in case of discrete systems. The conditional probability of the parameter θ given measurement outcome m is calculated via Bayes' law as

$$p(\theta|m) = \frac{p(m|\theta)p(\theta)}{p(m)}, \tag{5.2}$$

which is called the posterior distribution because one has updated the initial knowledge $p(\theta)$ with the measurement results. By repeating this updating procedure as illustrated in Fig. 5.1, where the posterior of the previous step serves as the prior at the next step, one obtains a more accurate value of the parameter θ.

After some measurements, the posterior distribution describes all available information about the parameter. Nevertheless, it is useful to look at the estimator and the variance of the posterior in order to evaluate the property of the posterior at a glance. The estimator provides a value for the parameter and is given by the mean value of the posterior

$$\begin{aligned} \hat{\theta}(m) &= \langle\theta\rangle \\ &= \int d\theta \; p(\theta|m)\,\theta. \end{aligned} \tag{5.3}$$

The variance shows the uncertainty in the estimation and stands for the confidence in the estimation, given by

$$V_{\text{post}}(m) = \int d\theta \; p(\theta|m)\left(\theta - \hat{\theta}(m)\right)^2. \tag{5.4}$$

Smaller variance indicates more precision in the estimation. Since the variance depends on measurement outcomes as seen in Eq. (5.4), a good figure of merit for the posterior is the average variance

$$\bar{V}_{\text{post}} = \int dm \; p(m)V_{\text{post}}(m), \tag{5.5}$$

which I will use to evaluate strategies in each estimation task. Note that here the mean value and the mean square error variance are defined by assuming that the parameter to

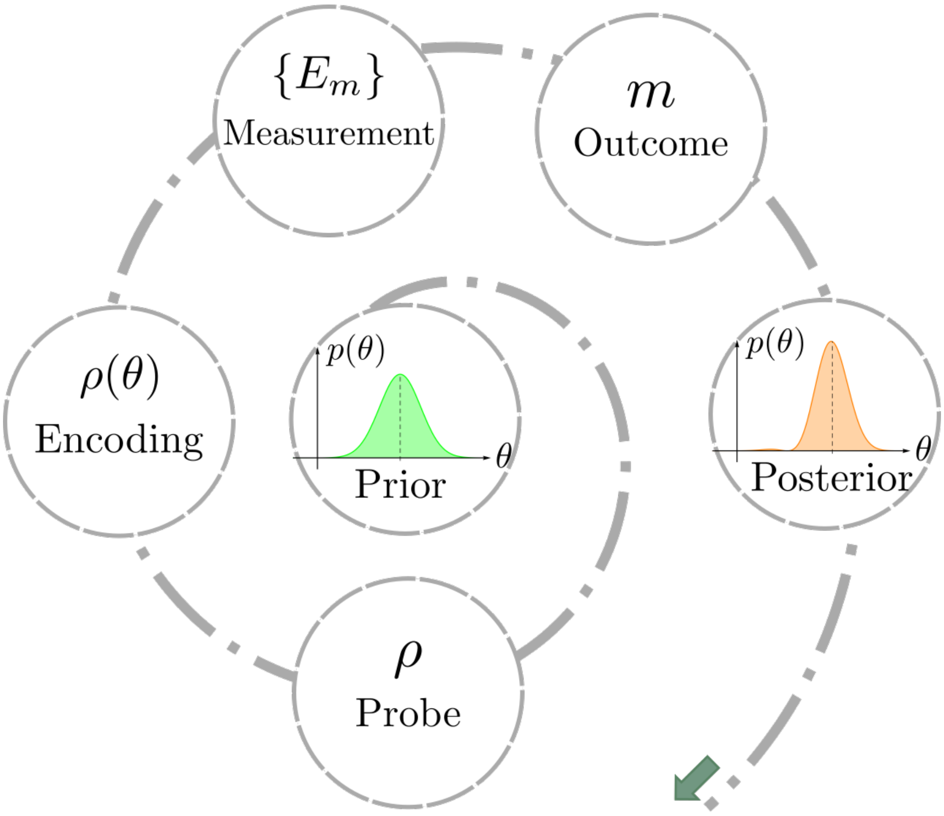

Figure 5.1: A overview of Bayesian quantum parameter estimation. In Bayesian estimation scenarios, the initial knowledge is encoded in the prior distribution $p(\theta)$, which is updated based on measurement results m, leading to a posterior distribution. Since one treats quantum systems, the measurement procedure includes preparing a probe state ρ into which the parameter θ is encoded. The measurement consists of a positive-operator valued measurement (POVM) with elements $E_m \geq 0$ satisfying $\int dm\ E_m = \mathbb{1}$, representing the possible outcome by m.

be estimated is distributed in the real number space $[-\infty, \infty]$. However, for example, in phase estimation, the parameter to be estimated follows a circular distribution, and hence these integrals are taken within the periodicity of phase, e.g. $[-\pi, \pi]$.

The precision of the estimation procedure depends on the form of the prior, which can be taken as any complicated distribution. Broad priors generally influence the outcome less than narrow priors. Therefore, it is important to take care of how much information is encoded in the prior. However, repetition of the estimation procedure decreases the influence of the prior, and the influence disappears asymptotically, cf. Chap. 13 in Ref. [290]. Consequently, it is convenient to encode one's knowledge approximately using a family of probability distributions with a few degrees of freedom. A good example is a Gaussian distribution.

A class of probability distributions is said to be conjugate to a given likelihood function, if priors within this class result in posterior distributions that belong to the same class. Therefore, by choosing the prior to be conjugate to the likelihood in this way, the updating process becomes easier since only a few characteristic parameters of the prior distribution are required to obtain the posterior distribution instead of a new full calculation in order to determine the posterior distribution. Gaussian distributions are self-conjugate with respect to the mean. For example, for Gaussian likelihood functions that encode the estimated parameter in their mean, the class of conjugate priors is Gaussian distributions. The following proposition is well known in statistical theory [290–292, 294] and will be used particularly in Sec. 5.2:

Proposition: Let the likelihood be Gaussian distributed, $p(m|\theta) = \mathcal{N}_m\big(\bar{m}(\theta), \tilde{\sigma}^2\big) \propto \mathcal{N}_\theta\big(\bar{\theta}(m), \sigma^2\big)$, where $\bar{\theta}(m)$ is the mean of the distribution of the parameter θ to be estimated. Then, a Gaussian prior is the natural conjugate, i.e. if the prior is Gaussian distributed with $p(\theta) = \mathcal{N}_\theta(\mu_0, \sigma_0^2)$, the posterior distribution $p(\theta|m)$ is also Gaussian with mean value $\mu_p = \big[\sigma^2\mu_0 + \sigma_0^2\bar{\theta}(m)\big]/(\sigma_0^2 + \sigma^2)$ and variance $\sigma_p^2 = (\sigma^2\sigma_0^2)/(\sigma_0^2 + \sigma^2)$.

5.1.2 Bayesian parameter estimation using quantum systems

One can apply the framework of Bayesian estimation to a quantum system. The parameter θ to be estimated is encoded into a probe state, given by a density operator ρ, by a transformation that is a completely positive and trace-preserving (CPTP) map. I consider that the transformation is a unitary operator U_θ, and the resulting state is written as $U_\theta \rho U_\theta^\dagger$. The measurement of the encoded state can be represented by a positive operator-valued measure (POVM) with elements $E_m \geq 0$, whose integral on the Hilbert space of the probe gives the identity, $\int dm\ E_m = \mathbb{1}$. In this case, the likelihood is given by

$$p(m|\theta) = \mathrm{Tr}\left[E_m \rho(\theta)\right]. \tag{5.6}$$

In local estimation scenarios with unbiased estimators $\hat{\theta}$, the variance $V(\hat{\theta})$ of the estimator is bounded by CRB as

$$V(\hat{\theta}) \geq \frac{1}{I\left(p(m|\theta)\right)}\,, \tag{5.7}$$

where $I\left(p(m|\theta)\right)$ is the FI of the likelihood $p(m|\theta)$ and is described by

$$I\left(p(m|\theta)\right) = \int dm\ p(m|\theta)\left(\frac{\partial}{\partial\theta}\log\left(p(m|\theta)\right)\right)^2 . \tag{5.8}$$

Note that $p(m|\theta)$ is composed of the density matrix ρ of the probe and the measurement results as shown Eq. (5.6). With the sample number infinite, the CRB (5.7) is always tight since it is saturated by the maximum likelihood estimator. Thus, local estimation problems can be interpreted as finding an estimation strategy with a likelihood $p(m|\theta)$ leading to a FI as large as possible. In the quantum setting, this corresponds to the task of determining suitable probe states ρ and measurements $\{E_m\}$. It is possible to optimise the FI analytically over all PVOMs, leading to the QFI $\mathcal{I}\left(p(m|\theta)\right)$ and Quantum CRB

$$V(\hat{\theta}) \geq \frac{1}{\mathcal{I}\left(p(\theta)\right)} . \tag{5.9}$$

The QFI can be described in terms of the Uhlmann fidelity $\mathcal{F}(\rho_1,\rho_2) = \left(\mathrm{Tr}\sqrt{\sqrt{\rho_1}\rho_2\sqrt{\rho_1}}\right)^2$ by

$$\mathcal{I}\left(\rho(\theta)\right) = \lim_{d\theta\to 0} 8\frac{1-\sqrt{\mathcal{F}(\rho(\theta),\rho(\theta+d\theta))}}{d\theta^2} . \tag{5.10}$$

Bayesian estimation scenarios have a counterpart of the CRB, which is called the Van Trees inequality and which bounds the average variance of the posterior as

$$\bar{V}_{\text{post}} \geq \frac{1}{I(p(\theta)) + \bar{I}(p(m|\theta))} , \tag{5.11}$$

where $I(p(\theta))$ is the FI of the prior $p(\theta)$, and $\bar{I}(p(m|\theta)) = \int d\theta\ I(p(m|\theta))p(\theta)$ is the average FI of the likelihood [295, 296]. This bound is often called Bayesian CRB [297]. A big difference from the CRB for local estimation scenarios is that this bound may not be tight, and there may be no way to achieve the equality.

For Bayesian quantum estimation problems, the Van Trees inequality can be modified to the Bayesian version of the quantum CRB by noting that the FI is bounded from above by the QFI: $\mathcal{I}(\rho(\theta)) \geq I(p(m|\theta))$. In additon, the QFI, $\mathcal{I}(\rho(\theta))$, is independent of θ if the encoding transformation U_θ is a unitary transformation. Consequently, one obtains $\mathcal{I}(\rho(\theta)) \geq \bar{I}(p(m|\theta))$. Thus, the Bayesian quantum CRB is given by

$$\bar{V}_{\text{post}} \geq \frac{1}{I(p(\theta)) + \mathcal{I}(\rho(\theta))} , \tag{5.12}$$

which is the lower bound of the average variance for all possible POVMs [293]. This bound may not be tight, similar to the Van Trees inequality (5.11).

While local estimation scenarios have some methods to construct optimal POVMs for fixed probe states, Bayesian estimation scenarios do not. Thus, optimisation of probes and measurements for Bayesian estimation has to be carried out on a case-by-case basis and is typically challenging. Moreover, even if one has an optimal set of a probe state and measurements for a given prior, a procedure to prepare the set may need complicated setups. Also, generally optimal sets of probe states and measurements are no longer optimal after even a single update. Thus, it is worth devising strategies for Bayesian estimation which give good performance and can be realised easily. In this work, I provide such strategies for a range of estimation problems in quantum optical setups.

5.1.3 Gaussian quantum optics

The scenario of interest is that the probe states are composed of the electromagnetic field. The goal of this work is to reveal the performance of Gaussian states in the frame of Bayesian estimation strategies. To set these states for this investigation, I briefly review some relevant concepts of Gaussian quantum optics below and loosely follow Ref. [22].

Multi-mode optical fields can be described as collection of bosonic modes. CV systems consist of N bosonic modes, i.e. N harmonic oscillators. I label each mode as k and represent a pair of annihilation and creation operators as $\{\hat{a}_k, \hat{a}_k^\dagger\}$. These mode operators satisfy the bosonic commutation relation $[\hat{b}_i, \hat{b}_j^\dagger] = \Omega_{ij}$, where

$$\hat{\mathbf{b}} = (\hat{a}_1, \hat{a}_1^\dagger, \ldots, \hat{a}_N, \hat{a}_N^\dagger)^{\mathrm{T}} \quad \text{and} \quad \boldsymbol{\Omega} = \bigoplus_{k=1}^{N} \begin{pmatrix} 0 & 1 \\ -1 & 0 \end{pmatrix} , \tag{5.13}$$

which is the symplectic form [298]. The mode operators can be translated into the quadrature operators, $\hat{q}_k = (\hat{a}_k^\dagger + \hat{a}_k)/\sqrt{2}$ and $\hat{p}_k = i(\hat{a}_k^\dagger - \hat{a}_k)/\sqrt{2}$. These operators correspond to generalised position and momentum observables for the mode k, and have continuous spectra and eigenstates, $\{|q\rangle\}_{q\in\mathbb{R}}$ and $\{|p\rangle\}_{p\in\mathbb{R}}$, respectively. In the phase space picture, let me write the quadrature operators as one single vector $\hat{\mathbf{x}} = (\hat{q}_1, \hat{p}_1, \ldots, \hat{q}_N, \hat{p}_N)^T$.

On one hand, any state of such a N-mode system is represented by a density operator $\rho \in \mathcal{D}(\mathcal{H}^{\otimes N})$. On the other hand, any state can also be described by its Wigner function $W(\mathbf{x})$ [299]. The characteristic function is defined by $\chi(\mathbf{x}) = \mathrm{Tr}[\rho D(\mathbf{x})]$, where $D(\mathbf{x}) = \exp\big(i\sqrt{2}\,\hat{\mathbf{x}}^{\mathrm{T}}\,\boldsymbol{\Omega}\,\mathbf{x}\big)$ is the Weyl displacement operator. By Fourier transforming the characteristic function $\chi(\mathbf{x})$, the Wigner function $W(\mathbf{x})$ is obtained, cf. Sec. 1.2.1.

Gaussian states: A state is called a Gaussian state if its Wigner function is given by a multivariate Gaussian distribution,

$$W(\mathbf{x}) = \frac{\exp\left(-(\mathbf{x}-\bar{\mathbf{x}})^{\mathrm{T}}\boldsymbol{\Gamma}^{-1}(\mathbf{x}-\bar{\mathbf{x}})\right)}{\pi^N\sqrt{\det[\boldsymbol{\Gamma}]}} . \tag{5.14}$$

Gaussian states can be determined by their first moment $\bar{\mathbf{x}} = \langle\mathbf{x}\rangle$ and the covariance matrix $\sigma = (\sigma_{i,j}) = \boldsymbol{\Gamma}/2$. The real and symmetric $2N \times 2N$ covariance matrix collects the second moments $\sigma_{ij} = \langle\{\hat{\mathbf{x}}_i - \langle\hat{\mathbf{x}}_i\rangle, \hat{\mathbf{x}}_j - \langle\hat{\mathbf{x}}_j\rangle\}\rangle/2$. This Gaussian state description with only the first moment and the covariance matrix allows one to compactly treat the states expanding in an infinite-dimensional Hilbert space with a finite number of degrees of freedom.

As reviewed in Sec. 1.2.2, single-mode Gaussian states include coherent states and squeezed states as well as the vacuum state. Coherent states are eigenstates of the annihilation operator $\hat{a}_k$ such that $\hat{a}_k \left|\alpha\right\rangle_k = \alpha \left|\alpha\right\rangle_k$. These states can be described by applying the displacement operator of the coherent amplitude $\alpha \in \mathbb{C}$,

$$\hat{D}_k(\alpha) = \exp\Big[\alpha\hat{a}_k^\dagger - \alpha^*\hat{a}_k\Big], \tag{5.15}$$

to the vacuum state $\left|0\right\rangle_k$ such that $\left|\alpha\right\rangle_k = \hat{D}_k(\alpha)\left|0\right\rangle_k$. For a single-mode coherent state $\left|\alpha\right\rangle_k$, the first moment is $\bar{\mathbf{x}} = \sqrt{2}(\mathrm{Re}[\alpha], \mathrm{Im}[\alpha])^T$. Also, the second moment corresponds to the identity matrix divided by 2, which means that the variance in $\hat{q}_k$ and $\hat{p}_k$ is 1/2 and saturates the uncertainty relation in a balanced way. Note that all coherent states have the same covariance matrices as the vacuum state (see Fig. 5.2).

There is another type of states saturating the uncertainty relation but in an imbalanced way, which is squeezed states. One-mode squeezing literally squeezes a state in the phase space and changes the covariance matrix but leaves its determinant the same (see Fig. 5.2). Squeezed states are generated by applying the following squeezing operator with squeezing parameter $\xi = r\,\mathrm{e}^{i\varphi}$,

$$\hat{S}_k(\xi) = \exp\left[\frac{\xi^*\hat{a}_k^2 - \xi\hat{a}_k^{\dagger 2}}{2}\right] \tag{5.16}$$

to the vacuum state $\left|0\right\rangle_k$ or displaced states. For the parameter $\xi = r\,\mathrm{e}^{i\varphi}$, $r \in \mathbb{R}$ is the squeezing strength and $\varphi \in [0, 2\pi]$ is the squeezing angle.

Every pure Gaussian state can be generated by these two operators from the vacuum state [22]. Such states are characterised by the displacement parameter $\alpha \in \mathbb{C}$, the squeezing amplitude $r \in \mathbb{R}$, and the squeezing angle $\varphi \in [0, 2\pi]$. If one restricts the squeezing amplitude to real values, it is necessary to apply a phase rotation

$$\hat{R}_k(\theta) = \exp\Big[-i\theta\hat{a}_k^\dagger\hat{a}_k\Big] \tag{5.17}$$

in order to describe the general pure single-mode Gaussian state such that

$$\left|\alpha, r\mathrm{e}^{i\varphi}\right\rangle = \hat{D}(\alpha)\hat{S}(r\mathrm{e}^{i\varphi})\left|0\right\rangle = \hat{D}(\alpha)\hat{R}(\varphi/2)\hat{S}(r)\left|0\right\rangle. \tag{5.18}$$

Note that the order of the operators is restricted, otherwise the first moment may depend on the squeezing strength and angle. The first moment is $\bar{\mathbf{x}} = \sqrt{2}(\mathrm{Re}(\alpha), \mathrm{Im}(\alpha))^T$, and the covariance matrix is

$$\sigma = \frac{1}{2}\begin{pmatrix} \cosh(2r) - \sinh(2r)\cos\varphi & \sinh(2r)\sin\varphi \\ \sinh(2r)\sin\varphi & \cosh(2r) + \sinh(2r)\cos\varphi \end{pmatrix}. \tag{5.19}$$

A unitary transformation is called a Gaussian transformation, if it maps all Gaussian states into Gaussian states. This class of unitary operations is created by Hamiltonians composed of (at most) second order polynomials of the mode operators. It is worth noting that every single-mode Gaussian unitary operation can be decomposed into displacement, rotation, squeezing operators, as shown in Eq. (5.18). Gaussian states and transformations are easy to treat theoretically and implement experimentally [286, 287].

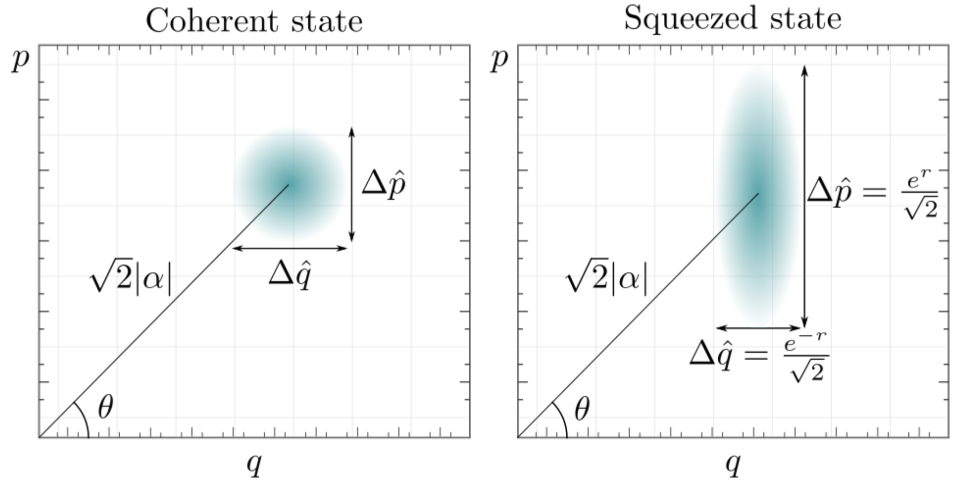

Figure 5.2: Plots of the Wigner functions for a coherent state and a squeezed state. The Wigner functions are given by the Gaussian distribution given in Eq. (5.14) and characterised with a displacement parameter α, a squeezing strength r, and a squeezing angle $\varphi = 2\theta$.

Gaussian measurements: Any measurement can be represented by a POVM, i.e. a set of positive operators $\{E_m\}$ which sum to the identity. For measurement schemes of CV systems, it is common to use continuous POVMs, which give a continuous set of operators and of measurement outcomes. A measurement is called Gaussian if it gives a Gaussian distribution of the outcomes when it is applied to a Gaussian state. The most commonly used Gaussian POVMs are heterodyne and homodyne detections. For the heterodyne detection, the POVM is composed of coherent states $\frac{1}{\pi}\{|\beta\rangle\langle\beta|\}_{\beta\in\mathbb{C}}$. The homodyne detection measures one mode of the quadrature, for example $\hat{q}$, and is composed of projectors of the quadrature $\{|q\rangle\langle q|\}_{q\in\mathbb{R}}$.

5.2 Displacement estimation

Here, I explore Bayesian estimation strategies for the displacement by using Gaussian probe states and Gaussian measurements, i.e. I suppose that a displacement operator $\hat{D}(\alpha)$ acts on a CV system where the initial state is a Gaussian state and that one wants to estimate the unknown displacement $\alpha = \alpha_{\mathrm{R}} + i\alpha_{\mathrm{I}}$ with $\alpha_{\mathrm{R}}, \alpha_{\mathrm{I}} \in \mathbb{R}$. As measurement schemes, I use heterodyne or homodyne detection and compare their results. These measurements are covariant under the action of displacement since the probability distribution of applying $\hat{D}(\alpha)$ to the probe state provides the same distribution translated by the displacement parameter α [300]. Thus, I set a squeezed vacuum state $|\xi\rangle = \hat{S}(\xi)|0\rangle$ as the initial probe state instead of using the general single-mode Gaussian state $\hat{D}(\alpha)\hat{S}(\xi)|0\rangle$. Furtheremore, I assume that the prior information of the displacement is encoded in a Gaussian distribution with the width σ_0 and the centre α_0 forming a prior distribution written as

$$p(\alpha) = \frac{1}{2\pi\sigma_0^2}\exp\left[-\frac{|\alpha-\alpha_0|^2}{2\sigma_0^2}\right] . \tag{5.20}$$

In the following, I investigate the performance of the estimation strategies based on heterodyne and homodyne detections, and consider cases of finite resource for probe states.

5.2.1 Heterodyne measurement

I first focus on estimation strategies based on heterodyne detection, where the measurement is described by the POVM $\frac{1}{\pi}\{|\beta\rangle\langle\beta|\}_{\beta\in\mathbb{C}}$. The set of coherent states $|\beta\rangle$ forms an overcomplete basis[1] with the completeness relation $\frac{1}{\pi}\int d\beta\ |\beta\rangle\langle\beta| = \mathbb{1}$. The liklihood to obtain the measurement outcome β given a displacement of α is represented by the fidelity between the coherent state $|\beta\rangle\langle\beta|$ and the probe state after applying the displacement operator, and is given by

$$\begin{aligned} p(\beta|\alpha) &= \frac{1}{\pi}\operatorname{Tr}\left[|\beta\rangle\langle\beta|\,\hat{D}(\alpha)\,|\xi\rangle\langle\xi|\,\hat{D}^{\dagger}(\alpha)\right] \\ &= \frac{1}{\pi}\operatorname{Tr}\left[|\beta-\alpha\rangle\langle\beta-\alpha|\,|\xi\rangle\langle\xi|\right] \\ &= \frac{1}{\pi}\mathcal{F}\left(|\beta-\alpha\rangle\langle\beta-\alpha|\,,|\xi\rangle\langle\xi|\right) \\ &= \frac{1}{\pi}\left|\langle\beta-\alpha|\xi\rangle\right|^{2}. \end{aligned} \tag{5.21}$$

Here, $\mathcal{F}(\rho_1,\rho_2) = \left(\operatorname{Tr}\left[\sqrt{\sqrt{\rho_1}\rho_2\sqrt{\rho_2}}\right]\right)^2$ is the Uhlmann's fidelity of the states ρ_1 and ρ_2, which corresponds to $\mathcal{F}(|\psi\rangle\,,|\phi\rangle) = |\,\langle\psi|\phi\rangle\,|^2$ for pure states. For the overlap between two Gaussian states, the form can be simplified and written in terms of the respective first moments $\bar{\mathbf{x}}_{1,2}$ and the second moments $2\sigma_{1,2} = \mathbf{\Gamma}_{1,2}$ (cf. Ref. [264]) as

$$\mathcal{F}(\rho_1,\rho_2) = \frac{2\exp\left[-(\bar{\mathbf{x}}_1-\bar{\mathbf{x}}_2)^T(\mathbf{\Gamma}_1+\mathbf{\Gamma}_2)^{-1}(\bar{\mathbf{x}}_1-\bar{\mathbf{x}}_2)\right]}{\sqrt{|\mathbf{\Gamma}_1+\mathbf{\Gamma}_2|+(1-|\mathbf{\Gamma}_1|)(1-|\mathbf{\Gamma}_2|)}-\sqrt{(1-|\mathbf{\Gamma}_1|)(1-|\mathbf{\Gamma}_2|)}}\,. \tag{5.22}$$

For simplicity, the probe state is squeezed only along one fixed direction, $\varphi = 0$. This simplifies the following calculation significantly. Specifically, this lets me write the likelihood $p(\beta|\alpha)$ and the posterior distribution as products of the respective distributions for the real α_{R} and the imaginary part α_{R} of the displacement. On the other hand, for an arbitrary squeezing angle φ, the resulting formulas are unwieldy and complicated, although quantitatively the formulas give the same behaviour as for $\varphi = 0$. Therefore, I stick to the case of $\varphi = 0$.

To use Eq. (5.22), I write $\rho_1 = |\beta-\alpha\rangle\langle\beta-\alpha|$ and $\rho_2 = |\xi\rangle\langle\xi|$, for which the first moments are

$$\bar{\mathbf{x}}_{\beta-\alpha} = \sqrt{2}\begin{pmatrix}\mathrm{Re}[\beta-\alpha]\\ \mathrm{Im}[\beta-\alpha]\end{pmatrix} = \sqrt{2}\begin{pmatrix}\beta_{\mathrm{R}}-\alpha_{\mathrm{R}}\\ \beta_{\mathrm{I}}-\alpha_{\mathrm{I}}\end{pmatrix} \quad \text{and} \quad \bar{\mathbf{x}}_{\xi} = \begin{pmatrix}0\\0\end{pmatrix} \tag{5.23}$$

---

[1] "An overcomplete basis" in this context means that even if a coherent state such as $\{|\beta\rangle\langle\beta|\}_{\beta=1}$ is taken off from the POVM $\frac{1}{\pi}\{|\beta\rangle\langle\beta|\}_{\beta\in\mathbb{C}}$, the POVM still maintains the completeness relation $\frac{1}{\pi}\int d\beta\ |\beta\rangle\langle\beta| = \mathbb{1}$. It may help one understand this, thinking that the vacancy of the coherent state $\{|\beta\rangle\langle\beta|\}_{\beta=1}$ is filled up by neighbouring coherent states such as $\{|\beta\rangle\langle\beta|\}_{\beta=1.0000\ldots}$ and $\{|\beta\rangle\langle\beta|\}_{\beta=0.9999\ldots}$.

and the second moments are

$$\boldsymbol{\Gamma}_{\beta-\alpha} = \begin{pmatrix} 1 & 0 \\ 0 & 1 \end{pmatrix} \quad \text{and} \quad \boldsymbol{\Gamma}_{\xi} = \begin{pmatrix} \mathrm{e}^{-2r} & 0 \\ 0 & \mathrm{e}^{2r} \end{pmatrix} . \tag{5.24}$$

As a result, the likelihood $p(\beta|\alpha)$ is written as

$$\begin{aligned} p(\beta|\alpha) &= \frac{1}{\pi \cosh r} \exp\left[-\frac{\mathrm{e}^{+r}(\beta_{\mathrm{R}} - \alpha_{\mathrm{R}})^2 + \mathrm{e}^{-r}(\beta_{\mathrm{I}} - \alpha_{\mathrm{I}})^2}{\cosh r} \right] \\ &= p(\beta_{\mathrm{R}}|\alpha_{\mathrm{R}})\, p(\beta_{\mathrm{I}}|\alpha_{\mathrm{I}}), \end{aligned} \tag{5.25}$$

where the distributions $p(\beta_i|\alpha_i)$ for $i = \mathrm{R}, \mathrm{I}$ are given by

$$p(\beta_i|\alpha_i) = \frac{\sqrt{2} \exp\left[-\frac{2(\beta_i - \alpha_i)^2}{1+\mathrm{e}^{\mp 2r}} \right]}{\sqrt{\pi (1 + \mathrm{e}^{\mp 2r})}} . \tag{5.26}$$

The upper and lower signs in $\mp$ correspond to the subscripts $i = \mathrm{R}$ and $i = \mathrm{I}$, respectively.

By using the likelihood and the prior, Bayes' law (5.2) informs one about the posterior distribution and the estimator. This allows one to evaluate the average variance of the posterior. However, these calculations can be simpler in the case where the prior and likelihood both are Gaussian. The proposition mentioned in Sec. 5.1.1 tells one that the posterior is also Gaussian, and its mean and variance can be represented by those of the likelihood and the prior. Notice in the representation used in the proposition, $\sigma = (1 + \mathrm{e}^{\pm 2r})/4$, $\mu_0 = \alpha_{0,i}$, and $\bar{\theta}(m) = \beta_i$, where the subscripts $i = \mathrm{R}, \mathrm{I}$ correspond to $+, -$, respectively. Therefore, the means are

$$\hat{\alpha}_i(\beta_i) = \frac{4\beta_i \sigma_0^2 + \alpha_{0,i}(1 + \mathrm{e}^{\mp 2r})}{4\sigma_0^2 + 1 + \mathrm{e}^{\mp 2r}}, \tag{5.27}$$

which are the estimators for the real and imaginary parts of the parameter α, and the variances are

$$\mathrm{Var}[p(\alpha_i|\beta_i)] = \left[\frac{1}{\sigma_0^2} + 2(1 \pm \tanh r) \right]^{-1} . \tag{5.28}$$

Here, I define the total variance of the posterior $p(\alpha|\beta)$ for the complex parameter α as

$$\mathrm{Var}[p(\alpha|\beta)] = \int d\alpha\, p(\alpha|\beta)\, |\alpha - \hat{\alpha}(\beta)|^2. \tag{5.29}$$

Since the real and imaginary parts of the posterior are independent, this total variance can be described by the sum of the variances of the two independent estimation parameters as

$$\begin{aligned}\mathrm{Var}[p(\alpha|\beta)] &= \mathrm{Var}[p(\alpha_{\mathrm{R}}|\beta_{\mathrm{R}})] + \mathrm{Var}[p(\alpha_{\mathrm{I}}|\beta_{\mathrm{I}})] \\ &= \left[\frac{1}{\sigma_0^2} + 2(1+\tanh r)\right]^{-1} + \left[\frac{1}{\sigma_0^2} + 2(1-\tanh r)\right]^{-1} . \end{aligned} \tag{5.30}$$

I note that the average total variance corresponds to the total variance given in Eq. (5.30), because Eq. (5.30) is independent of β.

The average total variance of the posterior depends only on the variance σ_0 of the prior and the squeezing strength r. For a fixed prior (with σ_0 fixed), the total average variance $\bar{V}_{\mathrm{post}}$ is minimised for $r = 0$ (no squeezing), as

$$\bar{V}_{\mathrm{post}}(r) \geq \bar{V}_{\mathrm{post}}(r=0) = \frac{2\sigma_0^2}{1+2\sigma_0^2} . \tag{5.31}$$

Regardless of the squeezing, the variances in both coordinates decrease with respect to the prior, but slowly, i.e. not exponentially. If one is interested in only one coordinate for the estimation, e.g. α_{R}, the squeezing is useful and reduces the variance monotonically for increasing r. For $r \to \infty$, the variance for estimation of α_{R} given in Eq. (5.30) reaches $(\sigma_0^{-2} + 4)^{-1}$, which originates from the intrinsic uncertainty of the coherent state basis associated with the POVM representing the heterodyne detection. In other words, regardless of the measurement outcome, the precision in the estimation is limited by the variance of the coherent state used for the measurement.

This result signals the advantage of homodyne detection as shown below. Coherent states minimise the product of uncertainties. However, if one has a desired coordinate, e.g. α_{R}, it is better to use a squeezed state basis which has a smaller variance in the desired coordinate. The homodyne detection, which will be discussed in the next section, can be thought of as a special case of a measurement in a basis of infinitely squeezed coherent states.

5.2.2 Homodyne measurement

I switch to estimation strategies using homodyne detection, which is described by the POVM $\{|q\rangle\langle q|\}_{q\in\mathbb{R}}$. As before, I use a squeezed state as the probe state to estimate the displacement α, and use the Gaussian distribution (5.20) as the prior. The likelihood to obtain the outcome q given the displacement α is provided by

$$\begin{aligned}p(q|\alpha) &= \mathrm{Tr}\left[|q\rangle\langle q|\,\hat{D}(\alpha)\,|\xi\rangle\langle\xi|\,\hat{D}^{\dagger}(\alpha)\right] \\ &= \left|\,\langle q|\hat{D}(\alpha)|\xi\rangle\right|^2 \\ &= \int_{-\infty}^{\infty} dp\; W(q,p), \end{aligned} \tag{5.32}$$

where $W(q,p)$ is the Wigner function of the Gaussian state $\hat{D}(\alpha)\,|\xi\rangle$. Here, I use the fact that the Wigner function of any Gaussian state is given by

$$\begin{aligned} W(x,p) &= W(\bar{\mathbf{x}}_\rho, \Gamma_\rho) \\ &= \frac{\exp\left[-\left(\begin{pmatrix} q \\ p \end{pmatrix} - \bar{\mathbf{x}}_\rho\right)^T \Gamma_\rho^{-1} \left(\begin{pmatrix} q \\ p \end{pmatrix} - \bar{\mathbf{x}}_\rho\right)\right]}{\pi\sqrt{|\Gamma_\rho|}} . \end{aligned} \tag{5.33}$$

Therefore, the likelihood $p(q|\alpha)$ can be written as

$$p(q|\alpha) = \frac{\exp\left[-\frac{2(\alpha_\mathrm{R}-\frac{q}{\sqrt{2}})^2}{\cosh 2r - \cos\varphi\ \sinh 2r}\right]}{\sqrt{\pi(\cosh 2r - \cos\varphi\ \sinh 2r)}} . \tag{5.34}$$

Notice that the likelihood $p(q|\alpha)$ does not depend on the imaginary part α_I of the displacement. That is because homodyne detection in one quadrature is completely blind to the orthogonal quadrature. Thus, the knowledge of the imaginary part α_I is not updated from the prior, and I focus on the real part α_R. Since the likelihood is a Gaussian distribution and can be written as a Gaussian distribution with the mean $\langle\alpha_\mathrm{R}\rangle = q/\sqrt{2}$ and the variance $\sigma^2 = (\cosh 2r - \cos\varphi \sinh 2r)/4$, the proposition mentioned in Sec. 5.1.1 ensures that the posterior is a Gaussian distribution with the mean

$$\hat{\alpha}_\mathrm{R} = \frac{2\sqrt{2}\,\sigma_0^2 q + \alpha_{0,\mathrm{R}}(\cosh 2r - \cos\varphi\ \sinh 2r)}{4\sigma_0^2 + \cosh 2r - \cos\varphi\ \sinh 2r}, \tag{5.35}$$

and the variance

$$\mathrm{Var}[p(\alpha_\mathrm{R}|q)] = \frac{\sigma_0^2(\cosh 2r - \cos\varphi\ \sinh 2r)}{4\sigma_0^2 + \cosh 2r - \cos\varphi\ \sinh 2r}. \tag{5.36}$$

The variance depends on the squeezing strength r and angle φ, and is minimised for $\varphi = 2n\pi$. Without loss of generality, I take $\varphi = 0$. In this case, the average variance of the posterior for the chosen coordinate q is given by

$$\bar{V}_\mathrm{post}^{\hat{q}} = \mathrm{Var}[p(\alpha_\mathrm{R}|q)] \overset{\varphi=0}{=} \left(\frac{1}{\sigma_0^2} + 4\mathrm{e}^{2r}\right)^{-1}, \tag{5.37}$$

whereas the average total variance is

$$\begin{aligned} \bar{V}_\mathrm{post} &= \bar{V}_\mathrm{post}^{\hat{q}} + \sigma_0^2 \\ &= \left(\frac{1}{\sigma_0^2} + 4\mathrm{e}^{2r}\right)^{-1} + \sigma_0^2. \end{aligned} \tag{5.38}$$

Figure 5.3 displays the posterior distributions for different squeezed probe states. While the marginal probability in the coordinate p remains unchanged, the marginal probability in the coordinate q becomes narrow.

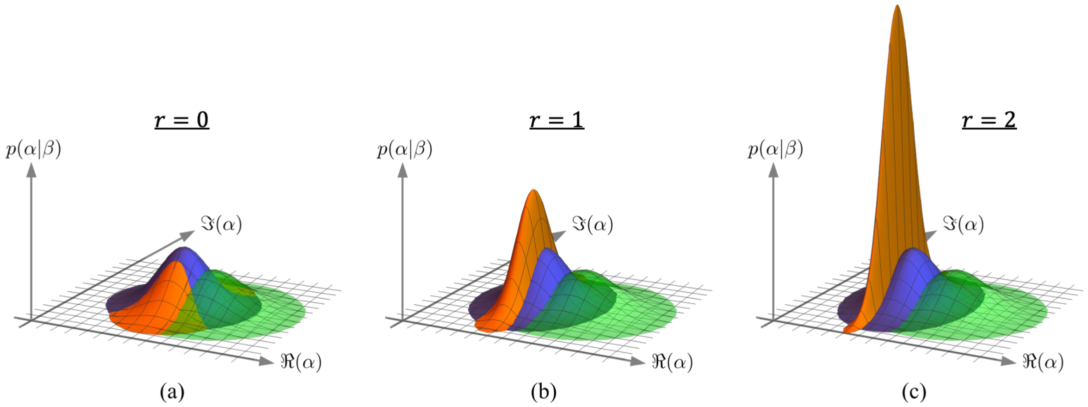

Figure 5.3: Displacement estimation using heterodyne and homodyne detection. The images show the same Gaussian prior (green) with initial standard deviation $\sigma_0 = 0.5$, and posterior distributions obtained for heterodyne (blue) and homodyne detection (orange) for different squeezing strengths of the probe state.

5.2.3 Comparison of measurement strategies

Let me now compare the results for the displacement estimation with heterodyne and homodyne measurements. For homodyne detection, squeezing decreases the average total variance in one quadrature exponentially as shown in Eq. (5.37), while squeezing does not affect the variance in the orthogonal quadrature. In the limit of $r \to \infty$, $\lim_{r\to\infty} \bar{V}_{\text{post}}^{\text{homodyne}} = \sigma_0^2$. Comparing this with the result (5.31) for heterodyne detection, for priors with variance $\sigma_0^2 \geq 1/2$, one observes $\bar{V}_{\text{post}}^{\text{homodyne}}(r) \geq \bar{V}_{\text{post}}^{\text{heterodyne}}(r=0)$. This shows that the homodyne detection scenario loses against the heterodyne detection scenario in this case regardless of how much the probe is squeezed for homodye detection. However, for more narrow priors, such as $\sigma_0^2 < 1/2$, where more knowledge is obtained, homodyne detection can outperform heterodyne detection if the squeezing is strong such as $r > -\frac{1}{2}\ln(1-2\sigma_0^2)$.

If one knows the direction of the displacement and focuses on the estimation of the amplitude, e.g. focuses on one quadrature q, then homodyne detection outperforms heterodyne detection for all prior widths and for all squeezing strength. The variance (5.28) of the heterodyne detection in the limit of $r \to \infty$ corresponds to the variance (5.37) of homodyne detection for $r = 0$, thus the one obtains,

$$\bar{V}_{\text{post}}^{\hat{q},\,\text{homodyne}} \leq \frac{\sigma_0^2}{1+4\sigma_0^2} \leq \bar{V}_{\text{post}}^{\hat{q},\,\text{heterodyne}}. \tag{5.39}$$

I compare these results with the optimal limit obtained from the Bayesian quantum CRB (5.12). For a Gaussian prior in a single parameter, the FI of the prior is $I[p(\alpha_{\text{R}})] = 1/\sigma_0^2$ according to Eq. (5.8). The QFI for a single-mode Gaussian state is bounded by $\mathcal{I}(\rho) \leq 4\mathrm{e}^{2r}$ (cf. Eq. (15) and subsequent text in Ref. [264]). Therefore, the Bayesian quantum CRB reads

$$\bar{V}_{\text{post}}^{\hat{q}} \geq \left(\frac{1}{\sigma_0^2} + 4\mathrm{e}^{2r}\right)^{-1}. \tag{5.40}$$

Comparison between this and Eq. (5.37) tells one that the homodyne detection with a squeezed probe state is the optimal strategy to estimate one coordinate of displacement or amplitude with known direction for a single-mode Gaussian state.

Finally, I consider repeating measurements and updating procedures, which can be implemented within the framework of conjugate priors. As shown, the posterior takes the same form as the prior. Since the posterior is used as the prior for the next measurement round, the recursive formula for the average variance is given by

$$\sigma_{m+1}^2 = \frac{\sigma_m^2 \operatorname{Var}[p(q|\alpha)]}{\sigma_m^2 + \operatorname{Var}[p(q|\alpha)]}, \tag{5.41}$$

where σ_m is the variance for round m. By noting that $\operatorname{Var}[p(q|\alpha)] = \mathrm{e}^{2r}/4$ depends on the squeezing but not the measurement round, the recursive equation can be solved, and the variance for round m is given by

$$\sigma_m^2 = \left(\frac{1}{\sigma_0^2} + 4m\, \mathrm{e}^{2r} \right)^{-1}. \tag{5.42}$$

For example, by repeating measurements, one can use a sequential measurement strategy providing both the real and imaginary parts of the displacement. For instance, one tunes the squeezing in the probe state and the direction of the homodyne detection to estimate the real part at the beginning, and then switch to estimation of the imaginary part.

5.3 Phase estimation

In this section, I discuss phase estimation employing Gaussian states and measurements in the framework of Bayesian estimation. Historically, phase estimation has been associated with interferometry [301], but nowadays, it is used broadly. Particularly, Bayesian phase estimation has been studied for various applications [302, 303] such as quantum error correction [304]. While there are some studies that identify the optimal settings in Gaussian environments [277, 305, 306], their focus is on the local estimation scenario, and thus they do not work in the framework of Bayesian phase estimation.

Here, I focus on situations where there is no prior information on the estimated parameter and hence local estimation cannot be employed in a meaningful way. The aim of this Bayesian phase estimation strategy is to identify the parameter precisely until local estimation can take over the rest of the estimation. One can use a circular Gaussian distributions (cf. Ref.[293]) for a more flexible prior and generalise the discussion below although these distributions entail mathematical complexity.

I consider scenarios where a phase rotation operator (5.17) is applied to a Gaussian state. The phase θ is completely unknown, and its range is $[-\pi, \pi)$. Thus, the prior is written as

$$p(\theta) = \frac{1}{2\pi} \tag{5.43}$$

so that it is normalised as $\int_{-\pi}^{\pi} d\theta \, p(\theta) = 1$. Below, I study the performance of heterodyne and homodyne measurements in this scenario. It is worth nothing that although the optical probe state (at fixed average energy) for local phase estimation is a single-mode squeezed state, this is not the case for Bayesian phase estimation, as will be seen below.

5.3.1 Heterodyne measurement

I consider probe states which are squeezed with strength $r = |\xi|$ before being displaced, described as $\hat{D}(\alpha)\hat{S}(re^{i\varphi})\,|0\rangle$ with $r \geq 0$ and $0 \leq \varphi < 2\pi$. While any Gaussian state can be described in this form with arbitrary complex numbers α and $\xi = re^{i\varphi}$, some freedom of the probe state can be removed without loss of generality. Since displacement and squeezing can be given with arbitrary strengths along arbitrary directions, the rotational symmetry of the phase estimation problem permits one to fix one of these directions. Therefore, I take positive values for α and also do not consider $\alpha = 0$. That is because for cases of $\alpha = 0$, the probe is a squeezed vacuum state and does not distinguish between rotations around θ and $\theta + \pi$ due to rotational invariance.

While the squeezing direction can be taken freely, I choose the optimal one, which is $\varphi = \pi$ (thus, $\xi = -r$) and where the probe state is squeezed along the quadrature p (its Wigner function spreads along the $\hat{q}$-quadrature; see Fig. 5.2). It can be intuitively understood that this is the optimal direction as the initial probe state is like a clock hand hitting three due to $\alpha > 0$. The more squeezed the initial probe state is, the clearer it is that the probe shows $\theta = 0$, and hence this also makes it clearer which direction the encoded probe turns. In the remainder of this section, I consider the probe state $\hat{D}(\alpha)\hat{S}(-r)\,|0\rangle$.

Since calculations for arbitrary values of r are complicated and unwieldy, I start with displaced probe states (coherent states) $\hat{D}(\alpha)\,|0\rangle$ and switch to squeezed displaced probe states $\hat{D}(\alpha)\hat{S}(-r)\,|0\rangle$ later.

Coherent probe state & heterodyne detection: The initial probe state is given by $\hat{D}(\alpha)\,|0\rangle$ with $\alpha > 0$. The phase rotation is represented by Eq. (5.17), and thus the encoded probe state is described as $\hat{R}(\theta)\,|\alpha\rangle = |\mathrm{e}^{-i\theta}\alpha\rangle$. Therefore, the likelihood to obtain an outcome $\beta \in \mathbb{C}$, given the phase θ, reads

$$\begin{aligned} p(\beta|\theta) &= \tfrac{1}{\pi}|\,\langle\,\beta\,|\,\mathrm{e}^{-i\theta}\alpha\,\rangle\,|^2 \\ &= \tfrac{1}{\pi}|\,\langle\,\mathrm{e}^{i\theta}\beta\,|\,\alpha\,\rangle\,|^2 \\ &= \tfrac{1}{\pi}\mathrm{e}^{-|\mathrm{e}^{i\theta}\beta-\alpha|^2}, \end{aligned} \tag{5.44}$$

where $|\mathrm{e}^{i\theta}\beta - \alpha|^2 = \alpha^2 + |\beta|^2 - 2\alpha|\beta|\cos(\theta - \phi_\beta)$ with $\beta = |\beta|\mathrm{e}^{-i\phi_\beta}$. I express the unconditional probability to obtain β as

$$\begin{aligned} p(\beta) &= \int_{-\pi}^{\pi} d\theta \, p(\theta)\, p(\beta|\theta) \\ &= \frac{\mathrm{e}^{-(\alpha^2+|\beta|^2)}}{\pi}\, I_0(2\alpha|\beta|), \end{aligned} \tag{5.45}$$

where $I_0(x)$ is the modified Bessel function of the first kind. Using Bayes' law (5.2), the posterior is given by

$$\begin{aligned} p(\theta|\beta) &= \frac{p(\theta)\,p(\beta|\theta)}{p(\beta)} \\ &= \frac{\mathrm{e}^{2\alpha|\beta|\cos\left(\theta-\phi_\beta\right)}}{2\pi\, I_0(2\alpha|\beta|)}\ . \end{aligned} \tag{5.46}$$

The phase range is considered as $[-\pi, \pi)$, and the points $\pm\pi$ are identical. Therefore, I take estimators and variances which are invariant under shifts by 2π. For the estimator, I choose $\hat{\theta}(\beta) = \arg\langle \mathrm{e}^{i\theta}\rangle_{p(\theta|\beta)}$, where

$$\begin{aligned} \langle \mathrm{e}^{i\theta}\rangle_{p(\theta|\beta)} &= \int_{-\pi}^{\pi} d\theta\, p(\theta|\beta)\mathrm{e}^{i\theta} \\ &= \int_{-\pi}^{\pi} d\theta\, \frac{\mathrm{e}^{2\alpha|\beta|\cos\left(\theta-\phi_\beta\right)}}{2\pi\, I_0(2\alpha|\beta|)}\mathrm{e}^{i\theta} \\ &= \mathrm{e}^{i\phi_\beta}\int_{-\pi}^{\pi} d\theta\, \frac{\mathrm{e}^{2\alpha|\beta|\cos\left(\theta-\phi_\beta\right)}}{2\pi\, I_0(2\alpha|\beta|)}\mathrm{e}^{i(\theta-\phi_\beta)}. \end{aligned} \tag{5.47}$$

Since

$$\int_{-\pi}^{\pi} d\theta\, \mathrm{e}^{2\alpha|\beta|\cos\left(\theta-\phi_\beta\right)} \sin(\theta-\phi_\beta) = 0, \tag{5.48}$$

I have

$$\langle \mathrm{e}^{i\theta}\rangle_{p(\theta|\beta)} = \mathrm{e}^{i\phi_\beta}\,\mathrm{Re}\left[\int_{-\pi}^{\pi} d\theta\, \frac{\mathrm{e}^{2\alpha|\beta|\cos\left(\theta-\phi_\beta\right)}}{2\pi\, I_0(2\alpha|\beta|)}\mathrm{e}^{i(\theta-\phi_\beta)}\right]. \tag{5.49}$$

This leads to the estimator

$$\begin{aligned} \hat{\theta}(\beta) &= \arg\left[\int_{-\pi}^{\pi} d\theta\, p(\theta|\beta)\mathrm{e}^{i\theta}\right] \\ &= \phi_\beta, \end{aligned} \tag{5.50}$$

which corresponds to the phase ϕ_β of the measurement outcome β.

To evaluate the performance of this estimation strategy, I calculate the average variance of the posterior as done in the above sections. Considering invariance under shifts by 2π, I choose the average of $\sin^2[\theta - \hat{\theta}(\beta)]$ instead of the average of $(\theta - \hat{\theta}(\beta))^2$. Specifically, the variance is given by

$$\begin{aligned} V_{\text{post}}(\beta) &= \int_{-\pi}^{\pi} d\theta\, p(\theta|\beta)\, \sin^2\left[\theta - \hat{\theta}(\beta)\right] \\ &= \frac{{}_0F_1(2;\alpha^2|\beta|^2)}{2\, I_0(2\alpha|\beta|)\,\Gamma(2)}, \end{aligned} \tag{5.51}$$

where ${}_0F_1(a;z)$ is the confluent hypergeometric function and $\Gamma(z)$ is the Gamma function. Notice that the chosen variance form is also invariant under shifts of the estimator by integer multiples of π, not just shift by even multiples of π. In principle, to quantify the width of the distribution, one can also use the Holevo variance [307], which are independent of shifts of the estimator. The reason I choose the average of $\sin^2[\theta-\hat{\theta}(\beta)]$ is to have better comparision with the homodyne detection scenario discussed in Sec. 5.3.2, where the phase range is $[0,\pi]$ and the interval is π.

As a result, the average variance is

$$\begin{aligned}\bar{V}_{\text{post}} &= \int d^2\beta \; p(\beta)\, V_{\text{post}}(\beta)\\ &= \frac{\mathrm{e}^{-\alpha^2}}{2\pi\,\Gamma(2)}\int_0^\infty d|\beta| \int_{-\pi}^{\pi} d\phi_\beta \; |\beta|\,\mathrm{e}^{-|\beta|^2}\;{}_0F_1(2;\alpha^2|\beta|^2)\\ &= \frac{\mathrm{e}^{-\alpha^2}}{\Gamma(2)}\int_0^\infty d|\beta|\,|\beta|\,\mathrm{e}^{-|\beta|^2}\;{}_0F_1(2;\alpha^2|\beta|^2)\\ &= \frac{1-\mathrm{e}^{-|\alpha|^2}}{2\,|\alpha|^2}.\end{aligned}\tag{5.52}$$

By rewriting this result in terms of the average photon number $n=|\alpha|^2$, it is observed that for $n\to\infty$ the average variance scales as $1/n$, which is the same scale of the quantum standard limit.

Displaced squeezed states & heterodyne detection: Here, I consider squeezing the probe state before displacing it, which is described as $\hat{D}(\alpha)\hat{S}(-r)\,|0\rangle$ with $\alpha>0$ and $r\geq 0$. For the heterodyne measurement, the likelihood to obtain the outcome β given the phase θ is

$$\begin{aligned}p(\beta|\theta) &= \frac{1}{\pi}|\,\langle\beta|\,\hat{R}(\theta)\hat{D}(\alpha)\hat{S}(-r)\,|0\rangle\,|^2\\ &= \frac{1}{\pi}|\,\langle\,\mathrm{e}^{i\theta}\beta\,|\,\alpha,-r\,\rangle\,|^2\\ &= \frac{1}{\pi}\mathcal{F}\big(|\mathrm{e}^{i\theta}\beta\rangle\,,|\alpha,-r\rangle\big).\end{aligned}\tag{5.53}$$

According to Eq. (5.22), the fidelity between these two Gaussian states $\rho_1=\big|\mathrm{e}^{i\theta}\beta\big\rangle\!\big\langle\mathrm{e}^{i\theta}\beta\big|$ and $\rho_2=|\alpha,-r\rangle\!\langle\alpha,-r|$ is provided by their first moments and second moments. Their first moments are

$$\bar{\mathbf{x}}_1=\sqrt{2}\begin{pmatrix}\mathrm{Re}(\mathrm{e}^{i\theta}\beta)\\ \mathrm{Im}(\mathrm{e}^{i\theta}\beta)\end{pmatrix}\quad\text{and}\quad\bar{\mathbf{x}}_2=\begin{pmatrix}\mathrm{Re}(\alpha)\\ \mathrm{Im}(\alpha)\end{pmatrix},\tag{5.54}$$

and their second moments are

$$\boldsymbol{\Gamma}_1=\begin{pmatrix}1&0\\0&1\end{pmatrix}\qquad\text{and}\qquad\boldsymbol{\Gamma}_2=\begin{pmatrix}\mathrm{e}^{-2r}&0\\0&\mathrm{e}^{2r}\end{pmatrix}.\tag{5.55}$$

Since $\det \mathbf{\Gamma}_1 = \det \mathbf{\Gamma}_2 = 1$ and $\det(\mathbf{\Gamma}_1 + \mathbf{\Gamma}_2) = 4\cosh^2 r$, the likelihood turns out to be

$$\begin{aligned} p(\beta|\theta) =& \frac{1}{\pi \cosh r} \exp\Big[-\frac{\mathrm{e}^{-r}\mathrm{Re}^2\left[\mathrm{e}^{i\theta}\beta - \alpha\right] + \mathrm{e}^{r}\,\mathrm{Im}^2\left[\mathrm{e}^{i\theta}\beta - \alpha\right]}{\cosh r}\Big] \\ =& \frac{\mathrm{e}^{-\alpha^2(1-\tanh r)-|\beta|^2}}{\pi \cosh r} \exp\Big[2\alpha|\beta|\cos(\theta - \phi_\beta) + |\beta|^2 \tanh r \cos\left[2(\theta - \phi_\beta)\right]\Big] \\ & \times \exp\Big[-2\alpha|\beta|\tanh r \cos(\theta - \phi_\beta)\Big]. \end{aligned} \tag{5.56}$$

I use the Jacobi-Anger expansion in terms of the modified Bessel functions of the first kind, i.e.

$$\mathrm{e}^{x\cos\theta} = \sum_{n=-\infty}^{\infty} I_n(x)\mathrm{e}^{in\theta}, \tag{5.57}$$

which is a useful tool for the calculations performed in this section. The unconditional probability to obtain β is

$$\begin{aligned} p(\beta) =& \frac{1}{2\pi}\int_{-\pi}^{\pi} d\theta\, p(\beta|\theta) \\ =& \sum_{n,m_1,m_2=-\infty}^{\infty} \int_{-\pi}^{\pi} d\theta\; \mathrm{e}^{i(n+2m_1+m_2)(\theta-\phi_\beta)} \frac{\mathrm{e}^{-\alpha^2(1-\tanh r)-|\beta|^2}}{2\pi^2\cosh r}\, \mathrm{e}^{i(n+m_1+m_2)\pi}\, I_n(-2\alpha|\beta|) \\ & \times I_{m_1}(-|\beta|^2\tanh r)\, I_{m_2}(2\alpha|\beta|\tanh r). \end{aligned} \tag{5.58}$$

I then make use of an identity

$$\int_{-\pi}^{\pi} d\theta\, \mathrm{e}^{i(n+2m_1+m_2)(\theta-\phi_\beta)} = \begin{cases} 2\pi & \text{if } n = -2m_1 - m_2 \\ 0 & \text{otherwise} \end{cases}, \tag{5.59}$$

such that I obtain

$$\begin{aligned} p(\beta) =& \frac{\mathrm{e}^{-\alpha^2(1-\tanh r)-|\beta|^2}}{\pi\cosh r} \\ & \times \sum_{m_1,m_2=-\infty}^{\infty} (-1)^{m_2} I_{2m_1+m_2}(2\alpha|\beta|) I_{m_1}(|\beta|^2\tanh r)\, I_{m_2}(2\alpha|\beta|\tanh r), \end{aligned} \tag{5.60}$$

where I use $I_n(x) = I_{-n}(x)$ and $I_n(-x) = (-1)^n I_n(x)$. Using Bayes' law (5.2), the posterior is obtained as $p(\theta|\beta) = p(\beta|\theta)/2\pi p(\beta)$. To obtain the estimator $\hat{\theta}(\beta) =$

$\arg\langle \mathrm{e}^{i\theta}\rangle_{p(\theta|\beta)}$, I calculate

$$\begin{aligned}\langle \mathrm{e}^{i\theta}\rangle_{p(\theta|\beta)} &= \int_{-\pi}^{\pi} d\theta\, p(\theta|\beta)\,\mathrm{e}^{i\theta}\\ &= \frac{1}{2\pi K}\sum_{n_1,n_2,n_3=-\infty}^{\infty} \mathrm{e}^{i(n_1+n_2+n_3)\pi} I_{n_1}(-2\alpha\,|\beta|)\, I_{n_2}(-|\beta|^2\tanh r)\, I_{n_3}(2\alpha|\beta|\tanh r)\\ &\quad\times \int_{-\pi}^{\pi} d\theta\, \mathrm{e}^{i\theta}\mathrm{e}^{i(n_1+2n_2+n_3)(\theta-\phi_\beta)}, \end{aligned} \tag{5.61}$$

where

$$K = \sum_{m_1,m_2=-\infty}^{\infty} (-1)^{m_2} I_{2m_1+m_2}(2\alpha\,|\beta|) I_{m_1}(-|\beta|^2\tanh r) I_{m_2}(2\alpha|\beta|\tanh r). \tag{5.62}$$

Here, I make use of an identity similar to Eq. (5.59),

$$\int_{-\pi}^{\pi} d\theta\, \mathrm{e}^{i\theta}\mathrm{e}^{i(n_1+2n_2+n_3)(\theta-\phi_\beta)} = \begin{cases} 2\pi\,\mathrm{e}^{i\phi_\beta} & \text{if } n_1=-2n_2-n_3-1\\ 0 & \text{otherwise,}\end{cases} \tag{5.63}$$

such that I obtain

$$\langle \mathrm{e}^{i\theta}\rangle_{p(\theta|\beta)} = \frac{\mathrm{e}^{i\phi_\beta}}{K}\sum_{n_2,n_3=-\infty}^{\infty} (-1)^{n_3} I_{2n_2+n_3+1}(2\alpha\,|\beta|) I_{n_2}(|\beta|^2\tanh r) I_{n_3}(2\alpha|\beta|\tanh r). \tag{5.64}$$

It is to be noted that $K \geq 0$, since K is a component of the probability $p(\beta)$, whose probability factor is non-negative. The remaining sum is real but may take positive and negative values. If the sum part is positive, the estimator corresponds to the phase of the outcome, $\hat{\theta}(\beta) = \arg\langle \mathrm{e}^{i\theta}\rangle_{p(\theta|\beta)} = \phi_\beta$, whereas the estimator is shifted by π, i.e. $\hat{\theta}(\beta) = \phi_\beta + \pi$, if it is negative.

Below, I calculate the variance of the posterior as done in the previous sections to see the performance of the heterodyne scenario. While it is unknown whether the estimator $\hat{\theta}(\beta)$ is ϕ_β or $\phi_\beta+\pi$, the value of the estimator $\hat{\theta}(\beta)$ does not affect the variance of the posterior, as shown below, particularly in Eq. (5.66). I take the average of $\sin^2[\theta-\hat{\theta}(\beta)]$ and find

$$\begin{aligned} V_{\text{post}}(\beta) &= \int_{-\pi}^{\pi} d\theta\, p(\theta|\beta)\,\sin^2\left[\theta-\hat{\theta}(\beta)\right]\\ &= \frac{1}{2\pi K}\sum_{\substack{n_1,n_2,n_3\\=-\infty}}^{\infty} I_{n_1}(-2\alpha\,|\beta|) I_{n_2}(-|\beta|^2\tanh r) I_{n_3}(2\alpha|\beta|\tanh r)\mathrm{e}^{i(n_1+n_2+n_3)\pi}\\ &\quad \int_{-\pi}^{\pi} d\theta\, \mathrm{e}^{i(n_1+2n_2+n_3)(\theta-\phi_\beta)}\,\sin^2[\theta-\hat{\theta}(\beta)]. \end{aligned} \tag{5.65}$$

Again, I make use of an identity similar to the ones in Eqs. (5.59) and (5.63),

$$\int_{-\pi}^{\pi} d\theta \, \mathrm{e}^{i(n_1+2n_2+n_3)(\theta-\phi_\beta)} \sin^2[\theta - \hat{\theta}(\beta)] = \begin{cases} \pi & \text{if } n_1 = -2n_2 - n_3 \\ -\frac{\pi}{2} & \text{if } n_1 = -2n_2 - n_3 \pm 2 \\ 0 & \text{otherwise,} \end{cases} \tag{5.66}$$

such that I obtain

$$\begin{aligned} V_{\text{post}}(\beta) = \frac{1}{2K} & \sum_{n_1,n_2,n_3=-\infty}^{\infty} (-1)^{n_1+n_2+n_3} I_{n_1}(-2\alpha\,|\beta|) I_{n_2}(-|\beta|^2 \tanh r) I_{n_3}(2\alpha|\beta| \tanh r) \\ & \times \big(\delta_{n_1,-2n_2-n_3+2} \frac{-1}{2} + \delta_{n_1,-2n_2-n_3} + \delta_{n_1,-2n_2-n_3-2} \frac{-1}{2}\big). \end{aligned} \tag{5.67}$$

To obtain the average variance of the posterior, I use polar coordinates $\beta = |\beta| \mathrm{e}^{-i\phi_\beta}$, such that

$$\begin{aligned} \bar{V}_{\text{post}} &= \int d^2\beta \; p(\beta) \, V_{\text{post}}(\beta) \\ &= \int_0^{\infty} d|\beta| \int_{-\pi}^{\pi} d\phi_\beta \frac{\mathrm{e}^{-\alpha^2(1-\tanh r)}}{2\pi \cosh r} \sum_{\substack{n_2,n_3 \\ =-\infty}}^{\infty} |\beta| \, \mathrm{e}^{-|\beta|^2} I_{n_2}(-|\beta|^2 \tanh r) I_{n_3}(2\alpha|\beta| \tanh r) \\ &\quad \times \frac{1}{2}(-1)^{n_2} \Big[2I_{-2n_2-n_3}(-2\alpha\,|\beta|) - I_{2-2n_2-n_3}(-2\alpha\,|\beta|) - I_{-2-2n_2-n_3}(-2\alpha\,|\beta|) \Big] \\ &= \frac{\mathrm{e}^{-\alpha^2(1-\tanh r)}}{\cosh r} \sum_{\substack{n_2,n_3 \\ =-\infty}}^{\infty} \int_0^{\infty} d|\beta| \, |\beta| \, \mathrm{e}^{-|\beta|^2} \, I_{n_2}(|\beta|^2 \tanh r) \, I_{n_3}(2\alpha|\beta| \tanh r) \frac{1}{2} \\ &\quad \times \Big[2I_{-2n_2-n_3}(-2\alpha\,|\beta|) - I_{2-2n_2-n_3}(-2\alpha\,|\beta|) - I_{-2-2n_2-n_3}(-2\alpha\,|\beta|) \Big], \end{aligned} \tag{5.68}$$

Finding an analytical expression for the above integeral is difficult, hence I have evaluated it numerically. On a side note, to check my analytical calculations until Eq. (5.68), I have confirmed that some values of Eq. (5.68) agree with full numerical results of $\bar{V}_{\text{post}}$ using Eq. (5.56).

I plot the average variance $\bar{V}_{\text{post}}$ for different squeezing strengths as a function of the square of displacement $|\alpha|^2$ (see Fig. 5.4(a)). One can see that squeezing improves the estimation precision. This result agrees with the intuition provided by the Wigner function: the probe state spreads along the $\hat{q}$-quadrature and displaces along the $\hat{q}$ axis, and rotating the probe around the origin by the phase rotation operator is virtually like spinning a clock hand. Squeezing narrows the width of the clock hand, which makes the measurement outcomes β match the phase precisely.

However, when considering a fixed average energy of the probe state, which is represented by $n = |\alpha|^2 + \sinh^2 r$, squeezing is beneficial only in certain regimes (see Fig. 5.4(b)). For relatively strong squeezing such as $r = 1$ and $r = 1.25$, the average variance is larger for squeezed displaced states than for purely displaced states with the same photon number (see the purple ($r = 1$) and brown lines ($r = 1.25$), and compare them to the blue line ($r = 0$).) For smaller squeezing such as $r = 0.75$, there is a regime

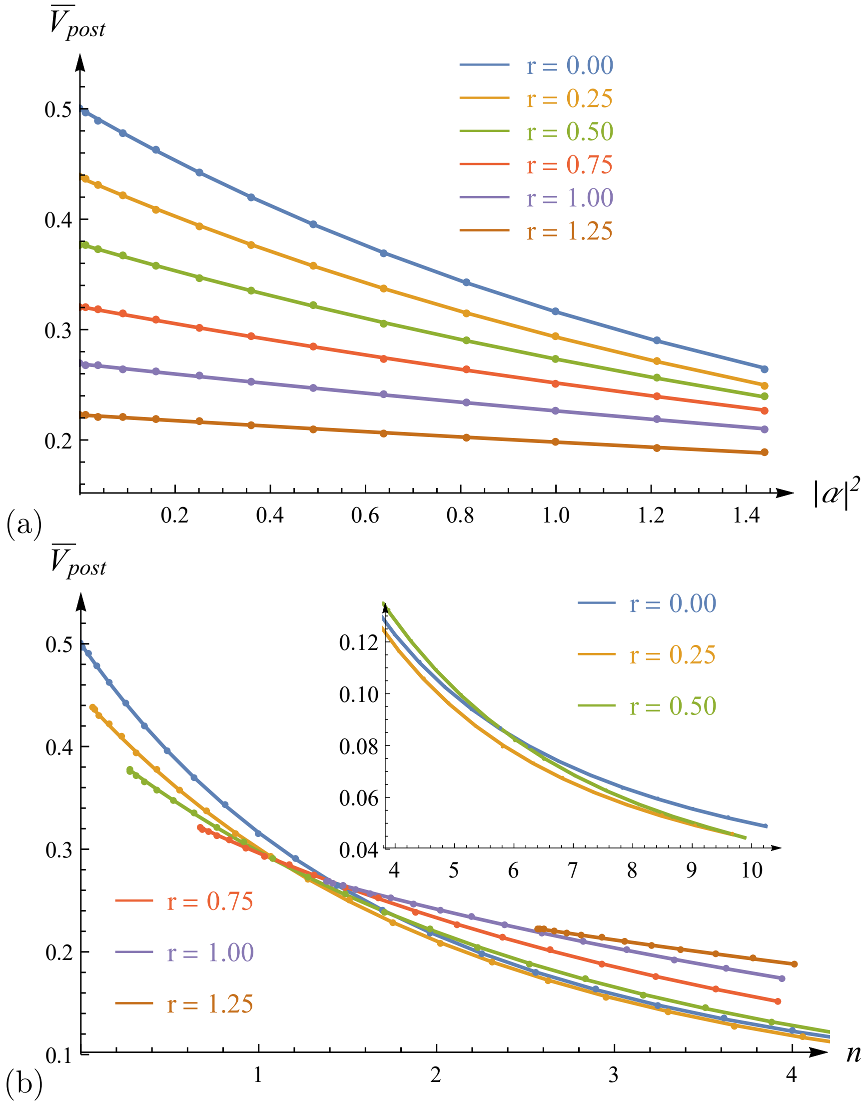

Figure 5.4: Bayesian phase estimation with single-mode Gaussian probes and heterodyne measurements. (a) The average variance $\bar{V}_{\text{post}}$ from Eq. (5.68) is shown for different values of $\alpha \geq 0$ and $r \geq 0$ as a function of $|\alpha|^2$. The line on the top represents the average variance for purely displaced probe states ($r = 0$) from Eq. (5.52). The lines below indicate results of numerically evaluating Eq. (5.68) when changing α for fixed values of r from $r = 0.25$ to $r = 1.25$ (top to bottom, starting at the second line from the top). (b) The average variance $\bar{V}_{\text{post}}$ is shown as a function of the average photon number $n = |\alpha|^2 + \sinh^2 r$. The lines do not start at $n = 0$ because the nonzero values of r give rise to non-zero average energies even for $\alpha = 0$. The inset shows how the lines for $r = 0$, $r = 0.25$, and $r = 0.5$ continue as n increases.

of small n where combination of squeezing and displacement for probes outperforms displaced probes (see the red line ($r = 0.75$)). These results indicate that the ratio between displacement and squeezing strength matters in terms of usefulness of the squeezing. On one hand, for even smaller values of r such as $r = 0.5$, purely coherent probe states are more efficient again for a regime of large n (see the green line ($r = 0.5$) in the inset). On the other hand, for slight squeezing $r = 0.25$, the squeezed probe states outperform pure coherent states for the entire regime I investigated numerically (see the orange line ($r = 0.25$) in the inset).

I point out that the advantage obtained from small squeezing $r = 0.25, 0.5$ is at least an order of magnitude smaller than the average variance for $r = 0$ achieved in the explored parameter range, and hence the advantage does not contribute significantly the phase estimation.

5.3.2 Homodyne measurement

Here, I switch to scenarios using homodyne detection. Since this measurement gives information about the $\hat{q}$-quadrature but does not do anything to the orthogonal $\hat{p}$-quadrature, one cannot distinguish between phases shifted by integer multiples of π. Therefore, the range of the phase is considered to be $[0, \pi]$, and the prior distribution is given by

$$p(\theta) = \frac{1}{\pi}. \tag{5.69}$$

Coherent states & homodyne detection: As in the previous section, I start with the simple case where the probe state is a coherent state $\hat{D}(\alpha)\,|0\rangle = |\alpha\rangle$ for $\alpha > 0$. The likelihood to obtain the outcome q given θ becomes

$$\begin{aligned} p(q|\theta) &= |\langle q|R(\theta)|\alpha\rangle|^2 \\ &= |\langle q|\mathrm{e}^{-i\theta}\alpha\rangle|^2 \\ &= \int_{-\infty}^{\infty} dp\, W(q,p)\,, \end{aligned} \tag{5.70}$$

where $W(q,p)$ is the Wigner function of the rotated coherent state $|\mathrm{e}^{-i\theta}\alpha\rangle$. By using Eq. (5.33) and noting that $\mathbf{\Gamma}_{\mathrm{e}^{-i\theta}\alpha} = \mathbb{1}_2$ and $\bar{\mathbf{x}}_{\mathrm{e}^{-i\theta}\alpha} = \sqrt{2}\alpha(\cos\theta, -\sin\theta)^T$, the likelihood is given by

$$p(q|\theta) = \frac{1}{\sqrt{\pi}}\mathrm{e}^{-\left(q-\sqrt{2}\alpha\cos\theta\right)^2}. \tag{5.71}$$

Similarly, the unconditional probability to obtain q is expressed as

$$\begin{aligned} p(q) &= \int_0^\pi d\theta\, p(\theta)\, p(q|\theta) \\ &= \frac{1}{\pi\sqrt{\pi}} \mathrm{e}^{-q^2-\alpha^2} \int_0^\pi d\theta\, \mathrm{e}^{2\sqrt{2}q\alpha\cos\theta} \mathrm{e}^{-\alpha^2\cos(2\theta)} \\ &= \frac{\mathrm{e}^{-q^2-\alpha^2}}{\pi\sqrt{\pi}} \int_0^\pi d\theta \Big[I_0(2\sqrt{2}q\alpha) I_0(-\alpha^2) + 2\, I_0(-\alpha^2) \sum_{n=1}^{\infty} I_n(2\sqrt{2}q\alpha) \cos(n\theta) \qquad (5.72) \\ &+ 2\, I_0(2\sqrt{2}q\alpha) \sum_{m=1}^{\infty} I_m(-\alpha^2) \cos(2m\theta) \\ &+ 4 \sum_{m,n=1}^{\infty} I_m(-\alpha^2) I_n(2\sqrt{2}q\alpha) \cos(n\theta) \cos(2m\theta) \Big], \qquad (5.73) \end{aligned}$$

where I use the Jacobi-Anger expression (5.57) in a real representation, expressed as

$$\mathrm{e}^{x\cos\theta} = I_0(x) + 2 \sum_{n=1}^{\infty} I_n(x)\, \cos(n\theta), \tag{5.74}$$

due to $I_n(x) = I_{-n}(x)$. I make use of the indentities $\int_0^\pi d\theta\, \cos n\theta = 0$ for any $n \geq 1$ and

$$\int_0^\pi d\theta\, \cos(n\,\theta) \cos(2m\,\theta) = \begin{cases} \frac{\pi}{2} & \text{if } \; n = 2m \\ 0 & \text{otherwise.} \end{cases} \tag{5.75}$$

As a result, the unconditional probability $p(q)$ is written as

$$\begin{aligned} p(q) &= \frac{\mathrm{e}^{-q^2-\alpha^2}}{\sqrt{\pi}} \Big[I_0(2\sqrt{2}q\alpha) I_0(-\alpha^2) + 2 \sum_{m=1}^{\infty} I_{2m}(2\sqrt{2}q\alpha) I_m(-\alpha^2) \Big] \\ &= \frac{\mathrm{e}^{-q^2-\alpha^2}}{\sqrt{\pi}} M, \end{aligned} \tag{5.76}$$

where

$$M = \sum_{m=-\infty}^{\infty} I_{2m}(2\sqrt{2}q\alpha) I_m(-\alpha^2). \tag{5.77}$$

Using Bayes' law (5.2), the posterior $p(\theta|q)$ is obtained as $p(q|\theta)/\pi\, p(q)$.

To determine the estimator $\hat{\theta}(q) = \arg\langle \mathrm{e}^{i\theta}\rangle_{p(\theta|q)}$, I calculate

$$\begin{aligned}
\langle \mathrm{e}^{i\theta}\rangle_{p(\theta|q)} &= \int_0^\pi d\theta\, p(\theta|q)\, \mathrm{e}^{i\theta} \\
&= \frac{1}{M}\frac{1}{\pi}\int_0^\pi d\theta \,\Big[I_0(2\sqrt{2}q\alpha) I_0(-\alpha^2)\mathrm{e}^{i\theta} + 2I_0(-\alpha^2)\sum_{n=1}^{\infty} I_n(2\sqrt{2}q\alpha)\cos(n\theta)\mathrm{e}^{i\theta} \\
&\qquad + 2I_0(2\sqrt{2}q\alpha)\sum_{m=1}^{\infty} I_m(-\alpha^2)\cos(2m\theta)\mathrm{e}^{i\theta} \\
&\qquad + 4\sum_{m,n=1}^{\infty} I_n(2\sqrt{2}q\alpha) I_m(-\alpha^2)\cos(n\theta)\cos(2m\theta)\mathrm{e}^{i\theta}\Big]. \qquad (5.78)
\end{aligned}$$

I make use of the identities $\int_0^\pi d\theta\, \mathrm{e}^{i\theta} = 2i$,

$$\int_0^\pi d\theta\, \cos(n\theta)\,\mathrm{e}^{i\theta} = \begin{cases} \frac{\pi}{2} & \text{if } n = 1 \\ \frac{i(1+(-1)^n)}{1-n^2} & \text{if } n \geq 2 \\ 0 & \text{otherwise,} \end{cases} \qquad (5.79)$$

and

$$\int_0^\pi d\theta\, \cos(n\theta)\cos(2m\theta)\mathrm{e}^{i\theta} = \begin{cases} \frac{\pi}{4} & \text{if } n = 2m \pm 1 \\ \frac{i(1+(-1)^n)(1-4m^2-n^2)}{(n-2m-1)(n-2m+1)(n+2m+1)(n+2m-1)} & \text{otherwise.} \end{cases} \qquad (5.80)$$

At the end, I obtain

$$\begin{aligned}
\langle \mathrm{e}^{i\theta}\rangle_{p(\theta|q)} &= \frac{1}{\pi M}\Bigg\{ 2iI_0(2\sqrt{2}q\alpha)\Big[I_0(-\alpha^2) + \sum_{m=1}^{\infty} I_m(-\alpha^2)\frac{2}{1-4m^2}\Big] \\
&\quad + 2I_0(-\alpha^2)\Big[\tfrac{\pi}{2}I_1(2\sqrt{2}q\alpha) + \sum_{n=2}^{\infty} I_n(2\sqrt{2}q\alpha)\tfrac{i(1+(-1)^n)}{1-n^2}\Big] \\
&\quad + 4\sum_{m=1}^{\infty} I_m(-\alpha^2)\,\Big[\tfrac{\pi}{4}I_{2m-1}(2\sqrt{2}q\alpha) + \tfrac{\pi}{4}I_{2m+1}(2\sqrt{2}q\alpha) \\
&\qquad + \sum_{\substack{n=1\\ n\neq 2m\pm 1}}^{\infty} I_n(2\sqrt{2}q\alpha)\tfrac{i(1+(-1)^n)(1-4m^2-n^2)}{(n-2m-1)(n-2m+1)(n+2m+1)(n+2m-1)}\Big]\Bigg\} \\
&= \frac{i}{\pi M}\Bigg\{\sum_{n=1}^{\infty}\tfrac{4}{1-4n^2}\left[I_0(-\alpha^2)I_{2n}(2\sqrt{2}q\alpha)+I_n(-\alpha^2)I_0(2\sqrt{2}q\alpha)\right] \\
&\quad + 2I_0(2\sqrt{2}q\alpha)I_0(-\alpha^2) + 8\sum_{m=1}^{\infty}\sum_{n=1}^{\infty} I_{2n}(2\sqrt{2}q\alpha)I_m(-\alpha^2) \\
&\qquad \times \frac{1-4m^2-4n^2}{(2n-2m-1)(2n-2m+1)(2n+2m+1)(2n+2m-1)}\Bigg\} \\
&\quad + \frac{1}{M}\Bigg\{I_0(-\alpha^2)I_1(2\sqrt{2}q\alpha) + \sum_{n=1}^{\infty} I_n(-\alpha^2)\Big[I_{2n-1}(2\sqrt{2}q\alpha) + I_{2n+1}(2\sqrt{2}q\alpha)\Big]\Bigg\}.
\end{aligned} \tag{5.81}$$

To obtain the phase of $\langle \mathrm{e}^{i\theta}\rangle_{p(\theta|q)}$, I express the real and imaginary parts of $\langle \mathrm{e}^{i\theta}\rangle_{p(\theta|q)}$ as

$$\mathrm{Re}[\langle \mathrm{e}^{i\theta}\rangle_{p(\theta|q)}] = \frac{\sum_{n=-\infty}^{\infty} I_{2n+1}(2\sqrt{2}q\alpha)I_n(-\alpha^2)}{\sum_{m=-\infty}^{\infty} I_{2m}(2\sqrt{2}q\alpha)I_m(-\alpha^2)} \tag{5.82}$$

and

$$\begin{aligned}
\mathrm{Im}[\langle \mathrm{e}^{i\theta}\rangle_{p(\theta|q)}] &= \frac{2}{\pi}\frac{\sum_{m,n=-\infty}^{\infty} I_{2n}(2\sqrt{2}q\alpha)I_m(-\alpha^2)}{\sum_{k=-\infty}^{\infty} I_{2k}(2\sqrt{2}q\alpha)I_k(-\alpha^2)} \\
&\quad \times \frac{1-4m^2-4n^2}{(2n-2m-1)(2n-2m+1)(2n+2m+1)(2n+2m-1)},
\end{aligned} \tag{5.83}$$

respectively, where I utilise the functions $C_{n,m}$ which are invariant under the exchanges $n \to -n$ and $m \to -m$ and satisfy

$$\sum_{n=1}^{\infty} C_{n,m} = \frac{1}{2}\left(\sum_{n=-\infty}^{\infty} C_{n,m} - C_{0,m}\right) \tag{5.84}$$

and

$$\sum_{m,n=1}^{\infty} C_{n,m} = \frac{1}{4}\left(\sum_{m,n=-\infty}^{\infty} C_{n,m} - \sum_{m=-\infty}^{\infty} C_{0,m} - \sum_{n=-\infty}^{\infty} C_{n,0} + C_{0,0} \right). \tag{5.85}$$

Therefore, the estimator is obtained from Eqs. (5.82) and (5.83) as

$$\hat{\theta}(q) = \arctan\left(\frac{\mathrm{Im}[\langle \mathrm{e}^{i\theta}\rangle]}{\mathrm{Re}[\langle \mathrm{e}^{i\theta}\rangle]} \right). \tag{5.86}$$

As can be seen, the form of the estimator looks even more complicated than its counterpart (5.52) in case of the heterodyne detection scenario. Therefore, I resort to numerical calculations of the variance and the average variance of the posterior. The results of the average variance are plotted as a function of $|\alpha|^2$ in Fig. 5.5, which will be discussed in the next section. On a side note, to check my analytical calculations until Eqs. (5.82) and (5.83), I have confirmed that some values of Eqs. (5.82) and (5.83) agree with full numerical results of $\mathrm{Re}[\langle \mathrm{e}^{i\theta}\rangle]$ and $\mathrm{Im}[\langle \mathrm{e}^{i\theta}\rangle]$ using Eq. (5.71).

Squeezed displaced states & homodyne detection: Now, I consider squeezing the probe before displacing it as before, and the probe state is described as $\hat{D}(\alpha)\hat{S}(r\mathrm{e}^{i\varphi})\,|0\rangle$ for $\alpha \geq 0$ and $0 \leq \varphi < 2\pi$. Although in the heterodyne detection scenario I found the optimal squeezing direction to be $\varphi = \pi$, the optimal squeezing direction for homodyne detection depends on the phase θ as shown below. Since the homodyne detection measures the value of the $\hat{q}$-quadrature, the squeezing direction of the probe state is optimal when the rotated probe state $\hat{R}(\theta)\hat{D}(\alpha)\hat{S}(r\mathrm{e}^{i\varphi})\,|0\rangle = \hat{R}(\theta)\hat{D}(\alpha)\hat{R}(\varphi/2)\hat{S}(r)\,|0\rangle$ is squeezed along the $\hat{q}$-quadrature so that the Wigner function is vertical to the q axis. Therefore, for any fixed θ the optimal squeezing direction satisfies $\theta + \frac{\varphi}{2} = m\pi$ for $m \in \mathbb{Z}$, i.e. $\varphi = 2(m\pi - \theta)$. However, since I consider a flat prior, i.e. no initial information on θ, the optimal direction cannot be determined. Therefore, I leave the squeezing direction as a variable for the following calculations.

The likelihood to obtain the outcome q given θ can be obtained as before from the first moment of the probe state, which is $\bar{\mathbf{x}} = \sqrt{2}\alpha(\cos\theta, -\sin\theta)^T$ and the covariance matrix, which is given in Eq. (5.19) with replacement $\varphi \to \varphi + 2\theta$. As a result, I have

$$\begin{aligned} p(q|\theta) &= |\langle q|R(\theta)\hat{D}(\alpha)\hat{S}(r\mathrm{e}^{i\varphi})|0\rangle|^2 \\ &= \frac{\exp\left[-\frac{\left(x-\sqrt{2}\alpha\cos\theta\right)^2}{\Gamma_{qq}(r,\varphi+2\theta)}\right]}{\sqrt{\pi\Gamma_{qq}(r,\varphi+2\theta)}}, \end{aligned} \tag{5.87}$$

where $\Gamma_{qq}(r,\varphi) = \cosh(2r) - \cos(\varphi)\sinh(2r)$. The unconditional probability $p(q)$ to obtain q is obtained from $p(q) = \int_0^\pi d\theta\, p(\theta)\, p(q|\theta)$ as done in the previous sections. However, the integration containing $p(q)$ turns out to be a formidable obstacle, and it seems difficult to find a closed analytical expression for it. Therefore, I proceed by numerically evaluating the unconditional probability, the posterior, the estimator, the variance of the posterior, and the average variance. I plot the resulting average variance $\bar{V}_{\mathrm{post}}$ as a function of $|\alpha|^2$ and as a function of the average photon number $n = |\alpha|^2 + \sinh^2 r$ in Figs. 5.5(a) and (b), respectively.

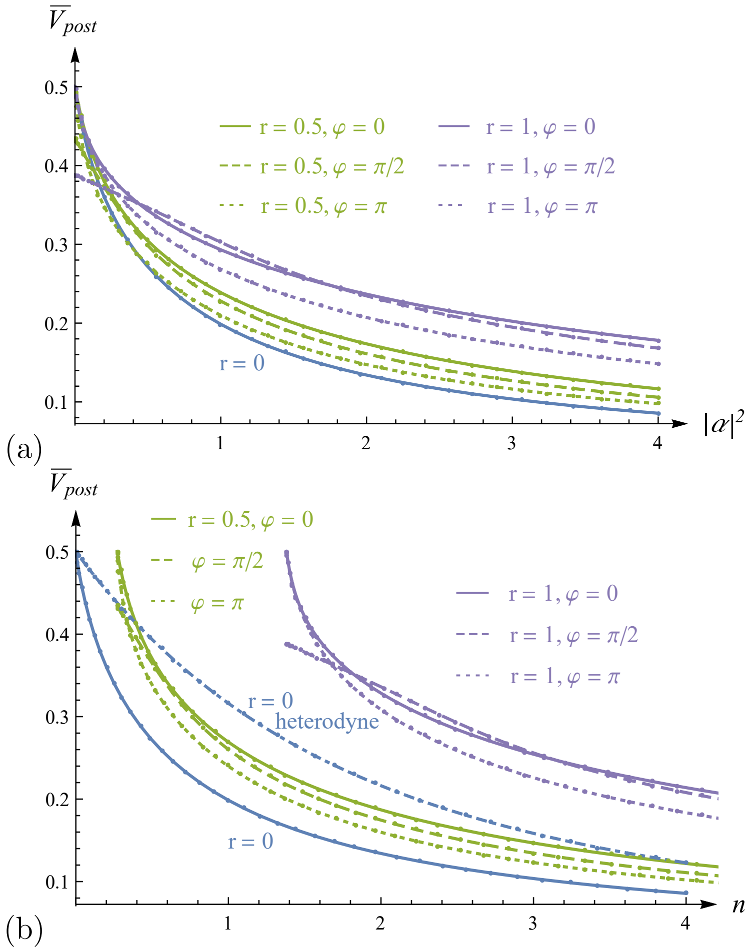

Figure 5.5: Bayesian phase estimation with single-mode Gaussian probes and homodyne measurements. (a) The average variance $\bar{V}_{\text{post}}$ is shown as a function of $|\alpha|^2$. Each curve corresponds to varying values of $\alpha \geq 0$, but fixed squeezing strength r from $r = 0$ (blue), over $r = 0.5$ (green), to $r = 1$ (purple), and fixed squeezing angle φ, from $\varphi = 0$ (solid), over $\varphi = \pi/2$ (dashed), to $\varphi = \pi$ (dotted). Curves for $\varphi = 3\pi/2$ are identical to those for $\varphi = \pi/2$ and hence are not plotted. (b) The average variance $\bar{V}_{\text{post}}$ is shown as a function of the average photon number $n = |\alpha|^2 + \sinh^2 r$ of the probe state. The colour-coding is the same as in (a), but the lines do not start at $n = 0$ because the nonzero values of r give rise to non-zero average energies even for $\alpha = 0$. In addition, (a) shows $\bar{V}_{\text{post}}$ for a coherent probe state ($r = 0$) and heterodyne detection from Eq. (5.52) as a blue dashed-dotted curve.

Certainly, squeezing improves the estimation to some extent, but for non-zero displacement, squeezing is less beneficial than pure displaced states with the same α (see Fig. 5.5(a)). When comparing probe states at fixed average energy, it is clearer that squeezed probe states show worse performance than displaced probe states, except for a regime of small α (see Fig. 5.5(b)). Furthermore, comparison with the result of heterodyne detection displays that homodyne detection perform better for coherent probe states. Thus, sets of coherent probe state and homodyne measurement are recommended to be used for Bayesian phase estimation. However, note that the homodyne detection covers only the range $[0, \pi]$. If one wishes to explore the overall range of phases, heterodyne detection should be chosen.

5.4 Squeezing strength estimation

Lastly, I will discuss estimation of the squeezing strength r of the squeezing operation $\hat{S}(\xi)$ with $\xi = re^{i\varphi}$. Note that I assume the squeezing angle φ is known in order to restrict myself to single-parameter Bayesian estimation. Also, estimation problems of the squeezing angle can come down to phase estimation problems due to $\hat{S}(\xi) = \hat{R}(\varphi/2)\hat{S}(r)$.

While optimal measurement strategies for a variation of the squeezing strength estimation have been studied in Refs. [308, 309], these optimal measurement schemes could be difficult to realise in practice. Thus, I consider Gaussian measurements as done above. Furthermore, I focus on homodyne detection and do not study heterodyne detection. That is because some previous works [263, 309] show that homodyne detection works better than heterodyne detection for this estimation problem due to reduced variances of strongly squeezed states associated with outcomes of homodyne detection and normal variances of coherent states associated with outcomes of heterodyne detection. This is also discussed in the displacement estimation section 5.2.2. Let me recall that not only the displacement estimation but also the phase estimation (Sec. 5.3.2) can work better with homodyne detection than heterodyne detection.

5.4.1 Homodyne detection

I take a general single pure Gaussian probe state, $|\xi\rangle = \hat{D}(\alpha)\hat{S}(\chi)|0\rangle$, as a probe, where the displacement is complex as $\alpha = \alpha_{\mathrm{R}} + i\alpha_{\mathrm{I}}$ for $\alpha_{\mathrm{R}}, \alpha_{\mathrm{I}} \in \mathbb{R}$, and the presqueezing parameter is written as $\chi = s\,\mathrm{e}^{i\psi}$ (let me call squeezing the probe state before encoding the parameter to be estimated as "presqueezing"). The parameter r to be estimated is applied to the probe as $\hat{S}(r)|\xi\rangle = \hat{S}(r)\hat{D}(\alpha)\hat{S}(\chi)|0\rangle$. The squeezing transformation to be estimated changes the first moment $\bar{\mathbf{x}}$ and covariance matrix σ into $\bar{\mathbf{x}} \mapsto M\bar{\mathbf{x}}$ and $\sigma \mapsto M\sigma M^T$ with a symplectic matrix of the form

$$M = \begin{pmatrix} \cosh r - \cos\varphi\ \sinh r & \sin\varphi\ \sinh r \\ \sin\varphi\ \sinh r & \cosh r + \cos\varphi\ \sinh r \end{pmatrix}. \tag{5.88}$$

Since the squeezing angle φ is assumed to be known, one can choose the reference frame accordingly, and therefore I choose $\varphi = 0$ and $r \in \mathbb{R}$ without loss of generality.

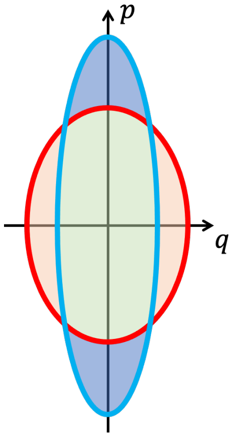

Figure 5.6: Sketch of the cross sections for the Wigner functions of a presqueezed vacuum state (the red circle) and its encoded state (the blue circle). The widths of these Wigner functions show the variances. The overlap between the two states is represented by the green area.

As done in the previous sections, the likelihood $p(q|r)$ is given by

$$\begin{aligned} p(q|r) &= \langle q|\hat{S}(r)|\xi\rangle \\ &= \frac{\exp\left(\frac{-\mathrm{e}^{2r}(\sqrt{2}\alpha_{\mathrm{R}}\mathrm{e}^{-r}-q)^2}{\cosh 2s-\cos\psi\ \sinh 2s}\right)}{\mathrm{e}^{-r}\sqrt{\pi(\cosh 2s-\cos\psi\ \sinh 2s)}}, \end{aligned} \tag{5.89}$$

where the parameter r to be estimated is included in not only the mean but also the variance of $p(q|r)$. Treating a non-elementary function such as $\exp[\exp(r)]$ makes it hard to analytically deal with this problem and obtain the posterior. Therefore, I will show numerical results for the squeezing estimation problem in this section.

In the next subsections, I will consider coherent probe states and presqueezed displaced probe states, and exclude presqueezed vacuum states since these states work poorly. That is because these probe states do not change the first moment but only the covariance matrix as illustrated in Fig. 5.6. The measurement outcomes of the overlap between the probe state and the encoded probe state (the green area depicted in Fig. 5.6) do not give information about the squeezing strength r. Thus, some of the measurement outcomes will be useless. However, the story is different in cases of displaced probe states. The transformation by the parameter to be estimated also affects the displacement of the probe state, which helps one with the squeezing estimation problem and will be discussed in the next section. In the following, I explore coherent probe states first and then presqueezed displaced probe states.

Coherent probe states: As seen in Eq. (5.89), the parameter to be estimated changes not only the covariance matrix but also the first moment. As illustrated in Fig. 5.7, the first moment follows hyperbolic trajectories in the phase space. Here, for simplicity I focus on trajectories along the q axis, where the displacement of the probe is purely real so that $\alpha = \alpha_{\mathrm{R}}$, i.e. I focus on states whose Wigner functions are depicted as blue ovals in Fig. 5.7. Since the mean of the probe changes along the q axis, it is

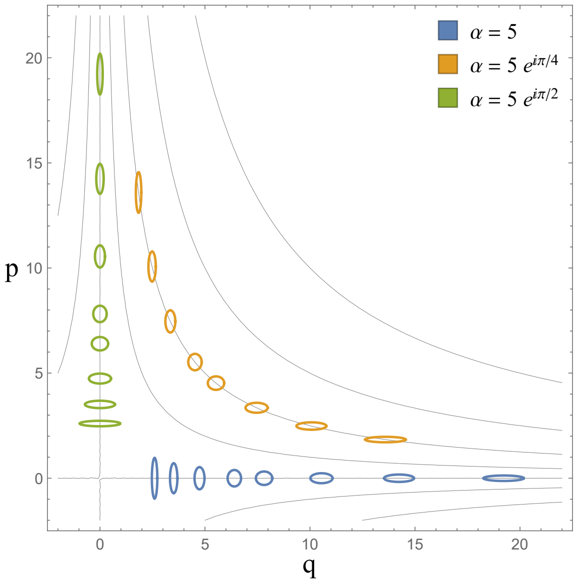

Figure 5.7: Cross sections of the Wigner functions of some coherent probe states after squeezing transformation. The ovals represent those Wigner functions with displacements $\alpha = 5$ (blue), $\alpha = 5\ \mathrm{e}^{i\pi/4}$ (orange) and $\alpha = 5\ \mathrm{e}^{i\pi/2}$ (green) after the encoding (squeezing) with strength $r = (-1,\ -0.7,\ -0.4,\ -0.1,\ 0.1,\ 0.4,\ 0.7,\ 1)$ is applied. While the shape of the Wigner function changes with varying squeezing strengths, the mean values $\langle\hat{q}\rangle$ and $\langle\hat{p}\rangle$ move along hyperbolic trajectories depicted by grey lines.

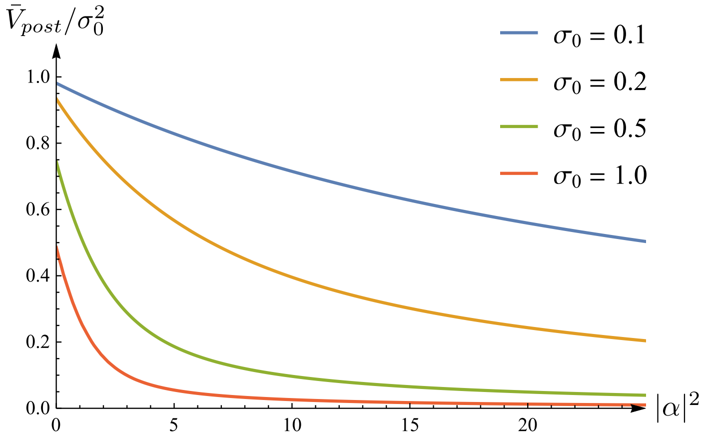

Figure 5.8: Bayesian squeezing strength estimation with coherent probe state. The ratios between the average variance of the posterior and the variance of the prior are plotted as a function of square of displacements of the probe state. Colours correspond to different prior variances. The prior is a Gaussian distribution with mean $r_0 = 1$ and variance σ_0^2.

convenient to use the homodyne measurements on q. To evaluate the performance of this strategy, I show numerical results of the average variance of the posterior in Fig. 5.8. One can see a reduction of the average variance for increasing displacement of the probe as expected.

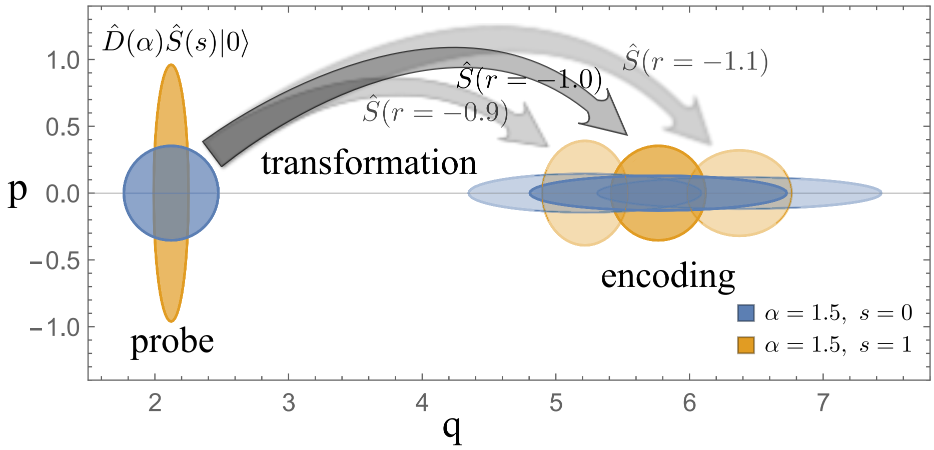

Figure 5.9: Cross sections of the Wigner functions of a unpresqueezed state and a presqueezed state. The blue oval in the left side represents an unpresqueezed probe ($s = 0$), and the blue ones in the right side are encoded states with strength ($r = -0.9, -1.0, -1.1$). The orange oval on the left side represents a presqueezed probe ($s = 0.5$), and the orange ones in the right side show states after encoding with the same strength as the unpresqueezed state.

Presqueezed displaced probe states: Here, I discuss the benefit from combining displacing and presqueezing the probe. For simplicity, I restrict the parameter to be estimated to negative values, i.e. $r < 0$, where the uncertainty in the $\hat{p}$-quadrature direction is reduced. Therefore, I presqueeze the probe states in a way to reduce the uncertainty in the opposite direction to that of the estimated squeezing, i.e. the $\hat{q}$-quadrature direction (see Fig. 5.9). That is, I restrict the presqueezing strength to positive values so that $\chi = s > 0$. As shown in Fig. 5.9, presqueezed probes spreading along the p axis are more distinguishable after encoding than unpresqueezed probes ($s = 0$). This indicates the advantages of presqueezing along the opposite direction to the squeezing to be estimated.

To confirm the advantages, I plot the average variance of the posterior for changes of presqueezing and displacement of probe states in Fig. 5.10. As seen in the panel (a), stronger presqueezing works better for the estimation. Furthermore, the panel (b) shows that the minimum points of $\bar{V}_{\text{post}}$ can be achieved with presqueezing and displacement both being non-zero (see the black dots). Combining presqueezing and displacement is therefore beneficial for this estimation.

5.5 Conclusions

In this chapter, I have presented a comprehensive study of Bayesian parameter estimation by applying single-mode Gaussian probe states and feasible Gaussian measurements. Bayesian estimation strategies permit one to have any prior uncertainty for the parameter to be estimated, e.g. one can start with flat priors and perform a small number of measurements, which local estimation strategies cannot handle. The focus of this study has not been on finding optimal probe states and measurement schemes whose

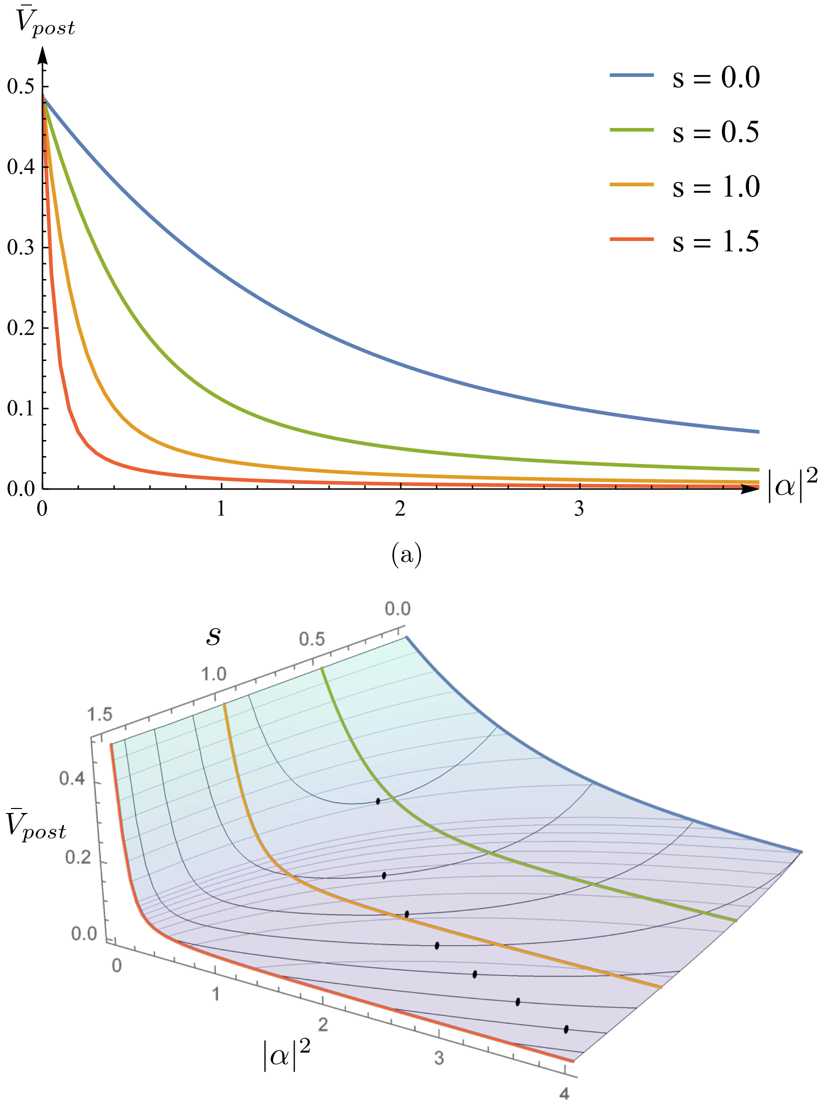

(a)

(b)

Figure 5.10: Bayesian squeezing strength estimation with presqueezed displaced probe states. The average variance of the posterior in presqueezed and displaced probe states is displayed. In (a), the average variance is plotted as a function of the square of displacement $|\alpha|^2$ for four values of s. In (b), the average variance is plotted as a function of presqueezing s and the square of displacement $|\alpha|^2$. The grey curves represent lines of constant photon number $n = |\alpha|^2 + \sinh^2(s)$, while the black dots mark the points where the average variance is minimised for a given photon number. The four curves from (a) are shown in the same color-coding. The prior used is a normal distribution with mean $r_0 = -0.5$ and variance $\sigma_0^2 = 1$.

precision reaches the HL, but I have aimed to reveal the precision limit with feasible ingredients (Gaussian states) and setups (heterodyne and homodyne detection).

In this work, I have considered three exemplary cases for CV quantum metrology. A summary of the findings for each case is as follows:

(i) Displacement estimation. I have displayed a full analytical expression for this estimation strategy. Importantly, I have shown that a set of a Gaussian probe and a Gaussian measurement is optimal according to Bayesian quantum CRB (5.12): squeezing a vacuum probe in the direction of the displacement to be estimated and implementing homodyne detection.

(ii) Phase estimation. Since probability distributions for phase are circular distributions, the mathematical treatment of this problem becomes complicated. Thus, I choose a flat prior, where one has no prior information of the parameter to be estimated and which is not suitable for local phase estimation. I have given a closed expression for the average variance of the posterior in cases of coherent probe states and heterodyne detection, while numerical treatment was given for other scenarios. I have shown that homodyne detection outperforms heterodyne detection although the phase range for the homodyne detection is half, i.e. $\theta \in [0, \pi]$. In case of using homodyne detection, it is the most efficient to concentrate on displaced probe states.

(iii) Single-mode squeezing strength estimation. Due to the complicated form of the likelihood, all treatments of this problem were performed numerically. However, the findings of the analysis are clear and show that it is the most efficient to make use of presqueezing and displacement both for the probe, in addition to implementing homodyne detection.

This comprehensive investigation shown here provides key references for Bayesian parameter estimations and will help further explorations for more complicated setups. Examples include identifying optimal setups which may be non-Gaussian but feasible [305] and investigating multi-mode Gaussian probe states which can have two-mode squeezing, i.e mode entanglement, and can bring another quantum feature not explored here [310]. Another example is multi-parameter estimation [311–314]. If the measurement basis for a parameter estimation is not orthogonal to that for another parameter estimation, these two estimations influence each other. It would be interesting to explore methods to avoid or weaken such influences.

Chapter 6

Simplifying multi-level thermal machines using virtual qubits

Investigating the control of thermal machines in the quantum regime allows one to explore the fundamental limits of thermodynamic tasks [23, 315–321], e.g. extracting work from correlation [25]. To study such processes, it is common to consider a few quantum-mechanical degrees of freedom interacting with a large environment, which one does not have detailed control over [322–327]. Higher-dimensional machines are harder to simulate exactly, and hence much of the focus is on models that are simple enough to be treatable by master equations, such as a few qubits. One important concept in this context is the framework of a virtual qubit [127, 130, 131]. This idea allows one to reduce the complexity of predicting relevant machine behaviours to reveal steady states and even transient dynamics of a two-level transition of interest by considering an effective two-level system involved with the transition. This framework has led to simplifying approaches and both quantitative and qualitative understanding [121, 126, 328, 329]. However, expanding the target system to multi-level systems beyond qubits is still a challenge.

In this work, I address this problem for three-level systems (qutrit), as well as arbitrary-level systems (qudits), coherently interacting with several virtual qubits in the context of reset master equations [130]. I investigate the steady state solution for three-level systems coupled to virtual qubits and compare it with an optical master equation approach to identify universal features, which both models predict, and identify properties of multi-level thermal machines. In this chapter, I start with the introduction of virtual qubits before presenting the findings of this work. I then propose a method to enhance the performance of the paradigmatic three-level maser/laser [106] to show advantages of the results obtained from this work. Throughout this work, I take $\hbar = 1$ and $k_\mathrm{B} = 1$.

This project has been accomplished in collaboration with Wolfgang Niedenzu and Marcus Huber. I have been involved with comprehensive discussion and performed all analytical calculations as well as numerical treatment of the full reset master equation. The work presented in this chapter is submitted to Quantum and is available on arXiv:2009.03832 [5].

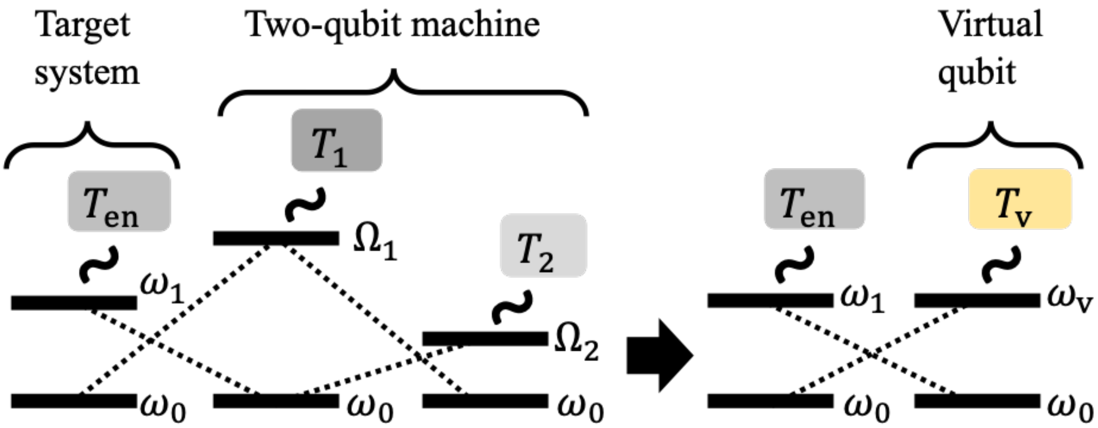

Figure 6.1: Sketch of a virtual qubit [127]. Left: a target qubit coupled to a two-qubit machine, where $\omega_1 - \omega_0 = \Omega_1 - \Omega_2$. Right: the target qubit effectively coupled to a virtual qubit, where $\omega_{\rm v} - \omega_0 = \Omega_1 - \Omega_2$ and $T_{\rm v}$ is given by Eq. (6.1). The dotted lines represent the coherent interactions given in Eq. (6.3). The wavy lines represent contact with baths whose temperatures are $T_{\rm en,1,2}$.

6.1 Two-qubit machine as a virtual qubit

First let me review the idea of virtual qubits, which has been proposed in Ref. [127]. Suppose that one has two qubits with energy spacings Ω_1 and Ω_2. Also assume that the qubits coherently interact with each other and are in contact with baths at temperatures T_1 and T_2, respectively. I refer to this set of qubits as a two-qubit machine composed of eigenstates $|0\rangle_1 |0\rangle_2$, $|0\rangle_1 |1\rangle_2$, $|1\rangle_1 |0\rangle_2$, and $|1\rangle_1 |1\rangle_2$. Here, I focus on $|0\rangle_1 |1\rangle_2$ and $|1\rangle_1 |0\rangle_2$, which are involved with the coherent interaction (cf. Fig. 6.1). Without loss of generality, I take $\Omega_1 > \Omega_2$ so that the ground state of the virtual qubit is given by $|0\rangle_1 |1\rangle_2$ and the excited state is given by $|1\rangle_1 |0\rangle_2$ with the energy spacing $\Omega_1 - \Omega_2$. The temperature of this virtual qubit, the so-called virtual temperature, is provided by the ratio between the ground state and the excited state, and is written as

$$T_{\rm v} = \frac{\Omega_1 - \Omega_2}{\Omega_1/T_1 - \Omega_2/T_2} . \tag{6.1}$$

Note that $T_{\rm v}$ can be negative, leading to population inversion, since it is not a real temperature. The virtual qubit decreases the Hilbert space effectively and helps one understand what role the two-qubit machine plays physically: $T_{\rm v} < T_{1,2,\rm en}$ means that the machine can cool down a target system; $T_{\rm v} > T_{1,2,\rm en}$ means that the machine can warm up a target system; $T_{\rm v} < 0$ means that a target system can extract work from the machine.

Here, I add another physical qubit with energy spacing $\omega_1 - \omega_0 = \Omega_1 - \Omega_2$ as a target system and coherently couple it to the two-qubit machine (see Fig. 6.1). Assuming that the target is subjected to the environment at temperature $T_{\rm en}$, the reset master equation

(RME) describing this composite system is provided by [130, 131]

$$\begin{aligned}\frac{\partial\rho_{\mathrm{tot}}}{\partial t} = -i\,[H,\rho_{\mathrm{tot}}] &+ Q_{\mathrm{en}}\left(\tau_{\mathrm{en}}\otimes \mathrm{Tr}_{\mathrm{tar}}[\rho_{\mathrm{tot}}]-\rho_{\mathrm{tot}}\right)\\ &+ Q_1\left(\tau_1\otimes \mathrm{Tr}_1[\rho_{\mathrm{tot}}]-\rho_{\mathrm{tot}}\right)\\ &+ Q_2\left(\tau_2\otimes \mathrm{Tr}_2[\rho_{\mathrm{tot}}]-\rho_{\mathrm{tot}}\right),\end{aligned} \tag{6.2}$$

where ρ_{tot} is the density matrix of the composite system. I define the thermalisation rates corresponding to the environment or each bath in contact with the two-qubit machine as $Q_{\mathrm{en},1,2}$, respectively. The density matrices $\tau_{\mathrm{en},1,2}$ are thermal states corresponding to the real temperatures T_{en}, T_1, and T_2. The partial traces over the target qubit or the machine's constitutes are represented by $\mathrm{Tr}_{\mathrm{tar},1,2}$, respectively. The Hamiltonian is given by

$$H=\sum_{k=0}^{1}\omega_k\,|k\rangle\langle k| + \sum_{i\in\{1,2\}}\Omega_i\sigma_i^+\sigma_i^- + g\,|0\rangle\langle 1|\,\sigma_1^+\sigma_2^- + \mathrm{h.c.}, \tag{6.3}$$

with $\sigma_i^+ = |1\rangle_i\,\langle 0|_i$ and g being the coupling strength. There, "h.c." means Hermitian conjugate. If the target qubit is cut off from the environment, the target is thermalised at the virtual temperature (6.1) regardless of $Q_{1,2}$. The steady state of the RME (6.3) has been calculated in Eq. (7) in Ref. [131]. However, there are some typographical errors in this paper, and so I show the form of the steady state here correctly, which is given by

$$\begin{aligned}\rho_{\mathrm{ss}} &= \tau_{\mathrm{en}} + \frac{q\gamma}{\Gamma_{\mathrm{en}}}Z_{\mathrm{en}}\\ &= \begin{pmatrix}\tau_{\mathrm{en}}^{\mathrm{g}}+q\gamma/\Gamma_{\mathrm{en}} & 0\\ 0 & \tau_{\mathrm{en}}^{\mathrm{e}}-q\gamma/\Gamma_{\mathrm{en}}\end{pmatrix},\end{aligned} \tag{6.4}$$

where I write $\tau_{\mathrm{en}}^{\mathrm{g,e}}$ for the ground / excited state of thermal state τ_{en},

$$q=\Gamma_1+\Gamma_2+\Gamma_{\mathrm{en}}, \tag{6.5}$$

$$Z_{\mathrm{en}} = |0\rangle\,\langle 0| - |1\rangle\,\langle 1| = \begin{pmatrix}1 & 0\\ 0 & -1\end{pmatrix}, \tag{6.6}$$

and

$$\gamma = \frac{-\tau_{\mathrm{en}}^{\mathrm{g}}\tau_1^{\mathrm{e}}\tau_2^{\mathrm{g}} + \tau_{\mathrm{en}}^{\mathrm{e}}\tau_1^{\mathrm{g}}\tau_2^{\mathrm{e}}}{2+\left(\Gamma_1+\Gamma_2+\Gamma_{\mathrm{en}}\right)^2/2g^2 + \sum_i q_i + \sum_{jk} Q_{jk}\Omega_{jk}}. \tag{6.7}$$

Here, $q_i = \Gamma_i/(q-\Gamma_i)$ leads to

$$\sum_i q_i = \frac{\Gamma_{\mathrm{en}}}{\Gamma_1+\Gamma_2} + \frac{\Gamma_1}{\Gamma_2+\Gamma_{\mathrm{en}}} + \frac{\Gamma_2}{\Gamma_{\mathrm{en}}+\Gamma_1}. \tag{6.8}$$

Also, I have

$$Q_{jk} = \frac{\Gamma_j q_k + \Gamma_k q_j}{q - \Gamma_j - \Gamma_k} = Q_{kj} \tag{6.9}$$

and

$$\Omega_{jk} = r'_j \bar{r}'_k + \bar{r}'_j r'_k = \Omega_{kj}, \tag{6.10}$$

where $r_i = \tau_i^{\mathrm{g}}$, $\bar{r}_i = \tau_i^{\mathrm{e}}$, and $r'_i = \bar{r}_i$ for $i = \alpha$, otherwise $r'_i = r_i$. This results in

$$\begin{aligned}\sum_{jk} Q_{jk}\Omega_{jk} &= Q_{\mathrm{en},1}\Omega_{\mathrm{en},1} + Q_{1,2}\Omega_{1,2} + Q_{\mathrm{en},2}\Omega_{\mathrm{en},2} \\ &= \frac{\Gamma_{\mathrm{en}} q_1 + \Gamma_1 q_{\mathrm{en}}}{\Gamma_2}\left(\tau_{\mathrm{en}}^{\mathrm{g}}\tau_1^{\mathrm{e}} + \tau_{\mathrm{en}}^{\mathrm{e}}\tau_1^{\mathrm{g}}\right) + \frac{\Gamma_1 q_2 + \Gamma_2 q_1}{\Gamma_{\mathrm{en}}}\left(\tau_1^{\mathrm{g}}\tau_2^{\mathrm{e}} + \tau_1^{\mathrm{e}}\tau_2^{\mathrm{g}}\right) \\ &\quad + \frac{\Gamma_{\mathrm{en}} q_2 + \Gamma_2 q_{\mathrm{en}}}{\Gamma_1}\left(\tau_{\mathrm{en}}^{\mathrm{g}}\tau_2^{\mathrm{g}} + \tau_{\mathrm{en}}^{\mathrm{e}}\tau_2^{\mathrm{e}}\right).\end{aligned} \tag{6.11}$$

Although this is the full analytical steady-state solution, this form looks complicated, and it is hard to interpret what role each parameter plays physically.

In general, the two-qubit machine is disturbed by interaction with the environment through the target qubit, and hence the virtual temperature (6.1) is not valid anymore. However, if the qubits inside the two-qubit machine are thermalised at the bath temperatures $T_{1,2}$ so quickly that $Q_{1,2} \gg Q_{\mathrm{en}}, g$, the virtual temperature (6.1) is still a valid concept. Assuming this regime, I replace the two-qubit machine with a bath at the virtual temperature (6.1) in the reset model, which results in constructing an effective reset master equation (effRME) of the target system, given by

$$\frac{\partial \rho}{\partial t} = Q_{\mathrm{en}}\left(\tau_{\mathrm{en}} - \rho\right) + q_{\mathrm{vir}}\left(\tau_{\mathrm{vir}} - \rho\right), \tag{6.12}$$

where q_{vir} is the effective thermalisation rate of the virtual qubit and τ_{vir} is a thermal state at the virtual temperature (6.1). Note that the density matrix ρ spans only the Hilbert space of the target system as $\{|0\rangle, |1\rangle\}$. The second term displays effective thermalisation performed by the virtual qubit. The steady state obtained from this effRME is given by

$$\rho_{\mathrm{ss}} = C\left(Q_{\mathrm{en}}\tau_{\mathrm{en}} + q_{\mathrm{vir}}\tau_{\mathrm{vir}}\right), \tag{6.13}$$

with the normalisation $C = (Q_{\mathrm{en}} + q_{\mathrm{vir}})^{-1}$. Comparison with the exact form (6.4) of the steady state leads to the derivation of the effective thermalisation rate q_{vir} of the virtual qubit, which is given by (note $Q_{1,2} \gg Q_{\mathrm{en}}, g$)

$$q_{\mathrm{vir}} = \frac{2g^2}{Q_1 + Q_2}\left(\tau_1^{\mathrm{g}}\tau_2^{\mathrm{e}} + \tau_1^{\mathrm{e}}\tau_2^{\mathrm{g}}\right). \tag{6.14}$$

It it worth discussing the temperature dependency. Note that the the ground state and the excited state of the virtual qubit are $|0\rangle_1 |1\rangle_2$ and $|1\rangle_1 |0\rangle_2$, respectively, therefore I denote the norm of the virtual qubit,

$$n_{\mathrm{vir}} = \tau_1^{\mathrm{g}}\tau_2^{\mathrm{e}} + \tau_1^{\mathrm{e}}\tau_2^{\mathrm{g}}. \tag{6.15}$$

In other words, the temperature dependency of q_{vir} originates from the norm n_{vir}. This is expected since the space of the virtual qubit is traced out when deriving the effRME (6.12) from the original RME (6.2).

6.2 Three-level system coupled to three two-qubit machines

In this section, I simplify a higher-dimensional system by applying the idea of the virtual qubit. Let me consider a three-level system with the energy spacing $\omega_{0,1,2}$ as a target system, while I study n-level systems at the end of this chapter. The target system is coupled to a few two-qubit machines, each of which can be regarded as a virtual qubit. With one machine coupled to the target system, the situation is essentially the same as the qubit target case shown in Fig. 6.1 and discussed in the previous section. With two machines coupled, two thermalisation processes exist at different levels in the target system, and the steady state turns out not to become a Gibbs state unless both of the virtual temperature are the same. For instance, if a machine with virtual temperature T_{v1} is coupled to the levels of $|0\rangle$ and $|1\rangle$, and another one with virtual temperature T_{v2} is coupled to the levels of $|0\rangle$ and $|2\rangle$, the steady state is written as $\rho_{\mathrm{ss}} = C\left(|0\rangle\langle 0| + \mathrm{e}^{-(\omega_1-\omega_0)/T_{\mathrm{v1}}}|1\rangle\langle 1| + \mathrm{e}^{-(\omega_2-\omega_0)/T_{\mathrm{v2}}}|2\rangle\langle 2|\right)$, with the normalisation $C = (1+\mathrm{e}^{-(\omega_1-\omega_0)/T_{\mathrm{v1}}}+\mathrm{e}^{-(\omega_2-\omega_0)/T_{\mathrm{v2}}})^{-1}$. As seen, these two thermalisation processes do not compete, and the population in each level is characterised by each of the virtual temperatures T_{v1} and T_{v2}. On the other hand, with all the levels occupied by three machines as shown in the right panel in Fig. 6.2, the three thermalisation processes compete unless all the virtual temperatures are equal.

Below, I use the idea of the virtual qubit to build an effRME as done for the qubit target system. To explore the parameter dependency of the effective rates, I discuss the steady state of the effRME and compare it with that of the full RME and the Gorini-Kossakowski-Lindblad-Sudarshan master equation (GKLSME) as two non-exclusive physical models for corresponding machine setup. At the end of this section, I study these models' relations to the effRME.

6.2.1 Effective reset master equation (effRME)

I consider a three-level system, called qutrit, coherently coupled to three pairs of two physical qubits, as represented in Fig. 6.2. I label as "A" the pair coupled to the levels of $|0\rangle$ and $|1\rangle$, as "B" the pair coupled to the levels of $|0\rangle$ and $|2\rangle$, and as "C" the pair coupled to the levels of $|1\rangle$ and $|2\rangle$. Each of the pairs contains two qubits with energy spacings Ω_{j1} and Ω_{j2}, and the qubits are in contact with baths whose temperatures are T_{j1} and T_{j2}, respectively, for $j \in \{\mathrm{A}, \mathrm{B}, \mathrm{C}\}$. Also, because of energy conservation, the energy spacings are restricted as $\omega_1 - \omega_0 = \Omega_{\mathrm{A1}} - \Omega_{\mathrm{A2}}$, $\omega_2 - \omega_0 = \Omega_{\mathrm{B1}} - \Omega_{\mathrm{B2}}$, and $\omega_2 - \omega_1 = \Omega_{\mathrm{C1}} - \Omega_{\mathrm{C2}}$.

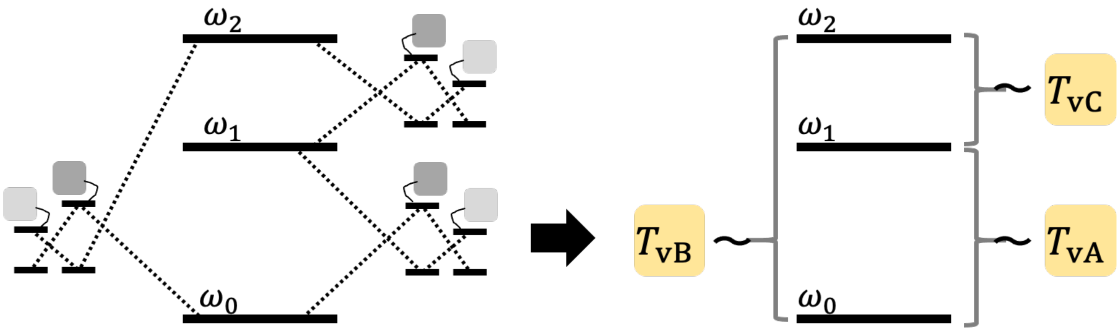

Figure 6.2: Simplification of two-qubit machines by using virtual qubits. Left: a qutrit coupled to three two-qubit machines. The dotted lines represent coherent interactions. Right: the qutrit with all the two-qubit machines simplified to be baths at their virtual temperatures.

Here, I assume that the thermalisation of the qubits inside the two-qubit machines is fast enough that the concept of the virtual temperatures is valid. The effRME of the target system is then given by

$$\frac{\partial \rho}{\partial t} = \sum_{j \in \{\mathrm{A,B,C}\}} q_j \left(\tau_j \otimes \mathrm{Tr}_j[\rho] - \rho \right), \tag{6.16}$$

where $q_{\mathrm{A,B,C}}$ is the effective thermalisation rate and $\mathrm{Tr}_{\mathrm{A,B,C}}$ represents partial tracing out the space of the qubit pair A, B, C. The states $\tau_{\mathrm{A,B,C}}$ represent thermal states at the virtual temperatures $T_{\mathrm{vA,vB,vC}}$, respectively, each of which is given by

$$T_{\mathrm{v}j} = \frac{\Omega_{j1} - \Omega_{j2}}{\Omega_{j1}/T_{j1} - \Omega_{j2}/T_2}. \tag{6.17}$$

The thermal states $\tau_{\mathrm{A,B,C}}$ are written as $\tau_{\mathrm{A}} = \tau_{\mathrm{A}}^{\mathrm{g}} |0\rangle\langle 0| + \tau_{\mathrm{A}}^{\mathrm{e}} |1\rangle\langle 1|$, $\tau_{\mathrm{B}} = \tau_{\mathrm{B}}^{\mathrm{g}} |0\rangle\langle 0| + \tau_{\mathrm{B}}^{\mathrm{e}} |2\rangle\langle 2|$, and $\tau_{\mathrm{C}} = \tau_{\mathrm{C}}^{\mathrm{g}} |1\rangle\langle 1| + \tau_{\mathrm{C}}^{\mathrm{e}} |2\rangle\langle 2|$, respectively, where $\tau_j^{\mathrm{g,e}}$ are the population of the ground and excited states. By solving the effRME (6.16) for $\partial\rho/\partial t = 0$, the steady state of the target system can be found as

$$\rho_{\mathrm{ss}} = C \left(q_{\mathrm{A}} q_{\mathrm{B}} \tau_{\mathrm{AB}} + q_{\mathrm{B}} q_{\mathrm{C}} \tau_{\mathrm{BC}} + q_{\mathrm{C}} q_{\mathrm{A}} \tau_{\mathrm{CA}} \right), \tag{6.18}$$

where the normalisation is $C = (q_{\mathrm{A}} q_{\mathrm{B}} \mathrm{Tr}[\tau_{\mathrm{AB}}] + q_{\mathrm{B}} q_{\mathrm{C}} \mathrm{Tr}[\tau_{\mathrm{BC}}] + q_{\mathrm{C}} q_{\mathrm{A}} \mathrm{Tr}[\tau_{\mathrm{CA}}])^{-1}$, and $\tau_{\mathrm{AB,BC,CA}}$ are the steady states with only two of the coherent couplings. They are written as

$$\tau_{\mathrm{AB}} = \tau_{\mathrm{A}}^{\mathrm{g}} \tau_{\mathrm{B}}^{\mathrm{g}} |0\rangle\langle 0| + \tau_{\mathrm{A}}^{\mathrm{e}} \tau_{\mathrm{B}}^{\mathrm{g}} |1\rangle\langle 1| + \tau_{\mathrm{A}}^{\mathrm{g}} \tau_{\mathrm{B}}^{\mathrm{e}} |2\rangle\langle 2|, \tag{6.19a}$$

$$\tau_{\mathrm{BC}} = \tau_{\mathrm{B}}^{\mathrm{g}} \tau_{\mathrm{C}}^{\mathrm{e}} |0\rangle\langle 0| + \tau_{\mathrm{B}}^{\mathrm{e}} \tau_{\mathrm{C}}^{\mathrm{g}} |1\rangle\langle 1| + \tau_{\mathrm{B}}^{\mathrm{e}} \tau_{\mathrm{C}}^{\mathrm{e}} |2\rangle\langle 2|, \tag{6.19b}$$

$$\tau_{\mathrm{CA}} = \tau_{\mathrm{C}}^{\mathrm{g}} \tau_{\mathrm{A}}^{\mathrm{g}} |0\rangle\langle 0| + \tau_{\mathrm{C}}^{\mathrm{g}} \tau_{\mathrm{A}}^{\mathrm{e}} |1\rangle\langle 1| + \tau_{\mathrm{C}}^{\mathrm{e}} \tau_{\mathrm{A}}^{\mathrm{g}} |2\rangle\langle 2|. \tag{6.19c}$$

Note that the above states are not normalised on purpose, i.e. $\mathrm{Tr}[\tau_{\mathrm{AB}}] \neq 1$, $\mathrm{Tr}[\tau_{\mathrm{BC}}] \neq 1$, and $\mathrm{Tr}[\tau_{\mathrm{CA}}] \neq 1$. It is worth clarifying that the steady state (6.18) is a combination of the steady states in cases where only two of the coherent couplings are present.

6.2.2 Reset master equation (RME)

Below I discuss the RME and compare the steady state of this model with the steady state (6.18) of the effRME. The RME describing the whole system is provided by

$$\frac{\partial \rho_{\mathrm{tot}}}{\partial t} = -i\left[H, \rho_{\mathrm{tot}}\right] + \sum_{j\in\mathcal{J}} Q_j\left(\tau_j \otimes \mathrm{Tr}_j[\rho_{\mathrm{tot}}] - \rho_{\mathrm{tot}}\right) \tag{6.20}$$

with Q_j being the thermalisation rate for $\mathcal{J} = \{\mathrm{A1}, \mathrm{A2}, \mathrm{B1}, \mathrm{B2}, \mathrm{C1}, \mathrm{C2}\}$. The Hamiltonian is given by

$$\begin{aligned} H = &\sum_{k=0}^{2} \omega_k \left|k\right\rangle\!\left\langle k\right| + \sum_{j\in\mathcal{J}} \Omega_j \sigma_j^+ \sigma_j^- \\ &+ \left[g_{\mathrm{A}} \left|0\right\rangle\!\left\langle 1\right| \sigma_{\mathrm{A1}}^+ \sigma_{\mathrm{A2}}^- + g_{\mathrm{B}} \left|0\right\rangle\!\left\langle 2\right| \sigma_{\mathrm{B1}}^+ \sigma_{\mathrm{B2}}^- + g_{\mathrm{C}} \left|1\right\rangle\!\left\langle 2\right| \sigma_{\mathrm{C1}}^+ \sigma_{\mathrm{C2}}^- + \mathrm{h.c.}\right] \end{aligned} \tag{6.21}$$

with $g_{\mathrm{A,B,C}}$ being the coupling strengths to each of the subsystems and the qubit frequencies being $\Omega_{\mathrm{A2}} = \Omega_{\mathrm{A1}} - (\omega_1 - \omega_0)$, $\Omega_{\mathrm{B2}} = \Omega_{\mathrm{B1}} - (\omega_2 - \omega_0)$, $\Omega_{\mathrm{C2}} = \Omega_{\mathrm{C1}} - (\omega_2 - \omega_1)$. Although the solution of $\partial \rho_{\mathrm{tot}}/\partial t = 0$ describes the steady state of the whole system, it is difficult to find an analytical solution due to the size of the system, which is $3 \times 2^2 \times 2^2 \times 2^2 = 192$. Note that the RME takes the joint system into account, whereas the effRME considers only the target system. Certainly, it is possible to numerically solve $\partial \rho_{\mathrm{tot}}/\partial t = 0$, but it is hard to understand what feature the steady state displays physically and what kind of parameters characterise the steady state. Therefore, the effRME is a useful tool to study such complicated systems.

To characterise the effective thermalisation rates $q_{\mathrm{A,B,C}}$, I numerically calculate the steady-state solution of the RME (6.20). Here, $\omega_0 = 0$ is taken, and the energy unit is set as half of the energy gap between the ground and first excited states of the qutrit, $(\omega_1 - \omega_0)/2 = \omega_1/2 = 1$. Also, a parameter regime is considered where the thermalisation rates $\{Q_i\}$ are larger than any other energy scales such that the virtual temperatures are effectively valid. By finding the population at each level in the RME solution corresponding to the effRME solution (6.18), I have obtained the parameter dependency of the effective thermalisation rates $q_{\mathrm{A,B,C}}$. Assuming that all the two-qubit machines have the same set of the bath temperatures so that $T_{j1} = T_{\mathrm{h}}$ and $T_{j2} = T_{\mathrm{c}}$ for $j \in \{\mathrm{A}, \mathrm{B}, \mathrm{C}\}$ in the numerical simulations, I plot the ratios of the effective thermalisation rates $q_{\mathrm{A,B,C}}$ as a function of the coherent interaction strength g_{B} and the hot bath temperature T_{h} (see Fig. 6.3). It is observed that the ratio q_i/q_j is in proportion to g_i^2/g_j^2 for $i, j \in \{\mathrm{A}, \mathrm{B}, \mathrm{C}\}$ and that the T_{h}-dependency of the ratio q_i/q_j agrees with the norm of the virtual qubits, similar to what was done in Eq. (6.15), which allows me to write

$$n_j = \tau_{j1}^{\mathrm{g}} \tau_{j2}^{\mathrm{e}} + \tau_{j1}^{\mathrm{e}} \tau_{j2}^{\mathrm{g}}. \tag{6.22}$$

These parameter dependencies are consistent with the effective thermalisation rate (6.14) in the cases of the qubit target.

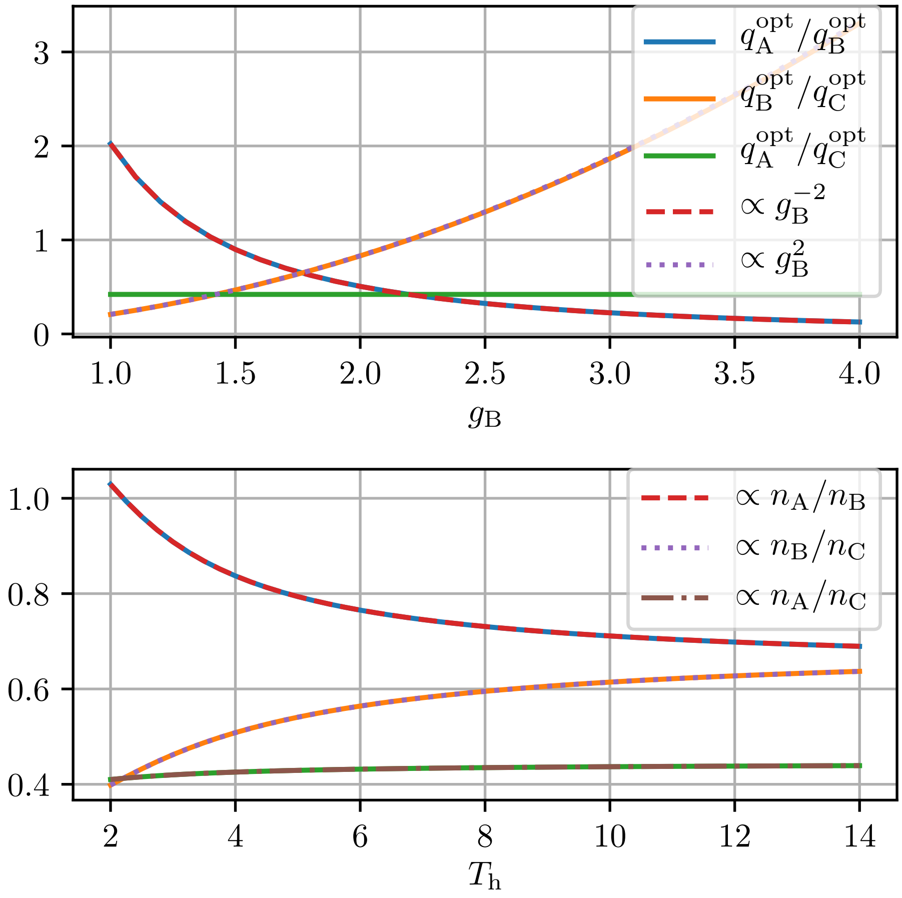

Figure 6.3: Optimal coupling coefficient rates between the target qutrit and the auxiliary qubits for which the state (6.18) is the steady-state solution of the RME (6.20) as a function of coherent interaction strength g_B (upper panel) and bath temperature $T_{j1} = T_h$ (lower panel). In the upper panel, the ratio q_A/q_B is proportional to $1/g_B^2$, and the ratio q_B/q_C is proportional to g_B^2. In the lower panel, the ratios q_i/q_j are proportional to the ratios n_i/n_j of the norms (6.22) of the virtual qubits for $i, j \in \{A, B, C\}$. I take $\omega_0 = 0$, and the energy unit is set as $(\omega_1 - \omega_0)/2 = \omega_1/2 = 1$. Both plots use the same parameter set, except for $T_{j1} = T_h = 3.1$ in the upper panel and $g_B = 1.5$ in the lower panel. Apart from the two parameters, the following is used: $\omega_2 = 3$, $\Omega_{A1} = 2.5$, $\Omega_{B1} = 4.5$, $\Omega_{C1} = 1.3$, $g_A = 1.2$, $g_C = 1.8$, $T_{j1} = T_h = 3.1$, $T_{j2} = T_c = 1.2$, $Q_{j1} = 70$, and $Q_{j2} = 50$ for $j \in \{A, B, C\}$.

6.2.3 Gorini-Kossakowski-Lindblad-Sudarshan master equation (GKLSME)

In the preceding sections, the idea of the virtual qubit is used to replace the full RME (6.20), which governs the composite system composed of the target qutrit and the six physical qubits (plus the thermalisation rates $\{Q_j\}$), with an effRME (6.16) which spans only the space of the target system, i.e. simply Eq. (6.20) is replaced with Eq. (6.16). In general, the mapping of the rates $\{Q_j\} \mapsto \{q_j\}$ is complicated. Nevertheless, it is found that the analytical relation (6.14) for the case of a target qubit, such as the dependency on interaction g and the hot temperature T_{h}, is reproduced for the case of a target qutrit as seen in Fig. 6.3.

The description of the physical system which the effRME (6.20) provides is not unique but dependent on the concrete physical setup. Also, the RME (6.20) is rather an ah-hoc model in a sense that it does not describe some physical interaction with the environment but rather a probabilistic swapping with a thermal state whose temperature corresponds to that of the environment [130]. Nevertheless, due to its CPTP (completely positive and trace-preserving) behaviour, the RME can be mapped into a GKLSME, known from conventional thermalisation models [244, 330, 331]. Generally, this mapping is an intricate function of the parameters such as the bath temperatures and can be explicitly derived in some special cases [332]. Furthermore, it is shown that by implementing the mapping from the RME to a GKLSME, the spontaneous emission rates Γ_j in the GKLSME (see below) must have a temperature-dependence. This is a feature that is not usually seen in GKLSMEs [244].

On the other hand, one can take the mapping the other way around, i.e. formulate the original system in terms of a GKLSME with independent rates Γ_j and cast it onto a "full" RME. Therefore, the rates Q_j in the RME become functions of the parameters. Thus, the temperature dependence of the effective rates q_j in the effRME does not correspond to the norm of the virtual qubits but contains additional terms. A question of which model is favourable, RME or GKLSME, depends on what parameters can be tuned in an actual system. I will come back to this discussion in the next section. In this section, I start with the GKLSME and reveal the dependency of the q_j on the parameters.

The GKLSME where a target qutrit is coupled to six physical qubits can be written as

$$\dot{\rho}_{\mathrm{tot}} = -i[H, \rho_{\mathrm{tot}}] + \sum_{j\in\mathcal{J}} \mathcal{L}_j \rho_{\mathrm{tot}}, \tag{6.23}$$

with the Hamiltonian (6.21) and the qubits $\mathcal{J} = \{\mathrm{A1}, \mathrm{A2}, \mathrm{B1}, \mathrm{B2}, \mathrm{C1}, \mathrm{C2}\}$. The Liouvillian

$$\mathcal{L}_j \rho = \Gamma_j(\bar{n}(\Omega_j, T_j) + 1)\mathcal{D}[\sigma_j^-] + \Gamma_j \bar{n}(\Omega_j, T_j)\mathcal{D}[\sigma_j^+], \tag{6.24}$$

describes the dissipative interaction of the jth auxiliary qubit with its bath (see also Fig. 6.1) at temperature $T_{j1} = T_{\mathrm{h}}$ and $T_{j2} = T_{\mathrm{c}}$ for $j \in \{\mathrm{A}, \mathrm{B}, \mathrm{C}\}$, respectively. Also, Γ_j is the jth qubit's spontaneous emission rate. I define the thermal population $\bar{n}(\omega, T) = [\exp(\omega/T) - 1]^{-1}$ of the bosonic bath and the dissipator $D[A] = 2A\rho A^\dagger - A^\dagger A\rho - \rho A^\dagger A$. Here, I consider mapping this equation to the effRME (6.16) and discuss how the effective rates $q_{\mathrm{A}}, q_{\mathrm{B}}, q_{\mathrm{C}}$ are related to the parameters of the GKLSME (6.23). To this end, one can integrate the GKLSME (6.23) for given parameters and set the analytical steady-state solution (6.18) as the initial state of the target state, while the qubits inside the machines are initialised to their respective thermal states. One can repeat this integration to minimise the Frobenius norm $\|\rho(t) - \rho(0)\|$ between the reduced density matrix of the qutrit at time t and the initial one for a sufficiently large fixed time $t > 0$. The Frobenius norm is given by

$$\|\rho(t) - \rho(0)\| = \sqrt{\mathrm{Tr}\left[(\rho(t) - \rho(0))^* \left(\rho(t) - \rho(0)\right)\right]}, \tag{6.25}$$

and quantifies the deviation of the time-evolved state and the initial state. Since the initial state is given by the steady state (6.18) and characterised with the effective rates $\{q_{\mathrm{A}}, q_{\mathrm{B}}, q_{\mathrm{C}}\}$, one can find the optimal parameter set $\{q_{\mathrm{A}}^{\mathrm{opt}}, q_{\mathrm{B}}^{\mathrm{opt}}, q_{\mathrm{C}}^{\mathrm{opt}}\}$ where the steady state (6.18) becomes the steady state solution of the RME (6.20) when the Frobenius norm $\|\rho(t) - \rho(0)\|$ is close to zero. Figure 6.4 shows the dependence of the effective rates q_j made by repeating this procedure for different hot temperatures T_{h} and interaction strengths g_{B}.

As shown in the upper panel in Fig. 6.4, the effective rates have the quadratic relation to the interaction strength,

$$\frac{q_i^{\mathrm{opt}}}{q_j^{\mathrm{opt}}} \propto \frac{g_i^2}{g_j^2} \text{ for } i, j \in \{\mathrm{A}, \mathrm{B}, \mathrm{C}\}, \tag{6.26}$$

which is also observed in the RME (see Fig. 6.3). One can confirm the same behaviour for varying g_{A} or g_{C}. Furthermore, as expected, the temperature dependence does not agree with the norm of the virtual qubits, which will be discussed more in the next section.

The simulations shown in Fig. 6.3 were implemented with the QuantumOptics.jl [333] Julia framework, and Optim.jl [334] was used for the numerical optimisation procedure.

6.2.4 Discussion and identifying the "knobs"

The system setup considered has an excess of parameters that characterise the system. Therefore, it is a question how the parameters influence the steady-state solution of the target qutrit. What Secs. 6.2.2 and 6.2.3 have shown is that the temperature dependence of the effective rates differs in the description of the system. In the RME, the temperature dependence corresponds to the norm of the virtual qubits, while in the GKLSME it does not. I address a question of why this occurs in the rest of this section.

First, note that in the RME the thermalisation rates Q_j for the physical qubits are supposed to be independent parameters, and the temperature dependence in the effective rates q_j^{opt} comes from the norm (6.15) only. Therefore, the mapped GKLSME from the RME has temperature-dependent spontaneous emission rates. On the other hand, in Sec. 6.2.3, I considered independent spontaneous emission rates. Thus, the temperature dependence differs in Figs. 6.3 and 6.4.

Surely, the RME can be cast onto the GKLSME form, but the parameter dependency in the mapped GKLSME form is not the same as for the usual GKLSMEs. More

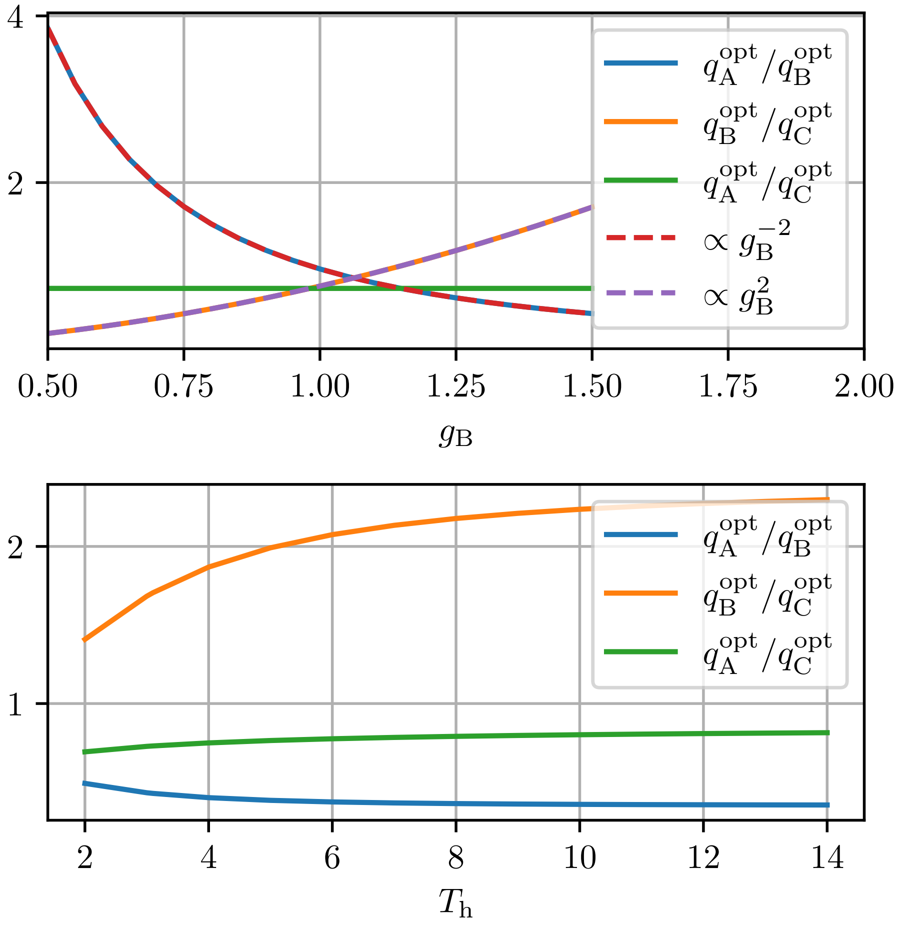

Figure 6.4: Optimal rates of the effRME (6.16) for which the state (6.18) is the steady-state solution of the GKLSME (6.23) as a function of the coherent coupling strength g_{B} (upper panel) and the hot bath temperature T_{h} (lower panel). I take $\omega_0 = 0$, and the energy unit is set as $(\omega_1 - \omega_0)/2 = \omega_1/2 = 1$. In the upper panel, $T_{\mathrm{h}} = 3.1$ is used, and in the lower panel, $g_{\mathrm{B}} = 1.5$ is used while the other parameters are the same: $\omega_0 = 0$, $\omega_1 = 2$, $\omega_2 = 3$, $g_{\mathrm{A}} = 1.2$, $g_{\mathrm{C}} = 1.8$, $\Omega_{\mathrm{A}1} = 2.5$, $\Omega_{\mathrm{B}1} = 4.5$, $\Omega_{\mathrm{C}1} = 1.3$, $T_{\mathrm{c}} = 1.2$, $\Gamma_{j2} = 50$ and $\Gamma_{j1} = 70$ for $j \in \{\mathrm{A}, \mathrm{B}, \mathrm{C}\}$, and $t = 10$.

specifically, the decay rates Γ_j do not depend on the temperatures [244], but the rates in the mapped GKLSME from the RME do, similar to Ref. [332]. Thus, the temperature dependence in the steady-state solution is determined by whether the $\{Q_j\}$ or the $\{\Gamma_j\}$ are defined as a set of independent parameters. I note that although the $\{\Gamma_j\}$ in the GKLSME description depend on the frequencies of the system [244], I still assume the $\{\Gamma_j\}$ to be independent since the dependency can be cancelled, e.g. by tuning the dipole moment of the qubit. In contrast, the same interaction dependence is seen in both of the models, the RME and the GKLSME, as shown in Figs. 6.3 and 6.4.

Let me re-emphasise what is discussed above. It is crucial to distinguish between the two models,

- RME with "free" Q_j
- GKLSME with "free" Γ_j

and also which mapping is used, from the RME to the GKLSME or the other way around. Therefore, the "knobs" to control the system are determined by which description governs the system. Both of the models have their respective pros and cons, depending on the actual setups.

6.3 Implementation: Improving a laser with population inversion

As an example of an application using the findings of this work, I propose a scheme to increase the output of a three-level laser by coupling it with two two-qubit machines. First, let me show a typical lasing mechanism [106, 335, 336] (see Fig. 6.5(a)). The laser consists of a three-level system in contact with a hot bath at temperature T_h and cold bath at temperature T_c. As the outcome of the laser is determined by the population ratio between the levels $|1\rangle$ and $|0\rangle$, one wants to increase the hot-bath temperature T_h and decrease the cold-bath temperature T_c in order to increase the population ratio: the optimal set is $T_\mathrm{h} \to \infty$ and $T_\mathrm{c} \to 0$. Below, I show that the population ratio can be increased by using two-qubit machines containing the hot and cold baths instead of attaching the baths directly to the three-level system.

First, I replace the hot bath coupled to the three-level system with a two-qubit machine whose virtual temperature is given by (cf. Eq. (6.17))

$$T_\mathrm{vB} = \frac{\Omega_\mathrm{B1} - \Omega_\mathrm{B2}}{\Omega_\mathrm{B1}/T_\mathrm{h} - \Omega_\mathrm{B2}/T_\mathrm{c}}, \tag{6.27}$$

where $\Omega_\mathrm{B2} = \Omega_\mathrm{B1} - (\omega_2 - \omega_0)$. Here, for a fair comparison, the hot- and cold-bath temperatures $T_\mathrm{h,c}$ used for the laser are also used for the two-qubit machine. For $T_\mathrm{h} > (\Omega_\mathrm{B1}/\Omega_\mathrm{B2})T_\mathrm{c}$, the virtual temperature T_vB is negative and causes population inversion between the levels $|2\rangle$ and $|0\rangle$ (see Fig. 6.5(b)), which is never observed by attaching real baths. This population inversion results in an increase of the population ratio between $|1\rangle$ and $|0\rangle$, and leads to better performance of the laser.

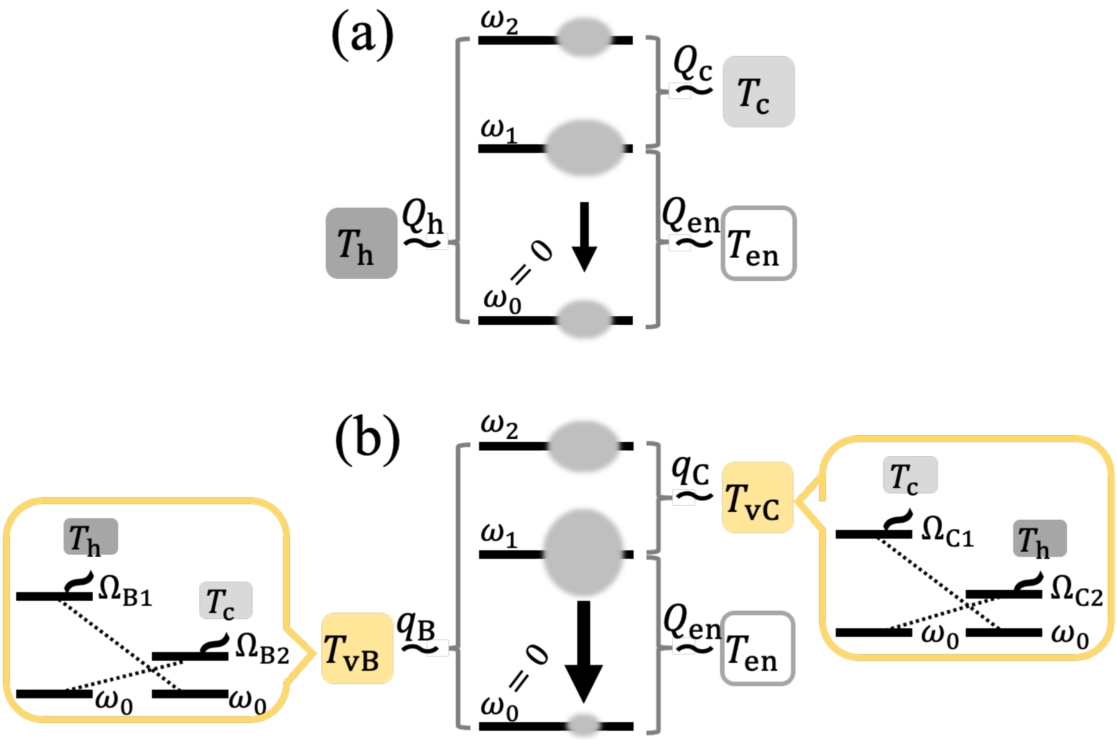

Figure 6.5: Sketches of (a) a typical laser mechanism with $T_{\rm h}$ being the hot-bath temperature and $T_{\rm c}$ being the cold-bath temperature, and (b) the proposed scheme improved by virtual temperatures, where $T_{\rm vB}$ [Eq. (6.27)] is negative and $T_{\rm vC}$ [Eq. (6.28)] is smaller than $T_{\rm c}$. The oval on each qutrit level represents this level's population. The lasing transition is also coupled to an environment at temperature $T_{\rm en}$.

Furthermore, the laser can be better by replacing the cold bath with another two-qubit machine whose virtual temperature is given by

$$T_{\mathrm{vC}} = \frac{\Omega_{\mathrm{C1}} - \Omega_{\mathrm{C2}}}{\Omega_{\mathrm{C1}}/T_{\mathrm{c}} - \Omega_{\mathrm{C2}}/T_{\mathrm{h}}} \,. \tag{6.28}$$

Note that the hot- and cold-bath temperatures are switched in comparison with T_{vB} in Eq. (6.27). Since $T_{\mathrm{h}} > T_{\mathrm{c}}$ and $\Omega_{\mathrm{C2}} = \Omega_{\mathrm{C1}} - (\omega_2 - \omega_1)$, T_{vC} is always lower than T_{c}.

Therefore, the ratio between the population p_1 at $|1\rangle$ and p_0 at $|0\rangle$ can be larger than that of the typical laser for $T_{\mathrm{h}} > (\Omega_{\mathrm{B1}}/\Omega_{\mathrm{B2}})T_{\mathrm{c}}$. This is shown in Fig. 6.6, where the population ratio p_1/p_0 is plotted as a function of T_{h} for a chosen parameter set (see the dashed lines). For the ideal cases where the lasing transition is not disturbed by environments (let me call these cases "lossless"), the optimal population inversion occurs for $T_{\mathrm{vB}} \to -0$ and $T_{\mathrm{vC}} \to +0$. Recall that the optimal parameter set for the typical laser is $T_{\mathrm{h}} \to \infty$ and $T_{\mathrm{c}} \to 0$. By tuning the bath temperatures as well as the energy spacings $\Omega_{\mathrm{B1,C1}}$, the virtual temperatures $T_{\mathrm{vB,vC}}$ can approach the optimal values.

Let me next consider more realistic cases where photon losses are caused through an additional environment at temperature T_{en}. This environment disturbs the lasing transition, and the additional coupling Q_{en} to the environment competes with the effective rates of the machines. That is, the steady state of the three-level system depends on the effective rates and the additional coupling. Thus, the optimal parameter set in this case is not the same as the lossless case anymore. Let me show this in details. By analogy with Eq. (6.18), the steady state of the three-level system in the proposed scheme is written as

$$\rho_{\mathrm{ss}} \propto \left(Q_{\mathrm{en}}\, q_{\mathrm{B}}\, \tau_{\mathrm{enB}} + q_{\mathrm{B}}\, q_{\mathrm{C}}\, \tau_{\mathrm{BC}} + q_{\mathrm{C}}\, Q_{\mathrm{en}}\, \tau_{\mathrm{Cen}}\right). \tag{6.29}$$

The states $\tau_{\mathrm{enB,BC,Cen}}$ are obtained on analogy to Eqs. (6.19). As shown in Figs. 6.3 and 6.4, the effective rates $q_{\mathrm{B,C}}$ depend on the parameters involved with the two-qubit machines. Thus, for example by tuning the bath temperatures $T_{\mathrm{h,c}}$ to adjust the virtual temperatures $T_{\mathrm{vB,vC}}$, the effective rates $q_{\mathrm{B,C}}$ also change. On the other hand, for the typical laser setup where the hot and cold baths are attached directly, the steady state becomes

$$\rho_{\mathrm{ss}} \propto \left(Q_{\mathrm{en}}\, Q_{\mathrm{h}}\, \tau_{\mathrm{enh}} + Q_{\mathrm{h}}\, Q_{\mathrm{c}}\, \tau_{\mathrm{hc}} + Q_{\mathrm{c}}\, Q_{\mathrm{en}}\, \tau_{\mathrm{cen}}\right), \tag{6.30}$$

where it is assumed that $Q_{\mathrm{en,h,c}}$ are independent parameters.

To demonstrate that the proposed scheme can work better than the typical laser setup even in the realistic case (let me call it "lossy"), I show the dependence of the population ratio p_1/p_0 obtained from Eqs. (6.29) and (6.30) when changing the hot-bath temperature T_{h} with the other parameters fixed. For a fair comparison between the typical laser and the proposed scheme, I relate the couplings $Q_{\mathrm{h,c,en}}$ and the effective rates $q_{\mathrm{B,C}}$ as

$$q_{\mathrm{B}} = Q_{\mathrm{h}} n_{\mathrm{B}} \tag{6.31a}$$

$$q_{\mathrm{C}} = Q_{\mathrm{c}} n_{\mathrm{C}}, \tag{6.31b}$$

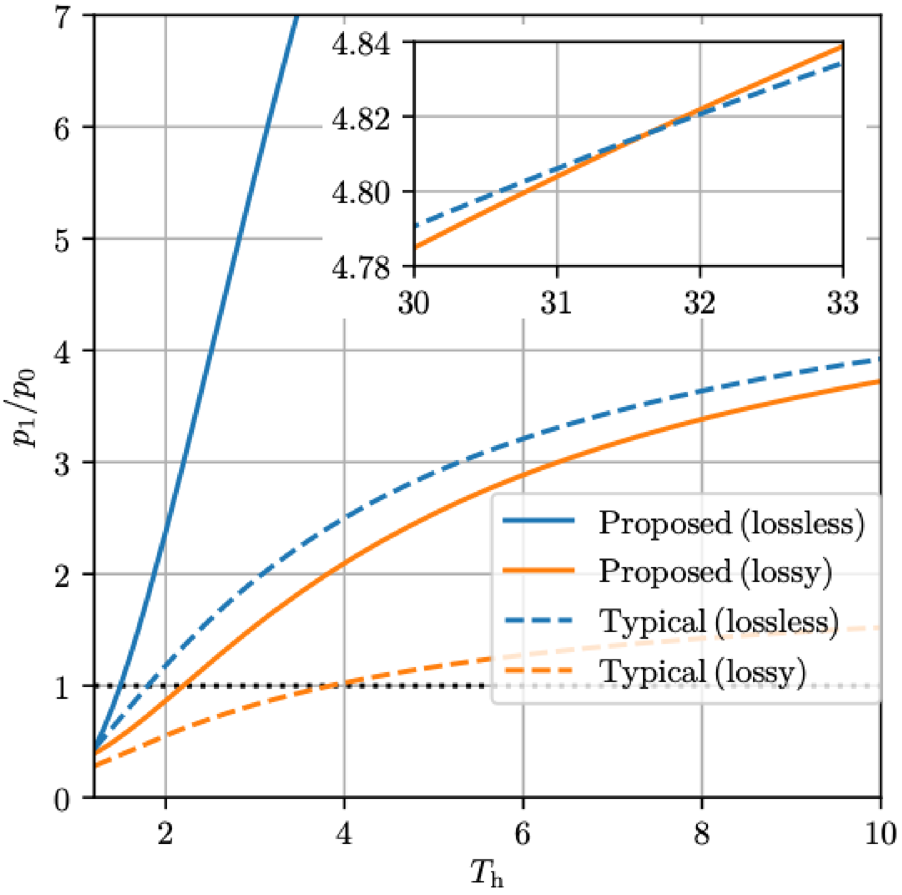

Figure 6.6: Population ratios p_1/p_0 of the levels $|1\rangle$ and $|0\rangle$ of the qutrit in the typical laser and in the proposed scheme when changing the hot temperature T_h. The population ratio p_1/p_0 is displayed in cases of the typical laser (directly coupled to the heat baths) and the proposed scheme (indirectly coupled to the baths via two-qubit machines that give rise to virtual temperatures) with and without photon loss. The dotted black line represents the lasing threshold $p_1/p_0 = 1$. "Lossless" ("lossy") means no (non-zero) photon loss. The inset zooms in on a regime that the proposed scheme with photon loss considered outperforms the lossless typical laser. The bath temperature and the thermalisation rate associated with loss of the laser output are assumed to be $T_\mathrm{en} = 7.2$ and $Q_\mathrm{en} = 0.1$. For the actual thermalisation rates, $Q_\mathrm{h} = 2$ and $Q_\mathrm{c} = 1.5$ are taken. The other parameters are the same as Figs. 6.3 and 6.4: $\omega_0 = 0$, $\omega_1 = 2$, $\omega_2 = 3$, $\Omega_\mathrm{B1} = 4.5$, $\Omega_\mathrm{C1} = 1.3$, $T_\mathrm{c} = 1.2$.

where the $n_{\mathrm{B,C}}$ are the norms (6.22) of the virtual qubits, since, as shown in Sec. 6.2.2, the temperature dependency of the effective rates are determined by the norms in the RME model. In other words, I assume that the details of the two-qubit machines can be described simply as Eqs. (6.31). Figure 6.6 shows that the setup containing the virtual qubits increases the lasing transition more than the typical laser (see the solid lines). For the chosen parameter set, the scheme considering photon loss outperforms the typical laser outcome even in the ideal case for $T_{\mathrm{h}} \gtrsim 32$ (see the inset). While I change T_{h} and fix the other parameters such as the qubit frequencies $\Omega_{\mathrm{B1,C1}}$, the lasing transition can be improved efficiently if the other parameters are also controlled.

6.4 Higher-dimensional target systems

Here, I move on to cases of higher-dimensional target systems. First, I reveal the steady-state solution of the effRME for n-level target systems. After that, I show details of the steady-state solution for $n = 4$ as an example.

6.4.1 Steady-state solution of n-level target system in the effRME

I discuss the steady state when a multi-level system is coupled to some two-qubit machines. For simplicity, let me stick to cases where all levels of the target are coupled to the machines without duplication. In these cases, for n-level target systems the number of the couplings is given by $\binom{n}{2} = n(n-1)/2$.

I generalise the effRME to n-level system cases. For distinct representation, I introduce a different notation of the coupling strength from that in Fig. 6.2. By defining $q_{k.l}$ as the thermalisation rate of the kth and lth levels ($k < l$), where the indices A, B, C in Fig. 6.2 correspond to $q_{0,1}$, $q_{0,2}$, and $q_{1,2}$, respectively, the effRME for n-level target system is described as

$$\frac{\partial \rho}{\partial t} = \sum_{l=1}^{n-1} \sum_{k=0}^{l-1} q_{k,l} \left(\tau_{k,l} \otimes \mathrm{Tr}_{k,l}[\rho] - \rho \right), \tag{6.32}$$

where $\tau_{k,l}$ is a thermal state at the virtual temperature associated with the kth and lth levels, and $\mathrm{Tr}_{k,l}$ traces out the space of the kth and lth levels. Here, off-diagonal terms in the density matrix can be ignored since in this model coherence cannot be created. Then, I simplify the equation as

$$\frac{\partial \rho}{\partial t} = \sum_{l=1}^{n-1} \sum_{k=0}^{l-1} q_{k,l} \left(-\tau^{\mathrm{e}}_{k,l} \rho^{(k)} + \tau^{\mathrm{g}}_{k,l} \rho^{(l)} \right) \left(|k\rangle\langle k| - |l\rangle\langle l| \right), \tag{6.33}$$

with $\rho^{(k)} = \langle k|\rho|k\rangle$ and always $k < l$. To obtain the steady-state solution, I solve $\partial \rho / \partial t = 0$, i.e.

$$\sum_{l=1}^{n-1} \sum_{k=0}^{l-1} C_{k,l} \left(|k\rangle\langle k| - |l\rangle\langle l| \right) = 0, \tag{6.34}$$

where $C_{k,l} = q_{k,l}\left(-\tau^{\mathrm{e}}_{k,l}\rho^{(k)} + \tau^{\mathrm{g}}_{k,l}\rho^{(l)}\right)$.

First, let me split the equation into two parts,

$$\sum_{l=1}^{n-1}\sum_{k=0}^{l-1} C_{k,l}\left|k\right\rangle\!\left\langle k\right| - \sum_{l=1}^{n-1}\sum_{k=0}^{l-1} C_{k,l}\left|l\right\rangle\!\left\langle l\right| = 0. \tag{6.35}$$

The first term can be written in a different form such as

$$\begin{aligned}\sum_{l=1}^{n-1}\sum_{k=0}^{l-1} C_{k,l}\left|k\right\rangle\!\left\langle k\right| &= \sum_{l=1}^{n-1} C_{0,l}\left|0\right\rangle\!\left\langle 0\right| + \sum_{l=2}^{n-1} C_{1,l}\left|1\right\rangle\!\left\langle 1\right| + \cdots + \sum_{l=n-1}^{n-1} C_{n-2,l}\left|n-2\right\rangle\!\left\langle n-2\right| \\ &= \sum_{s=0}^{n-2}\sum_{l=s+1}^{n-1} C_{s,l}\left|s\right\rangle\!\left\langle s\right| \\ &= \sum_{l=1}^{n-1} C_{0,l}\left|0\right\rangle\!\left\langle 0\right| + \sum_{s=1}^{n-2}\sum_{l=s+1}^{n-1} C_{s,l}\left|s\right\rangle\!\left\langle s\right|,\end{aligned} \tag{6.36}$$

and the second term can be rewritten as

$$\sum_{l=1}^{n-1}\sum_{k=0}^{l-1} C_{k,l}\left|l\right\rangle\!\left\langle l\right| = \sum_{l=1}^{n-2}\sum_{k=0}^{l-1} C_{k,l}\left|l\right\rangle\!\left\langle l\right| + \sum_{k=0}^{n-2} C_{k,n-1}\left|n-1\right\rangle\!\left\langle n-1\right|. \tag{6.37}$$

Therefore, the left hand side (l.h.s) of Eq. (6.35) is rewritten as

$$\begin{aligned}(\text{l.h.s}) &= \sum_{l=1}^{n-1} C_{0,l}\left|0\right\rangle\!\left\langle 0\right| - \sum_{k=0}^{n-2} C_{k,n-1}\left|n-1\right\rangle\!\left\langle n-1\right| \\ &\quad + \sum_{s=1}^{n-2}\sum_{l=s+1}^{n-1} C_{s,l}\left|s\right\rangle\!\left\langle s\right| - \sum_{l=1}^{n-2}\sum_{k=0}^{l-1} C_{k,l}\left|l\right\rangle\!\left\langle l\right| \\ &= \sum_{l=1}^{n-1} C_{0,l}\left|0\right\rangle\!\left\langle 0\right| - \sum_{k=0}^{n-2} C_{k,n-1}\left|n-1\right\rangle\!\left\langle n-1\right| \\ &\quad + \sum_{s=1}^{n-2}\left(\sum_{l=s+1}^{n-1} C_{s,l} - \sum_{k=0}^{s-1} C_{k,s}\right)\left|s\right\rangle\!\left\langle s\right|.\end{aligned} \tag{6.38}$$

Since all the terms in Eq. (6.35) are zero, n equations are obtained,

$$\sum_{l=s+1}^{n-1} C_{s,l} - \sum_{k=0}^{s-1} C_{k,s} = 0, \text{ for } \{1 \le k \le n-2 : \forall k \in \mathbb{Z}\}, \tag{6.39a}$$

$$\sum_{l=1}^{n-1} C_{0,l} = 0, \tag{6.39b}$$

$$\sum_{k=0}^{n-2} C_{k,n-1} = 0. \tag{6.39c}$$

The above equations can be written in a matrix form as

$$\mathbf{M}_n \vec{\rho}_{\rm ss} = \vec{0} \tag{6.40}$$

where $\vec{\rho}_{\rm ss} = (\rho_{\rm ss}^{(0)}, \rho_{\rm ss}^{(1)}, \ldots, \rho_{\rm ss}^{(n-1)})^T$ and $\mathbf{M}_n$ is a n-by-n matrix given by

$$\mathbf{M} = \begin{pmatrix} M_{0,0} & q_{0,1}\tau^{\rm g}_{0,1} & q_{0,2}\tau^{\rm g}_{0,2} & \cdots & q_{0,n-2}\tau^{\rm g}_{0,n-2} & q_{0,n-1}\tau^{\rm g}_{0,n-1} \\ q_{0,1}\tau^{\rm e}_{0,1} & M_{1,1} & q_{1,2}\tau^{\rm g}_{1,2} & \cdots & q_{1,n-2}\tau^{\rm g}_{1,n-2} & q_{1,n-1}\tau^{\rm g}_{1,n-1} \\ q_{0,2}\tau^{\rm e}_{0,2} & q_{1,2}\tau^{\rm e}_{1,2} & \ddots & \ddots & \vdots & \vdots \\ \vdots & \vdots & & & \vdots & \vdots \\ \vdots & \vdots & \ddots & \ddots & q_{n-3,n-2}\tau^{\rm g}_{n-3,n-2} & q_{n-3,n-1}\tau^{\rm g}_{n-3,n-1} \\ q_{0,n-2}\tau^{\rm e}_{0,n-2} & q_{1,n-2}\tau^{\rm e}_{1,n-2} & \cdots & q_{n-3,n-2}\tau^{\rm e}_{n-3,n-2} & M_{n-2,n-2} & q_{n-2,n-1}\tau^{\rm g}_{n-2,n-1} \\ q_{0,n-1}\tau^{\rm e}_{0,n-1} & q_{1,n-1}\tau^{\rm e}_{1,n-1} & \cdots & q_{n-3,n-1}\tau^{\rm e}_{n-3,n-1} & q_{n-2,n-1}\tau^{\rm e}_{n-2,n-1} & M_{n-1,n-1} \end{pmatrix} . \tag{6.41}$$

The diagonal terms are given by

$$M_{0,0} = -\sum_{s=1}^{n-1} q_{0,s}\tau^{\rm e}_{0,s} \ , \tag{6.42a}$$

$$M_{k,k} = -\left(\sum_{s=0}^{k-1} q_{s,k}\tau^{\rm g}_{s,k} + \sum_{s=k+1}^{n-1} q_{k,s}\tau^{\rm e}_{k,s}\right) \quad \text{for } 1 \leq k \leq n-2, \tag{6.42b}$$

$$M_{n-1,n-1} = -\sum_{s=0}^{n-2} q_{s,n-1}\tau^{\rm g}_{s,n-1} \ . \tag{6.42c}$$

Here, I add the normalisation constraint, $\text{Tr}[\rho_{\rm ss}] = 1$, into this simultaneous equation (6.40), and hence the total number of equations involved in the simultaneous equation is $(n+1)$. However, the number of the variables in $\vec{\rho}_{\rm ss}$ is n. This implies that there is one excess equation in the simultaneous equation. In fact, any equation written in Eq. (6.40) is dependent of other equations, (i.e. can be constructed from the rest of the equations). For example, the equation described by the first row in the matrix $\mathbf{M}$ is reproduced by taking a sum of the equations given by all other rows due to Eqs. (6.42) and multipying it by minus sign. Therefore, the removal of the first row from the matrix $\mathbf{M}$ poses no problem for solving the simultaneous equation. As below, I remove the first row and then add the normalisation constraint $\mathrm{Tr}[\rho_{\mathrm{ss}}] = 1$:

$$
\begin{aligned}
\mathbf{M}_n\vec{\rho}_{\mathrm{ss}} &= \begin{pmatrix}
M_{0,0} & q_{0,1}\tau^{\mathrm{g}}_{0,1} & \cdots & q_{0,n-2}\tau^{\mathrm{g}}_{0,n-2} & q_{0,n-1}\tau^{\mathrm{g}}_{0,n-1} \\
q_{0,1}\tau^{\mathrm{e}}_{0,1} & M_{1,1} & \cdots & q_{1,n-2}\tau^{\mathrm{g}}_{1,n-2} & q_{1,n-1}\tau^{\mathrm{g}}_{1,n-1} \\
q_{0,2}\tau^{\mathrm{e}}_{0,2} & q_{1,2}\tau^{\mathrm{e}}_{1,2} & \ddots & \vdots & \vdots \\
\vdots & \vdots & & \vdots & \vdots \\
\vdots & \vdots & \ddots & q_{n-3,n-2}\tau^{\mathrm{g}}_{n-3,n-2} & q_{n-3,n-1}\tau^{\mathrm{g}}_{n-3,n-1} \\
q_{0,n-2}\tau^{\mathrm{e}}_{0,n-2} & q_{1,n-2}\tau^{\mathrm{e}}_{1,n-2} & \cdots & M_{n-2,n-2} & q_{n-2,n-1}\tau^{\mathrm{g}}_{n-2,n-1} \\
q_{0,n-1}\tau^{\mathrm{e}}_{0,n-1} & q_{1,n-1}\tau^{\mathrm{e}}_{1,n-1} & \cdots & q_{n-2,n-1}\tau^{\mathrm{e}}_{n-2,n-1} & M_{n-1,n-1}
\end{pmatrix}
\begin{pmatrix}
\rho^{(0)}_{\mathrm{ss}} \\ \rho^{(1)}_{\mathrm{ss}} \\ \vdots \\ \vdots \\ \vdots \\ \vdots \\ \rho^{(n-1)}_{\mathrm{ss}}
\end{pmatrix} \\
&\rightarrow \begin{pmatrix}
0 & 0 & \cdots & 0 & 0 \\
q_{0,1}\tau^{\mathrm{e}}_{0,1} & M_{1,1} & \cdots & q_{1,n-2}\tau^{\mathrm{g}}_{1,n-2} & q_{1,n-1}\tau^{\mathrm{g}}_{1,n-1} \\
q_{0,2}\tau^{\mathrm{e}}_{0,2} & q_{1,2}\tau^{\mathrm{e}}_{1,2} & \ddots & \vdots & \vdots \\
\vdots & \vdots & & \vdots & \vdots \\
\vdots & \vdots & \ddots & q_{n-3,n-2}\tau^{\mathrm{g}}_{n-3,n-2} & q_{n-3,n-1}\tau^{\mathrm{g}}_{n-3,n-1} \\
q_{0,n-2}\tau^{\mathrm{e}}_{0,n-2} & q_{1,n-2}\tau^{\mathrm{e}}_{1,n-2} & \cdots & M_{n-2,n-2} & q_{n-2,n-1}\tau^{\mathrm{g}}_{n-2,n-1} \\
q_{0,n-1}\tau^{\mathrm{e}}_{0,n-1} & q_{1,n-1}\tau^{\mathrm{e}}_{1,n-1} & \cdots & q_{n-2,n-1}\tau^{\mathrm{e}}_{n-2,n-1} & M_{n-1,n-1}
\end{pmatrix}
\begin{pmatrix}
\rho^{(0)}_{\mathrm{ss}} \\ \rho^{(1)}_{\mathrm{ss}} \\ \vdots \\ \vdots \\ \vdots \\ \vdots \\ \rho^{(n-1)}_{\mathrm{ss}}
\end{pmatrix} \\
&\rightarrow \begin{pmatrix}
1 & 1 & \cdots & 1 & 1 \\
q_{0,1}\tau^{\mathrm{e}}_{0,1} & M_{1,1} & \cdots & q_{1,n-2}\tau^{\mathrm{g}}_{1,n-2} & q_{1,n-1}\tau^{\mathrm{g}}_{1,n-1} \\
q_{0,2}\tau^{\mathrm{e}}_{0,2} & q_{1,2}\tau^{\mathrm{e}}_{1,2} & \ddots & \vdots & \vdots \\
\vdots & \vdots & & \vdots & \vdots \\
\vdots & \vdots & \ddots & q_{n-3,n-2}\tau^{\mathrm{g}}_{n-3,n-2} & q_{n-3,n-1}\tau^{\mathrm{g}}_{n-3,n-1} \\
q_{0,n-2}\tau^{\mathrm{e}}_{0,n-2} & q_{1,n-2}\tau^{\mathrm{e}}_{1,n-2} & \cdots & M_{n-2,n-2} & q_{n-2,n-1}\tau^{\mathrm{g}}_{n-2,n-1} \\
q_{0,n-1}\tau^{\mathrm{e}}_{0,n-1} & q_{1,n-1}\tau^{\mathrm{e}}_{1,n-1} & \cdots & q_{n-2,n-1}\tau^{\mathrm{e}}_{n-2,n-1} & M_{n-1,n-1}
\end{pmatrix}
\begin{pmatrix}
\rho^{(0)}_{\mathrm{ss}} \\ \rho^{(1)}_{\mathrm{ss}} \\ \vdots \\ \vdots \\ \vdots \\ \vdots \\ \rho^{(n-1)}_{\mathrm{ss}}
\end{pmatrix} .
\end{aligned}
\tag{6.43}
$$

As a result, the full simultaneous equation becomes

$$
\mathbf{M}\begin{pmatrix}
\rho^{(0)}_{\mathrm{ss}} \\ \rho^{(1)}_{\mathrm{ss}} \\ \vdots \\ \rho^{(n-1)}_{\mathrm{ss}}
\end{pmatrix} = \begin{pmatrix} 1 \\ 0 \\ \vdots \\ 0 \end{pmatrix} , \tag{6.44}
$$

where the matrix $\mathbf{M}$ is now redefined as

$$\mathbf{M} = \begin{pmatrix} 1 & 1 & 1 & \cdots & 1 & 1 \\ q_{0,1}\tau^{\mathrm{e}}_{0,1} & M_{1,1} & q_{1,2}\tau^{\mathrm{g}}_{1,2} & \cdots & q_{1,n-2}\tau^{\mathrm{g}}_{1,n-2} & q_{1,n-1}\tau^{\mathrm{g}}_{1,n-1} \\ q_{0,2}\tau^{\mathrm{e}}_{0,2} & q_{1,2}\tau^{\mathrm{e}}_{1,2} & \ddots & \ddots & \vdots & \vdots \\ \vdots & \vdots & & & \vdots & \vdots \\ \vdots & \vdots & \ddots & \ddots & q_{n-3,n-2}\tau^{\mathrm{g}}_{n-3,n-2} & q_{n-3,n-1}\tau^{\mathrm{g}}_{n-3,n-1} \\ q_{0,n-2}\tau^{\mathrm{e}}_{0,n-2} & q_{1,n-2}\tau^{\mathrm{e}}_{1,n-2} & \cdots & q_{n-3,n-2}\tau^{\mathrm{e}}_{n-3,n-2} & M_{n-2,n-2} & q_{n-2,n-1}\tau^{\mathrm{g}}_{n-2,n-1} \\ q_{0,n-1}\tau^{\mathrm{e}}_{0,n-1} & q_{1,n-1}\tau^{\mathrm{e}}_{1,n-1} & \cdots & q_{n-3,n-1}\tau^{\mathrm{e}}_{n-3,n-1} & q_{n-2,n-1}\tau^{\mathrm{e}}_{n-2,n-1} & M_{n-1,n-1} \end{pmatrix}, \quad (6.45)$$

and the diagonal elements are given by Eqs. (6.42b) and (6.42c).

Let me distinguish the two cases where the matrix $\mathbf{M}$ is invertible and where it is not. In the latter case, the steady-state solution cannot be determined with the conditions I have. However, this issue can be avoided. For example, physically, this corresponds to the case where one machine is coupled to the levels $|0\rangle$ and $|1\rangle$ in a three-level system, and the population ratios between the levels $|0\rangle$ and $|2\rangle$ and between the levels $|1\rangle$ and $|2\rangle$ are not determined. In this case, the steady state cannot be defined rigorously, and this leads to nonexistence of inverse matrix of $\mathbf{M}$. If one sees this three-level system as a two-level system composed of the levels $|0\rangle$ and $|1\rangle$, the matrix $\mathbf{M}$ can become an invertible matrix.

Assuming that the matrix $\mathbf{M}$ is invertible, the solution $\vec{\rho}_{\mathrm{ss}}$ is given by

$$\vec{\rho}_{\mathrm{ss}} = \mathbf{M}^{-1} \begin{pmatrix} 1 \\ 0 \\ \vdots \\ 0 \end{pmatrix}. \quad (6.46)$$

According to Cramer's rule, the inverse matrix can be written as

$$\mathbf{M}^{-1} = \frac{1}{\det[\mathbf{M}]} \mathrm{adj}\,[\mathbf{M}], \quad (6.47)$$

where adj$[\mathbf{M}]$ is the adjugate of $\mathbf{M}$, given by adj$[\mathbf{M}] = [\{\Delta_{i,j}\}_{1\leq i,j\leq n}]^T$, i.e.

$$\mathrm{adj}[\mathbf{M}] = \begin{pmatrix} \Delta_{1,1} & \Delta_{2,1} & \cdots & \Delta_{n,1} \\ \Delta_{1,2} & \Delta_{2,2} & \cdots & \Delta_{n,2} \\ \vdots & \vdots & \ddots & \vdots \\ \Delta_{1,n} & \Delta_{2,n} & \cdots & \Delta_{n,n} \end{pmatrix}. \quad (6.48)$$

Here, $\Delta_{i,j}$ is a set of the cofactors of the matrix $\mathbf{M}$ and is defined as

$$\Delta_{i,j} = (-1)^{i+j} \begin{vmatrix} M_{0,0} & \cdots & M_{0,j-1} & M_{0,j+1} & \cdots & M_{0,n-1} \\ \vdots & \vdots & \vdots & \vdots & \vdots & \vdots \\ M_{i-1,0} & \cdots & M_{i-1,j-1} & M_{i-1,j+1} & \cdots & M_{i-1,n-1} \\ M_{i+1,0} & \cdots & M_{i+1,j-1} & M_{i+1,j+1} & \cdots & M_{i+1,n-1} \\ \vdots & \vdots & \vdots & \vdots & \vdots & \vdots \\ M_{n-1,0} & \cdots & M_{n-1,j-1} & M_{n-1,j+1} & \cdots & M_{n-1,n-1} \end{vmatrix} . \tag{6.49}$$

Furthermore, because of the mathematical properties of the determinant, one gets $\det[\mathbf{M}] = \sum_{s=1}^{n} \Delta_{1,s}$. The solution $\vec{\rho}_{\mathrm{ss}}$ then becomes

$$\vec{\rho}_{\mathrm{ss}} = \frac{1}{\sum_{s=1}^{n} \Delta_{1,s}} \begin{pmatrix} \Delta_{1,1} \\ \Delta_{1,2} \\ \vdots \\ \Delta_{1,n} \end{pmatrix} , \tag{6.50}$$

which is normalised as $\sum_{j=1}^{n} \rho_{\mathrm{ss}}^{(j)} = 1$ with $\rho_{\mathrm{ss}}^{(j)}$ being an element of the density matrix. In case of $n = 2$, the solution provides the thermal state associated with the virtual temperature, $\rho_{\mathrm{ss}} = (\tau_{0,1}^{\mathrm{g}}, \tau_{0,1}^{\mathrm{e}})^T$ as expected. In case of $n = 3$, the solution corresponds to Eq. (6.18).

6.4.2 Steady-state solution for $n = 4$

As an example, I consider cases of a four-level system being the target system and reveal what the steady state is. I note that the steady state (6.18) in the case of a qutrit being the target system is combined with another steady states where two pairs of levels are characterised by different temperatures, weighted with the effective rates q_j. Even for higher-dimensional systems, the same feature is observed as shown below. I imagine that one has a four-level system where each pair of energy levels is coupled to a two-qubit machine (in total the system is coupled to six machines). The steady-state solution turns out to be

$$\begin{aligned} \frac{\rho_{\mathrm{ss}}}{C} &= q_0^3 q_1^3 q_2^3 \; \tau_{012}^{333} \\ &+ q_0^3 q_1^3 q_0^2 \; \tau_{010}^{332} + q_0^3 q_1^3 q_1^2 \; \tau_{011}^{332} + q_0^3 q_2^3 q_0^1 \; \tau_{020}^{331} + q_0^3 q_2^3 q_1^2 \; \tau_{021}^{332} + q_1^3 q_2^3 q_0^1 \; \tau_{120}^{331} + q_1^3 q_2^3 q_0^2 \; \tau_{120}^{332} \\ &+ q_0^3 q_0^1 q_0^2 \; \tau_{000}^{312} + q_0^3 q_0^1 q_1^2 \; \tau_{001}^{312} + q_0^3 q_0^2 q_1^2 \; \tau_{001}^{322} + q_1^3 q_0^1 q_0^2 \; \tau_{100}^{312} + q_1^3 q_0^1 q_1^2 \; \tau_{101}^{312} + q_1^3 q_0^2 q_1^2 \; \tau_{101}^{322} \\ &+ q_2^3 q_0^1 q_0^2 \; \tau_{200}^{312} + q_2^3 q_0^1 q_1^2 \; \tau_{201}^{312} + q_2^3 q_0^2 q_1^2 \; \tau_{201}^{322} , \end{aligned} \tag{6.51}$$

where the normalisation C is given by the inverse of trace of the right hand side of Eq. (6.51), and 16 states such as τ_{012}^{333} in the solution are steady states in case of only three of the coherent couplings being present. For example,

$$\tau_{012}^{333} = \tau_{0,3}^{\mathrm{g}} \tau_{1,3}^{\mathrm{e}} \tau_{2,3}^{\mathrm{e}} \, |0\rangle\langle 0| + \tau_{0,3}^{\mathrm{e}} \tau_{1,3}^{\mathrm{g}} \tau_{2,3}^{\mathrm{e}} \, |1\rangle\langle 1| + \tau_{0,3}^{\mathrm{e}} \tau_{1,3}^{\mathrm{e}} \tau_{2,3}^{\mathrm{g}} \, |2\rangle\langle 2| + \tau_{0,3}^{\mathrm{e}} \tau_{1,3}^{\mathrm{e}} \tau_{2,3}^{\mathrm{e}} \, |3\rangle\langle 3| , \tag{6.52}$$

which is not normalised on purpose similar to Eq. (6.19), i.e. $\mathrm{Tr}[\tau^{333}_{012}] \neq 1$. In this state, three pair of the levels are characterised with different virtual temperatures.

The steady state (6.51) is composed of another 16 steady states where three of the couplings are active (e.g τ^{333}_{012}). However, notice that the steady state (6.51) does not include all the possible steady states with three couplings present. For example, a case is excluded where three machines are coupled to the transitions $|0\rangle$ and $|1\rangle$, $|0\rangle$ and $|3\rangle$, and $|1\rangle$ and $|3\rangle$. There are some differences between the excluded cases and the included cases. In the excluded cases, one level is free. For the above example, the level $|2\rangle$ does not interact with any of the machines. Furthermore, the excluded cases essentially correspond to the situation shown in Fig. 6.2, where the three thermalisation processes compete. As studied in Sec. 6.2.1, this type of steady states cannot simply be written with the virtual temperatures, but effective rates are required in contrast to Eq. (6.52). In brief, the steady-state solution (6.51) is formed of 16 steady states that coherently interact with three machines, where the thermalisation processes caused by the machines do not compete against each other.

6.5 Conclusions

Treating multiple thermal machines in the quantum regime is difficult due to the large size of the systems. In this work, I have considered virtual qubits to effectively simplify the steady state of an arbitrary-level target system coupled with different two-qubit machines. By means of reset-type master equations, an analytical solution for n-level target systems has been derived. In particular, I have investigated details of three-level target systems and compared their analytical solution with numerical results of the full reset-type master equation and an optical (GKLS) master equation. It has been shown that these two models show the same behaviour for interaction-dependence and a different one for temperature-dependence. Nevertheless, these models help one to design machines and reveal important properties of the target system. As an example of utility of the findings obtained here, I have shown that the lasing transition in a three-level laser can be improved by utilising population inversion brought by negative temperatures.

In further studies, I could use this simplification method to investigate thermodynamic properties in multi-level machines, where even three-level systems have not been well investigated yet. Furthermore, the exploration of four-level machines is interesting since they include two-qubit machines as a special case but allow for more general coherent transitions and bath interactions [15]. It is an interesting question whether this additional freedom allows for improvements in efficiency and power. In addition, while I focused on the steady-state regime in this work, taking into account the transient regime would make our proposed method more powerful. This can be done by taking off-diagonal terms related to coherent interactions between the target system and machines. An approach expanded to the transient regime would help one to study coherent / entanglement generation in multi-level thermal machines [337, 338].

Chapter 7

Conclusion

In this thesis, I have described different topics in cold atomic systems, metrology, and quantum thermodynamics. For completeness, I will briefly summarise these topics and give an outlook for each of them.

Chapter 2. Spin-orbit coupling in the presence of strong atomic correlations

In this project, I have studied a one-dimensional system of two interacting particles in the presence of spin-orbit coupling (SOC) in a harmonic trap. SOC in many-particle systems of cold and neutral atoms, where two different internal states are regarded as pseudo-spin states and coupling between these pseudo-spin degrees and the momentum of atoms is induced by lasers, has been well studied. A typical treatment is to apply the mean-field approximation to describe the system using a macroscopic wave-function. In the mean-field regime, the ground state is classified into three types: the stripe phase, the magnetised phase, and the single minimum phase [132]. However, the ground state beyond the mean-field regime is hardly explored. To implement an exact treatment for SOC in the presence of strong interactions, I have considered two interacting particles in a harmonic trap and found that in this regime, a new type of ground state appears which includes the anti-symmetric pseudo-spin state. This is interesting since the anti-symmetric pseudo-spin state is usually not seen in the ground states of bosonic systems. The emergence of this ground state can be observed by measuring the total density and momentum distributions as well as the entanglement between pseudo-spins and the real space (position/momentum). This work has been published in New Journal of Physics **22** 01305 (2020).

In this work, I have shown that there is a trade-off between pseudo-spin entanglement and entanglement between pseudo-spin and real-space. This indicates that SOC can work as a control parameter to dynamically generate or distribute entanglement in certain degrees of freedoms. An idea for further exploration of SOC is to use SOC to convert from mode-entanglement to spatial entanglement. Non-adiabatic transport involving spin flips using time-dependent SOC has been proposed [166], which shows the usefulness of SOC in terms of spatial separation. By utilising SOC for transport, one could create spatial entanglement: first create pseudo-spin entanglement in cold atomic systems by tuning contact interactions, and then add SOC to move different pseudo-spin states in different directions so that the initial entanglement becomes spatial entanglement (it is also possible to use magnetic fields for transport [339]). To create strongly entangled states, strong contact interactions are required, and hence the knowledge obtained in this work will be helpful.

Chapter 3. Dynamical phase transitions in one-dimensional ultra-cold quantum gases: from the continuum to the lattice

In this work, I have investigated two models of one-dimensional bosonic systems that have a superfluid to insulator transition in order to study the relation between dynamical orthogonality and dynamical phase transitions. First, I considered a Tonks-Girardeau (TG) gas trapped in a box potential as a continuous model. After suddenly switching on a lattice potential, the system responds with non-equilibrium dynamics, and I have calculated numerically the rate function and the momentum distribution. Indeed, the rate function shows non-analytical cusps, which indicates dynamical orthogonality with the initial state, however these non-analyticities have a different period from that of a typical physical observable (the peak of momentum distribution). Furthermore, as a discrete model, I have considered the tight binding model. The dynamics of the rate function and the parity operator, which was selected as the order parameter, were investigated. While these quantities display similar behaviour to the continuous model, they are helpful to understand why the orthogonality is connected to the observable only for deep quenches. Considering the results obtained for this work and the fact that it is hard or impossible to observe global orthogonality from local measurements on pure [185] or mixed states [186], I conclude that it is generally difficult to detect orthogonality from many-body local observables with current knowledge and technologies. However, it may be possible in some special cases of spin models such as in Ref. [173], and also some tools to detect orthogonality exist, for example the extension of ancilla based interferometery schemes [188–191]. This work has been published in New Journal of Physics **19** 113018 (2017).

It is known that strongly correlated many-body systems are sensitive to temperature [195–197], and therefore it is interesting to study the interplay between quantum criticality and thermometry [198]. As shown in this chapter, the TG gas is a good platform to study non-equilibrium phenomena in many-body systems since the system enables one to compute many-body quantities with single-particle states. In this work, I assumed zero temperature, but it is possible to take finite temperatures into account [199]. While it is theoretically interesting to observe drastic change in a phase transition with finite temperature, experimentally the system always has non-zero temperature. Therefore, considering finite temperature is necessary beyond theoretical interest. Furthermore, it is fascinating to evaluate thermodynamic properties of the pinning transition in the TG gas. There, one could investigate the existence of critical scaling as described by the Kibble-Zurek (KZ) mechanism [340, 341], which characterises correlation lengths and relaxation times while the system is crossing over to another phase. There are some report studying the KZ mechanism in weakly interacting bosons, i.e. in the mean-field regime [342], but strongly interacting bosons have been little studied in this regard.

Chapter 4. Quantum probe spectroscopy for cold atomic systems

In this work, I have considered coupling a qubit to a single site in a lattice system and proposed an approach to extract information about the lattice filling by monitoring the qubit. Since the coupling is assumed to be weak enough to not disturb the lattice system, the probing process can be done in a non-destructive way. I have shown that the energy spectrum of the lattice can be obtained from the Fourier transformed signal of the probe. Although it is expected that the probe dynamics is affected by the energy characteristics of the lattice, in this work I have shown explicitly how the energy spectrum can be probed by its influence on the impurity dynamics described with Bessel functions. Furthermore, I have considered a realistic model that takes into account a dephasing effect, described by a Lindblad formalism, and demonstrated that the proposed approach still works within a certain regime of dephasing. Since feasible systems and probes are considered, as well as parameter regimes, I believe that the proposed approach can be realised and contribute to developing new measurement techniques for cold atomic systems. This work has been published in New Journal of Physics **20** 103006 (2018).

By taking advantages of techniques available in cold atomic systems, simulating other physical systems such as condensed matter systems has been attracting attention. In this work, I have considered a tight binding model and proposed an approach to extract the energy spectrum of the system. On the other hand, it is also interesting to consider different models such as the Bose-Hubbard model, where finite interactions can be taken into account, and probe various quantities. An interesting research direction of impurity dynamics is to embed an impurity in a many-body system and probe the temperature of the system [198, 343]. Temperature is a characteristic quantity of many-body systems, and demand for thermometry is ubiquitous. For example, for Bose-Hubbard models in cold atoms, controlling the tunnelling rate requires one to know the temperature of the lattice. In particular, there has been growing attention to the temperature of cold atoms due to the demand for high parameter controllability to study quantum phase transitions at finite temperature [195, 196, 344] as well as quantum simulations [10–12]. One could consider non-destructive thermometers, based on the work shown in the chapter.

Chapter 5. Bayesian parameter estimation using Gaussian states and measurements

In this work, I have investigated Bayesian parameter estimation scenarios by using single-mode Gaussian probe states and Gaussian measurements. Bayesian estimation strategies allow one to assume any prior distribution of the parameter to be estimated, unlike local estimation strategies. This work has not focused on revealing optimal sets of probe state and measurement schemes whose precision achieves the Heisenberg limit. Rather, this work has aimed to analyse the precision limit in feasible environments. As a comprehensive study, it gives important references for Bayesian parameter estimations and will be a good basis for advanced investigation into more complicated setups.

I have studied three paradigmatic parameter estimation scenarios: (i) displacement, (ii) phase, and (iii) squeezing strength. (i) For displacement estimation, I have displayed that a set of squeezed vacuum probe states and homodyne detection is optimal and agrees with the Bayesian quantum Cramér-Rao bound. (ii) For phase estimation, assuming flat prior, I have shown that homodyne detection leads to more accurate estimation than heterodyne detection, while one should be aware that the phase range concerned by homodyne detection is half of the range which heterodyne detection can deal with. (iii) For squeezing strength estimation, I have exhibited that by implementing homodyne detection, a combination of presqueezing and displacement for the probes provides the most efficient strategy. This work has been submitted to Quantum Science and Technology and is available as arXiv:2009.03709.

The findings of this work are helpful to explore Bayesian parameter estimation more deeply. An option for future work is to construct optimal or nearly optimal measurements by combining Gaussian measurements [305]. The resulting measurements could be non-Gaussian measurements but should still be feasible. Another option is to consider two-mode Gaussian probe states using the same framework as this work, such that two-mode entanglement can be considered [310]. It can be expected that this allows one to uncover aspects not considered in this work. Furthermore, one could consider multi-parameter estimation [311–314] in the framework of Bayesian scenarios. In reality, there are many situations where one wants to estimate more than a single parameter. For example, in cases where the earth's magnetic field strength is to be estimated, it is described as a 2D-vector. I note that before going into this research direction, it is necessary to figure out which set of multiple parameters are experimentally interesting or even possible to be estimated at the same time by carefully considering experimental setups. If the measurement basis for one parameter estimation is not orthogonal to that of another parameter, these two measurements conflict, and one has a trade-off between the accuracy of these two measurement outcomes. It would be a key point to choose probe states and measurements that have none or little of this conflict.

Chapter 6. Simplifying multi-level thermal machines using virtual qubits

Recently, thermodynamics in the quantum regime has been studied experimentally [322–327]; therefore, designing quantum thermal machines has become more interesting. While there are some studies about few-qubit machines [23, 315–321], there are few about larger systems, i.e. multi-level machines, due to complexity of such large systems. Here, I have addressed the issue of this complexity by using the idea of a virtual qubit [127] and have proposed an approach for simplifying the master equation describing a multi-level system composed of several qubit-machines. By using reset-type master equations, an analytical steady-state solution for n-level target systems was found. Particularly, I have focused on three-level systems whose energy gaps all coherently interact with three two-qubit machines, and compared their analytical steady-state solution to numerical results of the full reset-type master equation and an optical (GKLS) master equation. I have found that these models show the same behaviour for interaction-dependence and a different one for temperature-dependence. Nevertheless, these models are still helpful for designing thermal machines and revealing the parameter dependence of the target system. As a paradigmatic example of this approach being useful, I have shown that the lasing transition in a three-level laser can be enhanced by population inversion of a virtual qubit. This work is planned to be submitted to Quantum and is available on arXiv:2009.03832.

Based on the proposed approach, one could explore thermodynamic properties of multi-level machines. First, it would be a good starting point to investigate three-level machines and four-level machines. Especially, four-level machines include two-qubit machines as a special case but allow for more coherent transitions of bath interactions [15]. These additional freedom could improve the efficiency and power of the machines [126]. Furthermore, while this work focused on the steady-state regime, it would be interesting to consider the transient regime, i.e. study the dynamics before the target state becomes time-independent. Although for the steady-state regime the off-diagonal terms of the density matrix of the target state were not important, in the transient regime these terms become more critical to characterise the time-evolved state. Since it is known that more coherence and entanglement are observed in the transient regime [337, 338], an approach that covers the transient regime would help one to design better thermal machines that utilise more quantum resources.

Overall conclusion

I have explored different systems such as cold atoms trapped in a harmonic trap or lattice and optical systems throughout my PhD to reveal non-classicality from different perspectives. Strong interactions in quantum systems are key ingredients for entanglement and lead to interesting, non-classical features. Nevertheless, certain situations require to weaken the interactions, e.g. when probing a target system, where strong interactions between the probe and the target could destroy information encoded in the target or even the target system itself. In addition, I have shown that not only entanglement but also squeezing in phase space can be benefical and contribute to achieving non-classical limits for precision for parameter estimation. As future work that utilises my knowledge obtained in all these projects, it would be interesting to explore the roles of non-classicality in interacting systems from a thermodynamic perspective [345, 346]. The tunable contact interactions of cold atoms allow one to explore correlations in many-particle systems [347], and these quantum correlations have the potential to not only enhance the performance of thermodynamic machines compared to single-particle machines [348] but also to be converted to work or heat [25]. Also, by taking advantages of the controllability of cold atoms, the realisation of a simple but powerful model, the quantum Szilard engines [349], which demonstrate a connection between thermodynamics and information, has been proposed [350]. Therefore, it would be interesting to investigate effects of strong interactions not only in heat-based engines but also in information-consuming engines [351].

Bibliography

[1] A. Usui, T. Fogarty, S. Campbell, S. A. Gardiner, and T. Busch, Spin–orbit coupling in the presence of strong atomic correlations, New Journal of Physics **22**, 013050 (2020).

[2] T. Fogarty, A. Usui, T. Busch, A. Silva, and J. Goold, Dynamical phase transitions and temporal orthogonality in one-dimensional hard-core bosons: from the continuum to the lattice, New Journal of Physics **19**, 113018 (2017).

[3] A. Usui, B. Buča, and J. Mur-Petit, Quantum probe spectroscopy for cold atomic systems, New Journal of Physics **20**, 103006 (2018).

[4] S. Morelli, A. Usui, E. Agudelo, and N. Friis, Bayesian parameter estimation using Gaussian states and measurements, (2020), arXiv:2009.03709 .

[5] A. Usui, W. Niedenzu, and M. Huber, Simplifying multi-level thermal machines using virtual qubits, (2020), arXiv:2009.03832 .

[6] W. D. Phillips, Nobel Lecture: Laser cooling and trapping of neutral atoms, Rev. Mod. Phys. **70**, 721 (1998).

[7] E. Cornell, Very Cold Indeed: The Nanokelvin Physics of Bose-Einstein Condensation. Journal of research of the National Institute of Standards and Technology **101**, 419 (1996).

[8] D. Barredo, V. Lienhard, S. de Léséleuc, T. Lahaye, and A. Browaeys, Synthetic three-dimensional atomic structures assembled atom by atom, Nature **561**, 79 (2018).

[9] I. Bloch, J. Dalibard, and W. Zwerger, Many-body physics with ultracold gases, Rev. Mod. Phys. **80**, 885 (2008).

[10] J. I. Cirac and P. Zoller, Goals and opportunities in quantum simulation, Nature Physics **8**, 264 (2012).

[11] I. M. Georgescu, S. Ashhab, and F. Nori, Quantum simulation, Rev. Mod. Phys. **86**, 153 (2014).

[12] T. H. Johnson, S. R. Clark, and D. Jaksch, What is a quantum simulator? EPJ Quantum Technol **1**, 10 (2014).

[13] M. A. Nielsen and I. L. Chuang, *Quantum Computation and Quantum Information: 10th Anniversary Edition*, 10th ed. (Cambridge University Press, New York, NY, USA, 2011).

[14] L. Pezzè, A. Smerzi, M. K. Oberthaler, R. Schmied, and P. Treutlein, Quantum metrology with nonclassical states of atomic ensembles, Rev. Mod. Phys. **90**, 035005 (2018).

[15] M. T. Mitchison, Quantum thermal absorption machines: refrigerators, engines and clocks, Contemporary Physics **60**, 164 (2019).

[16] A. Ghosh, V. Mukherjee, W. Niedenzu, and G. Kurizki, Are quantum thermodynamic machines better than their classical counterparts? The European Physical Journal Special Topics **227**, 2043 (2019).

[17] N. Gisin and R. Thew, Quantum communication, Nature Photonics **1**, 165 (2007).

[18] A. Boaron, G. Boso, D. Rusca, C. Vulliez, C. Autebert, M. Caloz, M. Perrenoud, G. Gras, F. Bussières, M.-J. Li, D. Nolan, A. Martin, and H. Zbinden, Secure Quantum Key Distribution over 421 km of Optical Fiber, Phys. Rev. Lett. **121**, 190502 (2018).

[19] A. Boaron, B. Korzh, R. Houlmann, G. Boso, D. Rusca, S. Gray, M.-J. Li, D. Nolan, A. Martin, and H. Zbinden, Simple 2.5 GHz time-bin quantum key distribution, Applied Physics Letters **112**, 171108 (2018).

[20] B. Korzh, C. C. W. Lim, R. Houlmann, N. Gisin, M. J. Li, D. Nolan, B. Sanguinetti, R. Thew, and H. Zbinden, Provably secure and practical quantum key distribution over 307 km of optical fibre, Nature Photonics **9**, 163 (2015).

[21] U. Andersen, G. Leuchs, and C. Silberhorn, Continuous-variable quantum information processing, Laser & Photonics Reviews **4**, 337 (2010).

[22] C. Weedbrook, S. Pirandola, R. García-Patrón, N. J. Cerf, T. C. Ralph, J. H. Shapiro, and S. Lloyd, Gaussian quantum information, Rev. Mod. Phys. **84**, 621 (2012).

[23] J. Goold, M. Huber, A. Riera, L. del Rio, and P. Skrzypczyk, The role of quantum information in thermodynamics—a topical review, Journal of Physics A: Mathematical and Theoretical **49**, 143001 (2016).

[24] F. Binder, L. A. Correa, C. Gogolin, J. Anders, and G. Adesso, eds., *Thermodynamics in the Quantum Regime* (Springer, Cham, 2019) pp. 37–66.

[25] G. Vitagliano, C. Klöckl, M. Huber, and N. Friis, Trade-Off Between Work and Correlations in Quantum Thermodynamics, in *Thermodynamics in the Quantum Regime*, Vol. 195, edited by F. Binder, L. Correa, C. Gogolin, J. Anders, and G. Adesso (Springer, Cham, 2018) pp. 731 – 750.

[26] W. Ketterle, Nobel lecture: When atoms behave as waves: Bose-Einstein condensation and the atom laser, Rev. Mod. Phys. **74**, 1131 (2002).

[27] P. Kapitza, Viscosity of Liquid Helium below the λ-Point, Nature **141**, 74 (1938).

[28] C. J. Pethick and H. Smith, *Bose-Einstien Condensation in Dilute Gases*, 2nd ed. (Cambridge University Press, 2008).

[29] M. H. Anderson, J. R. Ensher, M. R. Matthews, C. E. Wieman, and E. A. Cornell, Observation of Bose-Einstein Condensation in a Dilute Atomic Vapor, Science **269**, 198 (1995).

[30] K. B. Davis, M. O. Mewes, M. R. Andrews, N. J. van Druten, D. S. Durfee, D. M. Kurn, and W. Ketterle, Bose-Einstein Condensation in a Gas of Sodium Atoms, Phys. Rev. Lett. **75**, 3969 (1995).

[31] T. Hänsch and A. Schawlow, Cooling of gases by laser radiation, Optics Communications **13**, 68 (1975).

[32] W. Ketterle and N. V. Druten, Evaporative Cooling of Trapped Atoms, (Academic Press, 1996) pp. 181 – 236.

[33] E. L. Raab, M. Prentiss, A. Cable, S. Chu, and D. E. Pritchard, Trapping of Neutral Sodium Atoms with Radiation Pressure, Phys. Rev. Lett. **59**, 2631 (1987).

[34] S. Chu, J. E. Bjorkholm, A. Ashkin, and A. Cable, Experimental Observation of Optically Trapped Atoms, Phys. Rev. Lett. **57**, 314 (1986).

[35] M. A. Cazalilla, R. Citro, T. Giamarchi, E. Orignac, and M. Rigol, One dimensional bosons: From condensed matter systems to ultracold gases, Rev. Mod. Phys. **83**, 1405 (2011).

[36] I. Bloch, Ultracold quantum gases in optical lattices, Nature Physics **1**, 23 (2005).

[37] M. Greiner, O. Mandel, T. Esslinger, T. W. Hänsch, and I. Bloch, Quantum phase transition from a superfluid to a Mott insulator in a gas of ultracold atoms, Nature **415**, 39 (2002).

[38] E. Haller, R. Hart, M. J. Mark, J. G. Danzl, L. Reichsöllner, M. Gustavsson, M. Dalmonte, G. Pupillo, and H.-C. Nägerl, Pinning quantum phase transition for a Luttinger liquid of strongly interacting bosons, Nature **466**, 597 (2010).

[39] K. Lelas, T. Ševa, H. Buljan, and J. Goold, Pinning quantum phase transition in a Tonks-Girardeau gas: Diagnostics by ground-state fidelity and the Loschmidt echo, Phys. Rev. A **86**, 033620 (2012).

[40] G. E. Astrakharchik, K. V. Krutitsky, M. Lewenstein, F. Mazzanti, and J. Boronat, Optical lattices as a tool to study defect-induced superfluidity, Phys. Rev. A **96**, 033606 (2017).

[41] M. Olshanii, Atomic Scattering in the Presence of an External Confinement and a Gas of Impenetrable Bosons, Phys. Rev. Lett. **81**, 938 (1998).

[42] S. Inouye, M. R. Andrews, J. Stenger, H. J. Miesner, D. M. Stamper-Kurn, and W. Ketterle, Observation of Feshbach resonances in a Bose–Einstein condensate, Nature **392**, 151 (1998).

[43] C. Chin, R. Grimm, P. Julienne, and E. Tiesinga, Feshbach resonances in ultracold gases, Rev. Mod. Phys. **82**, 1225 (2010).

[44] Y. J. Lin, K. Jiménez-García, and I. B. Spielman, Spin-orbit-coupled Bose–Einstein condensates, Nature **471**, 83 (2011).

[45] T. Kovachy, P. Asenbaum, C. Overstreet, C. A. Donnelly, S. M. Dickerson, A. Sugarbaker, J. M. Hogan, and M. A. Kasevich, Quantum superposition at the half-metre scale, Nature **528**, 530 (2015).

[46] P. Wang, Z.-Q. Yu, Z. Fu, J. Miao, L. Huang, S. Chai, H. Zhai, and J. Zhang, Spin-Orbit Coupled Degenerate Fermi Gases, Phys. Rev. Lett. **109**, 095301 (2012).

[47] L. W. Cheuk, A. T. Sommer, Z. Hadzibabic, T. Yefsah, W. S. Bakr, and M. W. Zwierlein, Spin-Injection Spectroscopy of a Spin-Orbit Coupled Fermi Gas, Phys. Rev. Lett. **109**, 095302 (2012).

[48] N. T. Zinner and A. S. Jensen, Comparing and contrasting nuclei and cold atomic gases, Journal of Physics G: Nuclear and Particle Physics **40**, 053101 (2013).

[49] H. Takeuchi, K. Kasamatsu, M. Tsubota, and M. Nitta, Tachyon Condensation Due to Domain-Wall Annihilation in Bose-Einstein Condensates, Phys. Rev. Lett. **109**, 245301 (2012).

[50] E. Zohar, J. I. Cirac, and B. Reznik, Quantum simulations of lattice gauge theories using ultracold atoms in optical lattices, Reports on Progress in Physics **79**, 014401 (2016).

[51] S. Nascimbène, N. Navon, K. J. Jiang, F. Chevy, and C. Salomon, Exploring the thermodynamics of a universal Fermi gas, Nature **463**, 1057 (2010).

[52] K. Huang and C. N. Yang, Quantum-Mechanical Many-Body Problem with Hard-Sphere Interaction, Phys. Rev. **105**, 767 (1957).

[53] E. Fermi, Ricera Sci. **7**, 12 (1936).

[54] T. Busch, B.-G. Englert, K. Rzażewski, and M. Wilkens, Two Cold Atoms in a Harmonic Trap, Foundations of Physics **28**, 549 (1998).

[55] P. O. Fedichev, Y. Kagan, G. V. Shlyapnikov, and J. T. M. Walraven, Influence of Nearly Resonant Light on the Scattering Length in Low-Temperature Atomic Gases, Phys. Rev. Lett. **77**, 2913 (1996).

[56] K. M. Jones, E. Tiesinga, P. D. Lett, and P. S. Julienne, Ultracold photoassociation spectroscopy: Long-range molecules and atomic scattering, Rev. Mod. Phys. **78**, 483 (2006).

[57] T. L. Nicholson, S. Blatt, B. J. Bloom, J. R. Williams, J. W. Thomsen, J. Ye, and P. S. Julienne, Optical Feshbach resonances: Field-dressed theory and comparison with experiments, Phys. Rev. A **92**, 022709 (2015).

[58] T. Kinoshita, T. Wenger, and D. S. Weiss, A quantum Newton's cradle, Nature **440**, 900 (2006).

[59] B.-G. Englert, *Lecture on Quantum Mechanics, Volume 1: Basic Matters* (World Science Publishing Co. Pte. Ltd., 2006).

[60] M. Danos and J. Rafelski, *Pocketbook of Mathematical Functions* (the National Bureau of Standards, 1984).

[61] M. Girardeau, Relationship between Systems of Impenetrable Bosons and Fermions in One Dimension, Journal of Mathematical Physics **1**, 516 (1960).

[62] B. Paredes, A. Widera, V. Murg, O. Mandel, S. Fölling, I. Cirac, G. V. Shlyapnikov, T. W. Hänsch, and I. Bloch, Tonks–Girardeau gas of ultracold atoms in an optical lattice, Nature **429**, 277 (2004).

[63] T. Kinoshita, T. Wenger, and D. S. Weiss, Local Pair Correlations in One-Dimensional Bose Gases, Phys. Rev. Lett. **95**, 190406 (2005).

[64] A. Minguzzi and D. M. Gangardt, Exact Coherent States of a Harmonically Confined Tonks-Girardeau Gas, Phys. Rev. Lett. **94**, 240404 (2005).

[65] A. del Campo and J. G. Muga, Dynamics of a Tonks-Girardeau gas released from a hard-wall trap, EPL (Europhysics Letters) **74**, 965 (2006).

[66] R. Pezer and H. Buljan, Momentum Distribution Dynamics of a Tonks-Girardeau Gas: Bragg Reflections of a Quantum Many-Body Wave Packet, Phys. Rev. Lett. **98**, 240403 (2007).

[67] R. Citro, A. Minguzzi, and F. W. J. Hekking, Quantum stirring as a probe of superfluidlike behavior in interacting one-dimensional Bose gases, Phys. Rev. B **79**, 172505 (2009).

[68] M. Collura, S. Sotiriadis, and P. Calabrese, Equilibration of a Tonks-Girardeau Gas Following a Trap Release, Phys. Rev. Lett. **110**, 245301 (2013).

[69] M. D. Girardeau, E. M. Wright, and J. M. Triscari, Ground-state properties of a one-dimensional system of hard-core bosons in a harmonic trap, Phys. Rev. A **63**, 033601 (2001).

[70] J. Goold and T. Busch, Ground-state properties of a Tonks-Girardeau gas in a split trap, Phys. Rev. A **77**, 063601 (2008).

[71] J. Goold, M. Krych, Z. Idziaszek, T. Fogarty, and T. Busch, An eccentrically perturbed Tonks-Girardeau gas, New Journal of Physics **12**, 093041 (2010).

[72] M. A. Cazalilla, One-dimensional optical lattices and impenetrable bosons, Phys. Rev. A **67**, 053606 (2003).

[73] A. Lazarides and M. Haque, Strongly interacting one-dimensional bosons in optical lattices of arbitrary depth: From the Bose-Hubbard to the sine-Gordon regime and beyond, Phys. Rev. A **85**, 063621 (2012).

[74] D. W. Hallwood, T. Ernst, and J. Brand, Robust mesoscopic superposition of strongly correlated ultracold atoms, Phys. Rev. A **82**, 063623 (2010).

[75] C. Schenke, A. Minguzzi, and F. W. J. Hekking, Nonadiabatic creation of macroscopic superpositions with strongly correlated one-dimensional bosons in a ring trap, Phys. Rev. A **84**, 053636 (2011).

[76] C. Schenke, A. Minguzzi, and F. W. J. Hekking, Probing superfluidity of a mesoscopic Tonks-Girardeau gas, Phys. Rev. A **85**, 053627 (2012).

[77] J. Schloss, A. Benseny, J. Gillet, J. Swain, and T. Busch, Non-adiabatic generation of NOON states in a Tonks-Girardeau gas, New Journal of Physics **18**, 035012 (2016).

[78] K. Lelas, T. Ševa, and H. Buljan, Loschmidt echo in one-dimensional interacting Bose gases, Phys. Rev. A **84**, 063601 (2011).

[79] R. Pezer, T. Gasenzer, and H. Buljan, Single-particle density matrix for a time-dependent strongly interacting one-dimensional Bose gas, Phys. Rev. A **80**, 053616 (2009).

[80] I. Žutić, J. Fabian, and S. Das Sarma, Spintronics: Fundamentals and applications, Rev. Mod. Phys. **76**, 323 (2004).

[81] M. Z. Hasan and C. L. Kane, Colloquium: Topological insulators, Rev. Mod. Phys. **82**, 3045 (2010).

[82] J. Dalibard, F. Gerbier, G. Juzeliūnas, and P. Öhberg, Colloquium: Artificial gauge potentials for neutral atoms, Rev. Mod. Phys. **83**, 1523 (2011).

[83] J. Higbie and D. M. Stamper-Kurn, Periodically Dressed Bose-Einstein Condensate: A Superfluid with an Anisotropic and Variable Critical Velocity, Phys. Rev. Lett. **88**, 090401 (2002).

[84] J. Higbie and D. M. Stamper-Kurn, Generating macroscopic-quantum-superposition states in momentum and internal-state space from Bose-Einstein condensates with repulsive interactions, Phys. Rev. A **69**, 053605 (2004).

[85] Y. J. Lin, R. L. Compton, K. Jiménez-García, J. V. Porto, and I. B. Spielman, Synthetic magnetic fields for ultracold neutral atoms, Nature **462**, 628 (2009).

[86] Y.-J. Lin, R. L. Compton, K. Jiménez-García, W. D. Phillips, J. V. Porto, and I. B. Spielman, A synthetic electric force acting on neutral atoms, Nature Physics **7**, 531 (2011).

[87] J.-Y. Zhang, S.-C. Ji, Z. Chen, L. Zhang, Z.-D. Du, B. Yan, G.-S. Pan, B. Zhao, Y.-J. Deng, H. Zhai, S. Chen, and J.-W. Pan, Collective Dipole Oscillations of a Spin-Orbit Coupled Bose-Einstein Condensate, Phys. Rev. Lett. **109**, 115301 (2012).

[88] D. L. Campbell, R. M. Price, A. Putra, A. Valdés-Curiel, D. Trypogeorgos, and I. B. Spielman, Magnetic phases of spin-1 spin–orbit-coupled Bose gases, Nature Communications **7**, 10897 (2016).

[89] X. Luo, L. Wu, J. Chen, Q. Guan, K. Gao, Z.-F. Xu, L. You, and R. Wang, Tunable atomic spin-orbit coupling synthesized with a modulating gradient magnetic field, Scientific Reports **6**, 18983 (2016).

[90] Y. Zhang, M. E. Mossman, T. Busch, P. Engels, and C. Zhang, Properties of spin–orbit-coupled Bose–Einstein condensates, Frontiers of Physics **11**, 118103 (2016).

[91] J. I. Cirac, M. Lewenstein, K. Mølmer, and P. Zoller, Quantum superposition states of Bose-Einstein condensates, Phys. Rev. A **57**, 1208 (1998).

[92] M. J. Steel and M. J. Collett, Quantum state of two trapped Bose-Einstein condensates with a Josephson coupling, Phys. Rev. A **57**, 2920 (1998).

[93] B.-G. Englert, *Lecture on Quantum Mechanics, Volume 3: Perturbed Evolution* (World Science Publishing Co. Pte. Ltd., 2006).

[94] C. R. Hamner, *Experiments with dispersion engineered Bose-Einstein condensates: Raman dressing and novel optical lattices*, Ph.D. thesis, Washington State University (2014).

[95] N. R. Cooper and Z. Hadzibabic, Measuring the Superfluid Fraction of an Ultracold Atomic Gas, Phys. Rev. Lett. **104**, 030401 (2010).

[96] H.-R. Chen, K.-Y. Lin, P.-K. Chen, N.-C. Chiu, J.-B. Wang, C.-A. Chen, P.-P. Huang, S.-K. Yip, Y. Kawaguchi, and Y.-J. Lin, Spin–Orbital-Angular-Momentum Coupled Bose-Einstein Condensates, Phys. Rev. Lett. **121**, 113204 (2018).

[97] Z. Wu, L. Zhang, W. Sun, X.-T. Xu, B.-Z. Wang, S.-C. Ji, Y. Deng, S. Chen, X.-J. Liu, and J.-W. Pan, Realization of two-dimensional spin-orbit coupling for Bose-Einstein condensates, Science **354**, 83 (2016).

[98] L. Huang, Z. Meng, P. Wang, P. Peng, S.-L. Zhang, L. Chen, D. Li, Q. Zhou, and J. Zhang, Experimental realization of two-dimensional synthetic spin–orbit coupling in ultracold Fermi gases, Nature Physics **12**, 540 (2016).

[99] Y. Zhang, G. Chen, and C. Zhang, Tunable Spin-orbit Coupling and Quantum Phase Transition in a Trapped Bose-Einstein Condensate, Scientific Reports **3**, 1937 (2013).

[100] K. Jiménez-García, L. J. LeBlanc, R. A. Williams, M. C. Beeler, C. Qu, M. Gong, C. Zhang, and I. B. Spielman, Tunable Spin-Orbit Coupling via Strong Driving in Ultracold-Atom Systems, Phys. Rev. Lett. **114**, 125301 (2015).

[101] J. Yin, Y. Cao, Y.-H. Li, S.-K. Liao, L. Zhang, J.-G. Ren, W.-Q. Cai, W.-Y. Liu, B. Li, H. Dai, G.-B. Li, Q.-M. Lu, Y.-H. Gong, Y. Xu, S.-L. Li, F.-Z. Li, Y.-Y. Yin, Z.-Q. Jiang, M. Li, J.-J. Jia, G. Ren, D. He, Y.-L. Zhou, X.-X. Zhang, N. Wang, X. Chang, Z.-C. Zhu, N.-L. Liu, Y.-A. Chen, C.-Y. Lu, R. Shu, C.-Z. Peng, J.-Y. Wang, and J.-W. Pan, Satellite-based entanglement distribution over 1200 kilometers, Science **356**, 1140 (2017).

[102] H. Bernien, S. Schwartz, A. Keesling, H. Levine, A. Omran, H. Pichler, S. Choi, A. S. Zibrov, M. Endres, M. Greiner, V. Vuletić, and M. D. Lukin, Probing many-body dynamics on a 51-atom quantum simulator, Nature **551**, 579 (2017).

[103] J. Zhang, G. Pagano, P. W. Hess, A. Kyprianidis, P. Becker, H. Kaplan, A. V. Gorshkov, Z. X. Gong, and C. Monroe, Observation of a many-body dynamical phase transition with a 53-qubit quantum simulator, Nature **551**, 601 (2017).

[104] F. Arute, K. Arya, R. Babbush, D. Bacon, J. C. Bardin, R. Barends, R. Biswas, S. Boixo, F. G. S. L. Brandao, D. A. Buell, B. Burkett, Y. Chen, Z. Chen, B. Chiaro, R. Collins, W. Courtney, A. Dunsworth, E. Farhi, B. Foxen, A. Fowler, C. Gidney, M. Giustina, R. Graff, K. Guerin, S. Habegger, M. P. Harrigan, M. J. Hartmann, A. Ho, M. Hoffmann, T. Huang, T. S. Humble, S. V. Isakov, E. Jeffrey, Z. Jiang, D. Kafri, K. Kechedzhi, J. Kelly, P. V. Klimov, S. Knysh, A. Korotkov, F. Kostritsa, D. Landhuis, M. Lindmark, E. Lucero, D. Lyakh, S. Mandrà, J. R. McClean, M. McEwen, A. Megrant, X. Mi, K. Michielsen, M. Mohseni, J. Mutus, O. Naaman, M. Neeley, C. Neill, M. Y. Niu, E. Ostby, A. Petukhov, J. C. Platt, C. Quintana, E. G. Rieffel, P. Roushan, N. C. Rubin, D. Sank, K. J. Satzinger, V. Smelyanskiy, K. J. Sung, M. D. Trevithick, A. Vainsencher, B. Villalonga, T. White, Z. J. Yao, P. Yeh, A. Zalcman, H. Neven, and J. M. Martinis, Quantum supremacy using a programmable superconducting processor, Nature **574**, 505 (2019).

[105] H. P. Yuen, Two-photon coherent states of the radiation field, Phys. Rev. A **13**, 2226 (1976).

[106] H. E. D. Scovil and E. O. Schulz-DuBois, Three-Level Masers as Heat Engines, Phys. Rev. Lett. **2**, 262 (1959).

[107] J. E. Geusic, E. O. S. Bois, R. W. De Grasse, and H. E. D. Scovil, Three Level Spin Refrigeration and Maser Action at 1500 mc/sec, Journal of Applied Physics **30**, 1113 (1959).

[108] J. E. Geusic, E. O. Schulz-DuBios, and H. E. D. Scovil, Quantum Equivalent of the Carnot Cycle, Phys. Rev. **156**, 343 (1967).

[109] T. W. Hänsch and A. L. Schawlow, Cooling of gases by laser radiation, Optics Communications **13**, 68 (1975).

[110] D. J. Wineland, R. E. Drullinger, and F. L. Walls, Radiation-Pressure Cooling of Bound Resonant Absorbers, Phys. Rev. Lett. **40**, 1639 (1978).

[111] R. Alicki, The quantum open system as a model of the heat engine, Journal of Physics A: Mathematical and General **12**, L103 (1979).

[112] R. Kosloff, A quantum mechanical open system as a model of a heat engine, The Journal of Chemical Physics **80**, 1625 (1984).

[113] M. O. Scully, M. S. Zubairy, G. S. Agarwal, and H. Walther, Extracting Work from a Single Heat Bath via Vanishing Quantum Coherence, Science **299**, 862 (2003).

[114] D. J. Wineland, C. Monroe, W. M. Itano, D. Leibfried, B. E. King, and D. M. Meekhof, Experimental issues in coherent quantum-state manipulation of trapped atomic ions, J. Res. Natl Inst. Stand. Technol **103**, 259 (1997).

[115] F. Schmidt-Kaler, S. Gulde, M. Riebe, T. Deuschle, A. Kreuter, G. Lancaster, C. Becher, J. Eschner, H. H. ffner, and R. Blatt, The coherence of qubits based on single Ca ions, Journal of Physics B: Atomic, Molecular and Optical Physics **36**, 623 (2003).

[116] Y. Nakamura, Y. A. Pashkin, and J. S. Tsai, Coherent control of macroscopic quantum states in a single-Cooper-pair box, Nature **398**, 786 (1999).

[117] J. M. Martinis, S. Nam, J. Aumentado, and C. Urbina, Rabi Oscillations in a Large Josephson-Junction Qubit, Phys. Rev. Lett. **89**, 117901 (2002).

[118] I. Chiorescu, Y. Nakamura, C. J. P. M. Harmans, and J. E. Mooij, Coherent Quantum Dynamics of a Superconducting Flux Qubit, Science **299**, 1869 (2003).

[119] A. Shakouri, Recent Developments in Semiconductor Thermoelectric Physics and Materials, Annual Review of Materials Research **41**, 399 (2011).

[120] M. W. Doherty, N. B. Manson, P. Delaney, F. Jelezko, J. Wrachtrup, and L. C. Hollenberg, The nitrogen-vacancy colour centre in diamond, Physics Reports **528**, 1 (2013).

[121] P. Erker, M. T. Mitchison, R. Silva, M. P. Woods, N. Brunner, and M. Huber, Autonomous Quantum Clocks: Does Thermodynamics Limit Our Ability to Measure Time? Phys. Rev. X **7**, 031022 (2017).

[122] P. P. Hofer, J. B. Brask, M. Perarnau-Llobet, and N. Brunner, Quantum Thermal Machine as a Thermometer, Phys. Rev. Lett. **119**, 090603 (2017).

[123] J. B. Brask, G. Haack, N. Brunner, and M. Huber, Autonomous quantum thermal machine for generating steady-state entanglement, New Journal of Physics **17**, 113029 (2015).

[124] K. Joulain, J. Drevillon, Y. Ezzahri, and J. Ordonez-Miranda, Quantum Thermal Transistor, Phys. Rev. Lett. **116**, 200601 (2016).

[125] G. Manzano, R. Sánchez, R. Silva, G. Haack, J. B. Brask, N. Brunner, and P. P. Potts, Hybrid Thermal Machines: Generalized Thermodynamic Resources for Multitasking, (2020), arXiv:2009.03830 .

[126] R. Silva, G. Manzano, P. Skrzypczyk, and N. Brunner, Performance of autonomous quantum thermal machines: Hilbert space dimension as a thermodynamical resource, Phys. Rev. E **94**, 032120 (2016).

[127] N. Brunner, N. Linden, S. Popescu, and P. Skrzypczyk, Virtual qubits, virtual temperatures, and the foundations of thermodynamics, Phys. Rev. E **85**, 051117 (2012).

[128] F. Ciccarello, Collision models in quantum optics, Quantum Measurements and Quantum Metrology **4**, 53 (20 Dec. 2017).

[129] O. Arısoy, S. Campbell, and O. E. Müstecaplıoğlu, Thermalization of Finite Many-Body Systems by a Collision Model, Entropy **21**, 1182 (2019).

[130] N. Linden, S. Popescu, and P. Skrzypczyk, How Small Can Thermal Machines Be? The Smallest Possible Refrigerator, Phys. Rev. Lett. **105**, 130401 (2010).

[131] P. Skrzypczyk, N. Brunner, N. Linden, and S. Popescu, The smallest refrigerators can reach maximal efficiency, Journal of Physics A: Mathematical and Theoretical **44**, 492002 (2011).

[132] Y. Li, L. P. Pitaevskii, and S. Stringari, Quantum Tricriticality and Phase Transitions in Spin-Orbit Coupled Bose-Einstein Condensates, Phys. Rev. Lett. **108**, 225301 (2012).

[133] E. H. Lieb and W. Liniger, Exact Analysis of an Interacting Bose Gas. I. The General Solution and the Ground State, Phys. Rev. **130**, 1605 (1963).

[134] E. H. Lieb, Exact Analysis of an Interacting Bose Gas. II. The Excitation Spectrum, Phys. Rev. **130**, 1616 (1963).

[135] B. Sutherland, *Beautiful Models: 70 Years of Exactly Solved Quantum Many-Body Problems* (WORLD SCIENTIFIC, 2004).

[136] N. T. Zinner, A. G. Volosniev, D. V. Fedorov, A. S. Jensen, and M. Valiente, Fractional energy states of strongly interacting bosons in one dimension, EPL (Europhysics Letters) **107**, 60003 (2014).

[137] D. Pęcak, A. S. Dehkharghani, N. T. Zinner, and T. Sowiński, Four fermions in a one-dimensional harmonic trap: Accuracy of a variational-ansatz approach, Phys. Rev. A **95**, 053632 (2017).

[138] G. Bougas, S. I. Mistakidis, and P. Schmelcher, Analytical treatment of the interaction quench dynamics of two bosons in a two-dimensional harmonic trap, Phys. Rev. A **100**, 053602 (2019).

[139] Q. Guan, X. Y. Yin, S. E. Gharashi, and D. Blume, Energy spectrum of a harmonically trapped two-atom system with spin–orbit coupling, Journal of Physics B: Atomic, Molecular and Optical Physics **47**, 161001 (2014).

[140] Q. Guan and D. Blume, Spin structure of harmonically trapped one-dimensional atoms with spin-orbit coupling, Phys. Rev. A **92**, 023641 (2015).

[141] C. D. Schillaci and T. C. Luu, Energy spectra of two interacting fermions with spin-orbit coupling in a harmonic trap, Phys. Rev. A **91**, 043606 (2015).

[142] C. Zhu, L. Dong, and H. Pu, Harmonically trapped atoms with spin–orbit coupling, Journal of Physics B: Atomic, Molecular and Optical Physics **49**, 145301 (2016).

[143] D. Blume, M. W. C. Sze, and J. L. Bohn, Harmonically trapped four-boson system, Phys. Rev. A **97**, 033621 (2018).

[144] P. Mujal, A. Polls, and B. Juliá-Díaz, Spin-orbit-coupled bosons interacting in a two-dimensional harmonic trap, Phys. Rev. A **101**, 043619 (2020).

[145] Q. Guan and D. Blume, Energetics and structural properties of two- and three-boson systems in the presence of one-dimensional spin-orbit coupling, Phys. Rev. A **100**, 042708 (2019).

[146] H. Zhai, Degenerate quantum gases with spin–orbit coupling: a review, Reports on Progress in Physics **78**, 026001 (2015).

[147] R. H. Dicke, Coherence in Spontaneous Radiation Processes, Phys. Rev. **93**, 99 (1954).

[148] H. Lipkin, N. Meshkov, and A. Glick, Validity of many-body approximation methods for a solvable model: (I). Exact solutions and perturbation theory, Nuclear Physics **62**, 188 (1965).

[149] Y. Huang and Z.-D. Hu, Spin and field squeezing in a spin-orbit coupled Bose-Einstein condensate, Scientific Reports **5**, 8006 (2015).

[150] C. Hamner, C. Qu, Y. Zhang, J. Chang, M. Gong, C. Zhang, and P. Engels, Dicke-type phase transition in a spin-orbit-coupled Bose-Einstein condensate, Nature Communications **5**, 4023 (2014).

[151] L. Bakemeier, A. Alvermann, and H. Fehske, Quantum phase transition in the Dicke model with critical and noncritical entanglement, Phys. Rev. A **85**, 043821 (2012).

[152] S. Dusuel and J. Vidal, Continuous unitary transformations and finite-size scaling exponents in the Lipkin-Meshkov-Glick model, Phys. Rev. B **71**, 224420 (2005).

[153] P. Ribeiro, J. Vidal, and R. Mosseri, Thermodynamical Limit of the Lipkin-Meshkov-Glick Model, Phys. Rev. Lett. **99**, 050402 (2007).

[154] S. Campbell, Criticality revealed through quench dynamics in the Lipkin-Meshkov-Glick model, Phys. Rev. B **94**, 184403 (2016).

[155] W. K. Wootters, Entanglement of Formation of an Arbitrary State of Two Qubits, Phys. Rev. Lett. **80**, 2245 (1998).

[156] W. K. Wootters, Entanglement of Formation and Concurrence, Quantum Info. Comput. **1**, 27 (2001).

[157] T. Yu and J. H. Eberly, Sudden Death of Entanglement, Science **323**, 598 (2009).

[158] F. Serwane, G. Zürn, T. Lompe, T. B. Ottenstein, A. N. Wenz, and S. Jochim, Deterministic Preparation of a Tunable Few-Fermion System, Science **332**, 336 (2011).

[159] A. N. Wenz, G. Zürn, S. Murmann, I. Brouzos, T. Lompe, and S. Jochim, From Few to Many: Observing the Formation of a Fermi Sea One Atom at a Time, Science **342**, 457 (2013).

[160] A. Bergschneider, V. M. Klinkhamer, J. H. Becher, R. Klemt, L. Palm, G. Zürn, S. Jochim, and P. M. Preiss, Experimental characterization of two-particle entanglement through position and momentum correlations, Nature Physics **15**, 640 (2019).

[161] K. Osterloh, M. Baig, L. Santos, P. Zoller, and M. Lewenstein, Cold Atoms in Non-Abelian Gauge Potentials: From the Hofstadter "Moth" to Lattice Gauge Theory, Phys. Rev. Lett. **95**, 010403 (2005).

[162] A. Jacob, P. Öhberg, G. Juzeliūnas, and L. Santos, Cold atom dynamics in non-Abelian gauge fields, Applied Physics B **89**, 439 (2007).

[163] B. M. Anderson, J. M. Taylor, and V. M. Galitski, Interferometry with synthetic gauge fields, Phys. Rev. A **83**, 031602 (2011).

[164] Y.-X. Du, H. Yan, D.-W. Zhang, C.-J. Shan, and S.-L. Zhu, Proposal for a rotation-sensing interferometer with spin-orbit-coupled atoms, Phys. Rev. A **85**, 043619 (2012).

[165] S. Liang, Z.-C. Li, W. Zhang, L. Zhou, and Z. Lan, Stückelberg interferometry using spin-orbit-coupled cold atoms in an optical lattice, Phys. Rev. A **102**, 033332 (2020).

[166] X. Chen, R.-L. Jiang, J. Li, Y. Ban, and E. Y. Sherman, Inverse engineering for fast transport and spin control of spin-orbit-coupled Bose-Einstein condensates in moving harmonic traps, Phys. Rev. A **97**, 013631 (2018).

[167] S. M. Dickerson, J. M. Hogan, A. Sugarbaker, D. M. S. Johnson, and M. A. Kasevich, Multiaxis Inertial Sensing with Long-Time Point Source Atom Interferometry, Phys. Rev. Lett. **111**, 083001 (2013).

[168] V. Xu, M. Jaffe, C. D. Panda, S. L. Kristensen, L. W. Clark, and H. Müller, Probing gravity by holding atoms for 20 seconds, Science **366**, 745 (2019).

[169] T. Langen, R. Geiger, and J. Schmiedmayer, Ultracold Atoms Out of Equilibrium, Annual Review of Condensed Matter Physics **6**, 201 (2015).

[170] A. Polkovnikov, K. Sengupta, A. Silva, and M. Vengalattore, Colloquium: Nonequilibrium dynamics of closed interacting quantum systems, Rev. Mod. Phys. **83**, 863 (2011).

[171] J. Eisert, M. Friesdorf, and C. Gogolin, Quantum many-body systems out of equilibrium, Nature Physics **11**, 124 (2015).

[172] L. D'Alessio, Y. Kafri, A. Polkovnikov, and M. Rigol, From quantum chaos and eigenstate thermalization to statistical mechanics and thermodynamics, Advances in Physics **65**, 239 (2016).

[173] M. Heyl, A. Polkovnikov, and S. Kehrein, Dynamical Quantum Phase Transitions in the Transverse-Field Ising Model, Phys. Rev. Lett. **110**, 135704 (2013).

[174] M. Heyl, Dynamical Quantum Phase Transitions in Systems with Broken-Symmetry Phases, Phys. Rev. Lett. **113**, 205701 (2014).

[175] B. Žunkovič, M. Heyl, M. Knap, and A. Silva, Dynamical Quantum Phase Transitions in Spin Chains with Long-Range Interactions: Merging Different Concepts of Nonequilibrium Criticality, Phys. Rev. Lett. **120**, 130601 (2018).

[176] J. C. Halimeh and V. Zauner-Stauber, Dynamical phase diagram of quantum spin chains with long-range interactions, Phys. Rev. B **96**, 134427 (2017).

[177] I. Homrighausen, N. O. Abeling, V. Zauner-Stauber, and J. C. Halimeh, Anomalous dynamical phase in quantum spin chains with long-range interactions, Phys. Rev. B **96**, 104436 (2017).

[178] H. P. Büchler, G. Blatter, and W. Zwerger, Commensurate-Incommensurate Transition of Cold Atoms in an Optical Lattice, Phys. Rev. Lett. **90**, 130401 (2003).

[179] F. Cartarius, E. Kawasaki, and A. Minguzzi, Dynamical depinning of a Tonks-Girardeau gas, Phys. Rev. A **92**, 063605 (2015).

[180] A. del Campo, Long-time behavior of many-particle quantum decay, Phys. Rev. A **84**, 012113 (2011).

[181] M. Pons, D. Sokolovski, and A. del Campo, Fidelity of fermionic-atom number states subjected to tunneling decay, Phys. Rev. A **85**, 022107 (2012).

[182] A. Minguzzi, P. Vignolo, and M. Tosi, High-momentum tail in the Tonks gas under harmonic confinement, Physics Letters A **294**, 222 (2002).

[183] E. Lieb, T. Schultz, and D. Mattis, Two soluble models of an antiferromagnetic chain, Annals of Physics **16**, 407 (1961).

[184] D. Rossini, R. Fazio, V. Giovannetti, and A. Silva, Quantum quenches, linear response and superfluidity out of equilibrium, EPL (Europhysics Letters) **107**, 30002 (2014).

[185] J. Walgate, A. J. Short, L. Hardy, and V. Vedral, Local Distinguishability of Multipartite Orthogonal Quantum States, Phys. Rev. Lett. **85**, 4972 (2000).

[186] C. H. Bennett, D. P. DiVincenzo, C. A. Fuchs, T. Mor, E. Rains, P. W. Shor, J. A. Smolin, and W. K. Wootters, Quantum nonlocality without entanglement, Phys. Rev. A **59**, 1070 (1999).

[187] J. C. Budich and M. Heyl, Dynamical topological order parameters far from equilibrium, Phys. Rev. B **93**, 085416 (2016).

[188] J. Goold, T. Fogarty, N. Lo Gullo, M. Paternostro, and T. Busch, Orthogonality catastrophe as a consequence of qubit embedding in an ultracold Fermi gas, Phys. Rev. A **84**, 063632 (2011).

[189] M. Knap, A. Shashi, Y. Nishida, A. Imambekov, D. A. Abanin, and E. Demler, Time-Dependent Impurity in Ultracold Fermions: Orthogonality Catastrophe and Beyond, Phys. Rev. X **2**, 041020 (2012).

[190] A. Sindona, J. Goold, N. Lo Gullo, S. Lorenzo, and F. Plastina, Orthogonality Catastrophe and Decoherence in a Trapped-Fermion Environment, Phys. Rev. Lett. **111**, 165303 (2013).

[191] A. Sindona, J. Goold, N. L. Gullo, and F. Plastina, Statistics of the work distribution for a quenched Fermi gas, New Journal of Physics **16**, 045013 (2014).

[192] M. Cetina, M. Jag, R. S. Lous, I. Fritsche, J. T. M. Walraven, R. Grimm, J. Levinsen, M. M. Parish, R. Schmidt, M. Knap, and E. Demler, Ultrafast many-body interferometry of impurities coupled to a Fermi sea, Science **354**, 96 (2016).

[193] M. Lacki and M. Heyl, Dynamical quantum phase transitions in collapse and revival oscillations of a quenched superfluid, Phys. Rev. B **99**, 121107 (2019).

[194] S. A. Weidinger, M. Heyl, A. Silva, and M. Knap, Dynamical quantum phase transitions in systems with continuous symmetry breaking, Phys. Rev. B **96**, 134313 (2017).

[195] P. Zanardi, H. T. Quan, X. Wang, and C. P. Sun, Mixed-state fidelity and quantum criticality at finite temperature, Phys. Rev. A **75**, 032109 (2007).

[196] P. Zanardi, L. Campos Venuti, and P. Giorda, Bures metric over thermal state manifolds and quantum criticality, Phys. Rev. A **76**, 062318 (2007).

[197] P. Zanardi, M. G. A. Paris, and L. Campos Venuti, Quantum criticality as a resource for quantum estimation, Phys. Rev. A **78**, 042105 (2008).

[198] M. Mehboudi, A. Sanpera, and L. A. Correa, Thermometry in the quantum regime: recent theoretical progress, Journal of Physics A: Mathematical and Theoretical **52**, 303001 (2019).

[199] Y. Y. Atas, D. M. Gangardt, I. Bouchoule, and K. V. Kheruntsyan, Exact nonequilibrium dynamics of finite-temperature Tonks-Girardeau gases, Phys. Rev. A **95**, 043622 (2017).

[200] M.-G. Hu, M. J. Van de Graaff, D. Kedar, J. P. Corson, E. A. Cornell, and D. S. Jin, Bose Polarons in the Strongly Interacting Regime, Phys. Rev. Lett. **117**, 055301 (2016).

[201] N. B. Jørgensen, L. Wacker, K. T. Skalmstang, M. M. Parish, J. Levinsen, R. S. Christensen, G. M. Bruun, and J. J. Arlt, Observation of Attractive and Repulsive Polarons in a Bose-Einstein Condensate, Phys. Rev. Lett. **117**, 055302 (2016).

[202] I. Bloch, J. Dalibard, and S. Nascimbène, Quantum simulations with ultracold quantum gases, Nature Physics **8**, 267 (2012).

[203] R. A. Hart, P. M. Duarte, T.-L. Yang, X. Liu, T. Paiva, E. Khatami, R. T. Scalettar, N. Trivedi, D. A. Huse, and R. G. Hulet, Observation of antiferromagnetic correlations in the Hubbard model with ultracold atoms, Nature **519**, 211 (2015).

[204] E. Cocchi, L. A. Miller, J. H. Drewes, M. Koschorreck, D. Pertot, F. Brennecke, and M. Köhl, Equation of State of the Two-Dimensional Hubbard Model, Phys. Rev. Lett. **116**, 175301 (2016).

[205] M. F. Parsons, A. Mazurenko, C. S. Chiu, G. Ji, D. Greif, and M. Greiner, Site-resolved measurement of the spin-correlation function in the Fermi-Hubbard model, Science **353**, 1253 (2016).

[206] M. Boll, T. A. Hilker, G. Salomon, A. Omran, J. Nespolo, L. Pollet, I. Bloch, and C. Gross, Spin- and density-resolved microscopy of antiferromagnetic correlations in Fermi-Hubbard chains, Science **353**, 1257 (2016).

[207] L. W. Cheuk, M. A. Nichols, K. R. Lawrence, M. Okan, H. Zhang, E. Khatami, N. Trivedi, T. Paiva, M. Rigol, and M. W. Zwierlein, Observation of spatial charge and spin correlations in the 2D Fermi-Hubbard model, Science **353**, 1260 (2016).

[208] J. H. Drewes, L. A. Miller, E. Cocchi, C. F. Chan, N. Wurz, M. Gall, D. Pertot, F. Brennecke, and M. Köhl, Antiferromagnetic Correlations in Two-Dimensional Fermionic Mott-Insulating and Metallic Phases, Phys. Rev. Lett. **118**, 170401 (2017).

[209] W. S. Bakr, J. I. Gillen, A. Peng, S. Fölling, and M. Greiner, A quantum gas microscope for detecting single atoms in a Hubbard-regime optical lattice, Nature **462**, 74 (2009).

[210] J. F. Sherson, C. Weitenberg, M. Endres, M. Cheneau, I. Bloch, and S. Kuhr, Single-atom-resolved fluorescence imaging of an atomic Mott insulator, Nature **467**, 68 (2010).

[211] A. Recati, P. O. Fedichev, W. Zwerger, J. von Delft, and P. Zoller, Atomic Quantum Dots Coupled to a Reservoir of a Superfluid Bose-Einstein Condensate, Phys. Rev. Lett. **94**, 040404 (2005).

[212] M. Bruderer and D. Jaksch, Probing BEC phase fluctuations with atomic quantum dots, New Journal of Physics **8**, 87 (2006).

[213] C. Kollath, M. Köhl, and T. Giamarchi, Scanning tunneling microscopy for ultracold atoms, Phys. Rev. A **76**, 063602 (2007).

[214] C. Zipkes, S. Palzer, C. Sias, and M. Köhl, A trapped single ion inside a Bose-Einstein condensate. Nature **464**, 388 (2010).

[215] S. Schmid, A. Härter, and J. H. Denschlag, Dynamics of a Cold Trapped Ion in a Bose-Einstein Condensate, Phys. Rev. Lett. **105**, 133202 (2010).

[216] S. Will, T. Best, S. Braun, U. Schneider, and I. Bloch, Coherent interaction of a single fermion with a small bosonic field. Phys. Rev. Lett. **106**, 115305 (2011).

[217] S. Hunn, M. Hiller, D. Cohen, T. Kottos, and A. Buchleitner, Inelastic chaotic scattering on a Bose–Einstein condensate, Journal of Physics B: Atomic, Molecular and Optical Physics **45**, 085302 (2012).

[218] N. Spethmann, F. Kindermann, S. John, C. Weber, D. Meschede, and A. Widera, Dynamics of single neutral impurity atoms immersed in an ultracold gas. Phys. Rev. Lett. **109**, 235301 (2012).

[219] T. Fukuhara, A. Kantian, M. Endres, M. Cheneau, P. Schauß, S. Hild, D. Bellem, U. Schollwöck, T. Giamarchi, C. Gross, I. Bloch, and S. Kuhr, Quantum dynamics of a mobile spin impurity, Nature Physics **9**, 235 (2013).

[220] C. Sabín, A. White, L. Hackermuller, and I. Fuentes, Impurities as a quantum thermometer for a Bose-Einstein condensate, Scientific Reports **4**, 6436 (2014).

[221] L. A. Correa, M. Mehboudi, G. Adesso, and A. Sanpera, Individual Quantum Probes for Optimal Thermometry, Phys. Rev. Lett. **114**, 220405 (2015).

[222] D. Hangleiter, M. T. Mitchison, T. H. Johnson, M. Bruderer, M. B. Plenio, and D. Jaksch, Nondestructive selective probing of phononic excitations in a cold Bose gas using impurities, Phys. Rev. A **91**, 013611 (2015).

[223] T. H. Johnson, F. Cosco, M. T. Mitchison, D. Jaksch, and S. R. Clark, Thermometry of ultracold atoms via nonequilibrium work distributions, Phys. Rev. A **93**, 053619 (2016).

[224] T. J. Elliott and T. H. Johnson, Nondestructive probing of means, variances, and correlations of ultracold-atomic-system densities via qubit impurities, Phys. Rev. A **93**, 043612 (2016).

[225] M. Streif, A. Buchleitner, D. Jaksch, and J. Mur-Petit, Measuring correlations of cold-atom systems using multiple quantum probes, Phys. Rev. A **94**, 053634 (2016).

[226] M. T. Mitchison, T. H. Johnson, and D. Jaksch, Probing the dynamic structure factor of a neutral Fermi superfluid along the BCS-BEC crossover using atomic impurity qubits, Phys. Rev. A **94**, 063618 (2016).

[227] M. Hohmann, F. Kindermann, T. Lausch, D. Mayer, F. Schmidt, and A. Widera, Single-atom thermometer for ultracold gases, Phys. Rev. A **93**, 043607 (2016).

[228] F. Cosco, M. Borrelli, F. Plastina, and S. Maniscalco, Momentum-Resolved and Correlations Spectroscopy Using Quantum Probes, Phys. Rev. A **95**, 053620 (2017).

[229] M. Hohmann, F. Kindermann, T. Lausch, D. Mayer, F. Schmidt, E. Lutz, and A. Widera, Individual Tracer Atoms in an Ultracold Dilute Gas, Phys. Rev. Lett **118**, 263401 (2017).

[230] E. Bentine, T. L. Harte, K. Luksch, A. J. Barker, J. Mur-Petit, B. Yuen, and C. J. Foot, Species-selective confinement of atoms dressed with multiple radiofrequencies, Journal of Physics B: Atomic, Molecular and Optical Physics **50**, 094002 (2017).

[231] F. Schmidt, D. Mayer, Q. Bouton, D. Adam, T. Lausch, N. Spethmann, and A. Widera, Quantum Spin Dynamics of Individual Neutral Impurities Coupled to a Bose-Einstein Condensate, Phys. Rev. Lett. **121**, 130403 (2018).

[232] D. L. Underwood, W. E. Shanks, J. Koch, and A. A. Houck, Low-disorder microwave cavity lattices for quantum simulation with photons, Phys. Rev. A **86**, 023837 (2012).

[233] D. L. Underwood, W. E. Shanks, A. C. Y. Li, L. Ateshian, J. Koch, and A. A. Houck, Imaging photon lattice states by scanning defect microscopy, Phys. Rev. X **6**, 021044 (2016).

[234] J. L. O'Brien, A. Furusawa, and J. Vučković, Photonic quantum technologies, Nature Photonics **3**, 687 (2009).

[235] C. Poli, M. Bellec, U. Kuhl, F. Mortessagne, and H. Schomerus, Selective enhancement of topologically induced interface states in a dielectric resonator chain, Nature Communications **6**, 6710 (2015).

[236] M. Aspelmeyer, T. J. Kippenberg, and F. Marquardt, Cavity optomechanics, Rev. Mod. Phys. **86**, 1391 (2014).

[237] H.-J. Stöckmann, *Quantum chaos: An introduction* (CUP, Cambridge, UK, 2006).

[238] V. Fernández-Hurtado, J. Mur-Petit, J. J. García-Ripoll, and R. A. Molina, Lattice scars: surviving in an open discrete billiard, New Journal of Physics **16**, 035005 (2014).

[239] P. Haikka, S. McEndoo, and S. Maniscalco, Non-Markovian probes in ultracold gases, Phys. Rev. A **87**, 012127 (2013).

[240] C. Benedetti, F. Salari Sehdaran, M. H. Zandi, and M. G. A. Paris, Quantum probes for the cutoff frequency of Ohmic environments, Phys. Rev. A **97**, 012126 (2018).

[241] M. Abramowitz and I. A. Stegun, *Handbook of Mathematical Functions with Formulas, Graphs, and Mathematical Tables* (Dover, New York, 1972) , see Eqs. 9.1.42-45.

[242] H. Häffner, C. Roos, and R. Blatt, Quantum computing with trapped ions, Physics Reports **469**, 155 (2008).

[243] S. Kuhr, W. Alt, D. Schrader, I. Dotsenko, Y. Miroshnychenko, A. Rauschenbeutel, and D. Meschede, Analysis of dephasing mechanisms in a standing-wave dipole trap, Phys. Rev. A **72**, 023406 (2005).

[244] H. P. Breuer and F. Petruccione, *The Theory of Open Quantum Systems*, 1st ed. (OUP, Oxford, 2007).

[245] D. Gabor, Theory of communication. Part 1: The analysis of information, J Inst Electr Eng - Part III Radio Commun Eng **93**, 429 (1946).

[246] B. Boashash, *Time-Frequency Signal Analysis and Processing*, 2nd ed. (Elsevier, Oxford, UK, 2003).

[247] M. Hohmann, F. Kindermann, B. Gänger, T. Lausch, D. Mayer, F. Schmidt, and A. Widera, Neutral impurities in a Bose-Einstein condensate for simulation of the Fröhlich-polaron, EPJ Quantum Technology **2**, 23 (2015).

[248] M. Endres, H. Bernien, A. Keesling, H. Levine, E. R. Anschuetz, A. Krajenbrink, C. Senko, V. Vuletic, M. Greiner, and M. D. Lukin, Atom-by-atom assembly of defect-free one-dimensional cold atom arrays, Science **354**, 1024 (2016).

[249] Q. Bouton, J. Nettersheim, D. Adam, F. Schmidt, D. Mayer, T. Lausch, E. Tiemann, and A. Widera, Single-Atom Quantum Probes for Ultracold Gases Boosted by Nonequilibrium Spin Dynamics, Phys. Rev. X **10**, 011018 (2020).

[250] J. Nokkala, F. Galve, R. Zambrini, S. Maniscalco, and J. Piilo, Complex quantum networks as structured environments: engineering and probing, Scientific Reports **6**, 26861 (2016).

[251] D. Burgarth and K. Maruyama, Indirect Hamiltonian identification through a small gateway, New Journal of Physics **11**, 103019 (2009).

[252] D. Burgarth, K. Maruyama, and F. Nori, Indirect quantum tomography of quadratic Hamiltonians, New Journal of Physics **13**, 013019 (2011).

[253] Y. Kato and N. Yamamoto, Structure identification and state initialization of spin networks with limited access, New Journal of Physics **16**, 023024 (2014).

[254] K. Mayer, A. Rodriguez, and A. Buchleitner, Matter-wave scattering from interacting bosons in an optical lattice, Phys. Rev. A **90**, 023629 (2014).

[255] T. L. Harte, E. Bentine, K. Luksch, A. J. Barker, D. Trypogeorgos, B. Yuen, and C. J. Foot, Ultracold atoms in multiple radio-frequency dressed adiabatic potentials, Phys. Rev. A **97**, 013616 (2018).

[256] J. Mur-Petit and R. A. Molina, Chiral bound states in the continuum, Phys. Rev. B **90**, 035434 (2014).

[257] S. I. Mistakidis, G. C. Katsimiga, G. M. Koutentakis, T. Busch, and P. Schmelcher, Pump-probe spectroscopy of Bose polarons: Dynamical formation and coherence, Phys. Rev. Research **2**, 033380 (2020).

[258] R. Demkowicz-Dobrzański, J. Kołodyński, and M. Guţă, The elusive Heisenberg limit in quantum-enhanced metrology, Nature Communications **3**, 1063 (2012).

[259] B. M. Escher, L. Davidovich, N. Zagury, and R. L. de Matos Filho, Quantum Metrological Limits via a Variational Approach, Phys. Rev. Lett. **109**, 190404 (2012).

[260] R. Chaves, J. B. Brask, M. Markiewicz, J. Kołodyński, and A. Acín, Noisy Metrology beyond the Standard Quantum Limit, Phys. Rev. Lett. **111**, 120401 (2013).

[261] P. Sekatski, M. Skotiniotis, and W. Dür, Dynamical decoupling leads to improved scaling in noisy quantum metrology, New Journal of Physics **18**, 073034 (2016).

[262] P. Sekatski, M. Skotiniotis, J. Kołodyński, and W. Dür, Quantum metrology with full and fast quantum control, Quantum **1**, 27 (2017).

[263] R. Gaiba and M. G. A. Paris, Squeezed vacuum as a universal quantum probe, Phys. Lett. A **373**, 934 (2009).

[264] O. Pinel, P. Jian, N. Treps, C. Fabre, and D. Braun, Quantum parameter estimation using general single-mode Gaussian states, Phys. Rev. A **88**, 040102(R) (2013).

[265] A. Monràs, Phase space formalism for quantum estimation of Gaussian states, (2013), arXiv:1303.3682 .

[266] Z. Jiang, Quantum Fisher information for states in exponential form, Phys. Rev. A **89**, 032128 (2014).

[267] D. Šafránek, A. R. Lee, and I. Fuentes, Quantum parameter estimation using multi-mode Gaussian states, New Journal of Physics **17**, 073016 (2015).

[268] D. Šafránek and I. Fuentes, Optimal probe states for the estimation of Gaussian unitary channels, Phys. Rev. A **94**, 062313 (2016).

[269] L. Rigovacca, A. Farace, L. A. M. Souza, A. De Pasquale, V. Giovannetti, and G. Adesso, Versatile Gaussian probes for squeezing estimation, Phys. Rev. A **95**, 052331 (2017).

[270] D. Šafránek, Estimation of Gaussian quantum states, Journal of Physics A: Mathematical and Theoretical **52**, 035304 (2019).

[271] A. Rivas and A. Luis, Sub-Heisenberg estimation of non-random phase shifts, New Journal of Physics **14**, 093052 (2012).

[272] D. W. Berry, M. J. W. Hall, M. Zwierz, and H. M. Wiseman, Optimal Heisenberg-style bounds for the average performance of arbitrary phase estimates, Phys. Rev. A **86**, 053813 (2012).

[273] Y. R. Zhang, G. R. Jin, J. P. Cao, W. M. Liu, and H. Fan, Unbounded quantum Fisher information in two-pathinterferometry with finite photon number, Phys. A: Math. Theor. **46**, 035302 (2013).

[274] M. G. A. Paris, QUANTUM ESTIMATION FOR QUANTUM TECHNOLOGY, International Journal of Quantum Information **07**, 125 (2009).

[275] G. Tóth and I. Apellaniz, Quantum metrology from a quantum information science perspective, Journal of Physics A: Mathematical and Theoretical **47**, 424006 (2014).

[276] R. Demkowicz-Dobrzański, M. Jarzyna, and J. Kołodyński, Quantum limits in optical interferometry, Progress in Optics **60**, 345 (2015).

[277] C. Oh, C. Lee, L. Banchi, S.-Y. Lee, C. Rockstuhl, and H. Jeong, Optimal measurements for quantum fidelity between Gaussian states and its relevance to quantum metrology, Phys. Rev. A **100**, 012323 (2019).

[278] J. S. Sidhu and P. Kok, Geometric perspective on quantum parameter estimation, AVS Quantum Science **2**, 014701 (2020).

[279] L. J. Fiderer, J. Schuff, and D. Braun, Neural-Network Heuristics for Adaptive Bayesian Quantum Estimation, (2020), arXiv:2003.02183 .

[280] J. Rubio, P. Knott, and J. Dunningham, Non-asymptotic analysis of quantum metrology protocols beyond the Cramér-Rao bound, Journal of Physics Communications **2**, 015027 (2018).

[281] J. Rubio and J. Dunningham, Quantum metrology in the presence of limited data, New Journal of Physics **21**, 043037 (2019).

[282] J. Rubio and J. Dunningham, Bayesian multiparameter quantum metrology with limited data, Phys. Rev. A **101**, 032114 (2020).

[283] E. Martínez-Vargas, C. Pineda, F. Leyvraz, and P. Barberis-Blostein, Quantum estimation of unknown parameters, Phys. Rev. A **95**, 012136 (2017).

[284] V. Cimini, M. G. Genoni, I. Gianani, N. Spagnolo, F. Sciarrino, and M. Barbieri, Diagnosing Imperfections in Quantum Sensors via Generalized Cramér-Rao Bounds, Phys. Rev. Appl. **13**, 024048 (2020).

[285] M. Valeri, E. Polino, D. Poderini, I. Gianani, G. Corrielli, A. Crespi, R. Osellame, N. Spagnolo, and F. Sciarrino, Experimental adaptive Bayesian estimation of multiple phases with limited data, (2020), arXiv:2002.01232 .

[286] J. Klauder and B. Skagerstam, *Coherent States* (World Scientific Publishing, Singapore, 1985).

[287] U. L. Andersen, T. Gehring, C. Marquardt, and G. Leuchs, 30 years of squeezed light generation, Physica Scripta **91**, 053001 (2016).

[288] M. G. Genoni, S. Olivares, and M. G. Paris, Optical phase estimation in the presence of phase diffusion, Phys. Rev. Lett. **106**, 153603 (2011).

[289] V. Giovannetti, S. Lloyd, and L. Maccone, Quantum Metrology, Phys. Rev. Lett. **96**, 010401 (2006).

[290] G. D'Agostini, *Bayesian Reasoning in Data Analysis: A Critical Introduction* (World Scientific Publishing, Singapore, 2003).

[291] W. M. Bolstad, *Understanding Computational Bayesian Statistics* (John Wiley & Sons, New Jersey, USA, 2009).

[292] M. A. Amaral Turkman, C. D. Paulino, and P. Müller, *Computational Bayesian Statistics: An Introduction* (Cambridge University Press, Cambridge, U.K., 2019).

[293] N. Friis, D. Orsucci, M. Skotiniotis, P. Sekatski, V. Dunjko, H. J. Briegel, and W. Dür, Flexible resources for quantum metrology, New Journal of Physics **19**, 063044 (2017).

[294] H. Raïffa and R. Schlaifer, *Applied statistical decision theory*, 6th ed. (Harvard University, Boston, USA, 1961).

[295] H. L. Van Trees, *Detection, Estimation, and Modulation Theory: Detection, Estimation, and Linear Modulation Theory* (Wiley Online Library, 2001).

[296] S. M. Kay, *Fundamentals of statistical signal processing* (Prentice Hall, New Jersey, USA, 1993).

[297] R. D. Gill and B. Y. Levit, Applications of the van Trees Inequality: A Bayesian Cramér-Rao Bound, Bernoulli **1**, 59 (1995).

[298] Arvind, B. Dutta, N. Mukunda, and R. Simon, The real symplectic groups in quantum mechanics and optics, Pramana **45**, 471 (1995).

[299] E. Wigner, On the Quantum Correction For Thermodynamic Equilibrium, Phys. Rev. **40**, 749 (1932).

[300] G. Chiribella, G. M. D'Ariano, P. Perinotti, and M. F. Sacchi, Covariant quantum measurements that maximize the likelihood, Phys. Rev. A **70**, 062105 (2004).

[301] A. A. Michelson and E. W. Morley, On the relative motion of the Earth and the luminiferous ether, American Journal of Science **34**, 333 (1887).

[302] N. Wiebe and C. Granade, Efficient Bayesian Phase Estimation, Phys. Rev. Lett. **117**, 010503 (2016).

[303] S. Paesani, A. A. Gentile, R. Santagati, J. Wang, N. Wiebe, D. P. Tew, J. L. O'Brien, and M. G. Thompson, Experimental Bayesian Quantum Phase Estimation on a Silicon Photonic Chip, Phys. Rev. Lett. **118**, 100503 (2017).

[304] F. Martínez-García, D. Vodola, and M. Müller, Adaptive Bayesian phase estimation for quantum error correcting codes, New Journal of Physics **21**, 123027 (2019).

[305] C. Oh, C. Lee, C. Rockstuhl, H. Jeong, J. Kim, H. Nha, and S.-Y. Lee, Optimal Gaussian measurements for phase estimation in single-mode Gaussian metrology, npj Quantum Information **5**, 10 (2019).

[306] S. Ataman, Optimal Mach-Zehnder phase sensitivity with Gaussian states, Phys. Rev. A **100**, 063821 (2019).

[307] A. S. Holevo, in *Quantum Probability and Applications to the Quantum Theory of Irreversible Processes*, edited by L. Accardi, A. Frigerio, and V. Gorini (Springer Berlin Heidelberg, Berlin, Heidelberg, 1984) pp. 153–172.

[308] G. J. Milburn, J. Corney, E. M. Wright, and D. F. Walls, Quantum dynamics of an atomic Bose-Einstein condensate in a double-well potential, Phys. Rev. A **55**, 4318 (1997).

[309] G. Chiribella, G. M. D'Ariano, and M. F. Sacchi, Optimal estimation of squeezing, Phys. Rev. A **73**, 062103 (2006).

[310] D. Šafránek, A. R. Lee, and I. Fuentes, Quantum parameter estimation using multi-mode Gaussian states, New Journal of Physics **17**, 073016 (2015).

[311] J. Liu, H. Yuan, X.-M. Lu, and X. Wang, Quantum Fisher information matrix and multiparameter estimation, Journal of Physics A: Mathematical and Theoretical **53**, 023001 (2019).

[312] J. S. Sidhu and P. Kok, Geometric perspective on quantum parameter estimation, AVS Quantum Science **2**, 014701 (2020).

[313] L. Bakmou, M. Daoud, and R. ahl laamara, Multiparameter quantum estimation theory in quantum Gaussian states, Journal of Physics A: Mathematical and Theoretical **53**, 385301 (2020).

[314] R. Demkowicz-Dobrzański, W. Górecki, and M. Guţă, Multi-parameter estimation beyond quantum Fisher information, Journal of Physics A: Mathematical and Theoretical **53**, 363001 (2020).

[315] R. Alicki, The quantum open system as a model of the heat engine, Journal of Physics A: Mathematical and General **12**, L103 (1979).

[316] R. Kosloff, A quantum mechanical open system as a model of a heat engine, The Journal of Chemical Physics **80**, 1625 (1984).

[317] R. Kosloff, Quantum Thermodynamics: A Dynamical Viewpoint, Entropy **15**, 2100 (2013).

[318] D. Gelbwaser-Klimovsky, W. Niedenzu, and G. Kurizki, Thermodynamics of Quantum Systems Under Dynamical Control, Advances In Atomic, Molecular, and Optical Physics **64**, 329 (2015).

[319] S. Vinjanampathy and J. Anders, Quantum thermodynamics, Contemporary Physics **57**, 545 (2016).

[320] A. Ghosh, W. Niedenzu, V. Mukherjee, and G. Kurizki, Thermodynamic Principles and Implementations of Quantum Machines, in *Thermodynamics in the Quantum Regime*, edited by F. Binder, L. A. Correa, C. Gogolin, J. Anders, and G. Adesso (Springer, Cham, 2019) pp. 37–66.

[321] S. Bhattacharjee and A. Dutta, Quantum thermal machines and batteries, (2020), arXiv:2008.07889 .

[322] J. V. Koski, V. F. Maisi, J. P. Pekola, and D. V. Averin, Experimental realization of a Szilard engine with a single electron, National Academy of Sciences **111**, 13786 (2014).

[323] J. Roßnagel, S. T. Dawkins, K. N. Tolazzi, O. Abah, E. Lutz, F. Schmidt-Kaler, and K. Singer, A single-atom heat engine, Science **352**, 325 (2016).

[324] J. Klaers, S. Faelt, A. Imamoglu, and E. Togan, Squeezed Thermal Reservoirs as a Resource for a Nanomechanical Engine beyond the Carnot Limit, Phys. Rev. X **7**, 031044 (2017).

[325] J. P. S. Peterson, T. B. Batalhão, M. Herrera, A. M. Souza, R. S. Sarthour, I. S. Oliveira, and R. M. Serra, Experimental Characterization of a Spin Quantum Heat Engine, Phys. Rev. Lett. **123**, 240601 (2019).

[326] D. von Lindenfels, O. Gräb, C. T. Schmiegelow, V. Kaushal, J. Schulz, M. T. Mitchison, J. Goold, F. Schmidt-Kaler, and U. G. Poschinger, Spin Heat Engine Coupled to a Harmonic-Oscillator Flywheel, Phys. Rev. Lett. **123**, 080602 (2019).

[327] J. Klatzow, J. N. Becker, P. M. Ledingham, C. Weinzetl, K. T. Kaczmarek, D. J. Saunders, J. Nunn, I. A. Walmsley, R. Uzdin, and E. Poem, Experimental Demonstration of Quantum Effects in the Operation of Microscopic Heat Engines, Phys. Rev. Lett. **122**, 110601 (2019).

[328] G. Manzano, R. Silva, and J. M. R. Parrondo, Autonomous thermal machine for amplification and control of energetic coherence, Phys. Rev. E **99**, 042135 (2019).

[329] S. Seah, S. Nimmrichter, and V. Scarani, Refrigeration beyond weak internal coupling, Phys. Rev. E **98**, 012131 (2018).

[330] G. Lindblad, On the generators of quantum dynamical semigroups, Communications in Mathematical Physics **48**, 119 (1976).

[331] V. Gorini, A. Kossakowski, and E. C. G. Sudarshan, Completely positive dynamical semigroups of N-level systems, Journal of Mathematical Physics **17**, 821 (1976).

[332] A. Tavakoli, G. Haack, M. Huber, N. Brunner, and J. B. Brask, Heralded generation of maximal entanglement in any dimension via incoherent coupling to thermal baths, Quantum **2**, 73 (2018).

[333] S. Krämer, D. Plankensteiner, L. Ostermann, and H. Ritsch, QuantumOptics.jl: A Julia framework for simulating open quantum systems, Computer Physics Communications **227**, 109 (2018).

[334] P. K. Mogensen and A. N. Riseth, Optim: A mathematical optimization package for Julia, The Journal of Open Source Software **3**, 615 (2018).

[335] E. Boukobza and D. J. Tannor, Three-Level Systems as Amplifiers and Attenuators: A Thermodynamic Analysis, Phys. Rev. Lett. **98**, 240601 (2007).

[336] W. Niedenzu, M. Huber, and E. Boukobza, Concepts of work in autonomous quantum heat engines, Quantum **3**, 195 (2019).

[337] J. B. Brask and N. Brunner, Small quantum absorption refrigerator in the transient regime: Time scales, enhanced cooling, and entanglement, Phys. Rev. E **92**, 062101 (2015).

[338] M. T. Mitchison, M. P. Woods, J. Prior, and M. Huber, Coherence-assisted single-shot cooling by quantum absorption refrigerators, New Journal of Physics **17**, 115013 (2015).

[339] G. Vitagliano, M. Fadel, A. Usui, N. Friis, and M. Huber, Entanglement detection in Bose-Einstein condensates, (2020), in prep.

[340] T. W. B. Kibble, Topology of cosmic domains and strings, Journal of Physics A: Mathematical and General **9**, 1387 (1976).

[341] W. H. Zurek, Cosmological experiments in superfluid helium? Nature **317**, 505 (1985).

[342] J. Beugnon and N. Navon, Exploring the Kibble–Zurek mechanism with homogeneous Bose gases, Journal of Physics B: Atomic, Molecular and Optical Physics **50**, 022002 (2017).

[343] M. T. Mitchison, T. Fogarty, G. Guarnieri, S. Campbell, T. Busch, and J. Goold, In Situ Thermometry of a Cold Fermi Gas via Dephasing Impurities, Phys. Rev. Lett. **125**, 080402 (2020).

[344] P. Zanardi, P. Giorda, and M. Cozzini, Information-Theoretic Differential Geometry of Quantum Phase Transitions, Phys. Rev. Lett. **99**, 100603 (2007).

[345] A. Hartmann, V. Mukherjee, W. Niedenzu, and W. Lechner, Many-body quantum heat engines with shortcuts to adiabaticity, Phys. Rev. Research **2**, 023145 (2020).

[346] A. Hartmann, V. Mukherjee, G. B. Mbeng, W. Niedenzu, and W. Lechner, Multi-spin counter-diabatic driving in many-body quantum Otto refrigerators, (2020), arXiv:2008.09327 .

[347] G. D. Chiara and A. Sanpera, Genuine quantum correlations in quantum many-body systems: a review of recent progress, Reports on Progress in Physics **81**, 074002 (2018).

[348] J. Jaramillo, M. Beau, and A. del Campo, Quantum supremacy of many-particle thermal machines, New Journal of Physics **18**, 075019 (2016).

[349] S. W. Kim, T. Sagawa, S. De Liberato, and M. Ueda, Quantum Szilard Engine, Phys. Rev. Lett. **106**, 070401 (2011).

[350] J. Bengtsson, M. N. Tengstrand, and S. M. Reimann, Bosonic Szilard engine assisted by Feshbach resonances, Phys. Rev. A **97**, 062128 (2018).

[351] J. Bengtsson, M. N. Tengstrand, A. Wacker, P. Samuelsson, M. Ueda, H. Linke, and S. M. Reimann, Quantum Szilard Engine with Attractively Interacting Bosons, Phys. Rev. Lett. **120**, 100601 (2018).

[352] P. Jeszenszki, H. Luo, A. Alavi, and J. Brand, Accelerating the convergence of exact diagonalization with the transcorrelated method: Quantum gas in one dimension with contact interactions, Phys. Rev. A **98**, 053627 (2018).

Appendix A

Matrix representation of the Hamiltonian (2.5)

In this appendix, I give details of the matrix representation of the Hamiltonian (2.5) for two interacting bosons trapped in a harmonic trap in the presence of SOC, used for the calculations in Chap. 2. Starting by ordering the basis states of the harmonic oscillator according to their total energy and the value of n_+,

$$
\begin{aligned}
&\left|0,0,\downarrow\downarrow\right\rangle, \left|0,0,\mathrm{S}\right\rangle, \left|0,0,\uparrow\uparrow\right\rangle, \left|0,1,\mathrm{A}\right\rangle, \\
&\left|1,0,\downarrow\downarrow\right\rangle, \left|1,0,\mathrm{S}\right\rangle, \left|1,0,\uparrow\uparrow\right\rangle, \left|1,1,\mathrm{A}\right\rangle, \\
&\left|0,2,\downarrow\downarrow\right\rangle, \left|0,2,\mathrm{S}\right\rangle, \left|0,2,\uparrow\uparrow\right\rangle, \left|0,3,\mathrm{A}\right\rangle, \\
&\left|2,0,\downarrow\downarrow\right\rangle, \left|2,0,\mathrm{S}\right\rangle, \left|2,0,\uparrow\uparrow\right\rangle, \left|2,1,\mathrm{A}\right\rangle, \\
&\left|1,2,\downarrow\downarrow\right\rangle, \left|1,2,\mathrm{S}\right\rangle, \left|1,2,\uparrow\uparrow\right\rangle, \left|1,3,\mathrm{A}\right\rangle, \\
&\left|3,0,\downarrow\downarrow\right\rangle, \left|3,0,\mathrm{S}\right\rangle, \left|3,0,\uparrow\uparrow\right\rangle, \left|3,1,\mathrm{A}\right\rangle, \cdots,
\end{aligned}
$$

one can produce a matrix representation of the Hamiltonian without the interaction term H_{int} as

$$
H - H_{\text{int}} = \begin{pmatrix}
A_{0,0} & B_1 & C_2 & 0 & 0 & 0 & 0 & 0 & 0 & \cdots \\
B_1^\dagger & A_{1,0} & 0 & B_2 & C_2 & 0 & 0 & 0 & 0 & \cdots \\
C_2^\dagger & 0 & A_{0,2} & 0 & B_1 & 0 & C_4 & 0 & 0 & \cdots \\
0 & B_2^\dagger & 0 & A_{2,0} & 0 & B_3 & 0 & C_2 & 0 & \cdots \\
0 & C_2^\dagger & B_1^\dagger & 0 & A_{1,2} & 0 & 0 & B_2 & 0 & \cdots \\
0 & 0 & 0 & B_3^\dagger & 0 & A_{3,0} & 0 & 0 & B_4 & \cdots \\
0 & 0 & C_4^\dagger & 0 & 0 & 0 & A_{0,4} & 0 & 0 & \cdots \\
0 & 0 & 0 & C_2^\dagger & B_2^\dagger & 0 & 0 & A_{2,2} & 0 & \cdots \\
0 & 0 & 0 & 0 & 0 & B_4^\dagger & 0 & 0 & A_{4,0} & \cdots \\
\vdots & \vdots & \vdots & \vdots & \vdots & \vdots & \vdots & \vdots & \vdots & \ddots
\end{pmatrix}, \tag{A.1}
$$

where each element is a 4 × 4 matrix such that

$$A_{n,2u} = \begin{pmatrix} n+2u+1 & \Upsilon & 0 & 0 \\ \Upsilon & n+2u+1 & \Upsilon & i\Lambda\sqrt{2u+1} \\ 0 & \Upsilon & n+2u+1 & 0 \\ 0 & -i\Lambda\sqrt{2u+1} & 0 & n+2u+2 \end{pmatrix}, \tag{A.2}$$

$$B_n = \begin{pmatrix} i\Lambda\sqrt{n} & 0 & 0 & 0 \\ 0 & 0 & 0 & 0 \\ 0 & 0 & -i\Lambda\sqrt{n} & 0 \\ 0 & 0 & 0 & 0 \end{pmatrix}, \tag{A.3}$$

$$C_{2u} = \begin{pmatrix} 0 & 0 & 0 & 0 \\ 0 & 0 & 0 & 0 \\ 0 & 0 & 0 & 0 \\ 0 & i\Lambda\sqrt{2u} & 0 & 0 \end{pmatrix} \tag{A.4}$$

for integer $n, u \geq 0$. A more compact representation, which also makes the structure of the matrix elements clear, is given by

$$H - H_{\text{int}} = \begin{pmatrix} \mathcal{A}_0 & \mathcal{B}_1 & \mathcal{C}_2 & 0 & 0 & 0 & \cdots \\ \mathcal{B}_1^\dagger & \mathcal{A}_1 & \mathcal{B}_2 & \mathcal{C}_2 & 0 & 0 & \cdots \\ \mathcal{C}_2^\dagger & \mathcal{B}_2^\dagger & \mathcal{A}_2 & \mathcal{B}_3 & \mathcal{C}_4 & 0 & \cdots \\ 0 & \mathcal{C}_2^\dagger & \mathcal{B}_3^\dagger & \mathcal{A}_3 & \mathcal{B}_4 & \mathcal{C}_4 & \cdots \\ 0 & 0 & \mathcal{C}_4^\dagger & \mathcal{B}_4^\dagger & \mathcal{A}_4 & \mathcal{B}_5 & \cdots \\ 0 & 0 & 0 & \mathcal{C}_4^\dagger & \mathcal{B}_5^\dagger & \mathcal{A}_5 & \cdots \\ \vdots & \vdots & \vdots & \vdots & \vdots & \vdots & \ddots \end{pmatrix}, \tag{A.5}$$

where for even and odd indices

$$\mathcal{A}_{2N} = \begin{pmatrix} A_{0,2N} & 0 & \cdots & 0 & 0 \\ 0 & A_{2,2(N-1)} & \cdots & 0 & 0 \\ \vdots & \vdots & \ddots & \vdots & \vdots \\ 0 & 0 & \cdots & A_{2(N-1),2} & 0 \\ 0 & 0 & \cdots & 0 & A_{2N,0} \end{pmatrix}, \tag{A.6}$$

$$\mathcal{A}_{2N+1} = \begin{pmatrix} A_{1,2N} & 0 & \cdots & 0 & 0 \\ 0 & A_{3,2(N-1)} & \cdots & 0 & 0 \\ \vdots & \vdots & \ddots & \vdots & \vdots \\ 0 & 0 & \cdots & A_{2(N-1)+1,2} & 0 \\ 0 & 0 & \cdots & 0 & A_{2N+1,0} \end{pmatrix}, \tag{A.7}$$

$$\mathcal{B}_{2N} = \begin{pmatrix} 0 & B_2 & 0 & \cdots & 0 & 0 \\ 0 & 0 & B_3 & \cdots & 0 & 0 \\ \vdots & \vdots & \vdots & \ddots & \vdots & \vdots \\ 0 & 0 & 0 & \cdots & B_{2(N-1)} & 0 \\ 0 & 0 & 0 & \cdots & 0 & B_{2N} \end{pmatrix}, \tag{A.8}$$

$$\mathcal{B}_{2N+1} = \begin{pmatrix} B_1 & 0 & \cdots & 0 & 0 \\ 0 & B_3 & \cdots & 0 & 0 \\ \vdots & \vdots & \ddots & \vdots & \vdots \\ 0 & 0 & \cdots & B_{2(N-1)+1} & 0 \\ 0 & 0 & \cdots & 0 & B_{2N+1} \end{pmatrix}, \tag{A.9}$$

$$\mathcal{C}_{2N} = \begin{pmatrix} C_{2N} & 0 & \cdots & 0 & 0 & 0 \\ 0 & C_{2(N-1)} & \cdots & 0 & 0 & 0 \\ \vdots & \vdots & \ddots & \vdots & \vdots & \vdots \\ 0 & 0 & \cdots & C_4 & 0 & 0 \\ 0 & 0 & \cdots & 0 & C_2 & 0 \end{pmatrix}. \tag{A.10}$$

The terms containing the delta-function type interactions are given by

$$\begin{aligned} H_{\text{int}} &= \left[g\,|{\downarrow\downarrow}\rangle\langle{\downarrow\downarrow}| + g_{\uparrow\downarrow}\left(|\mathrm{S}\rangle\langle\mathrm{S}| + |\mathrm{A}\rangle\langle\mathrm{A}|\right) + g\,|{\uparrow\uparrow}\rangle\langle{\uparrow\uparrow}|\right]\delta(|x_1 - x_2|) \\ &= \frac{1}{\sqrt{2}}\left[g\,|{\downarrow\downarrow}\rangle\langle{\downarrow\downarrow}| + g_{\uparrow\downarrow}\left(|\mathrm{S}\rangle\langle\mathrm{S}| + |\mathrm{A}\rangle\langle\mathrm{A}|\right) + g\,|{\uparrow\uparrow}\rangle\langle{\uparrow\uparrow}|\right]\delta(x_-). \end{aligned} \tag{A.11}$$

As the interactions do not affect the COM degree of freedom or the pseudo-spin degrees, the interaction energy matrix elements are given by

$$\begin{aligned} \langle m, 2u, {\downarrow\downarrow}|H_{\text{int}}|n, 2\nu, {\downarrow\downarrow}\rangle &= \frac{g}{\sqrt{2}}\delta_{m,n}\int dx_-\ \phi_{2u}(x_-)\,\phi_{2\nu}(x_-)\,\delta(x_-) \\ &= \frac{g}{\sqrt{2}}\delta_{m,n}\phi_{2u}(0)\phi_{2\nu}(0), \end{aligned} \tag{A.12a}$$

$$\langle m, 2u, \mathrm{S}|H_{\text{int}}|n, 2\nu, \mathrm{S}\rangle = \frac{g_{\uparrow\downarrow}}{\sqrt{2}}\delta_{m,n}\phi_{2u}(0)\phi_{2\nu}(0), \tag{A.12b}$$

$$\langle m, 2u, {\uparrow\uparrow}|H_{\text{int}}|n, 2\nu, {\uparrow\uparrow}\rangle = \frac{g}{\sqrt{2}}\delta_{m,n}\phi_{2u}(0)\phi_{2\nu}(0), \tag{A.12c}$$

$$\langle m, 2u+1, \mathrm{A}|H_{\text{int}}|n, 2\nu+1, \mathrm{A}\rangle = \frac{g_{\uparrow\downarrow}}{\sqrt{2}}\delta_{m,n}\phi_{2u+1}(0)\phi_{2\nu+1}(0) = 0, \tag{A.12d}$$

where the $\phi_n(x)$ are the eigenstates of harmonic oscillator in the position representation and

$$\begin{aligned} \frac{1}{\sqrt{2}}\phi_{2u}(0)\phi_{2\nu}(0) &= \frac{1}{\sqrt{2\pi}}\left(-\frac{1}{2}\right)^{u+\nu}\frac{\sqrt{(2u)!(2\nu)!}}{u!\nu!} \\ &\equiv f_{u,\nu} = f_{\nu,u}. \end{aligned} \tag{A.13}$$

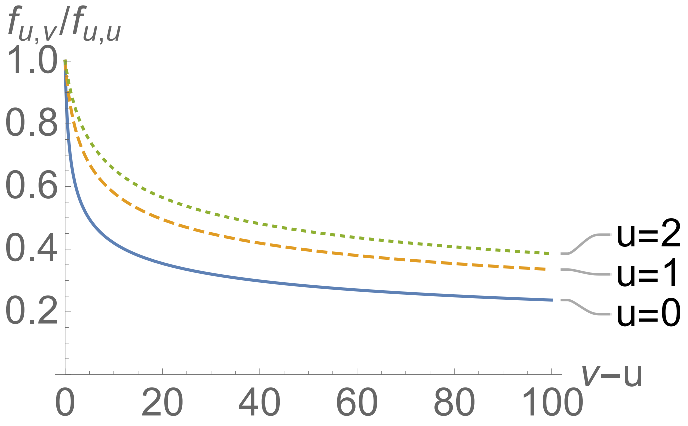

Figure A.1: Plot of the ratios $f_{u,\nu}/f_{u,u}$, each of which is given by (A.13). The off-diagonal term $f_{u,\nu}$ quantifies the strength of coupling caused by the contact interactions. The ratio is decaying to zero proportionally to $1/(\nu-u)$, i.e. not exponentially, which requires one to consider sufficient energy levels to ensure convergence within the system. This is reflected by the fact that it is difficult to describe non-smooth behaviour due to finite interactions with smooth functions composed of the eigenstates of the harmonic oscillator. However, a speed-up method for describing the non-smooth behaviours with some artificial non-smooth functions exists [352].

Note that the off-diagonal terms $f_{u,\nu}$ for $u<\nu$ are smaller than the diagonal terms $f_{u,u}$ and disappear for increasing difference $|\nu-u|$ (see Fig. A.1). The interaction term H_{int} can then be represented using $f_{u,\nu}$ as

$$\begin{aligned} H_{\text{int}} = \sum_{n=0}^{\infty}\sum_{u=0}^{\infty}\sum_{\nu=0}^{\infty} f_{u,\nu}\big(g\,|n,2u,\downarrow\downarrow\rangle\langle n,2\nu,\downarrow\downarrow| + g_{\uparrow\downarrow}\,|n,2u,\mathrm{S}\rangle\langle n,2\nu,\mathrm{S}| \\ + g\,|n,2u,\uparrow\uparrow\rangle\langle n,2\nu,\uparrow\uparrow|\big) \end{aligned} \tag{A.14}$$

and expressed in a matrix form as

$$H_{\text{int}} = \begin{pmatrix} F_{0,0} & 0 & F_{0,1} & 0 & 0 & 0 & F_{0,2} & 0 & 0 & \cdots \\ 0 & F_{0,0} & 0 & 0 & F_{0,1} & 0 & 0 & 0 & 0 & \cdots \\ F_{1,0} & 0 & F_{1,1} & 0 & 0 & 0 & F_{1,2} & 0 & 0 & \cdots \\ 0 & 0 & 0 & F_{0,0} & 0 & 0 & 0 & F_{0,1} & 0 & \cdots \\ 0 & F_{1,0} & 0 & 0 & F_{1,1} & 0 & 0 & 0 & 0 & \cdots \\ 0 & 0 & 0 & 0 & 0 & F_{0,0} & 0 & 0 & 0 & \cdots \\ F_{2,0} & 0 & F_{2,1} & 0 & 0 & 0 & F_{2,2} & 0 & 0 & \cdots \\ 0 & 0 & 0 & F_{1,0} & 0 & 0 & 0 & F_{1,1} & 0 & \cdots \\ 0 & 0 & 0 & 0 & 0 & 0 & 0 & 0 & F_{0,0} & \cdots \\ \vdots & \vdots & \vdots & \vdots & \vdots & \vdots & \vdots & \vdots & \vdots & \ddots \end{pmatrix}, \tag{A.15}$$

where each element is a 4×4 matrix such that

$$\begin{aligned} F_{u,\nu} &= \begin{pmatrix} f_{u,\nu} g & 0 & 0 & 0 \\ 0 & f_{u,\nu} & 0 & 0 \\ 0 & 0 & f_{u,\nu} & 0 \\ 0 & 0 & 0 & 0 \end{pmatrix} \\ &= F_{\nu,u}. \end{aligned} \tag{A.16}$$

Similar to Eq. (A.5), it can be written in a compact form as

$$H_{\text{int}} = \begin{pmatrix} \mathcal{F}_{0,0} & 0 & \mathcal{F}_{0,1} & 0 & \mathcal{F}_{0,2} & 0 & \cdots \\ 0 & \mathcal{F}_{0,0} & 0 & \mathcal{F}_{0,1} & 0 & \mathcal{F}_{0,2} & \cdots \\ \mathcal{F}_{0,1}^{\dagger} & 0 & \mathcal{F}_{1,1} & 0 & \mathcal{F}_{1,2} & 0 & \cdots \\ 0 & \mathcal{F}_{0,1}^{\dagger} & 0 & \mathcal{F}_{1,1} & 0 & \mathcal{F}_{1,2} & \cdots \\ \mathcal{F}_{0,2}^{\dagger} & 0 & \mathcal{F}_{1,2}^{\dagger} & 0 & \mathcal{F}_{2,2} & 0 & \cdots \\ 0 & \mathcal{F}_{0,2}^{\dagger} & 0 & \mathcal{F}_{1,2}^{\dagger} & 0 & \mathcal{F}_{2,2} & \cdots \\ \vdots & \vdots & \vdots & \vdots & \vdots & \vdots & \ddots \end{pmatrix}, \tag{A.17}$$

where for $N \leq M$ the matrix elements are given by the 4×4 matrices in Eq. (A.16) and the additional $M - N$ columns are filled with zeros

$$\mathcal{F}_{N,M} = \begin{bmatrix} F_{N,M} & 0 & \cdots & 0 & 0 & 0 & \cdots & 0 \\ 0 & F_{N-1,M-1} & \cdots & 0 & 0 & 0 & \cdots & 0 \\ \vdots & \vdots & \ddots & \vdots & \vdots & \vdots & \cdots & \vdots \\ 0 & 0 & \cdots & F_{1,M-N+1} & 0 & 0 & \cdots & 0 \\ 0 & 0 & 0 & 0 & F_{0,M-N} & \underbrace{0 & \cdots & 0}_{M-N} \end{bmatrix}. \tag{A.18}$$

The full Hamiltonian can then finally be expressed in a compact form as

$$H = \begin{pmatrix} \mathcal{A}_0 + \mathcal{F}_{0,0} & \mathcal{B}_1 & \mathcal{C}_2 + \mathcal{F}_{0,1} & 0 & \mathcal{F}_{0,2} & 0 & \cdots \\ \mathcal{B}_1^{\dagger} & \mathcal{A}_1 + \mathcal{F}_{0,0} & \mathcal{B}_2 & \mathcal{C}_2 + \mathcal{F}_{0,1} & 0 & \mathcal{F}_{0,2} & \cdots \\ \mathcal{C}_2^{\dagger} + \mathcal{F}_{0,1}^{\dagger} & \mathcal{B}_2^{\dagger} & \mathcal{A}_2 + \mathcal{F}_{1,1} & \mathcal{B}_3 & \mathcal{C}_4 + \mathcal{F}_{1,2} & 0 & \cdots \\ 0 & \mathcal{C}_2^{\dagger} + \mathcal{F}_{0,1}^{\dagger} & \mathcal{B}_3^{\dagger} & \mathcal{A}_3 + \mathcal{F}_{1,1} & \mathcal{B}_4 & \mathcal{C}_4 + \mathcal{F}_{1,2} & \cdots \\ \mathcal{F}_{0,2}^{\dagger} & 0 & \mathcal{C}_4^{\dagger} + \mathcal{F}_{1,2}^{\dagger} & \mathcal{B}_4^{\dagger} & \mathcal{A}_4 + \mathcal{F}_{2,2} & \mathcal{B}_5 & \cdots \\ 0 & \mathcal{F}_{0,2}^{\dagger} & 0 & \mathcal{C}_4^{\dagger} + \mathcal{F}_{1,2}^{\dagger} & \mathcal{B}_5^{\dagger} & \mathcal{A}_5 + \mathcal{F}_{2,2} & \cdots \\ \vdots & \vdots & \vdots & \vdots & \vdots & \vdots & \ddots \end{pmatrix}. \tag{A.19}$$